# Domain wall dynamics in magnetic nanostructures: Effect of magnetic field and electric current

Ales Hrabec

## To cite this version:

Ales Hrabec. Domain wall dynamics in magnetic nanostructures: Effect of magnetic field and electric current. Materials Science [cond-mat.mtrl-sci]. Université de Grenoble, 2011. English. NNT: 2011GRENY056. tel-00767418

HAL Id: tel-00767418
https://theses.hal.science/tel-00767418

Submitted on 19 Dec 2012

UNIVERSITÉ DE GRENOBLE

## THÈSE

Pour obtenir le grade de

**DOCTEUR DE L'UNIVERSITÉ DE GRENOBLE**

Spécialité: **Physique des matériaux**

Arrêté ministériel: 7 août 2006

Présentée par

**Aleš Hrabec**

Thèse dirigée par **Stefania PIZZINI**
et codirigée par **Laurent RANNO**

préparée au sein de **l'Institut Néel, CNRS, École Doctorale de Physique**

# Etude de la dynamique de l'aimantation dans des nanostructures à aimantation perpendiculaire: effet du champ magnétique et du courant électrique

Thèse soutenue publiquement le **6 December 2011**
devant le jury composé de :

**Alexandra MOUGIN**
Chargé de recherche, CNRS/Université Paris Sud, Rapporteur
**Stéphane MANGIN**
Professeur, Université Henri Poincaré, Nancy, Rapporteur
**Mairbek CHSHIEV**
Professeur, CEA/Université de Grenoble, Membre
**Fausto SIROTTI**
Directeur de recherche, CNRS/Synchrotron Soleil, Paris, Membre
**Stefania PIZZINI**
Directeur de recherche, CNRS/Université de Grenoble, Directrice de thèse
**Laurent RANNO**
Maitre de Conférence, CNRS/Université de Grenoble, Co-directeur de thèse

# Contents

# Introduction

Faster and faster. Smaller and smaller. Cheaper and cheaper. Men ask for more and more. In the last decades, one got used that the technological progress moves ahead like never before. We are living in exceptional times. Cars are becoming faster, steam drive was replaced by petrol, petrol is now being replaced by hydrogen and by electric energy. Power plants are running on coal, petrol, radioactive sources. However, the planet's energy sources are not inexhaustible. 'It is too late to be pessimists'. The dawn of use of renewable resources is unavoidable. Scientists predict that one has only a few decades to change the way one lives and avert the depletion of natural resources and the catastrophic evolution of the Earth's climate. Such effort goes ahead hand in hand with scientific progress and any tiny part of Science has its own importance. Only the time will reveal the rate of the particular relevance. One indivisible part of the technological tasks is the information storage and the access to it.

We have always needed to store information - to retain our memory, our knowledge, our tidings for future generations or the art. 32 000 years old cave paintings have been discovered in France and Spain, the geniture of the Sumerian archaic cuneiform script and the Egyptian hieroglyphs about 5000 years before Christ are probably the best testaments of first human's information storage ambitions. The first magnetic recording device was demonstrated and patented by the Danish inventor Poulsen in 1898. Poulsen made a magnetic recording of his voice on a length of piano wire. The history of magnetic recording traces the development of the technical breakthroughs which took place during the century from Paulsen's experiment to nowadays ubiquitous audio, video, and data recording technologies including tape recorders, video cassette recorders, mobile phones and computer hard drives.

In this technological age, a huge amount of information needs to be stored in a digital form. The density of stored data follows Moore's law which predicts doubling of the transistors per surface area every two years. In 2010, the minimum feature size in silicon circuit was about 30 nm. By 2020 the extrapolated transistor size will approach an atomic size. The huge amount of stored data reciprocally requires fast data access. Present electronics is based on the transport of electrical charges and until recently the spin of electron was not considered in electrical transport devices. The spin offers an extra parameter for electronics and the study of electronics based on spin parameter is called spin electronics or spintronics.

In 1988, the discovery of the giant magnetoresistance gave an enormous impulse to the industrial interest in spintronics applications. Albert Fert and Peter Grünberg, the main inventors of giant magnetoresistance, were awarded the Nobel prize in 2007. It was shown at the end of 1990's that a spin polarized current can act on the magnetization state and eventually it can lead to the magnetization reversal. Controlling the magnetization of nanodevices using local electric currents instead of externally applied magnetic fields opens a wide spectrum for increasing the data storage density and the speed of the data recording and readout. Nowadays, manipulation of domain walls, constituting local deformations of the magnetization separating two uniformly and oppositely magnetized domains, solely by an electric current is becoming an appealing issue. This is convenient for the shift register media which might use the third vertical dimension to store the data. This would lead to a gigantic increase of the data storage densities. To compete with other technologies, high-speed operation, and hence fast domain wall propagation, is essential. However, the power consumption in such devices is not negligible since the typical current densities required for current induced domain wall manipulation are of the order of $10^{11}$-$10^{12}$ A/m$^2$. Scientists all around the world are looking for materials and ways to make the domain wall manipulation as easy as possible.

The goal of this thesis is to study the potentially promising materials for current-induced domain wall motion. In the first chapter I review a basic background in magnetism, nanomagnetism and spin dependent transport, which will help to reader to follow more easily the topics discussed in this thesis. Chapter 2 reviews the recent progress and the state of the art of domain wall dynamics in systems with perpendicular anisotropy. In Chapter 3 I introduce material properties of ferrimagnetic alloy of $\mathrm{Gd}_{1-x}\mathrm{Co}_x$ with an induced composition gradient which will be used for magnetization dynamics studies described in Chapter 4.

The second material studied in this thesis is a trilayer of $\mathrm{Pt}\backslash\mathrm{Co}\backslash\mathrm{AlO}_x$, a system already shown to be suitable for fast and reproducible domain wall manipulation. Chapter 5 then deals with the magnetic and material parameters leading to the unique properties giving rise to very efficient spin-transfer torque. In Chapter 6 I experimentally test and proof a hypothesis connecting the spin-transfer torque efficiency with a transverse magnetic field having as origin the Rashba field at the Co interfaces.

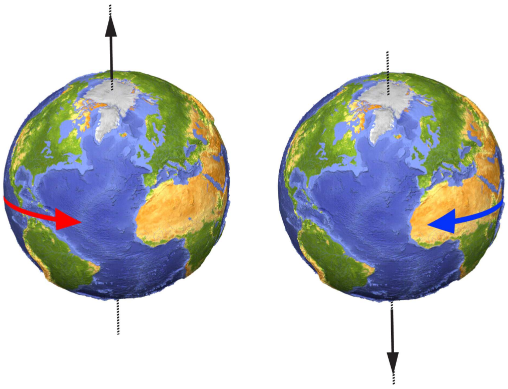

# Introduction

De plus en plus rapide. De plus en plus petit. De moins en moins cher. Les hommes demandent de plus en plus. Dans les dernières décennies, on s'est habitué au fait que le progrès technologique va de l'avant comme jamais auparavant. Nous vivons des temps exceptionnels. Les voitures sont de plus en plus rapides, l'entraînement à vapeur a été remplacé par l'essence, l'essence est maintenant remplacée par de l'hydrogène et de l'énergie électrique. Les centrales électriques fonctionnent au charbon, à l'essence, avec des sources radioactives. Cependant, les sources énergétiques de la planète ne sont pas inépuisables. "Il est trop tard pour être pessimiste". L'aube de l'utilisation des ressources renouvelables est inévitable. Les scientifiques prédisent que l'on ne dispose que de quelques décennies pour changer la façon dont on vit et éviter l'épuisement des ressources naturelles et de l'évolution catastrophique de celle du climat de la Terre. Ces efforts se concrétisent de pair avec le progrès scientifique et chaque partie infime de la science a sa propre importance. Seul le temps révélera le taux de la particulière pertinence. Une partie indivisible des tâches technologiques est le stockage et l'accès à l'information.

Nous avons toujours besoin de stocker des informations - de conserver notre mémoire, notre savoir, nos nouvelles pour les générations futures ou l'art. Des peintures rupestres vielles de 32 000 ans ont été découvertes en France et en Espagne. La génération de la l'écriture cunéiforme sumérienne archaïque et les hiéroglyphes Egyptiens d'environ 5000 ans avant Jésus-Christ sont probablement les meilleurs témoignages de la première ambition humaine de conserver l'information. Le premier dispositif pour l'enregistrement magnétique a été démontré et breveté par l'inventeur danois Poulsen en 1898. Poulsen enregistra sa voix sur une longueur de corde à piano. L'histoire de l'enregistrement magnétique retrace le développement des percées techniques qui ont eu lieu au cours du siècle, de l'expérience Paulsen aux omniprésents enregistreurs audio, vidéo et aux enregisteurs de données, y compris les magnétophones, magnétoscopes, téléphones portables et les disques durs d'ordinateur.

En cette ère technologique, une énorme quantité d'information doit être stockée sous forme numérique. La densité des données stockées suit la loi de Moore qui prédit le doublement des transistors par surface tous les deux ans. En 2010, la taille minimum des structures dans des circuits de silicium était d'environ 30 nm. En 2020 la taille extrapolée des transistors abordera la taille atomique. L'énorme quantité de données stockées nécessite réciproquement l'àcces rapide aux données. L'électronique actuelle est basée sur le transport de charges électriques et jusqu'à récemment, le spin de l'électron n'est pas pris en compte dans les dispositifs de transport d'électricité. Le spin offre un paramètre supplémentaire pour l'électronique et l'étude de l'électronique basée sur le paramètre de spin est appelée électronique de spin ou spintronique.

En 1988, la découverte de la magnétorésistance géante a donné une impulsion énorme à l'intérêt dans les applications industrielles de la spintronique. Albert Fert et Peter Grünberg, principals inventeurs de la magnétorésistance géante, ont reçu le prix Nobel en 2007. Vers la fin de 1990 il a été montré qu'un courant polarisé en spin peut agir sur l'état d'aimantation et conduire éventuellement à l'inversion de l'aimantation. Le contrôle de l'aimantation des nanodispositifs utilisant des courants électriques locaux plutôt que des champs magnétiques appliqués, ouvre un large spectre pour augmenter la densité de stockage de données et la rapidité de l'enregistrement des données et la lecture. Aujourd'hui, la manipulation des parois de domaines - constituant des déformations locales de l'aimantation séparant deux domaines aimantés de façon uniforme et opposées - uniquement par un courant électrique devient une question intéressante. Ceci est pratique pour des médias utilisant des registres à décalage, qui pourraient utiliser la troisième dimension verticale pour stocker les données. Cela conduirait è une augmentation gigantesque de la densité de stockage de données. Pour rivaliser avec les autres technologies, le fonctionnement à haute vitesse, et donc une propagation rapide des parois de domaine, est essentielle. Cependant, la consommation d'énergie dans de tels dispositifs n'est pas négligeable puisque les densités de courant typiques requises pour la manipulation courante des parois de domaines sont de l'ordre de $10^{11}$-$10^{12}$ A/m$^2$. Les scientifiques du monde entier sont à la recherche de matériaux et moyens pour rendre la manipulation des parois de domaine aussi facile que possible.

L'objectif de cette thèse est d'étudier les matériaux potentiellement prometteurs pour mouvement des parois induit par courant. Dans le premier chapitre je passe en revue une formation de base en magnétisme, transport et nanomagnétisme dépendant du spin, ce qui permettra au lecteur de suivre plus facilement les sujets abordés dans cette thèse. Dans le chapitre 2 je passe en revue les progrès récents et l'état de l'art de la dynamique de parois de domaines dans les systèmes à anisotropie perpendiculaire. Dans le chapitre 3, j'introduis les propriétés des matériaux en alliage ferrimagnétique de $\mathrm{Gd}_{1-x}\mathrm{Co}_x$ avec un gradient de composition induite, qui va être utilisé pour des études dynamique de l'aimantation décrit dans Chapitre 4.

Le second matériau étudié dans cette thèse est une tricouche de $\mathrm{Pt}\backslash\mathrm{Co}\backslash\mathrm{AlO}_x$, un système déjà montré être adapté a la manipulation rapide et reproductible des parois de domaine. Le chapitre 5 traite ensuite avec les paramètres magnétiques et du matériau conduisant a des propriétés uniques donnant lieu à un couple de transfert de spin très efficace. Dans le chapitre 6, je teste expérimentalement et je donne la preuve d'une hypothèse reliant l'efficacité du couple de transfert de spin à la présence d'un champ magnétique transversal ayant pour origine l'effet Rashba à l'interface du cobalt.

# Chapter 1

# Basic concepts of (nano)magnetism

The basic microscopic entity of magnetism is an electron which carries a net magnetic moment $\vec{\mu}$ of electronic origin. In a solid, an assembly of such moments behaves differently depending on the mutual interaction and basically we can distinguish the following magnetic phases:

- **Paramagnetism** characterizes substances which are composed of magnetic atoms with a weak mutual interaction. When an external magnetic field is applied, an induced magnetization in the field direction appears and the average amplitude of the moments is no longer zero. When the atomic moment amplitude does not depend on the field - localized magnetism (e.g. diluted oxides), the magnetization can be described by the Brillouin function. On the other hand, the magnetic moment can be also induced by the external field - band paramagnetism (e.g. platinum).

- **Antiferromagnetic** materials exhibit zero total magnetization. This is caused by the negative (exchange) interaction between neighboring atoms which tends to align the magnetic moments antiparallelly. The antiferromagnetic alignment is no longer preserved above the so-called Néel temperature $T_{\mathrm{N}}$ where the thermal energy becomes large enough to destroy the long-range magnetic ordering. $T_{\mathrm{N}}$ is then a measure of the antiferromagnetic interaction.

- **Ferromagnetism**, contrary to the latter case, can be characterized by a positive (exchange) interaction between neighboring atoms which favors parallel arrangement of magnetic moments. Below the so-called Curie temperature ($T_{\mathrm{c}}$) a spontaneous magnetization appears. In analogy with the Néel temperature in antiferromagnets, spontaneous magnetization ($M_s$) vanishes due to the thermal agitation at the Curie temperature. However a ferromagnetic material is not necessarily magnetized without any applied magnetic field below the $T_{\mathrm{c}}$. Due to the many competing energies, the ferromagnets is in general divided into small regions, the so-called magnetic domains, which exhibit each the spontaneous magnetization. Such magnetic domains are separated by a transition region, the domain wall. The only three elements which are ferromagnetic at ambient temperature are Fe, Ni and Co.

- **Ferrimagnetic** materials exhibit ferromagnetic and antiferromagnetic interaction at the same time. Two (or more) magnetic sublattices can be defined. Each magnetic lattice exhibits ferromagnetic behaviour but these two sublattices interact in such a way that antiparallel alignment of these two sublattices is favoured. In a special case the two magnetic sublattices can compensate each other so the total magnetization can vanish. Typically, this is the case of intermetallic compounds such as TbFe, GdFeCo, GdCo, etc.

- The alignment of the atomic moments does not need to be necessarily collinear, so more 'exotic' magnetic phases can be distinguished. For example, in some disordered and amorphous materials the magnetic moments at low temperature establish in more or less random directions. The group of such random magnetic phases is collectively called **spin glasses**. **Superparamagnetism** is another concept of magnetism named by Néel for tiny ($\sim 10\,\mathrm{nm}$) ferromagnetic particles. In these particles in a certain temperature range (above the blocking temperature and below $T_\mathrm{c}$) the total magnetic moment of all the coupled atoms fluctuates randomly ($k_\mathrm{B}T$ fluctuations are higher than anisotropy). Particles whose magnetization changes spontaneously are analogous to paramagnetic atoms, except that their magnetic moment is much larger.

This work deals with both ferromagnetic and ferrimagnetic materials, so a special attention will be devoted to these two cases.

## 1.1 Ferromagnetism

A material is called ferromagnetic when it shows a spontaneous magnetization in the absence of an external field. In this section, we will briefly remind some basic properties of ferromagnetic materials which arise from quantum mechanics.

The electron configuration of an atom is based on two relevant contributions. The Pauli exclusion principle does not allow two electrons to be in the same quantum state. The Coulomb interaction favours orbital fillings which separate the electron density.

### 1.1.1 Magnetism of atom

Every electron is described by a set of 4 quantum numbers: $n$ (energy level), $l$ (angular quantum number $L^2 = \hbar^2 l(l+1)$), $m_l$ (magnetic quantum number giving the projection of angular momentum $L_z = m_l\hbar$) and $m_s$ (spin projection quantum number). The $l$ number specifies the shape of angular electron densities. In chemistry $l = 0$ corresponds to the $s$ orbital, $l = 1$ to the $p$ orbital, $l = 2$ to the $d$ orbital (Fig. 1.1) and $l = 3$ to the $f$ orbital.

In an isolated atom, the filling of the electronic levels is driven by Hund's empirical rules:

1. Maximization of the total atomic spin angular momentum $\vec{S}$.
2. Maximization of the total atomic orbital angular momentum $\vec{L}$.
3. The consequence of the spin-orbit interaction $\lambda\vec{L}\cdot\vec{S}$ (which will be discussed later) is that the value of total angular momentum $J$ assumes in the lowest energy state

$$\begin{array}{ll} J = |L - S|, & \text{if the electron shell is less than half full,} \\ J = L + S, & \text{if the electron shell is more than half full,} \\ J = S, & \text{if the electron shell is exactly half full}(L = 0). \end{array} \tag{1.1}$$

However, we will see in the following that this rule is not always true. In materials where some other energies have a higher importance, this rule is disobeyed.

The magnetic moment is related to the total angular momentum $\vec{J}$ by relation

$$\vec{\mu} = -g\mu_\mathrm{B}\vec{J}, \tag{1.2}$$

where $g$ is the so-called $g$-factor or Landé factor and $\mu_\mathrm{B}$ is the Bohr magneton.

The consequence of these rules is that all isolated atoms with partially filled orbital levels have non-zero spin moments.

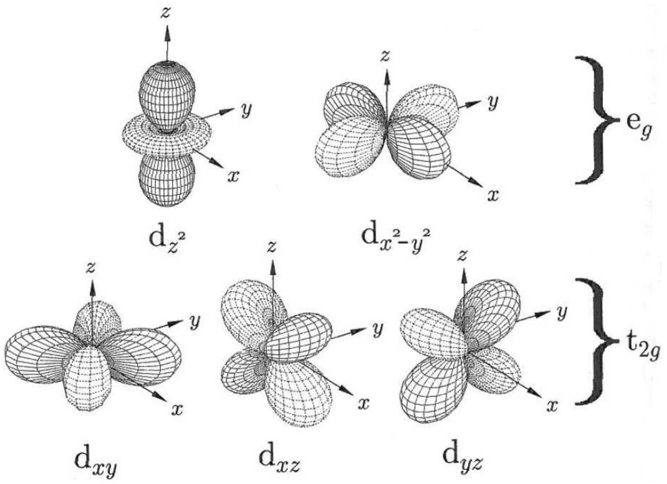

Figure 1.1: The angular distribution of the electron density of 5 different types $d$ orbitals in cubic symmetry environment which can be divided according to the theory of molecular symmetry into two groups: $t_{2g}$ and $e_g$. [1]

### 1.1.2 Crystal field

In solids the electronic states are perturbed by the local environment due to the crystal field, an electric field derived from the neighbouring atoms. This field has an important impact on the energy levels. Only the $s$ orbital has spherical symmetry whereas the other orbitals have a pronounced angular dependence. Due to the different orbital shapes the orbitals have different energies in the surrounding crystal field.

The character of the crystal field effect crucially depends on the symmetry of the local environment. The common case is the octahedral symmetry which is represented by six discrete points, producing a crystal field lying at the vertex of an octahedron. The situation with negatively charged vertices is shown in Fig. 1.2(a). The overlap of two different $d$ orbitals is shown in the $xy$ plane in Fig. 1.2(b) and (c). The $d_{xy}$ orbital has a lower overlap with the neighbouring orbitals than the $d_{x^2-y^2}$ orbital so it has a lower electrostatic energy. According to the theory of molecular symmetry, the orbitals can be divided into two groups: $t_{2g}$ and $e_g$. Hence the $t_{2g}$ group will be lowered in energy and the $e_g$ levels will raise in energy with respect to the isolated atom. The crystal field then leads to an energy splitting $\Delta$ as shown in Fig. 1.2(d).

Reciprocally, one can also consider the situation where the vertices are occupied by cations. Then the $e_g$ levels would have lower energy than $t_{2g}$ levels.

The filling of the orbitals then depends on the competition between the crystal field energy and the Coulomb interaction. The Coulomb interaction tends to fill orbitals in such a way that they are not doubly occupied, whereas the crystal field prefers filling the orbitals with lower energy ($t_{2g}$ in the octahedral symmetry case). The latter case leads to the so-called orbital quenching, so the $L \to 0$. Then the third Hund's rule is disobeyed and $J \simeq S$.

### 1.1.3 Spin-orbit interaction

So far, the spin and orbital angular momenta have been considered as independent. However, the spin-orbit interaction connects these two quantities. Then $\vec{L}$ and $\vec{S}$ are no longer conserved and the total angular momentum $\vec{J} = \vec{L} + \vec{S}$ becomes a constant of the motion. The spin-orbit interaction describes the effect of the electron orbital motion on its spin.

One can consider an electron which orbits around the nucleus with a velocity $\vec{v}$. From the electron

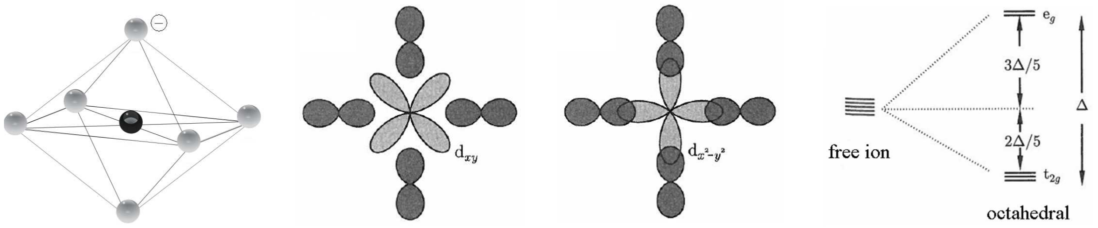

(a) (b) (c) (d)

Figure 1.2: (a) Atomic configuration in case of octahedral environment with a negative charge on the vertex. (b) In this configuration the $d_{xy}$, $d_{xz}$ and $d_{yz}$ orbitals will be lower in energy than the $d_{z^2}$ and $d_{x^2-y^2}$ (c). (d) The three lower-energy orbitals are collectively referred to as $t_{2g}$, and the two higher-energy orbitals as $e_g$. The two groups differ by energy $\Delta$ which is often called the crystal-field splitting parameter. [1]

rest frame it sees a positive charge motion, so the electron is in the center of a current loop which generates a magnetic field [1]:

$$\vec{B} = \frac{\vec{\varepsilon} \times \vec{v}}{c^2} \tag{1.3}$$

where $\vec{\varepsilon}$ is the electric field, which in the case of spherical potential reads

$$\vec{\varepsilon} = -\frac{\vec{r}}{r}\frac{\mathrm{d}V(r)}{\mathrm{d}r}.$$

Making use of the definition $\vec{L} = \vec{r} \times \vec{p}$ leads to

$$\vec{B} = \frac{1}{mc^2}\frac{1}{r}\frac{\mathrm{d}V}{\mathrm{d}r}\vec{L}.$$

The potential energy of the spin moment $\mu_s = -g\mu_\mathrm{B}S/\hbar$

$$U = -\mu_s \cdot B = \frac{g\mu_\mathrm{B}}{\hbar mc^2}\frac{1}{r}\frac{\mathrm{d}V}{\mathrm{d}r}\vec{L}\cdot\vec{S} = \lambda\vec{L}\cdot\vec{S}. \tag{1.4}$$

The consequence of the spin-orbit interaction follows from equation (1.4). The angular momentum tends to align the spin of the electron with preferential crystal axes and the spin-orbit interaction hence creates the magnetocrystalline anisotropy. The strength of such an anisotropy is then given by the spin-orbit interaction and the anisotropy of the environment.

The magnetocrystalline anisotropy should not be confused with the macroscopic shape anisotropy which is arising from the dipolar interaction in non-spherical samples, which will be discussed later.

### 1.1.4 Rashba effect

The Rashba interaction is a specific case of the spin-orbit interaction. It plays an important role only in systems where a uniform electric field, perpendicular to the plane in which the electrons are moving, is present.

In the absence of the spin-orbit interaction the state of the spin cannot be manipulated by use of an electric field because the spin state is independent of the angular momentum so

$$D\left(\vec{k},\uparrow\right) = D\left(\vec{k},\downarrow\right).$$

This is no more valid in the case of spin-orbit interaction when the angular momentum and spin are no longer independent quantities. The spin-orbit interaction removes the level degeneracy corresponding to levels with spin parallel or antiparallel to the orbit. Nevertheless, such a splitting is forbidden for systems with a center of inversion [4]. Apart from the materials without the inversion center, a special case with broken symmetry comes up at the crystal surface/interface. At the interface the spin degeneracy can be lifted so $D\left(\vec{k},\uparrow\right) \neq D\left(\vec{k},\downarrow\right)$. Rashba showed in 1960 [5] that the spin state $\vec{s}$ of an electron having momentum $\hbar\vec{k}$ can then be manipulated by an electric field $E\vec{e}_z$. This results in a magnetic field in the rest frame of the electron

$$\vec{H}_\mathrm{R} = \alpha_\mathrm{R}\left(\vec{e}_z \times \vec{k}\right) \tag{1.5}$$

where the parameter $\alpha_\mathrm{R}$ depends on the strength of the spin-orbit coupling and the intensity of the electric field.

The electric field in equation (1.5) can originate from the presence of an electric dipole which is formed in the surface vicinity. In the case of a metal, the density of the free electron gas must go to zero at the surface. The density of a free electron gas is described by the Weyl-Laue theorem [2] and is schematically shown in Fig. 1.3(a). The density of free electron gas $\rho(x)$ increases from zero at the surface up to the bulk value $\rho_\mathrm{V}$. Hence, close to the metal surface an electron depleted zone is created giving rise to the existence of an electric field which can be in approximation considered as perpendicular to the surface. The change of potential can be observed over a distance of the order of the Fermi wavelength $\lambda_\mathrm{F}$ [4]. In the case of a Au(111) surface $\lambda_\mathrm{F} \approx 5\mathring{A}$. Such a potential gradient can significantly change in the case of an interface or the presence of adsorbants.

However, the size of the splitting, estimated by using the surface potential gradient, is a few orders of magnitude smaller compared with experimental values [3]. This discrepancy is caused by the fact that the free electron model does not account for regions of steep nuclear potential gradients near atomic cores which is shown more realistically in Fig. 1.3(b) in the case of a Co/$\mathrm{Al_2O_3}$/Co sandwich.

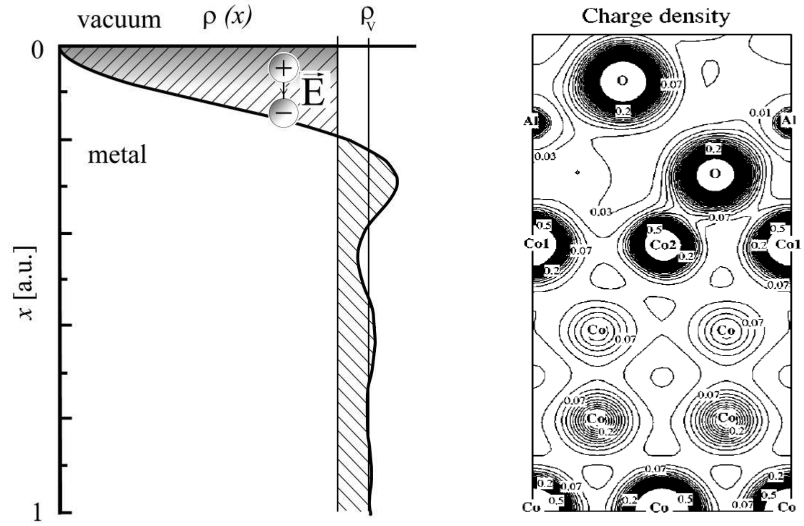

(a) (b)

Figure 1.3: (a) Density of the free electron gas $\rho(x)$ close to the metal/vacuum interface (x=0). The potential gradient gives rise to an electric field $\vec{E}$. (b) Charge-density contours of the O-terminated Co/$\mathrm{Al_2O_3}$/Co magnetic tunnel junction as calculated by Oleinik *et al.* [6].

One can consider the Hamiltonian of a free-electron in a system with the included spin-orbit term correction

$$\mathcal{H} = \frac{\hbar^2 k^2}{2m} + \mathcal{H}_\mathrm{SO}$$

which leads to a parabolic dispersion with a shift of its minimum

$$E = \frac{k^2}{2m} \pm \alpha_{\mathrm{R}} k.$$

The principle of the Rashba splitting is shown on the constant energy contours resulting from intersection between the electronic bands with the $(k_x, k_y)$ plane. In case of a non-magnetic material consisting of low $Z$ atoms, the resulting contour is a circle with degenerate spin levels. When a non-magnetic high $Z$ material is considered, close to a surface with an appropriate surface potential gradient, then the free-electron like dispersion will be split in two parabolas. In the $(k_x, k_y)$ plane these two levels are represented by two concentric circles [Fig. 1.4(a)]. These two states have opposite spin polarizations which are always perpendicular to the electron propagation direction. However, the net spin polarization at the surface is zero and the system remains non-magnetic.

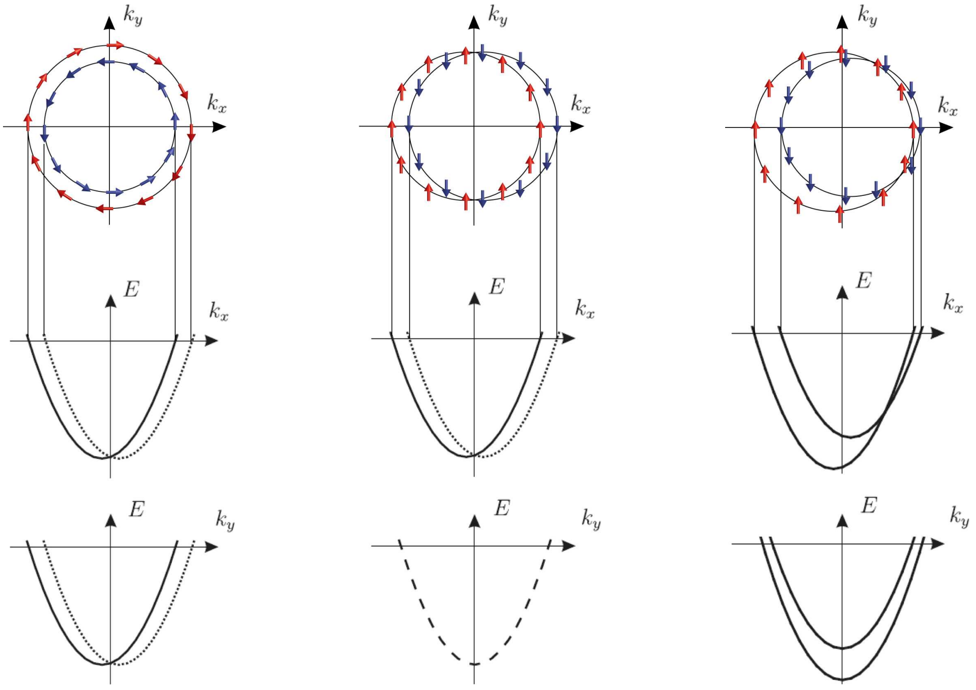

(a) (b) (c)

Figure 1.4: (a) Schematic representations of the electronic structure of a nonmagnetic surface in the case of Rashba spin-orbit splitting. (b) Hypothetical example of a ferromagnetic material with no exchange splitting with the quantization axis along the $y$ direction. (c) Situation of a magnetic surface with exchange and Rashba splittings. [7]

The situation is different in the case of a ferromagnetic surface, where all the spins are aligned along the quantization axis $y$. In this case the Rashba interaction does break the rotational symmetry and scales from a maximum value in the case in the $\vec{k} \perp \vec{s}$ direction to zero when $\vec{k} \| \vec{s}$. In a hypothetical example without exchange splitting, the contours for the two spin directions are represented by two circles which are mutually shifted [Fig. 1.4(b)]. This can be directly seen from the triple-vector product in equation (1.5) which is linear in the wave vector $\vec{k}$ and the spin orientation is fixed. The net magnetization is in this unreal case zero. In a real magnetic systems the exchange interaction dominates over the spin-orbit interaction which results in the situation shown in Fig. 1.4(c).

The change of magnetic moment due to the broken symmetry was experimentally observed for example at the surface of Ni [8], at a Cu/Co/Cu(100) interface [9] or at a Au\Co\Au thin film [10]. The Rashba effect was theoretically and experimentally investigated at the magnetic surface of heavy

Gd(0001) metal by Krupin *et al.* [11]. They have studied the impact of the surface oxidation on the effective electric field. It was found that in the case of an uncovered Gd surface the electric field is small giving rise to a small Rashba splitting. Additional adsorption of oxygen on Gd(0001) leads to the formation of a p(1×1)O/Gd(0001) superstructure. In the case of the oxidized magnetic surface the effective electric field changes sign and the rather asymmetric charge distribution at the interface reveals the high effective field. Hence the Rashba effect is enhanced.

Charge-density contours of the Co/$Al_2O_3$ were calculated by Oleinik *et al.* [6] and are presented in Fig. 1.3(b). This partial localization of the electron density induces high gradients of potential resulting in the electric field needed for the Rashba effect observation. The Rashba splitting is typically experimentally investigated by means of photoemission experiments.

## 1.2 Band structure of ferromagnets

All the described effects imply that in ferromagnets the electrons form complicated band structures. Ferromagnetic ordering occurs when in an electron system the two directions of spins (↑ and ↓) are unbalanced, i.e. the system is spin polarized. Such a behaviour results from a balance between atomic-like exchange interaction and interatomic hybridization [12].

A basic model of ferromagnetism was proposed by Stoner for the description of ferromagnetic metals with free-electron dispersion. This model assumes that spin-up and spin-down bands are spontaneously relatively shifted by an energy $\Delta_{xc}$. This process can be observed only when the so-called Stoner criterion is fulfilled:

$$Ug(E_\mathrm{F}) \geq 1, \tag{1.6}$$

where $U$ is the (exchange) energy representing the Coulomb interaction from the atom environment and $g(E_\mathrm{F})$ is the density of states at the Fermi level $E_\mathrm{F}$ [1]. So the existence of a spontaneous magnetization requires a strong Coulomb effect and a large density of states at the Fermi level.

A simplified model of a transition metal band structure is shown in Fig. 1.5. The Fermi level crosses the $d$ band ($3d$) in such a way that the spin-up states are fully occupied whereas the spin-down states are only partially filled. The $s$ states ($4s$) have a negligible splitting at equilibrium. Since the $d$ electrons have higher effective mass, they are considered as localized electrons and the $s$ electrons, due to their low effective mass, are considered as delocalized electrons.

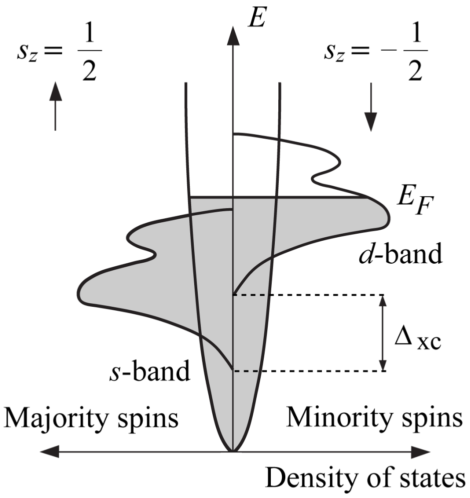

Figure 1.5: Density of states at the Fermi level $E_\mathrm{F}$ showing spontaneous magnetization in transition metals. The two bands are mutually shifted by the exchange splitting energy $\Delta_{xc}$.

## 1.3 Energies in Micromagnetism

In this thesis we are interested in studying magnetism of thin films on sub-micrometer scales where the atomic description is not possible. Micromagnetism treats the ferromagnetic material as a continuum and models its magnetic configuration. Domain theory and micromagnetism are based on the variational principle which is derived from thermodynamic principles based on Landau free energy $G_{\mathrm{L}}$ minimization.

In this section we will describe the four fundamental energies which play an important role.

### 1.3.1 Exchange Energy

This contribution arises from the short-range Coulomb interaction and the Pauli exclusion. Its basic consequence is that the adjacent magnetic moments prefer to be aligned collinearly. Any deviations from this ideal case induce an energy penalty. The exchange Hamiltonian reads:

$$\mathcal{H}_{\mathrm{ex}} = -\sum_{i \neq j} \mathcal{J}_{i,j} \vec{S}_i \cdot \vec{S}_j \tag{1.7}$$

where $\mathcal{J}_{ij}$ is the exchange constant which has units of energy. $\mathcal{J} > 0$ indicates a ferromagnetic interaction leading to the parallel spin alignment and $\mathcal{J} < 0$ indicates an antiferromagnetic interaction preferring the antiparallel spin alignment. If we assume only one dominant magnetic interaction between identical spins, so $\mathcal{J}_{i,j} = \mathcal{J}$ and $Z$ is the number of nearest neighbours, then we can define the Curie temperature

$$T_C = \frac{2Z\mathcal{J}S(S+1)}{3k_B}. \tag{1.8}$$

In the approximation of continuous magnetization, the exchange energy expression can be written as

$$E_{\mathrm{ex}} = \int_V A\left[(\nabla \mathbf{m_x})^2 + (\nabla \mathbf{m_y})^2 + (\nabla \mathbf{m_z})^2\right] \mathrm{d}V$$

where $A\,(\mathrm{J/m})$ is the exchange stiffness coefficient, which is in general temperature dependent. The magnitude of the exchange stiffness constant can be estimated $A \sim \mathcal{J}S^2 Z_c/a$, where $a$ is the lattice parameter and $Z_c$ is the number of atoms per unit cell.

The exchange interaction is isotropic so it does not define any preferential magnetization direction. In other words, the energy is constant when all the spins are coherently rotated, so this energy by itself gives rise to the uniform magnetization state.

### 1.3.2 Anisotropy Energy

In a crystalline material, the magnetization aligns preferentially along certain crystallographic directions: this is one of the aspects of the magnetic anisotropy which can be explained by the symmetry of the local environment.

In general, there are two distinct origins of magnetocrystalline anisotropy: The magnetic electron orbits, which are coupled to the spins via spin-orbit coupling, are interacting with the crystallographic structure, so that the magnetization prefers to align along well-defined crystallographic axes (easy axes). The second origin of the magnetocrystalline anisotropy arises from the dipole-dipole interaction leading to the 'head-to-tail' configuration of magnetic moments [13].

It should be distinguished between crystal anisotropy and induced anisotropy related to deviations from ideal crystal symmetry.

The first term of the magnetocrystalline energy in the case of uniaxial symmetry is given by the formula

$$E_{\mathrm{K}} = \int_V K \sin^2(\theta) \mathrm{d}V$$

where $\theta$ is the angle between the magnetization and the easy axis and $K$ is the first order anisotropy constant.

Materials with a low magnetic anisotropy are called soft magnetic materials while materials with a large magnetic anisotropy are called hard magnetic materials. The largest value of uniaxial anisotropy can be found in hexagonal and other uniaxial crystals like Co, $\mathrm{YCo_5}$ or FePt ($K_u \sim 10^6\,\mathrm{J/m^3}$). In cubic crystals like Fe the anisotropy is of the order of $K_u \sim 10^4\,\mathrm{J/m^3}$. On the other hand, the smallest values of anisotropies can be found in amorphous ferromagnets and cubic alloys ($K_u \sim 10^1\,\mathrm{J/m^3}$).

### 1.3.3 Zeeman Energy

If an external magnetic field $\vec{H}_{\mathrm{app}}$ is applied, the magnetization $\vec{M}$ is submitted to a torque which tends to align it into the field direction. The corresponding Zeeman energy term is then

$$E_{\mathrm{Z}} = -\mu_0 \int_V \vec{M} \cdot \vec{H}_{\mathrm{app}} \mathrm{d}V. \tag{1.9}$$

### 1.3.4 Magnetic Dipolar Energy

So far, all of the described energy contributions favour a uniform magnetization configuration. The magnetic domain structure is created in order to minimize the stray field and the magnetic energy stored outside the sample.

The magnetic dipolar energy has the same nature as the Zeeman energy but the origin of the field are the magnetic moments themselves. Such a field is called stray or demagnetizing field. The magnetic dipolar energy, also called the demagnetizing energy, can be written as

$$E_{\mathrm{d}} = -\frac{\mu_0}{2} \int_V \vec{H}_{\mathrm{d}} \cdot \vec{M} \mathrm{d}V.$$

In the special case of a uniformly magnetized ellipsoid, this field can be calculated analytically by using

$$\vec{H}_{\mathrm{d}} = -N\vec{M} \tag{1.10}$$

where $N$ is the demagnetizing tensor. The demagnetizing factor $N$ is in a general case a matrix and its basic property is that the trace of the matrix is equal to one, so $N_x + N_y + N_z = 1$.

A very useful concept in micromagnetism is the magnetic charge. Volume magnetic charges arise whenever the magnetization is nonuniform in such a way that $\vec{\nabla} \cdot \vec{M} \neq 0$. Surface magnetic charges arise whenever the magnetization has a component normal to an external or internal surface. The tendency to minimize surface charges leads to the fact that the magnetization tends to be parallel to the surfaces in soft magnetic materials. This leads to the so-called shape anisotropy. For example, in needle-shaped samples the magnetization usually lies along the long axis.

An important quantity related to the competition between the exchange energy and the demagnetizing energy is the so-called exchange length $\Lambda$, defined as:

$$\Lambda = \sqrt{\frac{A}{\mu_0 M_{\mathrm{s}}^2}}$$

which separates the zone where the exchange interaction dominates from the zone where the dipolar interactions dominate. When the distance is smaller than the exchange length, the magnetic moment cannot deviate much from the direction of its neighbours. In cobalt, for example, the exchange length is $\Lambda \simeq 3.5\,\mathrm{nm}$.

The exchange length gives the relevant scale to mesh samples in micromagnetic finite element models.

### 1.3.5 Energy Minimization

The Landau free energy can be calculated from the sum of energies described above:

$$G_{\mathrm{L}} = E_{\mathrm{ex}} + E_{\mathrm{K}} + E_{\mathrm{Z}} + E_{\mathrm{d}}.$$

The main issue of micromagnetism is to find the magnetization distribution in order to minimize the Landau free energy. One of the many ways to find the solutions was proposed by Brown [14] by employing the variational principle. It turns out that the magnetization in the equilibrium state is parallel to the effective field $H_{\mathrm{eff}}$. This field is composed of contributions from each energy:

$$\vec{H}_{\mathrm{eff}} = -\frac{1}{\mu_0}\frac{\partial G_{\mathrm{L}}}{\partial \vec{M}}.$$

The torque on the magnetization vanishes in such an equilibrium state, so that

$$\vec{M} \times \vec{H}_{\mathrm{eff}} = \vec{0}.$$

The Brown's equations have to take into account also the proper boundary conditions. Several numerical solvers (public code OOMMF, ...) for such an energy minimization have been recently developed.

## 1.4 Domain walls

Minimization of the free energy in magnetic materials leads to the formation of magnetic domains. A magnetic domain describes a region where the magnetization is uniform and usually parallel to an easy magnetization axis while the region separating the two domains is called a domain wall. The number and the size of the domains is governed by the competition between the relevant energies.

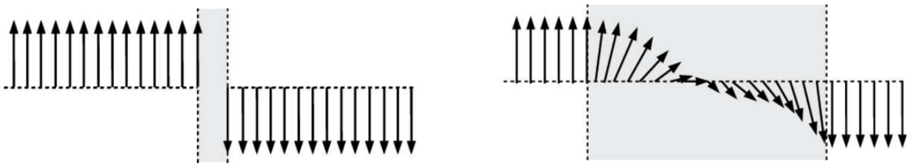
(a) (b)

Figure 1.6: A narrow domain wall with an abrupt transition between the two neighbouring domains (a) represents a high cost in exchange energy while a wide domain wall (b) represents a high cost in anisotropy energy.

Two domains separated by a narrow domain wall are shown in Fig. 1.6(a) with the magnetization along the easy anisotropy axis. Such an abrupt change of magnetization represents a high cost in exchange energy. In Fig. 1.6(b) is shown a smooth angular dependence of the magnetization between two adjacent domains occurring in a wide domain wall. This configuration lowers the exchange energy. On the other hand, the deviation of all these moments from the easy magnetization axis costs some anisotropy energy. The domain wall width is then determined by the relative value of $K$ and $A$.

The existence of magnetic domains was proposed in 1907 by Pierre Weiss and it was confirmed only in 1931 by the Bitter visualization technique. The transition region between two domains was analytically described by F. Bloch in 1932.

### 1.4.1 Domain wall description

The domain walls can be basically distinguished according to the angle between the two surrounding domains. A 90° domain wall separates domains with mutually perpendicular magnetization orientations, a 180° domain wall separates domains with antiparallel magnetization directions. A peculiar

360° domain wall separates two domains with a parallel magnetization configuration, which can be formed when two 180° domain walls meet.

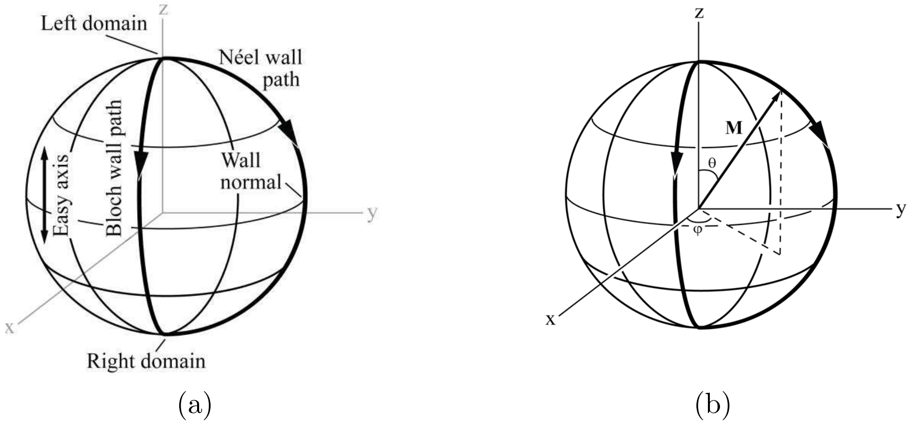

Figure 1.7: (a) Sphere of possible magnetization directions in a domain wall. The south and north pole correspond to the domain orientations and the meridian describes the magnetization reorientation in the wall. (b) Definition of the spherical coordinate system.

Let's discuss the simplest case of a 180° wall. The magnetization orientation within the wall can be shown on the sphere of possible magnetization directions in Fig. 1.7(a). The magnetization direction of a left domain pointing up coincides with the north pole of the sphere and the magnetization of the right domain pointing down coincides with the south pole. Hence it is convenient to use spherical coordinates as shown in Fig. 1.7(b). Two basic cases can be distinguished [15]:

- The magnetization path lies in a plane perpendicular to the plane of the domain magnetization $M(r, \theta, \varphi = 0)$. Such a domain wall is called a **Bloch wall** [Fig. 1.8(a)].
- The magnetization path lies in the plane of the domain magnetization $M(r, \theta, \varphi = \pi/2)$. This kind of domain wall is called a **Néel wall** [Fig. 1.8(b)].

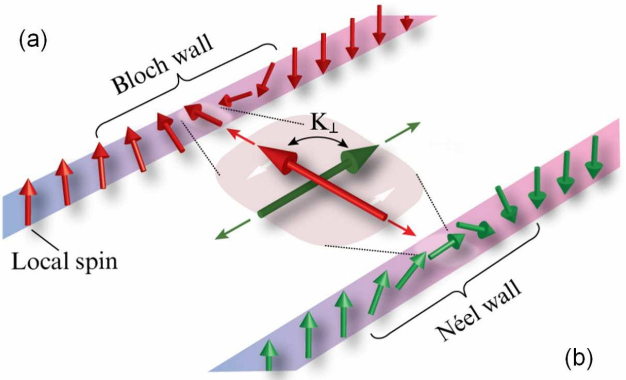

Figure 1.8: (a) A 180° Bloch domain wall which is characterized by magnetization rotation in the direction perpendicular to the domain magnetization plane. (b) A Néel wall with the magnetization rotation within the plane of the domain magnetization. [73]

Since in this thesis we will deal with materials containing Bloch domain walls, we focus here on the description of this particular case. When ignoring the effect of surface charges, such a domain wall can be described by

$$\varphi(y) = 0, \tag{1.11}$$

$$\theta(y) = \pm 2 \arctan \exp\left(\frac{y}{\Delta_0}\right), \tag{1.12}$$

where

$$\Delta_0 = \sqrt{\frac{A}{K}} \tag{1.13}$$

is the domain wall width. The domain wall width $\Delta_0$ is thus defined by a compromise based on the material constants $A$ and $K$.

The total wall energy per unit surface $\gamma$ can be written as a sum of the exchange and anisotropy energies [16]:

$$\gamma = E^{\mathrm{w}}_{\mathrm{ex}} + E^{\mathrm{w}}_{\mathrm{K}} = \int_{-\infty}^{+\infty} \left[ A \left(\frac{\mathrm{d}\theta}{\mathrm{d}y}\right)^2 + A \sin\theta \left(\frac{\mathrm{d}\varphi}{\mathrm{d}y}\right)^2 + K \sin^2\theta \right] \mathrm{d}y. \tag{1.14}$$

By substituting the (1.11) and (1.12) in the expression (1.14), one can find that the total wall energy per unit area is:

$$\gamma = 4\sqrt{AK}.$$

The exchange and the anisotropy contribute by the same weight to the domain wall energy.

### 1.4.2 Domain walls in confined structures

A magnetic film is called thin when its thickness is comparable to the domain wall width. Magnetic thin films can be divided into the two basic categories: in-plane anisotropy films and films with perpendicular anisotropy. When the dimensions of the magnetic material are laterally reduced, as in the case of patterned magnetic nanostructures [17], the effect of magnetic charges starts to play an important role and to influence the properties of the domain walls.

An important parameter of a nanostructure is its aspect ratio (width over thickness). When the aspect ratio is increased from the order of unity (sphere, cube) to a larger values (wires, stripes), the domain wall retrieves an additional degree of freedom to create different substructures across the wire.

A domain wall can be understood as a quasi-particle, which can be manipulated for instance by an external magnetic field, a spin-polarized current and by variations of the sample geometry.

#### Domain walls in in-plane anisotropy structures

The main effect of a nanostructured geometry in materials with small in-plane volume anisotropy is that the magnetization is confined along the long axis in order to minimize the demagnetizing energy. In such conditions when two domains are present, two magnetization configurations are possible: tail-to-tail or head-to-head domain walls.

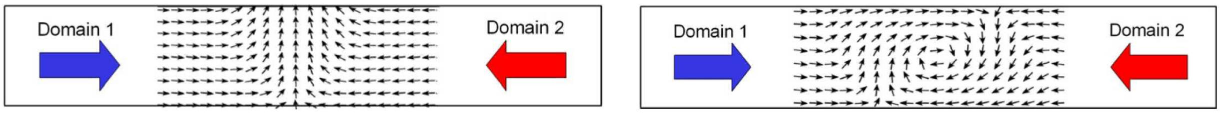

(a) (b)

Figure 1.9: Top view of the spin structure of (a) a transverse head-to-head domain wall and (b) a vortex head-to-head domain wall. [18]

Depending on the stripe width and thickness, two types of domain walls can be observed: a transverse wall [Fig. 1.9(a)] or a vortex wall [Fig. 1.9(b)]. These domain wall structures can be stable or metastable depending on the wire aspect ratio. The condition of existence of either domain wall type can be described by a phase diagram which was calculated by Nakatani [19] for Permalloy in the case of no bulk anisotropy. A symmetric transverse wall has a reflection symmetry around a line perpendicular to the strip axis while it is lacking the symmetry about the stripe axis. Such an asymmetry is less prominent in narrower stripes so the transverse wall becomes stable in thin and narrow wires. On the other hand, the vortex structure has rather a rotational symmetry so the exchange energy is more significant. Such a domain wall becomes stable in wider and thick wires. Beside these two basic types of domain walls, more complex asymmetric transverse walls can be found in some parts of the phase diagram.

### Domain walls in structures with perpendicular anisotropy

A completely different situation arises when the anisotropy is strong enough to keep the magnetization perpendicular to the film surface.

Films with the perpendicular anisotropy can be characterized by the quality factor $Q$, defined as:

$$Q = \frac{2K_u}{\mu_0 M_s^2}, \tag{1.15}$$

which expresses the competition between the uniaxial anisotropy $K_u$ and the demagnetizing energy. The magnetization lies in the film plane when $Q < 1$ and out-of-plane when $Q > 1$. When $Q \sim 1$ the magnetization creates an intermediate ripple-like structure in order to minimize surface and internal magnetic charges.

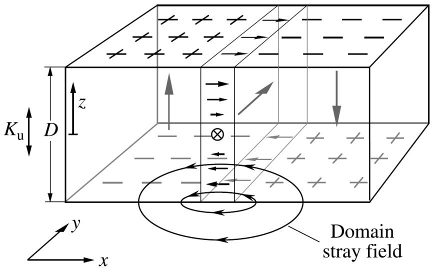

Figure 1.10: Schematics of the stray field and the wall structure in a perpendicular-anisotropy film. The perfect Bloch wall appears in the center of the sample thickness and it is modified due to the unbalanced stray field towards the sample surface. Such a Bloch wall flux closure regions are called Néel caps. [15]

If we ignore the effect of the demagnetizing field, the shape of the domain wall in a perpendicularly magnetized material can be described by (1.11) and (1.12). Such a wall is called a perfect 180° Bloch wall. Nevertheless, a stray field, arising from the presence of magnetic charges at the film surface, influences the shape of the domain wall. This field can be expressed in the wall center by [20]:

$$H_x(z) = 4M \ln\left(\frac{z}{D-z}\right),$$

where $D$ is the film thickness and $z$ is taken to be zero at the film surface. The twisting angle can be calculated by

$$\varphi(z) = \begin{cases} \arcsin(H_x/8M), & |H_x| \leq 8M, \\ \pm\pi/2, & |H_x| \geq 8M. \end{cases}$$

Such a domain wall is illustrated in Fig. 1.10. The domain wall is a perfect Bloch wall in the center of the film where $\varphi = 0$. Away from the center of the film, the stray field tilts the magnetization away from the transverse direction. This can be also illustrated on the sphere of possible magnetization paths shown in Fig. 1.7(a). The magnetization path lies between the Bloch wall path (in the center) and the Néel wall path (above a critical depth): $\varphi(z) \in < 0, \pi/2 >$.

The impact of the perpendicular anisotropy on the domain wall shape was simulated by Emori [21]. A 120 nm wide Co wire with the quality factor $Q$ ranging from 0 up to 1.6 was considered as a model system. The resulting magnetization configuration is shown in Fig. 1.11. In Fig. 1.11(a) is shown a transverse domain wall which is initialized in the wire when no perpendicular anisotropy is present. When $Q \sim 1$ the magnetization cants out of the plane and the transverse wall becomes distorted. When $Q > 1$ the wire is magnetized out-of-plane and a Bloch domain wall is formed. When the perpendicular anisotropy is further increased, the Bloch wall becomes narrower as shown in Fig. 1.11(d) and (e).

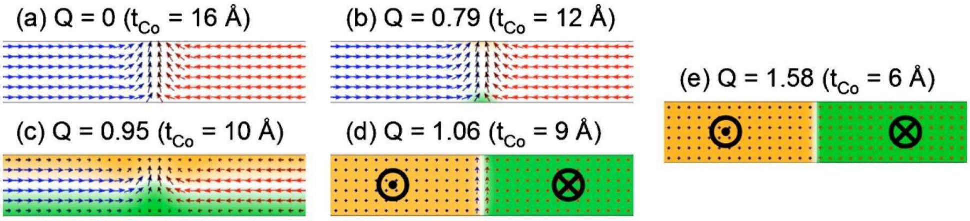

Figure 1.11: Demonstration of the impact of the perpendicular magnetic anisotropy on the initialized domain wall in a 120 nm wide Co stripe. The $z$ component of the magnetization is emphasized by yellow color for the 'up' configuration and by green color for the 'down' magnetization configuration. [21]

## 1.5 Field Induced Magnetization Dynamics

So far, we have described the magnetization in an equilibrium state. However, none of the properties mentioned so far allow to describe how the equilibrium state is achieved. A model describing the effect of an effective magnetic field on the magnetization was proposed in 1935 by Landau and Lifshitz [22]. The starting point in exploring the equation describing the magnetization dynamics is:

$$\frac{\partial \vec{M}}{\partial t} = -\gamma \vec{M} \times \mu_0 \vec{H}_{\text{eff}} \tag{1.16}$$

where $\gamma$ is the gyromagnetic ratio which in the case of the free electron is $1.76086 \times 10^{11}$ rad $\text{s}^{-1}\text{T}^{-1}$. The modulus of $\vec{M}$ is assumed to be constant under the applied magnetic field. The effective field gives rise to a torque which changes the magnetization in the torque direction. The magnetization then precesses around the effective field with the Larmor angular velocity $\omega = \gamma \mu_0 H_{\text{eff}}$. The projection of the magnetization into the field direction does not change so the energy of the system, i.e. the magnetization gyrates at an equipotential level (Fig. 1.12(a)).

Equation (1.16) in such a form would not lead to a parallel alignment of $\vec{H}_{\text{eff}}$ and $\vec{M}$. To do so, a phenomenological dissipation term was added to the precessional term. Historically, two different phenomenological approaches were proposed.

- **Landau-Lifshitz (LL) equation**
  Landau and Lifshitz proposed the dissipative term in the form

$$\frac{\partial \vec{M}}{\partial t} = -\gamma \vec{M} \times \mu_0 \vec{H}_{\text{eff}} - \frac{\lambda}{M_s} \left[ \vec{M} \times \left( \vec{M} \times \mu_0 \vec{H}_{\text{eff}} \right) \right], \tag{1.17}$$

  where $\lambda$ expresses the speed of the magnetization relaxation.

- **Landau-Lifshitz-Gilbert (LLG) equation**
  In 1955 Gilbert introduced another type of damping which is similar to a viscous force [23]:

$$\frac{\partial \vec{M}}{\partial t} = -\gamma \vec{M} \times \mu_0 \vec{H}_{\text{eff}} + \frac{\alpha}{M_s} \left( \vec{M} \times \frac{\partial \vec{M}}{\partial t} \right). \tag{1.18}$$

  This damping described by the parameter $\alpha$, is proportional to the time variation of the magnetization and is perpendicular to the magnetization trajectory.

The magnetization trajectory when including damping is shown in Fig. 1.12(b). Magnetization still precesses with the Larmor angular velocity around the effective field but due to the energy dissipation it spirals towards the equilibrium position.

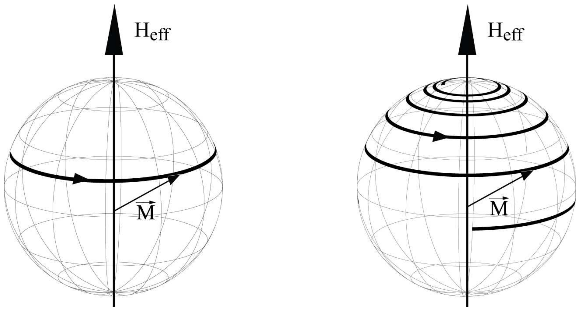

(a) (b)

Figure 1.12: Magnetization dynamics in the case of no damping (a) and when including the $\alpha$ damping (b) which causes magnetization spiraling to the equilibrium position due to the energy dissipation.

It has been shown by Mallinson [24] that the LLG equation is mathematically equivalent to the LL equation. However, the two equations do not express the same physics. In the case of very small damping ($\alpha \ll 1$) the two forms of damping are equivalent. The difference between the two phenomenological approaches to the energy dissipation becomes more apparent when the damping is increased. This is depicted in Fig. 1.13. In the case of the LL equation the azimuthal precession is not changed by the damping but the magnitude of $\dot{M}$ increases. In the limit case when $\lambda \to \infty$, the magnetization will align immediately with the effective field without any precession, which is equal to a fast magnetization relaxation.

In order to demonstrate the effect of the damping in the LLG equation, one can define three different regions for extreme influence of the $\alpha$ damping. When the $\alpha \ll 1$ the system behaves as non-dissipative and the trajectory of the magnetization stays circular. When the $\alpha \gg 1$ the magnetization dynamics is frozen as in the case of a high viscous medium. It can be seen from Fig. 1.13(b) that the radial component responsible for the energy dissipation takes the maximum value when $\alpha = 1$. The fastest magnetization switching then would be observed in the case when $\alpha = 1$.

It should be noted here that from equation (1.16) it does not follow the intuitive fact that we should be able to switch the magnetization with a field antiparallel to the magnetization. The torque exerted on the magnetization is zero and the magnetization is then in a metastable position. The probability of switching is close to zero when $T \to 0\,\text{K}$. However, due to the thermal excitation at finite temperature, a 'poke' leading to the non-zero torque is always present.

The precessional magnetization behaviour attracted a lot of interest recently. Much shorter switching reversal times can be achieved by using precessional switching rather than using an antiparallel field. A magnetic field perpendicular to the magnetization direction, where the maximum torque is exerted, is applied for a half precessional period, leading to a sub-nanosecond magnetization reorien-

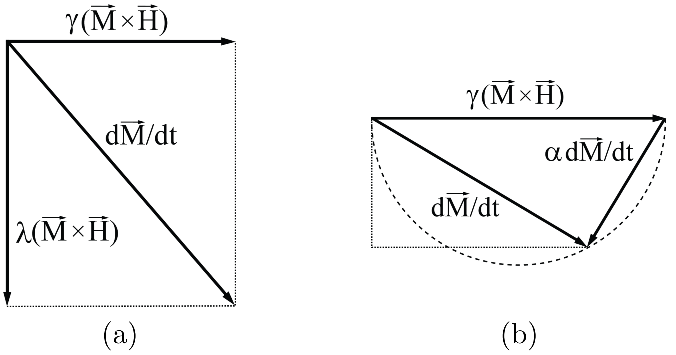

Figure 1.13: Vectors for Landau-Lifshitz equation with high damping parameter (a) and for Landau-Lifshitz-Gilbert equation (b).

tation [25], [26], [27]. The reversal time $\tau$ can be calculated by

$$\tau = \frac{1}{\omega\alpha} = \frac{1+\alpha^2}{\alpha\gamma}\frac{1}{H_{\text{eff}}}, \tag{1.19}$$

where $\omega$ is the precessional frequency.

It follows directly from equation (1.19) that the reversal time can be reduced by increasing the external field. However, the ultimate speed of precessional magnetic switching was shown by Tudosa *et al.* [28] who attributed this limiting behaviour to a momentary collapse of the ferromagnetic order of the spins under the short and high-field pulse.

We will come back to the fast magnetization switching using a femtosecond laser pulses in Chapter 4.

### 1.5.1 Collective magnetization dynamics

When a magnetic system is placed in a magnetic field $\mu_0 H_{\text{ext}}$, the energy levels are split due to the Zeeman effect. Such a system is then able to absorb energy from an additional oscillating magnetic field at defined frequencies falling into the radio-frequency range. In experiments typically, these two fields are mutually perpendicular. No resonance occurs when these two fields are parallel. The resonance occurs when the magnetization precession is synchronized with the applied AC field. This resonance is called the ferromagnetic resonance.

In ferromagnets we have to carefully distinguish between the applied field and the effective field. The demagnetizing field which has to be taken into account can be considered for an ellipsoid in the form of equation (1.10). When the external magnetic field is applied along $z$ direction, the resonance frequency reads

$$\omega_0 = \gamma\mu_0\sqrt{\left[H_{\text{ext}} + (N_x - N_z)M_s\right]\left[H_{\text{ext}} + (N_y - N_z)M_s\right]}, \tag{1.20}$$

where $\gamma$ is the gyromagnetic ratio. This equation is often called the Kittel equation for the resonance frequency. Here we show its solution for two special cases:

- for a thin film with $H_{\text{ext}}$ perpendicular to the film plane ($N_x$=$N_y$=0, $N_z$=1) the resonant frequency is
$$\omega_0 = \gamma\mu_0(H_{\text{ext}} - M_{\text{s}}); \tag{1.21}$$
- for a thin film with $H_{\text{ext}}$ in the plane of the film ($N_y$=$N_z$=0, $N_x$=1) the resonant frequency is
$$\omega_0 = \gamma\mu_0\sqrt{H_{\text{ext}}(H_{\text{ext}} + M_{\text{s}})}. \tag{1.22}$$

| | g-factor |
|---|---|
| Fe | 2.08 |
| Co | 2.17 |
| Ni | 2.18 |
| Gd | 1.95 |

Table 1.1: $g$-factors for metallic ferromagnets. [13]

Equation (1.20) can become more complicated when the magnetocrystalline anisotropy cannot be neglected. The ferromagnetic resonance then provides a measurement of $M_\mathrm{s}$.

A problem arises when we define the gyromagnetic ratio $\gamma$ in equation (1.20) due to the ambiguity of the $g$-factor definition. The gyromagnetic ratio reads

$$\gamma = -\frac{g\mu_B}{\hbar}$$

where $g$ is the $g$-factor which is expressed by

$$g = \frac{3}{2} + \frac{S(S+1) - L(L+1)}{2J(J+1)}, \tag{1.23}$$

leading to values $\leq 2$. When the orbital moment $L$ contribution to the total angular momentum is negligible, i.e. $L \rightarrow 0$, then $g \sim 2$. However, the experimentally obtained values for ferromagnetic metals shown in the table 1.1 are often higher than 2.

### 1.5.2 Field-induced domain wall dynamics

The detailed analytical solution of the Bloch domain wall dynamics was shown by Mougin *et al.* [29]. Here we point out some of the basic features describing the behaviour of an ideal 180° Bloch wall, which in the case of a thin film can be described by equations (1.11) and (1.12).

For the description of domain wall dynamics we define the two parameters including the demagnetizing factors $N_x$, $N_y$ and $N_z$:

$$\theta(y) = \pm 2 \arctan \exp\left(\frac{y - y_0}{\Delta}\right), \tag{1.24}$$

$$\Delta = \sqrt{\frac{A}{K + \frac{\mu_0}{2} M_s^2 (N_x \cos^2\varphi + N_y \cos^2\varphi - N_z)}} \tag{1.25}$$

where $y_0$ is the position of the domain wall center where in the case of an ideal Bloch wall $\theta = \pi/2$.

The magnetization dynamics is given by the LLG equation (1.18). It can be shown that the azimuthal velocities $\dot{\theta}$ and $\dot{\varphi}$ are

$$\dot{\theta} = -\frac{\gamma}{M_s}\Gamma_\theta,$$
$$\dot{\varphi} = -\frac{\gamma}{M_s}\Gamma_\varphi$$

where $\Gamma_\theta$ and $\Gamma_\varphi$ are the azimuthal components of the total torque $\vec{\Gamma}$. The total torque exerted on such a domain wall is composed from three different contributions

$$\vec{\Gamma} = \vec{\Gamma}_H + \vec{\Gamma}_D + \vec{\Gamma}_\alpha \tag{1.26}$$

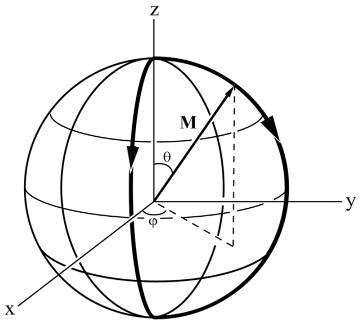

Figure 1.14: Definition of the spherical coordinates.

where $\vec{\Gamma}_H$ is the torque originating from the external field, $\vec{\Gamma}_D$ corresponds to the effect of demagnetizing field and $\vec{\Gamma}_\alpha$ is the damping torque. The total azimuthal components then are calculated as [29]

$$\Gamma_\theta = M_s^2(N_y - N_x)\sin\theta\sin\varphi\cos\varphi + \frac{\alpha M_s}{\gamma}\dot{\varphi}\sin\theta,$$

$$\Gamma_\varphi = -M_s^2\sin\theta\cos\theta\left[N_x\cos^2\varphi + N_y\sin^2\varphi - N_z\right] - \frac{\alpha M_s}{\gamma}\dot{\theta} - M_s H\sin\theta.$$

The magnetization amplitude $M_s$ is supposed to be constant, so the $\Gamma_r$ must equal to zero.

### Steady domain wall motion

First we discuss the so-called steady (or stationary) domain wall motion. In this regime the azimuthal component $\varphi$ does not change with time ($\dot{\varphi} = 0$) so the corresponding torque component $\Gamma_\varphi$ has to vanish. One can calculate that in the domain wall center (where the torque $\Gamma_\varphi$ has an extremum):

$$\sin 2\varphi = \frac{2H}{\alpha M_s(N_y - N_x)}.$$

This equation can be valid only if

$$H \leq \frac{\alpha M_s}{2} \mid N_y - N_x \mid .$$

The maximum field for which the domain wall moves steadily is called the Walker field:

$$H_\mathrm{W} = \frac{\alpha M_s}{2} \mid N_y - N_x \mid . \tag{1.27}$$

Above the Walker field the domain wall stability is broken and $\dot{\varphi} \neq 0$. This limit case is also known as the Walker breakdown. The wall velocity can be obtained from the relation $v = -\frac{\Delta}{\sin\theta}\dot{\theta}$. In the center of the wall where $\theta = \pi/2$

$$v_\mathrm{st} = \frac{\gamma\Delta}{\alpha}H.$$

In the steady regime the domain wall velocity is proportional to the applied field. The dependence of the velocity on the applied field is defined by the domain wall mobility

$$\mu_\mathrm{st} = \frac{\gamma\Delta}{\alpha}. \tag{1.28}$$

The measurement of the domain wall mobility is one of the possible ways to determine the parameter $\alpha$, although this is subjected to errors as it implies the knowledge of $\Delta$ and $\gamma$.

**Precessional domain wall motion**

When $H > H_\mathrm{W}$ the relation $\dot{\varphi} = 0$ is no longer valid and the domain wall starts oscillating around the wire axis. The domain wall also starts undergoing periodical transformations and the domain wall changes its width during the period. One can obtain the average domain velocity [29]

$$\bar{v}_\mathrm{pr} = \frac{\gamma\Delta\alpha}{1+\alpha^2}H. \tag{1.29}$$

The mobility in the precessional regime is then defined as

$$\mu_\mathrm{pr} = \frac{\gamma\Delta\alpha}{1+\alpha^2}. \tag{1.30}$$

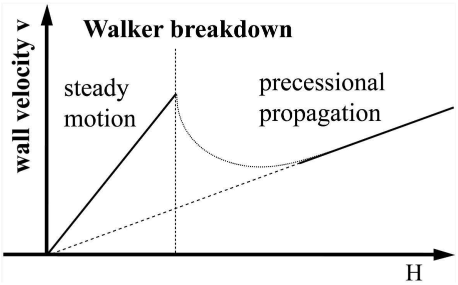

Figure 1.15: Velocity-field dependence of the domain wall. [29]

The field dependence of the domain wall velocity is shown in Fig. 1.15. The domain wall velocity increases linearly up to the Walker breakdown where $\varphi = 45°$. Beyond the Walker breakdown the velocity drops down due to the domain wall transformations which reduce the average velocity and the angle $\varphi \in (0°, 360°)$. When the external field is further increased the velocity reaches the precessional regime described by the equation (1.29).

### 1.5.3 Imperfect samples

An important feature of this ideal sample is the extension of the steady regime down to zero field. Nevertheless, defects of different possible origins are always present in real samples. The defects might be related to local variations of magnetic parameters $A$ and $K$, a change of the film thickness, magnetic impurities or edge roughness in the case of nanostripes. This defect distribution gives rise to the potential energy variation in the film.

A nanostripe including some defects and the corresponding potential energy landscape is shown in Fig. 1.16. The domain wall is in the initial state at position $x_1$ which is the local energy minimum. We say that the domain wall is pinned at position $x_1$. In order to displace the domain wall to the position $x_2$, the domain wall has to overcome the energy barrier $E'_\mathrm{p}$. When the domain wall can overcome all the energy barriers in the nanostripe $E > E''_\mathrm{p}$, it can move in the nanostripe without any pinning. In this particular case, energy is delivered to the system via the applied external magnetic field. The magnetic field $\mu_0 H$ produces a pressure on the domain wall via the Zeeman energy term. The field for which the Zeeman energy equals the energy barrier $E''_\mathrm{p}$, is called the propagation field. Such a field is different from a coercive field $H_\mathrm{c}$ which could be measured by magnetometry. The coercive field mechanism includes the domain wall nucleation, domain wall propagation and its annihilation whereas in this case the domain wall is already present in the nanostripe and the propagation field describes only the energy associated to the domain wall displacement. In magnetic nanostripes edge roughness is a source of pinning centers which play an important role, so often $H_\mathrm{p} > H_\mathrm{N}$. Minimization of this effect is one of the big issues for the nanowires fabrication.

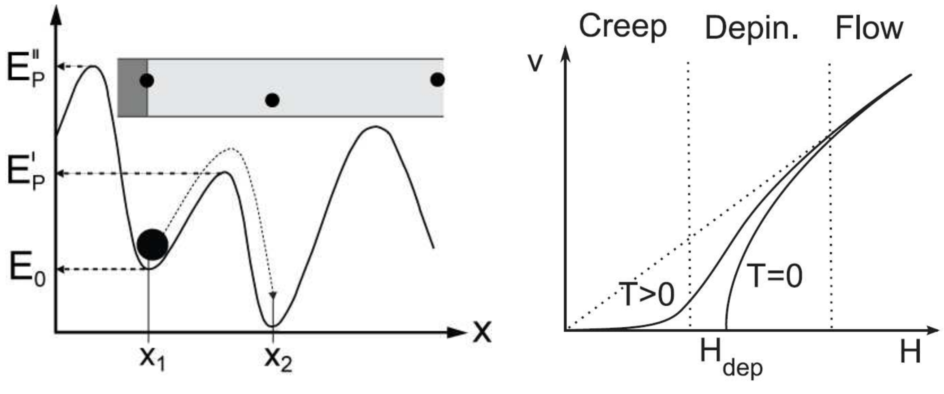

(a) (b)

Figure 1.16: (a) Schematic view of a nanostripe containing two regions with opposite magnetization, represented by the white and black color separated by a domain wall. Such a domain wall is pinned to defects in the nanostripe, which constitute an energy minimum. (b) Graph showing the three different regimes for domain wall propagation in the presence of defects. [30]

The influence of the pinning mechanism on domain wall dynamics is shown in Fig. 1.16(b). At zero temperature the domain wall does not move below the depinning field $H_{\mathrm{dep}}$, where it is able to overcome all local energy barriers. At finite temperature this sharp transition is smeared due to thermal activation and the wall can move even when $H < H_{\mathrm{dep}}$. The region where domain wall displacements are based on thermally activated hopping, is known as the creep regime.

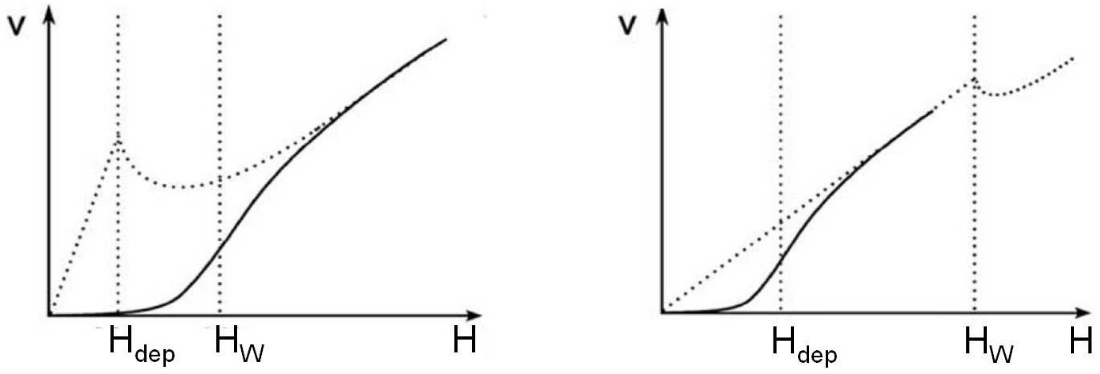

(a) (b)

Figure 1.17: Demonstration of how the limited maximum applied field and low field creep prevent to distinguish the steady and precessional regimes. [30]

When $H \gg H_{\mathrm{dep}}$, the pinning potential wells become less and less visible for the domain wall so the domain wall velocity enters the so-called flow (viscous) regime as it is shown in Fig. 1.16(b).

When no Walker breakdown is observed, difficulties arise to identify the domain wall propagation regime. The observed flow regime may therefore correspond either to the steady or the precessional regime. A problem then also arises for the determination of $\alpha$, due to the two different mobility definitions (1.28) and (1.30), as discussed in the case of Pt/Co/Pt films in [30]. The two possible experimental scenarios explaining the absence of experimentally observed Walker field are demonstrated in Fig. 1.17. In Fig. 1.17(a) is shown the case when the Walker breakdown presence can be hidden by the creep regime behaviour when $H_{\mathrm{W}} \leq H_{\mathrm{dep}}$. In Fig. 1.17(b) is shown the case when the Walker breakdown field cannot be experimentally achieved.

The average velocity in the creep regime [31], known as the collective creep law, in the case of a Bloch wall in a disordered medium is

$$v = v_0 \exp\left[-\left(\frac{U_c}{k_\mathrm{B}T}\right)\left(\frac{H_\mathrm{dep}}{H}\right)^{\eta}\right], \tag{1.31}$$

where $U_\mathrm{c}$ is a scaling energy constant, $k_\mathrm{B}$ is the Boltzmann constant, $H_\mathrm{dep}$ is the depinning field and $\eta$ is the universal dynamic exponent. It has been shown that $\eta = 1/4$ in the case of a one-dimensional domain wall structure and $\eta = 1/2$ in case of a thick magnetic film [32].

## 1.6 Domain wall propagation under transverse magnetic fields

The impact of a magnetic field applied along the hard-axis on the field-induced domain wall dynamics was theoretically studied by several groups on systems with in-plane magnetization [33], [34] and experimentally observed by Yang *et al.* [35]. In the calculations a 5 nm thick and 100 nm wide Permalloy wire was considered, according to the phase diagram [19], a transverse domain wall is stable in the static case.

The static profile of a domain wall is given by the competition of different energies. The transverse field modifies the magnetization configuration via the Zeeman term and tends to align the magnetic moments parallel to the field. This configuration costs in demagnetizing energy due to the charges which are created on the stripe edges. The transverse field itself does not make the domain wall move but it modifies its structure and width. The resulting domain wall width is illustrated in Fig. 1.18(a). The domain wall is becoming wider when the applied field is parallel to the domain wall core.

Fig. 1.18(b) shows domain wall dynamics under the application of longitudinal and transverse magnetic fields. The transverse field is ranging from -400 Oe (antiparallel to the wall core) up to 400 Oe (parallel to the wall core). For a small longitudinal field below the Walker breakdown, the increased (decreased) domain wall width by positive (negative) transverse bias fields results in the increased (decreased) domain wall mobility - see equation (1.28). As it is evident from Fig. 1.18(b), the Walker breakdown field is also changed. The transverse field stabilizes the transverse domain wall and prevents its transformations which lead to lower velocities. Above the Walker breakdown the domain wall velocity dramatically drops and the motion becomes more complex.

One possible way to experimentally apply the transverse field is to use an additional coil or a permanent magnet. Another possibility is to create an internal transverse field exploiting the Oersted field. Such a field is always created around a moving electron according to Ampére's law. When a current passes through a wire, it creates the Oersted field which acts on the wire itself and in a magnetic wire distorts the magnetization configuration. One can use a multilayer wire as was shown by Uhlíř *et al.* [36] in the case of NiFe/Cu/Co stripes. In this case a significant part of the current passes through the Cu layer so the center of the current distribution is below the center of the magnetic layer, which results in a net Oersted field in the NiFe layer. It has been shown that during the application of the current pulse the magnetization in the soft NiFe turns into the transverse field direction.

Another way to apply a transverse magnetic field during the current pulse is the already mentioned Rashba field. This source of internal magnetic field does not require any additional sources or a power consumption. The field is always present in the layer during the application of current pulses and its amplitude depends on the material parameters and on the electric current density.

## 1.7 Transport properties of ferromagnets

Before moving ahead to the interaction between the electric current and the magnetic lattice, we will point out some of the basics concerning the transport properties of ferromagnetic materials.

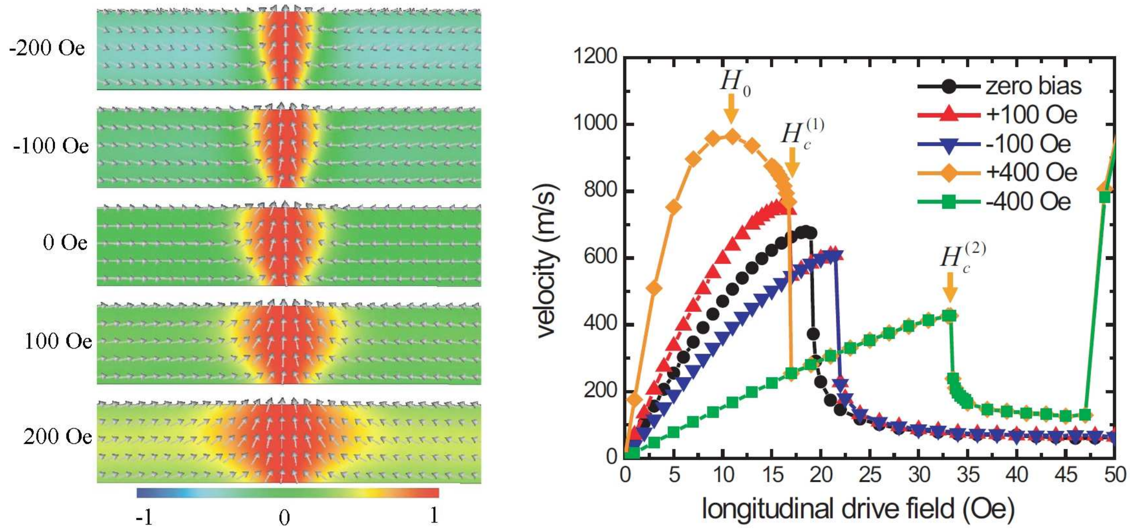

(a) (b)

Figure 1.18: (a) Domain wall modification under the effect of transverse field. [34] (b) Numerical simulations of domain wall velocity as a function of magnetic field for different amplitudes of transverse field. [35]

### 1.7.1 Spin polarization

The typical band structure of a transition metal was shown in Fig. 1.5. The $s$ electrons, presenting a negligible band splitting, have low effective mass and high mobility, so they are considered as delocalized. Conduction is then mainly caused by these $s$ electrons whereas the $d$ electrons are heavy and more localized. The $d$ band is split by the exchange splitting $\Delta_{xc}$ and therefore is responsible for the spontaneous magnetization.

The magnetization is simply given by the difference between spin-up and spin-down populations. However, the electric current is carried only by the electrons in the conduction band close to the Fermi level $E_\mathrm{F}$. The two populations are carried in two separated channels. In the case of ferromagnets the two populations are usually unbalanced so the majority of the current is carried by one spin or the other. Such a property characterizes spin polarization which is defined by [37]:

$$P = \frac{g_\uparrow(E_\mathrm{F}) - g_\downarrow(E_\mathrm{F})}{g_\uparrow(E_\mathrm{F}) + g_\downarrow(E_\mathrm{F})}$$

where $g_\uparrow(E_\mathrm{F})$ and $g_\downarrow(E_\mathrm{F})$ are the densities of states at the Fermi level for spin-up and spin-down populations. The value of $P$ then lies between 0, for non-magnetic materials, and 1 for a perfectly polarized materials (half metallic ferromagnets) where only spins of one type are present at the Fermi level [38].

In transport experiments it is necessary to take into account the fact that the electrons have different mobilities. Several bands are usually crossing the Fermi level ($s$ and $d$ in the Fig. 1.5) so the electrons at the Fermi level have different Fermi velocities, effective masses, etc. Hence the measured value of the spin polarization depends on the experimental setup used for its determination. Some of the various definitions such as tunnel current spin polarization, ballistic current spin polarization or diffusive current spin polarization are reviewed in [37].

### 1.7.2 Magnetoresistance

When a current defined by current density $\vec{j}$ is flowing through a homogeneous ferromagnet, an electric field is generated. This electric field depends on a number of effects [39]

$$\vec{E} = \rho(\vec{B})\vec{j} + \rho_{\mathrm{AMR}}(\vec{u}_m \cdot \vec{j})\vec{u}_m + \rho_{\mathrm{OHE}}\vec{B} \times \vec{j} + \rho_{\mathrm{EHE}}\vec{M} \times \vec{j} + \rho_{\mathrm{sdiff}}\vec{j} \tag{1.32}$$

where $\vec{u}_m$ is a unit vector in the magnetization direction and $\vec{B}$ is the external field.

- The first term is known as the **longitudinal resistance** which usually varies as $B^2$. The external magnetic field disturbs the electron trajectory and the larger probability of scattering will give rise to an increase of resistivity.

- The second term is the **anisotropic magnetoresistance (AMR)** which arises due to the spin-orbit effect. The resistivity of the ferromagnet depends on the orientation of the magnetization with respect to the electric current direction. The magnitude of AMR can be defined by

$$\mathrm{AMR} = \frac{\rho_{\parallel} - \rho_{\perp}}{\rho_{\perp}}$$

  In $3d$ alloys this effect leads to the larger probability of $s - d$ scattering of electrons in the direction of magnetization, so $\rho_{\parallel} > \rho_{\perp}$.

- The third term in equation (1.32) is known as the **ordinary Hall effect (OHE)**. The OHE is the simple result of the Lorentz force acting on the moving electrons. This force deflects them from the straight trajectory and gives rise to a transverse electric field which can be detected as a Hall voltage. The Hall voltage $V_H$ is proportional to the external field $B$ and inversely proportional to the density of charges $n$.

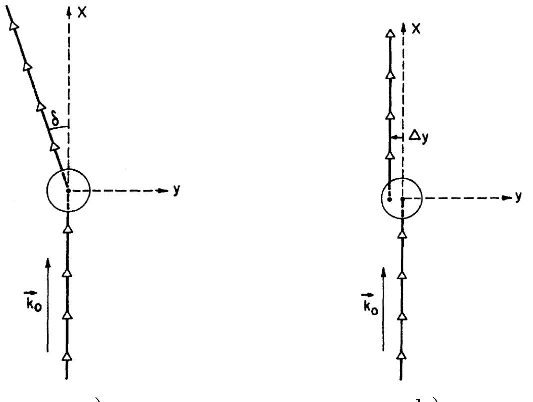

a) b)

Figure 1.19: Motion of an electron represented by the vector $\vec{k}_0$ before and after scattering by a central potential in case of (a) skew scattering (b) side-jump scattering. [41]

- The next term is the **extraordinary Hall effect (EHE)** which occurs in ferromagnetic materials. The electrons moving in the ferromagnetic environment have different probabilities to scatter on each side. Two different mechanisms have been proposed to be the microscopical origins: side-jump mechanism and skew mechanism. The skew scattering [40], shown in Fig. 1.19(a), is characterized by a constant deflecting angle $\delta$ on the scattering centers. The predicted correlation between the longitudinal resistance $\rho$ and the Hall resistivity is $\rho_{\mathrm{EHE}}^{\mathrm{skew}} \propto \rho$. The side-jump mechanism [41], depicted in Fig. 1.19(b), has a quantum mechanical origin and it results in a constant deviation $\Delta y$ from the charge's trajectory at the point of scattering. This mechanism scales as $\rho_{\mathrm{EHE}}^{\mathrm{S-J}} \propto \rho^2$. These two terms are often superimposed so the Hall resistivity can be written as

$$\rho_{\mathrm{EHE}} = a\rho + b\rho^2$$

where $a$ and $b$ are constants.

- The last term represents additional scattering due to the **spin diffusion effect**. This term plays a role when the material is magnetically inhomogeneous. An example can be shown for the interface between ferromagnetic and non-magnetic material. When a spin polarized current is injected from a ferromagnet to a non-magnetic material, the polarization has to relax to its equilibrium value. As it does not happen instantaneously but on a characteristic distance called spin diffusion length or spin flip length $l_{\mathrm{sf}}$, the current can be polarized even in a non-magnetic material. Such a procedure is used for spin injection into semiconductors which permits to measure the polarization of the carrier density.

  This effect was for example demonstrated in 2005 by Crowel *et al.* [42] and is shown in Fig. 1.20. Kerr microscopy was used to directly image the spin accumulation in gallium arsenide which was connected by ferromagnetic source and drain electrodes. After the injection, electrons have initial spin orientation $\vec{s}$ along $\vec{M}$. A small in-plane magnetic field is applied forcing the injected electrons to precess in the $x$-$z$ plane. The $z$ spin component is proportional to the Kerr rotation $\theta_k$ which reveals the spin excess close to the electrodes.

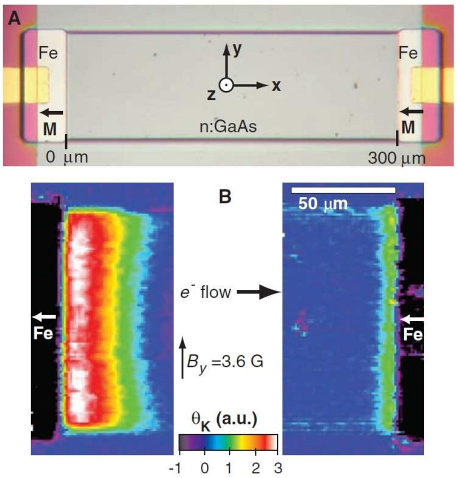

Figure 1.20: (A) Ferromagnet-semiconductor device used for spin accumulation imaging. (B)Images of Kerr rotation angle $\theta_k$ showing the spin accumulation near the injection electrodes. [42]

The same effect can occur in the case of a domain wall since the domain wall represents a smooth interface between two magnetically different regions. One can expect a significant spin accumulation effect in case of a very thin wall when the domain wall width is much smaller than the spin diffusion length.

### 1.7.3 Spin relaxation

In metals, the conduction is a diffusive process if we do not consider superconductivity or ballistic transport. In the diffusive regime the electrons experience collisions and they change their velocity $\vec{v}$. Statistically, the electrons are scattered every scattering time $\tau_{\mathrm{s}}$ (or also momentum relaxation time). The mean free path is the average distance covered by a moving electron between two collisions. The mean free path $\lambda$ can be calculated by using $\lambda = v_F \tau_s$ where $v_F$ is the Fermi velocity. Apparently, in ferromagnetic materials the two spin directions have different velocities and scattering times which give rise to different mean free paths $\lambda_\downarrow \neq \lambda_\uparrow$. For example in Al $\lambda_\downarrow = \lambda_\uparrow = 12\,\mathrm{nm}$ whereas in Co $\lambda_\uparrow = 20\,\mathrm{nm}$ and $\lambda_\downarrow = 1\,\mathrm{nm}$ at 300 K [13].

However, another parameter is as important for spintronics. An electron has to remember its spin state as long as possible so the information can be transferred over long distances. This characteristic length is called spin diffusion length or spin flip length $\lambda_{sf}$. If we define the spin scattering time as $\tau_{\mathrm{sf}}$, the spin flip length can be calculated by [13]

$$l_{\mathrm{sf}} = \sqrt{D_e \tau_{\mathrm{sf}}} \tag{1.33}$$

where $D_e$ is the diffusion constant. Typically, this distance is much longer than the mean free path. For example in Al $l_{\mathrm{sf}} = 350\,\mathrm{nm}$ and in Co $l_{\mathrm{sf}} = 40\,\mathrm{nm}$ at 300 K.

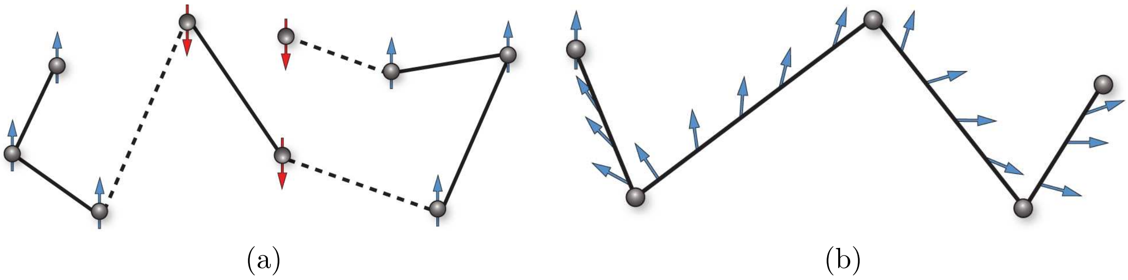
(a) (b)

Figure 1.21: Spin relaxation mechanisms for conduction electrons: (a) Elliott–Yafet mechanism. Impurities and phonons can induce transitions between ↑ and ↓ states leading to the spin relaxation. (b) D'yakonov-Perel' mechanism which is relevant for systems lacking inversion symmetry.

Since the scattering is spin-dependent in ferromagnetic metals, the spin relaxation process is more complicated. The spin-dependent scattering process is expressed by Matthiessen's rule which summarizes all the possible contributions to the resistivity like electron-magnon scattering or electron-electron interaction [44]. The spin relaxation mechanism then refers to the process that brings an unbalanced population of spin states into equilibrium as it was shown in the previous section.

Here we refer to two spin-independent relaxation mechanisms which have been proposed for non-magnetic semiconductors and metals [43] but we will show further that they can play an important role in ferromagnetic materials.

- **Elliott-Yafet mechanism** - Fig. 1.21(a)
  Elliott-Yafet mechanism is relevant for systems having central symmetry. The elementary process is scattering of an electron at phonons (high temperature) or at impurities (low temperature) in a system with spin-orbit coupling. The momentum scattering itself does not lead to spin relaxation. The periodic spin-orbit interaction is important due to the fact that it couples the spin with the electron motion. Only the momentum scattering in combination with the spin orbit interaction is able to bring the spin populations into the equilibrium.

- **D'yakonov-Perel' mechanism** - Fig. 1.21(b)
  Another efficient mechanism of spin relaxation was found in systems lacking inversion symmetry (such systems are described more in detail in the case of Pt\Co\AlO$_x$). The broken symmetry lifts the spin degeneracy so the two spins having the same momentum have no longer the same energy. This spin splitting can be equivalently described by introducing an intrinsic $\vec{k}$ dependent magnetic field.

  One can consider an electron with a momentum $\vec{k}$ which precesses around the magnetic field $\vec{B}(\vec{k})$. The electron scatters into a new momentum $\vec{k}'$ and it begins to precess around the new field direction $\vec{B}(\vec{k}')$. The electron rotates with a different frequency and in a different direction between the collisions. If we define the average Larmor frequency $\Omega_{\mathrm{av}}$ and $\tau_{\mathrm{s}}$ as the momentum relaxation time then we can consider two limiting cases:

i) When $\tau_{\mathrm{s}}\Omega_{\mathrm{av}} \geq 1$, the spin precesses a full cycle before being scattered to another momentum state. The spin dephasing depends on the dispersion of the Larmor frequencies. The spin is irreversibly lost after $\tau_{\mathrm{s}}$ when randomizing scattering takes place. In this case the spin scattering time is proportional to the dispersion of the Larmor frequencies $\Delta\Omega$:

$$\tau_{\mathrm{sf}} \approx \frac{1}{\Delta\Omega}.$$

ii) The case when $\tau_{\mathrm{s}}\Omega_{\mathrm{av}} \leq 1$ is usually called the D'yakonov-Perel' mechanism. This regime can be viewed from the point of view of individual electrons as a spin precession about fluctuating magnetic fields, whose magnitude and direction change randomly with the average time step of $\tau_{\mathrm{s}}$. The spin is scattered before finishing the full cycle of the Larmor precession and it rotates only by an angle $\delta\Phi = \tau_{\mathrm{s}}\Omega_{\mathrm{av}}$. As a result the spin phase follows a random walk. The spin relaxation rate induced by the D'yakonov-Perel' mechanism will be inversely proportional to the momentum scattering rate:

$$\tau_{\mathrm{sf}} = \frac{1}{\Omega_{\mathrm{av}}^2 \tau_{\mathrm{s}}}. \tag{1.34}$$

It should be pointed here that the higher the intrinsic magnetic field, the smaller the spin relaxation time.

In an external applied magnetic field the randomly changing axis starts to be suppressed as the spin starts to precess around the preferential direction. As soon as the external magnetic field is strong enough, the D'yakonov-Perel' spin relaxation mechanism vanishes.

The striking difference between the Elliott-Yafet and D'yakonov-Perel' mechanisms is their opposite dependence on $\tau_{\mathrm{s}}$. The effectiveness of the D'yakonov-Perel' mechanism decreases with increased scattered efficiency while the Elliott-Yafet is increased.

## 1.8 Current-induced domain wall motion

The pioneering description of the effect of an electric current on the domain wall was published by Berger in the 1970s [45]. He suggested that the magnetic field caused by the nonuniform current distribution across the wall, will exert a dragging force on the domain wall.

### 1.8.1 Slonczewski's model

The more generally accepted theory of the influence of a spin-polarized current on the domain wall was proposed by Slonczewski [46] in 1996. The theory is based on angular momentum conservation. Spin transfer torque arises whenever the flow of spin-angular momentum is not constant over the sample. Slonczewski considered a model system based on two ferromagnetic layers which are separated by a thin spacer layer in current-perpendicular-to-plane (CPP) configuration. The role of the spacer is to decrease the interlayer exchange coupling (RKKY) [47]. On the other hand, the thickness of the spacer must be as small as possible in order to keep the spin polarization of the electron current, i.e. smaller than the spin diffusion length. The ferromagnetic layers are represented by macrospin vectors $\hbar\vec{S}_1$ and $\hbar\vec{S}_2$. When passing the electric current, the first layer works as an emitter of spin polarized current and the second layer represents an absorber of the spin polarized current. The theory is based on the angular momentum conservation which leads to the adiabatically rotating magnet vectors in the absorbing layer. The derived spin dynamics reads

$$\frac{\mathrm{d}\vec{S}_1}{\mathrm{d}t} = \frac{j\xi}{e}\vec{s}_1 \times (\vec{s}_1 \times \vec{s}_2) \tag{1.35}$$

where $\vec{s}_i = \vec{S}_i/S_i$ are the unit vectors of the magnetic moment orientation in the two ferromagnetic layers , $j$ is the current density and the function $\xi$ is given by [46]

$$\xi = \left[-4 + (1+P)^3 \left(3 + \vec{s}_1 \cdot \vec{s}_2\right)/4P^{3/2}\right]^{-1}$$

including the current spin polarization $P$. The spin transfer then vanishes when the mutual orientation of the macrospins is parallel or antiparallel.

A spin-torque oscillator used for spin-transfer torque investigations is shown in Fig. 1.22(a). For example, Houssameddine *et al.* [48] used a Pt/Co multilayer with out-of-plane magnetization as the fixed layer and a permalloy layer as the free layer.

We have already shown that if the magnetization deviates from its equilibrium position, it will start precessing around the effective field $\vec{H}_{\text{eff}} = (0, 0, H_{\text{eff}})$. The damping torque will push the magnetization back to its lowest energy position along the $z$ axis. The direction of the torque is shown in Fig. 1.22(b).

When a current is applied, the direction of the spin-transfer torque can be either parallel or antiparallel to the damping term [Fig. 1.22(b)] depending on the current orientation. When the current orientation is such that the spin-transfer torque is parallel to the damping torque, it increases the effective damping value, so the magnetization spirals faster to the $z$ direction. When the current creates an opposite torque, the effective damping is decreased and the precessional motion is less damped [Fig. 1.22(c)].

In a certain range of current densities, the spin-transfer torque can compensate the damping torque, and this leads to an undamped precession of the magnetization at some angle as a direct response to the current [Fig. 1.22(d)]. From the energy point of view, the energy dissipated from the system due to the damping is balanced by the energy pumped to the system due to the transfer of angular momentum. When the spin-torque is increased it can lead to a big negative effective damping so the state in $-z$ becomes as the state with the lowest energy. This process depicted in Fig. 1.22(e) thus leads to the magnetization reversal.

The occurrence of these three basic regimes (and even more complex regimes) was explored for example in [49] and was experimentally shown in [48].

### 1.8.2 Modified Landau-Lifshitz-Gilbert equation

Slonczewski's work launched an avalanche of studies devoted to the spin transfer torque phenomenon. The spin transfer torque was generalized in the LLG equation for continuously varying magnetization as is the case of magnetic domain wall [50], [51]. The additional term was derived supposing that the conduction electron spin axis follows the local magnetization direction. Such an assumption is known as the adiabatic condition so this term is often called adiabatic. It is therefore justified for large domain wall widths. The modified equation

$$\frac{\partial \vec{M}}{\partial t} = -\gamma \vec{M} \times \mu_0 \vec{H}_{\text{eff}} + \frac{\alpha}{M_s}\left(\vec{M} \times \frac{\partial \vec{M}}{\partial t}\right) - \left(\vec{u} \cdot \vec{\nabla}\right)\vec{M} \tag{1.36}$$

where $\vec{u}$ stands as a vector along the direction of current

$$\vec{u} = \frac{Pg\mu_{\text{B}}}{2eM_{\text{s}}}\vec{j}. \tag{1.37}$$

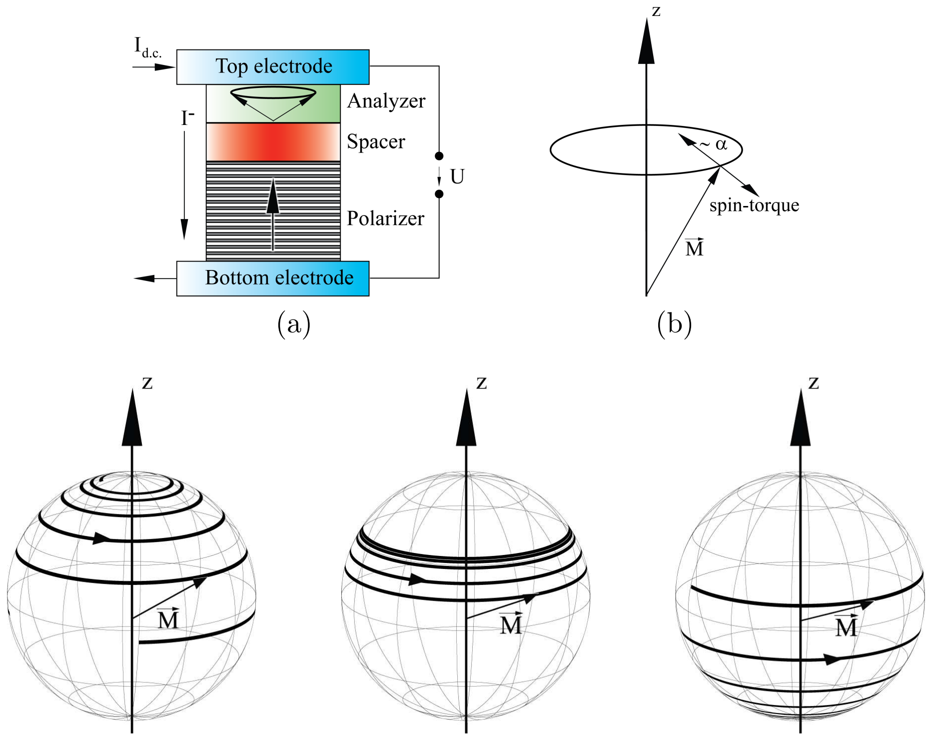

(a) (b)

(c) (d) (e)

Figure 1.22: (a) Schematic diagram a spin-torque oscillator consisting of a perpendicular polarizer and a free layer. (b) Directions of damping $\alpha$ and spin-torque acting on the free layer magnetization. The easy axis of the magnetization in the polarizer coincides with the $z$ axis. (c) For currents below a critical current, the magnetization in the free layer will spiral towards the equilibrium position $z$. (d) In the special case, for larger currents, the effective damping becomes negative and $M$ may achieve a dynamical equilibrium state, so the magnetization will keep precessing around the $z$ axis. (e) Large spin-torque leads to a big negative effective damping so the state in $-z$ becomes as the state with the lowest energy.

The spin diffusion length is typically of the order of a nanometer in usual ferromagnetic metals while the domain wall width is about 100 nm [52]. Thus, the approximations of current polarization adiabaticity and full transfer of angular momentum can be described by equation (1.36).

Tatara and Kohno [53] demonstrated qualitatively the consequence of equation (1.36). It was found experimentally that the domain wall does not move until a critical current value. The domain wall only distorts and tilts its magnetization out of the easy plane. The wall is not driven to the steady motion but just displaced by a certain distance which is a consequence of the absorbed transferred spin. The transferred energy is stored in the demagnetizing energy form. Nevertheless, the anisotropy can absorb the energy only up to a critical current density [53]:

$$j_{\mathrm{cr}} = \frac{eM_{\mathrm{s}}^2}{a^3\hbar} K\Delta$$

where $a$ is the lattice parameter, $\Delta$ is the static domain wall width and $K$ is the transverse anisotropy.

Above this current density the transverse anisotropy is no longer able to accept all the transferred energy and the domain wall starts moving. The domain wall velocity is $v \propto \sqrt{j^2 - j_{\mathrm{cr}}^2}$.

Thiaville *et al.* [51] have performed quantitative numerical simulations in the case of a thin and narrow permalloy stripe. These results revealed a big discrepancy with experimental results [54] showing that the theoretical critical current density value is about one order of magnitude lower than the experimental one.

About one year later, in 2005, Thiaville *et al.* [55] introduced corrections to the perfect adiabatic spin transfer in the micromagnetic models. Such a non-adiabatic contribution is characterized by a parameter $\beta$, so that the modified LLG equation reads:

$$\frac{\partial \vec{M}}{\partial t} = -\gamma \vec{M} \times \mu_0 \vec{H}_{\text{eff}} + \frac{\alpha}{M_s}\left(\vec{M} \times \frac{\partial \vec{M}}{\partial t}\right) - \left(\vec{u}\cdot\vec{\nabla}\right)\vec{M} + \frac{\beta}{M_\text{s}}\vec{M} \times \left[\left(\vec{u}\cdot\vec{\nabla}\right)\vec{M}\right]. \tag{1.38}$$

The analytical solution of equation (1.38) can be found by employing the 1D model [29]. In this case the sum of the torques exerted on the domain wall can be written as

$$\vec{\Gamma} = \vec{\Gamma}_H + \vec{\Gamma}_D + \vec{\Gamma}_\alpha + \vec{\Gamma}_u + \vec{\Gamma}_\beta, \tag{1.39}$$

where $\Gamma_u$ and $\vec{\Gamma}_\beta$ are the adiabatic and non-adiabatic torques which can be expressed by

$$\vec{\Gamma}_u = \frac{M_\text{s} u}{\gamma}\frac{\sin\theta}{\Delta}\vec{e}_\theta,$$

$$\vec{\Gamma}_\beta = -\beta\frac{M_\text{s} u}{\gamma}\frac{\sin\theta}{\Delta}\vec{e}_\varphi.$$

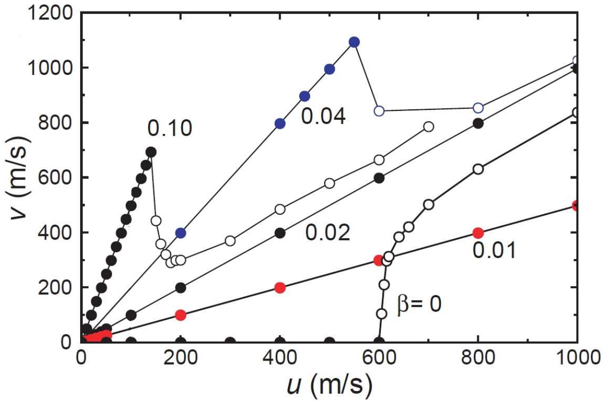

Figure 1.23: Transverse domain wall velocity as a function of spin-polarized current density $u$ in a 120 nm × 5 nm permalloy wire with ($M_\text{s} = 8\times10^5$ A/m, $\alpha = 0.02$ and no anisotropy). For $u = 100$ m/s the corresponding current density $j = 5.7 \times 10^{11}$ A/m$^2$. [55]

In the steady regime $\dot{\varphi} = 0$ when $\Gamma_\varphi$=0:

$$\sin 2\varphi = \frac{H + (\beta-\alpha)\frac{u}{\gamma\Delta}}{\frac{\alpha M_s}{2}(N_y - N_x)}.$$

Like in the case of an applied magnetic field, one can find the Walker breakdown current density $J_\text{W}$

$$J_\text{W} = \frac{\alpha e M_\text{s}^2}{g\mu_\text{B}P}\frac{\gamma\Delta}{|\beta-\alpha|}|N_y - N_x|. \tag{1.40}$$

The domain wall velocity below the Walker breakdown reads

$$v_\text{steady} = \frac{\beta}{\alpha}u \tag{1.41}$$

and the time averaged velocity above the Walker breakdown

$$\bar{v} = \frac{1+\alpha\beta}{1+\alpha^2}u. \tag{1.42}$$

This behaviour is qualitatively similar to the one derived in the case of an applied magnetic field. The effect of spin polarized current is thus somewhat equivalent to an additional magnetic field. It can be directly seen from equation (1.41) that the only contribution to the domain wall velocity is the non-adiabatic part of spin transfer torque. Above the Walker breakdown the domain wall velocity drops due to the domain wall transformations and then asymptotically approaches the velocity given by equation(1.42) when $J \gg J_\mathrm{W}$.

The result of micromagnetic numerical simulations demonstrating the role of the $\beta$ parameter is shown in Fig. 1.23 for parameters given in the figure caption. The higher non-adiabatic torque $\beta$ will increase the domain wall mobility given by equation (1.41). However, increasing the $\beta$ parameter shifts the position of the Walker breakdown to lower currents given by equation (1.40). In order to keep the domain wall dynamics in the steady regime the Walker breakdown can be prevented by some alternative ways which we will describe in the following text.

### 1.8.3 Particle approximation of current-induced spin torque

Magnetic electrons can be divided into two categories: localized electrons responsible for the local magnetization and delocalized electrons which are conducting the electric current. The interaction between these two types of electrons is expressed by the $s-d$ Hamiltonian: $H_{s-d} = -J_{ex}\vec{s}\cdot\vec{S}$ where $<\vec{S}>/S = -\vec{M}/M_s$ and $\vec{s}$ is the conduction electron spin.

The dynamics of a conduction magnetic moment $\vec{\mu} = -g\mu_\mathrm{B}\vec{s}$ can be described by [56]

$$\frac{\mathrm{d}\vec{\mu}}{\mathrm{d}t} = \frac{J_\mathrm{ex}S}{\hbar}\vec{m}\times\vec{\mu} - \frac{1}{\tau_{sf}}\left(\vec{\mu}-\vec{m}\right),$$

where $\vec{m}$ is the unitary vector of local magnetization and $\tau_\mathrm{sf}$ refers to the spin-flip relaxation time. The first term of the right-hand side represents magnetic moment precession around the exchange field. The second term represents spin-flip relaxation of the magnetic moment to the equilibrium direction along the magnetization $\vec{m}$, i.e. the damping.

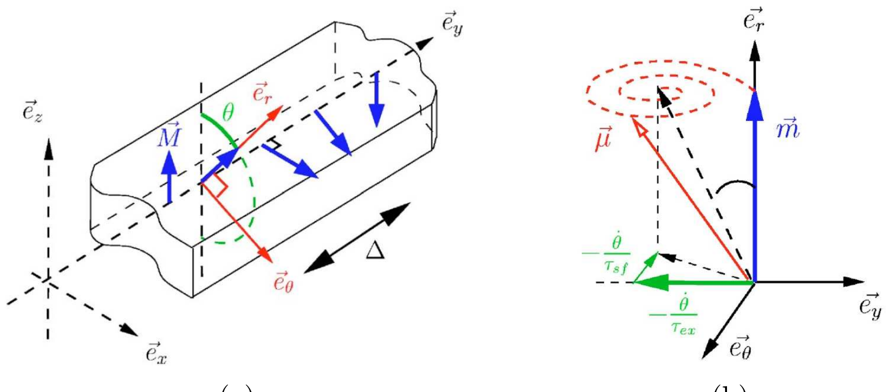

(a) (b)

Figure 1.24: (a) Scheme of a Bloch domain wall with width $\Delta$. The frame moving with the conduction electron is defined by the vectors ($\vec{e}_r$,$\vec{e}_\theta$,$\vec{e}_y$). (b) The conduction electron with magnetic moment $\vec{\mu}$ is precessing about the effective field. [56]

Vanhaverbeke and Viret [56] considered the frame defined by ($\vec{e}_r$,$\vec{e}_\theta$,$\vec{e}_y$) moving with the electron crossing a Bloch domain wall as it is shown in Fig. 1.24(a). Before the electron reaches the domain wall, its spin is aligned parallel to the local magnetization. When it enters the domain wall, the local magnetization begins to rotate while the incoming electron's spin rotation is mistracked. The magnetic moment then starts precessing around an effective field [Fig. 1.24(b)] which is composed of the magnetization, its rotation vector and a component along $e_\theta$ coming from the spin relaxation [56]:

$$< \vec{\mu} >= \frac{g\mu_{\mathrm{B}}}{2} \begin{pmatrix} 1 \\ -\dot{\theta}\tau_{\mathrm{sf}} \\ -\dot{\theta}\tau_{\mathrm{ex}} \end{pmatrix}$$

where $\dot{\theta}$ is the speed of the rotation of the frame and $\tau_{\mathrm{ex}} = \hbar/SJ_{\mathrm{ex}}$.

A reaction torque on the magnetization is created due to the fact that the effective field is misaligned with respect to the magnetization. The torque exerted on the domain wall is composed of two contributions:

$$\begin{aligned} \left.\frac{\mathrm{d}\vec{M}}{\mathrm{d}t}\right|_{\mathrm{st}} &= \frac{jPg\mu_{\mathrm{B}}}{2e}\frac{\partial\vec{m}}{\partial y}, \\ \left.\frac{\mathrm{d}\vec{M}}{\mathrm{d}t}\right|_{\mathrm{sf}} &= -\frac{jPg\mu_{\mathrm{B}}}{2e}\frac{\tau_{\mathrm{ex}}}{\tau_{\mathrm{sf}}}\left(\vec{m} \times \frac{\partial\vec{m}}{\partial y}\right) \end{aligned}$$

where $j$ is the amplitude of the current density and $P$ is the current polarization.

The first term corresponds to the adiabatic part of the torque and it does not lead to the domain wall motion. As explained before, it only pushes the magnetization until the moment when the equilibrium with the demagnetizing torque is established. The second term stands as the non-adiabatic contribution. Its amplitude is given by the ratio $\tau_{\mathrm{ex}}/\tau_{\mathrm{sf}}$ which according to the theory of Zhang and Li [57] is also equal to the $\beta$ parameter introduced in equation (1.38):

$$\beta = \frac{\tau_{\mathrm{ex}}}{\tau_{\mathrm{sf}}}. \tag{1.43}$$

This term arises from the spin-flip scattering events which do not conserve the total angular momentum. In comparison to the adiabatic part, the amplitude of this torque is reduced by a factor $\beta$ which is typically around 1/30-1/100. Despite the fact that its amplitude is much smaller than the amplitude of the adiabatic torque, this is the term which pushes the domain wall forward.

The amplitude of $\beta$ is crucial for the domain wall velocities. Thus magnetic materials with low spin relaxation times are good potential candidates for efficient current-induced domain wall displacement. Recently, Miron *et al.* [58] have shown that the $\beta \cong 1$ in Pt\Co\AlO$_x$ trilayer which leads to high domain wall velocities.

Nevertheless, the origin of the phenomenological $\beta$ parameter is still unclear and it is a big issue of debate.

# Chapter 2

# Domain wall dynamics in perpendicular anisotropy systems

Recently, intensive attention has been devoted to materials with perpendicular anisotropy, especially due to the possible applications to devices based on spin-polarized current. The domain wall width is much thinner in materials with perpendicular anisotropy. This fact should lead to high efficiency of spin-transfer torque and therefore to higher domain wall velocities. However, despite the enormous interest in these materials and some very promising results, many fundamental questions concerning the spin-transfer torque mechanism still remain unanswered.

Here we review the most frequent origins of the perpendicular anisotropy, the recent progress and the state of the art of domain wall dynamics in systems with perpendicular anisotropy.

## 2.1 Induced perpendicular anisotropy

The ordered states of magnetic materials arise from the exchange interaction between pairs of atomic spins. This behaviour is described by the Hamiltonian in equation (1.7) where the strength of the exchange interaction between the spins $\vec{S}_i$ and $\vec{S}_j$ is expressed by the exchange constant $J_{i,j}$. The amplitude of $J$ depends upon the distance separating the spins, but not upon the direction of the position vector joining the spins, so that this interaction is isotropic. The orientation of the spins becomes anisotropic via the spin orbit interaction which couples the spins to the crystal lattice.

We have shown in Section 1.4.2 that in materials having quality factor $Q > 1$, the magnetization easy axis points out of the film plane. This requires either a high uniaxial perpendicular anisotropy or combination of a moderate anisotropy and a lower spontaneous magnetization $M_s$. In general, the matter behaves differently down in the nanoworld, so one can expect that different mechanisms leading to the induced perpendicular anisotropy become relevant in films with reduced thickness. The film is called thin when the mechanism originating from the film surface or interface starts to play an important role. Here we briefly show the basic properties of thick and thin films.

### 2.1.1 Thick films

The energy required to rotate the spin system of a domain away from the easy direction is just the energy required to overcome the anisotropy barrier. In most materials the spin–orbit coupling is fairly weak, and so the magnetocrystalline anisotropy is not strong. Rare-earth metals are a special class of materials, where the spin–orbit coupling is strong because of the high atomic number $Z$. Once the spin-orbit is strong enough, the direction of the magnetization depends on the type and orientation of the crystallographic lattice so the film texture plays a key role. The magnetocrystalline anisotropy then reflects the crystal symmetry and it is an intrinsic property of the material so the largest value of anisotropy are found in hexagonal and other uniaxial crystals. Another source of perpendicular anisotropy is the induced anisotropy. This anisotropy, for example, can arise when a stress is applied in the out-of-plane direction.

Films with perpendicular anisotropy were extensively studied because of their applications to magneto-optic recording devices. Perpendicular recording permits higher areal densities of the magnetic records. An important group of magneto-optical recording devices was based on amorphous rare-earth transition metal alloys (Gd–Fe, Gd–Co, etc.). With respect to what was said above, no anisotropy is expected in amorphous material. Nevertheless, these alloys present under certain conditions strong perpendicular anisotropy. There exist several explanations for its origin and they will be discussed further.

### 2.1.2 Thin films

X\Co ultrathin layers, where X=Pt, Pd, Au, Ir, Ni, etc., constitute a special class of materials with perpendicular anisotropy. In these bilayers the X layer is able to induce the perpendicular anisotropy which via the interfacial spin-orbit interaction. Spin-orbit interaction is able to induce large anisotropy energies in ultrathin films as compared to bulk materials.

One can consider two main sources of magnetic anisotropy in X\Co systems: demagnetizing interaction and spin–orbit interaction. In thin films the demagnetizing interaction is always present and induce the in-plane magnetization orientation. In 1954 Néel showed [59] that breaking the symmetry at the surface should result in magnetic anisotropies differing from the bulk. The absence of atoms at the interface causes a reduction of the $3d$ band energy which is more pronounced for the case of out-of-plane orbitals than for in-plane orbitals. Similarly, Co $3d$-Pt $5d$ interfacial hybridization has an effect on magnetic anisotropy at Co\Pt interface [60]. The induced anisotropy strongly depends on the splitting energy separating the $t_{2g}$ and $e_g$ orbitals $\Delta = E(t_{2g}) - E(e_g)$. The total anisotropy of thin films can be described by two effective bulk and interface anisotropy terms

$$K_{\text{eff}} = K_v + \frac{K_{\text{s}}}{t} \tag{2.1}$$

where the $K_v$ term ($K_v < 0$) is the bulk anisotropy contribution which tends to align the magnetization parallel to the film plane, $t$ is the film thickness and the $K_s$ term is the interface anisotropy ($K_s > 0$). The volume anisotropy $K_v$ depends on demagnetization energy, magnetocrystalline anisotropy (hcp or fcc structure) and magnetoelastic energy (lattice mismatch) [61].

The role of the $K_{\text{eff}}$ is shown in Fig. 2.1(a). Den Broeder *et al.* [62] proved the validity of equation (2.1) for Pd\Co multilayers. Films with $K_{\text{eff}} > 0$ show perpendicular magnetic anisotropy. This is true for very thin layers where the surface anisotropy dominates. When the Co layer thickness increase, this interfacial contribution plays a less and less important role and at some critical thickness ($t_\perp = -K_{\text{s}}/K_{\text{v}}$), the volume anisotropy outweighs the interface effect and the spontaneous magnetization turns into the plane. The intercept in Fig. 2.1(a) designates the surface anisotropy and the slope designates the volume anisotropy contribution which is negative accordingly with the theory. [1]

A very important aspect of the existence of perpendicular magnetic anisotropy is the film quality. Many factors such as roughness or formation of interface alloys may cause a reduction in perpendicular magnetic anisotropy. Hence the different growth modes (molecular beam epitaxy, sputtering, electrodeposition, etc.), deposition rates or deposition temperatures followed by an annealing will induce different interface anisotropies.

The results for different deposition techniques is summarized in Fig. 2.1(b). It is clear that different induced Co orientations have different interface and volume anisotropies. It turns out that the strongest perpendicular anisotropy is present in the (111) orientation where $K_{\text{s}} = 0.97\,\text{mJ/m}^2$, indicating a big exchange splitting $\Delta$.

---

[1] Sometimes two interfaces are considered and then equation (2.1) reads $K_{\text{eff}} = K_v + 2K_{\text{s}}/t$.

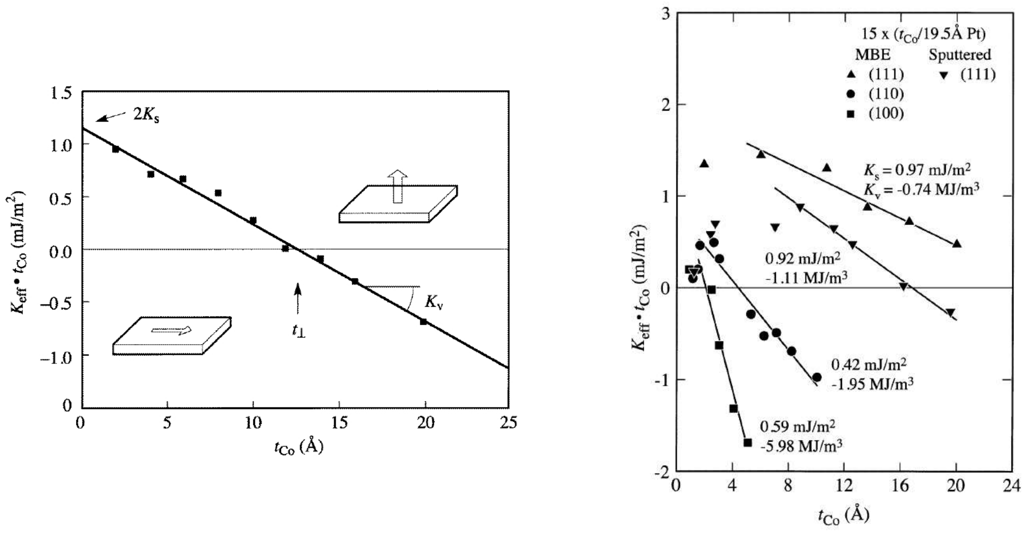

(a) (b)

Figure 2.1: (a) Thickness dependent effective anisotropy anisotropy of symmetric Pt/Co/Pt stack. The intercept corresponds to the interface anisotropy ($2K_s$), the slope gives the volume contribution. (b) Different volume and interface anisotropy contributions in epitaxial Co/Pt multilayers induced by different lattice orientation. [62]

This interfacial effect can be even increased by use of a multilayer sandwich. Description of this and some other cases leading to the anisotropy enhancement goes beyond the scope of this thesis. The goal of this sub-chapter was to provide an intuitive description of the perpendicular anisotropy origin. For further reading we refer here to review paper [63] and references therein.

## 2.2 Field-induced domain wall motion in materials with perpendicular anisotropy

The field-induced magnetization reversal in materials with perpendicular anisotropy is relatively old topic. In the old publications [64] or in the recent review book of J. M. D. Coey [13], was proposed a phenomenological dependence of the field-induced domain wall velocity as

$$v = \mu(H - H_0), \tag{2.2}$$

where $\mu$ is the domain wall mobility, leading to a threshold field $H_0$. This model was proposed for interpreting phenomenologically data in analogy to solid friction. The above variation of the velocity was found when the pinning energy barrier was much higher than $kT$. More recent works show that several cases have to be distinguished:

1. Perfect samples, without any type of defects that could pin the walls during their propagation. The field-induced motion then can be described by the simplest 1D model described in Section 1.5.2. This model gives a description of the domain wall motion evidencing a steady regime at low field, and a precessional regime at high field, separated by the Walker field $H_W$ defined by equation (1.27). This behaviour was confirmed by a number of experiments with low planar anisotropy. Nevertheless, for films with out-of-plane anisotropy, such a behaviour has been clearly observed only in the case of (Ga,Mn)As films at low temperatures [65]. This is related to the fact that the out-of-plane anisotropy distribution is not negligible and it controls the pinning mechanism over the sample.

2. Samples with intrinsic randomly distributed nano-defects giving weak pinning strength for the walls (nanocrystalline boundaries, atomic steps, etc.). At low fields, not efficient enough to overcome pinning barriers, a thermally activated dynamic creep regime is expected for the wall velocity. The domain wall motion is described by the collective creep law expressed by equation (1.31): $v \sim v_0 \exp(-H^{-0.25})$.

   Since the anisotropy is much larger in systems with perpendicular anisotropy, the domain wall is narrower as compared to systems with in-plane anisotropy. Difference between the interaction of a narrow Bloch wall and of a wide Néel wall with pinning centers is shown in Fig. 2.2. The pinning centers are represented by the corresponding energy landscape $E_\mathrm{p}$. The wide domain wall is spread over a larger distance so it rather feels the average of the potential than the deep minima of the potential energy. This is the reason why the narrow domain wall interacts very strongly with the presence of randomly distributed nanometric defects which give rise to high pinning forces.

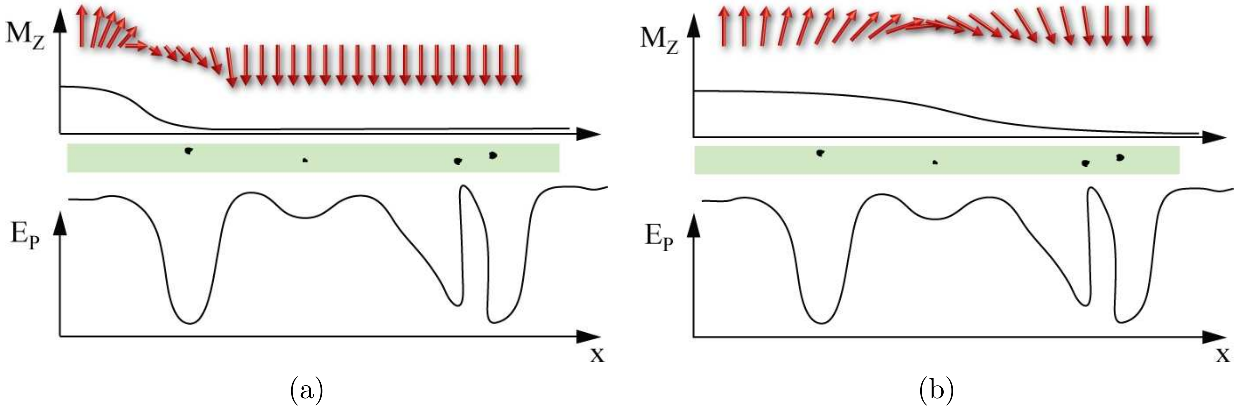

(a) (b)

Figure 2.2: Illustration of domain wall interaction with a nonuniform potential energy distribution in the case of (a) a narrow Bloch domain wall and (b) wide Néel domain wall.

   For example, in the case the of Au/Co/Au [66] or Ag/Fe/Ag(001) films [67] it was not possible to access to the flow regime, probably due to the quality of the interfaces. Hence the measured data were described by equation (2.2) as is shown in Fig. 2.3(a) in the case of Ag/Fe/Ag(001) film. However, in order to recover the domain wall mobility described by the LLG equation, the field has to be increased in order to overcome the creep regime and therefore reach the regime where the domain wall becomes insensitive to the energy landscape. In fact, the domain wall mobility defined by equation (2.2) will be reduced when the flow regime is achieved. The flow regime was reached for example in the case of Pt/Co/Pt [30] where the film quality was improved and the pinning strength reduced. Then the domain wall mobility $\mu$ can be defined according to the LLG equation satisfying relation $v = \mu H$.

3. Samples with hard extrinsic pinning centers (rough substrates, pinholes, growth anomalies, etc.). In this case the hard pinning leads to very rough or dendritic-like domain structure in low field from which it becomes hard to extract any domain wall velocity.

## 2.3 Current-induced domain wall motion in systems with perpendicular anisotropy - State of the art

Systems in which domain walls are manipulated using spin polarized currents may become a key technology for non-volatile memories. However, there are several requirements to be fulfilled for

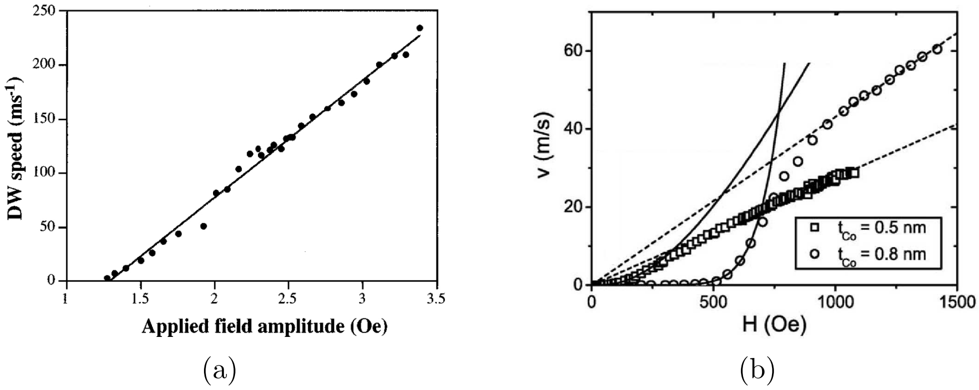

(a) (b)

Figure 2.3: (a) Experimentally measured dependence of domain wall velocity as a function of applied field in the case of Ag/Fe/Ag(001) film [67]. The fitted domain wall mobility according to equation (2.2) is $\mu = 108\,\mathrm{m/s/Oe}$. (b) Domain-wall velocity as a function of applied magnetic field, for Pt/Co/Pt films. Clearly, the low field creep regime (solid line) and flow regime (dashed line) can be distinguished. The domain wall mobility in the case of 0.8 nm thick Co layer $\mu = 0.043\,\mathrm{m/s/Oe}$. [30]

industrial applications: low threshold current values above which the domain wall starts moving, low Joule heating, reproducible domain wall displacements and low drive current densities. In materials having in-plane magnetic anisotropy the domain wall width is large ($\sim 100\,\mathrm{nm}$) so the magnetization rotation in the wall is relatively smooth, which gives rise to a significant contribution of the adiabatic spin torque. Using narrow domain walls in materials with perpendicular anisotropy is expected to increase the non-adiabatic part of spin transfer torque.

Micromagnetic simulations predict that the spin transfer torque effect in perpendicular anisotropy systems can be enhanced [68], [69]. Notably the value of the critical current density is drastically reduced. On the other side, the narrow domain wall strongly interacts with pinning defects [70] which can affect the value of threshold current. In practice, the electrical domain wall manipulation has been observed on few experimental systems with perpendicular anisotropy. Here we review some of them:

- The very first system with perpendicular anisotropy, where the current induced domain wall displacement was observed in the absence of a magnetic field, was a ferromagnetic p-type semiconductor **(Ga,Mn)As** [71]. Domain wall velocities of 20 m/s at $J \sim 10^{10}\mathrm{A/m^2}$ were achieved. Nevertheless, the experiments were performed at low temperatures due to the fact that the Curie temperature of the semiconductor is $T_\mathrm{c} \simeq 119\,\mathrm{K}$.

- The first demonstration of the current-driven domain wall motion in a metallic magnetic system with perpendicular magnetic anisotropy in the absence of a magnetic field was shown by Tanigawa *et al.* in 2008 [72]. In **CoCrPt** wire velocity of 0.05 m/s was achieved at current density of $1.7\times10^{12}$ A/m$^2$.

- Domain wall velocities up to 40 m/s at $J = 1.4\times10^{12}$ A/m$^2$ were obtained in **Co/Ni** wire with perpendicular anisotropy [73].

- In **Pt/Co/Pt** trilayers only the creep regime was achieved with the velocities about $10^{-4}$ m/s by applying current densities of $j \simeq 1 \times 10^{11}$ A/m$^2$ [74].

- Moore *et al.* [75] have studied domain wall motion in $\mathbf{Pt\backslash Co\backslash AlO}_x$ nanowires and the mechanism of domain wall displacement was clarified later by Miron *et al.* [76]. It has been shown that in the range of current densities $J = (1.5\text{–}1.8)\times10^{12}$ A/m$^2$ the domain wall mobility saturates. The domain wall enters to the flow regime, i.e. it moves reproducibly, with velocities up to 400 m/s.

It is believed that the main reason for the high spin transfer efficiency is the broken symmetry structure giving rise to the intrinsic Rashba field.

This system has been also studied during this work and will be described in Chapters 5 and 6.

- The current-induced domain wall motion was also investigated recently in **Ta/CoFeB/MgO** system [77]. The authors also attribute the current-induced domain wall motion to the broken symmetry of the multilayer stack.

- A special class of materials which are potential candidates for efficient current induced domain wall manipulation, are **intermetallic ferrimagnets**. Recently it has been proposed by Komine *et al.* [78] that the spin torque efficiency should be enhanced in the vicinity of the compensation composition.

  This is the other system which was studied in this work and will be described in Chapters 3 and 4.

## 2.4 Domain wall displacement detection methods

From all the experimental results, it appears that the typical values of current densities required for efficient current-induced domain wall motion are in the order of $10^{12}\,\mathrm{A/m^2}$. Such high current densities require patterned nanostructures, typically in the shape of nanostripes of sub-micron width. The fabrication methods and physical properties of nanostructures with dimensions on the sub-micron to nanometer scale are reviewed in [17]. The domain wall motion can be detected by several ways. Here we briefly review some of the commonly used techniques.

- **Magnetoresistance based devices**
  Any deviation of magnetization direction from the uniform alignment influences the resistivity. Hence also the domain wall has an impact on the measured resistivity. The resistivity contribution can be either positive [79] or negative [80]. Such a typical device is shown in Fig. 2.4(a). The domain wall is created in the vicinity of the A contact and then it is displaced by the spin polarized current towards the contact B. The domain wall is detected at the contact B by the abrupt change of the measured resistance. The domain wall velocity then can be easily determined from the measured travelled time and from the known distance between the contacts A and B.

  It has been also shown that this tool is sensitive enough to distinguish transverse wall from vortex wall, and therefore to measure the transformations which domain walls undergo above the Walker breakdown [81].

- **Hall probe-based devices**
  The principle of extraordinary Hall effect, which can be applied to ferromagnetic metals, has been described in Section 1.7. A device including a Hall probe is shown in Fig. 2.4(b). The Hall resistivity is measured in a defined position which is called a Hall cross. Hence the magnetization is probed at a local position. The domain wall is detected at this position when it passes through the Hall cross and the magnetization changes step-likely.

- **Giant magnetoresistance-based devices**
  The giant magnetoresistance (GMR) was discovered in 1988 independently by Albert Fert and Peter Grünberg who were awarded the Nobel prize in physics in 2007. They discovered that parallel alignment of two ferromagnetic layers separated by a nonmagnetic spacer features lower resistance than in the case when they are aligned in antiparallel configuration. The GMR ratio is defined as

$$\mathrm{GMR} = \frac{R_{\mathrm{AP}} - R_{\mathrm{P}}}{R_{\mathrm{P}}}$$

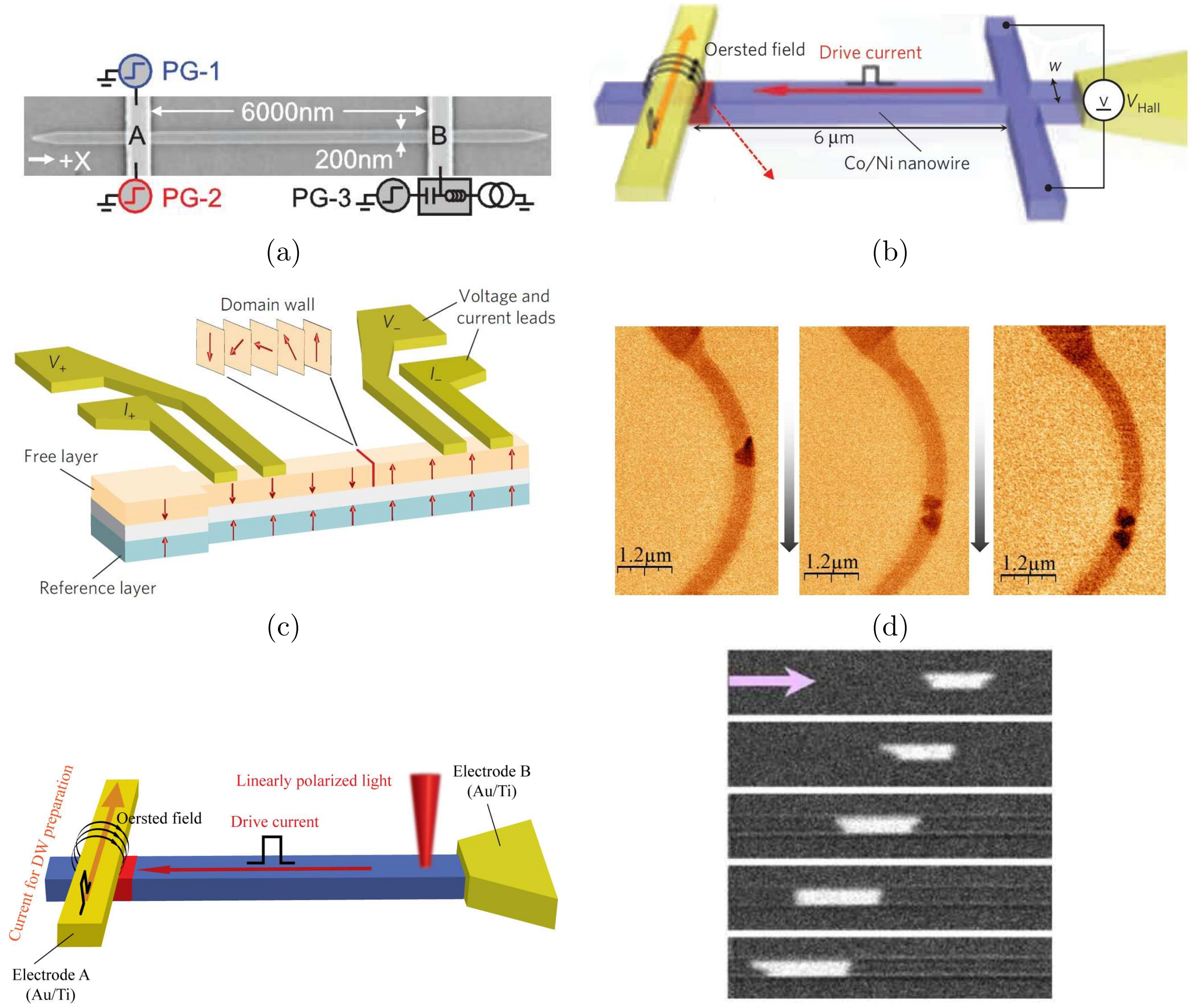

(a) (b) (c) (d) (e) (f)

Figure 2.4: Illustration of methods for domain wall displacement measurement (a) magnetoresistance based device [81], (b) extraordinary Hall effect-based device [73], (c) giant magnetoresistance-based device [82], (d) magnetic force microscopy detection [83], (e) focused magneto-optical Kerr microscopy detection, (f) wide-field Kerr microscopy [85].

where $R_P$ and $R_{AP}$ is the resistance of the parallel and antiparallel state respectively.

This property can be used to detect the domain wall position in a nanostripe using an electric measurement of the resistance. The spatial resolution depends on the GMR ratio. The higher the ratio, the higher the spacial resolution. This device is shown in Fig. 2.4(c). The domain wall propagation is detected in the free layer of a spin valve by measuring the GMR between the $V_+$ and $V_-$ pads as a function of time [82].

- **Magnetic force microscopy detection**
  A magnetic force microscope (MFM) is a variety of atomic force microscope which is based on the interaction between a sharp tip and a sample. If the tip is coated with a ferromagnetic material then it is also sensitive to the presence of magnetic charges. When the topological and magnetic contrast are detected, they can be subtracted and the purely magnetic contrast can be obtained.

  Static images of current-induced domain wall displacement in a Permalloy nanowire before and after the application of 1 ns long current pulses are shown in Fig. 2.4(d) [83]. This method is characterized by very good spatial resolution, typically less than 20 nm, so the domain wall internal structure can be resolved. On the other hand, the scanning method has the disadvantage of being very slow.

- **Focused magneto-optical Kerr microscopy detection**
  This technique is based on magneto-optical effect, i.e. on the interaction between polarized light and sample magnetization. This effect was discovered by John Kerr in 1877. He found that when a linearly polarized light interacts with a magnetic sample, the polarization rotates by an angle $\theta_\mathrm{K}$ upon reflection from a non-transparent sample. The sense of the rotation is switched when the magnetization is reversed. In general, the reflected light is elliptically polarized with the main axes rotated by the angle $\Theta_\mathrm{K}$. The obtained contrast, beside other aspects, depends on the angle $\Theta_\mathrm{K}$.

  Depending on the geometry of the plane of incidence of the polarized light and the magnetization, three configurations can be distinguished:

  - In the polar Kerr effect configuration, which is shown in Fig. 2.5(a), the magnetization is perpendicular to the film surface.
  - In the longitudinal Kerr effect configuration, which is shown in Fig. 2.5(b), the magnetization lies in the sample surface and it is parallel to the plane of light incidence.
  - In the transverse Kerr effect configuration, which is shown in Fig. 2.5(c), the magnetization lies in the film surface and it is perpendicular to the plane of light incidence.

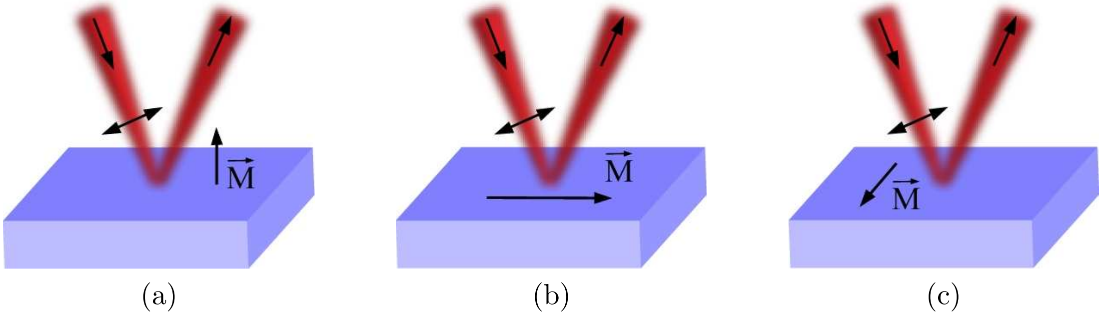

Figure 2.5: Three basic configurations of the magneto-optical Kerr effect (a) Polar Kerr microscopy; (b) Longitudinal Kerr microscopy; (c) Transverse Kerr microscopy.

A device based on the Kerr effect domain wall detection is shown in Fig. 2.4(e) and was experimentally used, for example, in [84]. The domain wall is displaced by the spin polarized current and the magnetization state at a given position is measured by the focused linearly polarized beam. The resolution of the technique is limited by the wavelength of the light and the numerical aperture of the objective, defining the spot diameter focused on the wire.

- **Wide-field Kerr microscopy**

  This microscopy is based on the same principle as in the case of focused Kerr microscopy. The light of linearly polarized and its rotation is analyzed using a polarizer/analyser couple in quasi-extinction geometry. The desired geometry (polar, longitudinal, transverse) can be selected by defining the aperture diaphragm shape which is placed in the optical path.

  In this work at Institut Néel, a commercial Zeiss optical microscope adapted for magneto-optical detection has been used. Since all the magnetic systems studied in the frame of this thesis contained perpendicular anisotropy, we used essentially the polar Kerr microscopy configuration. Since the Kerr rotation depends on the light wavelength, it can be appropriately chosen with respect to the material. In our case we used either an arc lamp having a wide spectrum in the visible spectra, or a high power light emitting diode of wavelength 630 nm, which is better adapted to Kerr effect of Co.

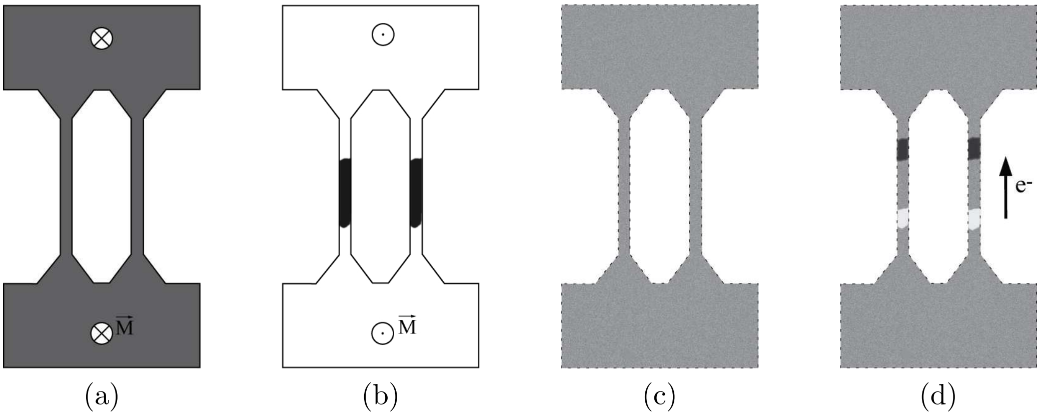

(a) (b) (c) (d)

Figure 2.6: Illustration of the differential method application during the Kerr microscopy: (a) Magnetic saturation. (b) Partial reversal of magnetization. (c) Differential image. (d) Differential image after a current pulse.

In a Kerr microscope, sample regions with different magnetization directions give rise to different Kerr rotations, which are translated in different intensities in the CCD camera. These differences are usually small, and to improve the contrast the images have to be mathematically treated. The contrast can be enhanced mathematically by using the so-called differential method which is illustrated in Fig. 2.6. As it will be described in the following chapters, our samples always consist of a number of nanowires connected to two large injection pads. At the beginning, the sample is magnetically saturated in such a way, that the magnetization is pointing 'down'. This state corresponds for example to the dark contrast. In the next step, which is shown in Fig. 2.6(b), we reverse the magnetization using magnetic field pulses in the pads and we inject the domain walls into the wires. The white contrast then corresponds to the magnetization pointing 'up'. This image is then taken as a reference and any other pictures are processed in such a way that they are mathematically subtracted from the reference image. When no change of the contrast is observed, the image stays 'gray' as it is shown in Fig. 2.6(c). Fig. 2.6(d) shows the change of the contrast after the application of a current pulse causing the domain walls to move towards the top of the line. Since the two domain walls in the wire separate regions with 'up-down' and 'down-up' magnetization, the obtained contrast is opposite for the two domain wall movements. Such an image can be further processed as it is described in the following text.

Fig. 2.4(f) shows a sequence of snapshots of current-induced domain wall motion in GaMnAs nanowires [85]. Two domain walls are moved in the same direction by a 10 $\mu$s long current pulse. The domain wall velocity then can be determined from the distance which the domain wall travelled during the pulse.

# Chapter 3

# $Gd_{1-x}Co_x$ thin films with induced composition gradient

In this chapter I will introduce some basic concepts of the magnetism of $Gd_{1-x}Co_x$ films with perpendicular anisotropy. This is the first system where I have studied both field and current induced domain wall motion.

## 3.1 Ferrimagnetism

A ferrimagnet can be considered as an antiferromagnet with two inequivalent sublattices, so that the total magnetic moment can differ from zero. The difference between the ordering in ferromagnetic and ferrimagnetic materials is schematically shown in Fig. 3.1. We can define two different magnetic sublattices in a ferrimagnet. The magnetic moments in each sublattice are interacting ferromagnetically whereas these two sublattices are coupled antiferromagnetically.

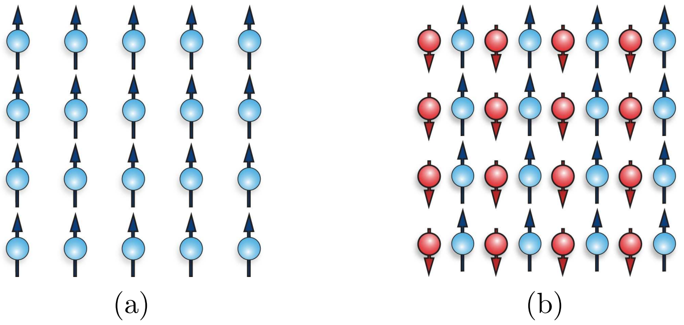

(a) (b)

Figure 3.1: (a) Magnetic configuration of a ferromagnetic material. (b) In a ferrimagnet two (or more) mutually antiparallel different sublattices can be distinguished.

A large subgroup of ferrimagnets consists of magnetic oxides. The most famous ferrimagnetic oxide is the so-called magnetite ($Fe_3O_4$), a constituent of lodestone[1], the first permanent magnet discovered by man. Another example of magnetic oxides are rare-earth iron garnets which are known for their very important magneto-optical properties. Their chemical formula is $R_3Fe_5O_{12}$, where R=Gd, Tb, Dy, Yb, etc. When the rare-earth atomic positions are occupied by nonmagnetic yttrium ions, in the $Y_3Fe_5O_{12}$ garnet (YIG), the material presents excellent high-frequency magnetic properties and a narrow ferromagnetic resonance linewidth so it is often used in GHz oscillators.

---

[1] from Middle English 'leading stone' because of its use in the first magnetic compasses

A special class of ferrimagnets are intermetallic compounds consisting of solid phases of two or more metallic elements. There exist several hundreds of intermetallic compounds composed of rare-earth metals and $3d$ metals. Their magnetic properties have been reviewed by Franse and Radwanski [86]. This class of materials is used in many applications such as high-performance permanent magnets ($SmCo_5$, $Nd_2Fe_{14}B$) or for magneto-optic recording (TbFeCo). Due to its electronic properties and metallic behaviour, this class of ferrimagnets is interesting for spintronics.

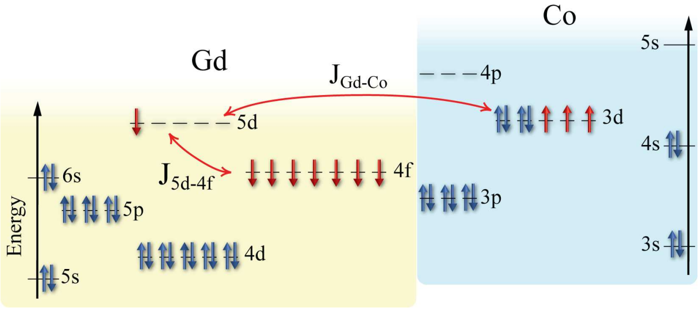

Figure 3.2: Schematic illustration of the origin of the ferrimagnetic interaction in Gd-Co. The negative exchange interaction $J_{\mathrm{GdCo}}$ causes the antiparallel alignment of Gd $5d$ magnetic moments with respect to Co $3d$ magnetic moments. Due to this 'bridge' the Gd $4f$ magnetic moments, which are parallel to the $5d$ moment via direct exchange, are indirectly aligned oppositely to the Co $3d$ magnetic moments.

The key to understand intermetallic compound ferrimagnetism is the interaction between localized $4f$ rare-earth (RE) moments and more delocalized $3d$ transition metal (TM) magnetic moments. The valence band of RE element is formed of $5d$ electrons. From the Stoner criterion expressed by equation (1.6) it follows that the $5d$ electrons in these elements are not able to form $5d$ moments of their own. Nevertheless, these $5d$ electrons play a crucial role in the magnetic coupling between the $4f$ and $3d$ moments. This is due to the different degree of mixing of spin-up and spin-down rare-earth $5d$ with the TM $3d$ states. Due to the exchange splitting of the $3d$ band, the mixing of $3d$ states and $5d$ states is larger for spin-down electrons than for spin-up electrons. This leads to a larger $3d$ character of the $5d$ spin-down band than of the spin-up band. The overall $5d$ moment is then antiparallel to the overall $3d$ moment. When $4f$ electrons are present in the RE element[2], the ferromagnetic intra-atomic exchange interaction between the $4f$ moments and the $5d$ moments leads to antiparallel alignment between $3d$ and $4f$ spins in the case of heavy RE.

This is schematically shown in Fig. 3.2 in the case of Gd-Co compound. The $5d$ electron conveys an indirect antiferromagnetic interaction between Gd $4f$ and Co $3d$ magnetic moments. The half-filled shell $4f^7$ of gadolinium contributes a large magnetic moment $S = 7\mu_{\mathrm{B}}$ opposed to that of the cobalt $S \sim 1.5\mu_{\mathrm{B}}$. In reality this picture is more complicated due to the existence of a band structure which can be very complex. This was calculated by Malik *et al.* in the case of $GdCo_5$ compound [87]. It was found that the conduction band is Co-like, so the current polarization depends mostly on the Co states close to the Fermi level.

We can represent the exchange interaction between the various spins in the sublattices $A$ and $B$ by means of the Hamiltonian described by equation (1.7):

$$\mathcal{H}_{\mathrm{ex}} = -\sum_{i \neq j} J_{i,j} \vec{S}_i \cdot \vec{S}_j$$

where the exchange constant $J_{A,A} \neq J_{B,B}$ and $J_{A,B} < 0$. $J_{A,A}$ and $J_{B,B}$ are in general positive quantities but this is not necessary.

---

[2] There are no $4f$ moments in the rare-earth elements La, Lu or Y.

The total magnetization of the system is then given by a superposition of the sublattice magnetizations $\vec{M}_{\text{tot}} = \vec{M}_{\text{A}} + \vec{M}_{\text{B}}$. In the special case when the two sublattices are oppositely magnetized, the total magnetization is:

$$M_{\text{tot}} = M_{\text{A}} - M_{\text{B}}. \tag{3.1}$$

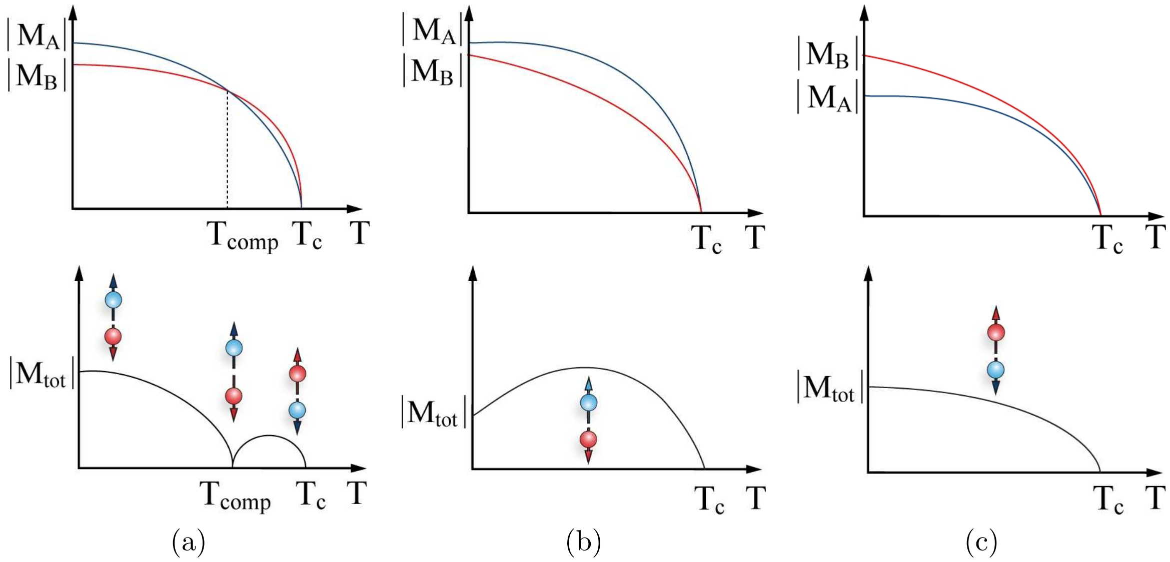

Figure 3.3: Temperature dependence of $A$ and $B$ sublattice magnetizations and of the total magnetization $M_{\text{tot}}$ which is given by equation (3.1) for different concentrations of $A$ and $B$ atoms.

In a mean field model, each magnetization sublattice can be modeled using the Brillouin theory. For the $A$ sublattice it reads

$$M_A = N\mu_A B_J\left(\frac{\mu_0\vec{\mu}_A\vec{H}_A}{k_{\text{B}}T}\right) \tag{3.2}$$

where $N$ is the number of atoms per unit volume, $B_J$ is the Brillouin function and the magnetic moment $\mu_A$ defined by equation (1.2). The term $\vec{H}_A$ expresses the so-called mean internal magnetic field which takes into account the interaction between the spins on nearest-neighbor atoms. The mean field acting on the $A$ sublattice is

$$\vec{H}_A = \vec{H}_{\text{app}} + \lambda_{AA}\vec{M}_A - \lambda_{AB}\vec{M}_B,$$

where $\vec{H}_{\text{app}}$ is the applied magnetic field, $\vec{M}_A$ and $\vec{M}_B$ are the magnetizations of $A$ and $B$ sublattices respectively, $\lambda_{AA}$ is the $A-A$ intrasublattice molecular field coefficient and $\lambda_{AB}$ is the $A-B$ intersublattice molecular field coefficient. The mean field acting on the $B$ sublattice can be described in a similar way, where the intrasublattice molecular field coefficient reads $\lambda_{AB} = \lambda_{BA}$. These equations are not independent - the magnetization of the $A$ sublattice depends on the $B$ sublattice and vice versa and such model should be solved self-consistently. The detailed calculation is presented in Section 3.5.

Since the temperature dependencies of these sublattices, given by equation (3.2), are different, the temperature dependence of the total magnetization can be more complicated than in the case of ferromagnetic materials. In Fig. 3.3 are shown typical temperature dependencies of the magnetization for three different concentrations of the $A$ and $B$ elements. In a certain range of concentrations the so-called compensation temperature $T_{\text{comp}}$ can be found. At this temperature the two magnetic sublattice magnetizations cancel each other and the total macroscopic magnetization vanishes. When increasing the temperature above the compensation temperature, the total magnetization increases first and then decreases down to zero at the Curie temperature $T_{\text{c}}$. The material becomes paramagnetic above this temperature. The concentration of $A$ is restricted to a certain range to keep $T_{\mathrm{comp}}$, because $T_{\mathrm{comp}} \in (0, T_{\mathrm{c}})$.

In this thesis I have studied domain wall dynamics in ferrimagnetic amorphous alloy of Gd$_{1-x}$Co$_x$. Thus I will limit myself to the description of Gd$_{1-x}$Co$_x$ properties, which are presented hereafter.

## 3.2 Applications of Gd$_{1-x}$Co$_x$ alloy

Ferrimagnetic (Tb, Gd)$_{1-x}$(Fe, Co)$_x$ amorphous alloys with $0.7 < x < 0.8$ were widely studied in the 1980s due to their particular relevance for magneto-optical recording [88]. The range of compositions $0.7 < x < 0.8$ gives rise to the appearance of the compensation temperature close to room temperature. The existence of compensation temperature close to room temperature is essential for a magneto-optic recording medium based on a ferrimagnetic material. The required properties for such applications are the existence of a large macroscopic uniaxial magnetic anisotropy ($K_{\mathrm{u}} > 0$) and large magneto-optical coefficients.

The principle of the magneto-optical recording was described in detail by Daval *et al.* [89]. During the magneto-optical recording process a short and high power focussed laser beam pulse raises the temperature of the perpendicularly magnetized medium as it is depicted in Fig. 3.4(a). The coercive field diverges at the compensation temperature but it is remarkably reduced when the temperature is raised [Fig. 3.4(b)]. The external applied magnetic field is then able to reverse locally the direction of magnetization in the heated region. When the temperature of the hot spot returns to its read state, the reversed magnetized domain persists. Readout of information employs the polar Kerr effect using a linearly polarized light. The recorded track can therefore be readout by the same focussed laser beam that was used for recording the information, using a smaller power.

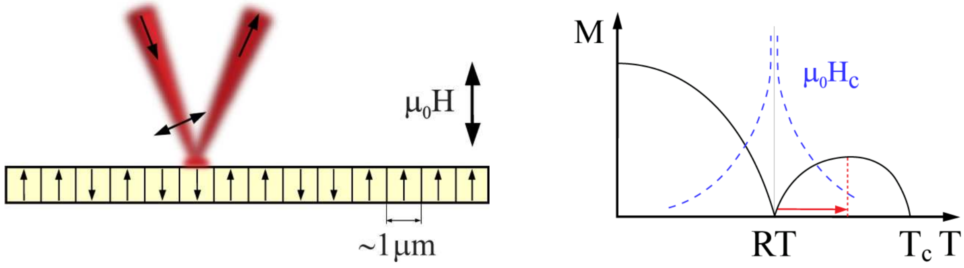

(a) (b)

Figure 3.4: (a) The principle of heat-assisted magneto-optical recording. (b) The temperature is increased by the laser beam pulse in order to increase the local magnetization and thus to decrease the local coercive field. The external magnetic field $\mu_0 H$ then can reverse the bit magnetization.

The amorphous alloys present also some other advantages for magneto-optical applications. Because of a relatively high resistivity, the films exhibit a rather low thermal conductivity and this also allows for reasonable writing laser powers. An inherent drawback in every technique based on the magneto-optical recording is the media noise which is ascribed to optical losses. This noise is generated by reflectivity or refractive index inhomogeneities, local stresses, defects, surface roughness, and overall by grain structure [89]. The grain size in amorphous films is less than 3 nm, which is orders of magnitude smaller than the wavelength of optical lasers. These undesirable effects are then remarkably eliminated in the amorphous alloys.

The physical limitation of magneto-optical recording technique is imposed by the wavelength of light and by the minimum radius of a stable cylindrical domain, which does not allow to use bit sizes smaller than a micrometer. From this follows that the magneto-optical recording is no longer a competitive method. Nevertheless, the discovery of the spin-transfer torque effect and implementation of spin-transfer torque to magnetic memories recently gave rise to a new interest for the use of these materials. As mentioned above, compensated ferrimagnets have been also proposed recently as interesting candidates for spin torque induced domain wall motion applications, as it is expected that spin torque efficiency should be enhanced in the vicinity of the compensation temperature [78].

## 3.3 Magnetic properties of $\mathrm{Gd}_{1-x}\mathrm{Co}_x$ alloy

### 3.3.1 Perpendicular anisotropy

In 1973 was discovered that sputtered amorphous thin films of Gd-Co and Gd-Fe can show perpendicular anisotropy [90]. It was also proven that such thin films containing cylindrical domains were suitable for magneto-optical recording. Note that no macroscopic magnetic anisotropy is expected to be present in an ideal amorphous state. Macroscopic magnetic anisotropy implies the presence of a structural anisotropy at least on a nanometer scale, together with an interaction between magnetic moments and the anisotropic structure. Thermally evaporated films of amorphous Gd-Co have been found to have an in-plane anisotropy. On the other hand, Gd-Co films have perpendicular anisotropy when magnetron sputtering technique is used for the film growth. Several possible origins of the perpendicular magnetic anisotropy can be found in the literature. Here we list the most cited ones illustrating the ambiguity of the possible anisotropy origin.

- **Short-range order of the crystal structure**
  Mergel *et al.* [91] have proposed a pseudocrystalline model of the magnetic anisotropy in amorphous alloys. They suggested that during the layer-by-layer growth a pseudocrystalline planar structure is formed with an averaged orientation of the axis in the film plane. Such an effect is supposed to be purely atomistic, involving structures over slightly more than nearest neighbours distance. Such a crystallographic structure would give rise to a perpendicular anisotropy via spin-orbit coupling. However, convincing evidence for atomic-scale structural anisotropy in Gd-Co amorphous films has not been obtained by diffraction techniques so far.

- **Pair ordering model**
  In the model proposed by Mizoguchi *et al.* [92] the anisotropy is arising from magnetic dipolar interaction which involves anisotropically distributed atomic moments. The pair ordering model seeks the origin of the magnetic anisotropy in a redundance of pairs of the same atoms aligned in the direction normal to the film plane with respect to the number of pairs oriented in the plane. The pair ordering and dipolar interaction lead to a relation between the uniaxial anisotropy and the sublattice magnetizations [93]:

  $$K_u = \sum C_{i,j} \vec{M}_i \vec{M}_k, \tag{3.3}$$

  where $C_{i,j}$ is the pair ordering coefficient. It was shown by Taylor and Gangulee [94] that in evaporated Gd-Co alloy $C_{i,j} > 0$. From equation (3.3) it appears therefore that the Gd-Co pairs contribute to in-plane anisotropy while the Co-Co and Gd-Gd pairs contribute to perpendicular anisotropy.

  Maksymowicz *et al.* [95] found that Gd-Gd pair ordering may play the dominant role in inducing magnetic anisotropy. Contrary to the previous study, Twarowski *et al.* [96] have found that the main contribution to the perpendicular anisotropy is the Co-Co pair interaction. This well illustrates the difficulties in the recognition of the source of the perpendicular anisotropy.

- **Stress induced anisotropy**
  Tagaki *et al.* [97] have shown that a considerable part (10-30%) of the perpendicular anisotropy in Gd-Co sputtered films originates from the internal planar stress due to the substrate constraint.

They found also that this stress is very sensitive to the argon pressure and to the substrate bias voltage during the sputtering.

- **Semi-Columnar growth**
  Perpendicular anisotropy in oxygen contaminated Gd-Co amorphous films was also studied by means of transmission electron microscopy [98]. It was found that sufficient uniaxial anisotropy in amorphous film can be developed when cylindrically or elliptically shaped Co-rich regions are present in the film.

In conclusion, despite the fact that the Gd$_{1-x}$Co$_x$ alloys were intensively studied in the past, no clear explanation of the perpendicular anisotropy has been published so far.

### 3.3.2 Magnetization process of Gd$_{1-x}$Co$_x$ alloy

The typical hysteresis loop illustrating the magnetization process in a general ferrimagnetic alloy is sketched in Fig. 3.5. The ferrimagnetic saturation state can be achieved with a low external field $\mu_0 H_{\mathrm{s1}}$ called the ferrimagnetic saturation field. At this point all the majority magnetic moments are aligned parallel to the external field and constitute a collinear structure with the minority magnetic moments which are opposed to the external magnetic field. Such a configuration is a result of the Zeeman energy described by equation (1.9) and of the antiparallel alignment given by $3d$-$4f$ indirect interaction. The total magnetization in this collinear regime can be calculated by equation (3.1).

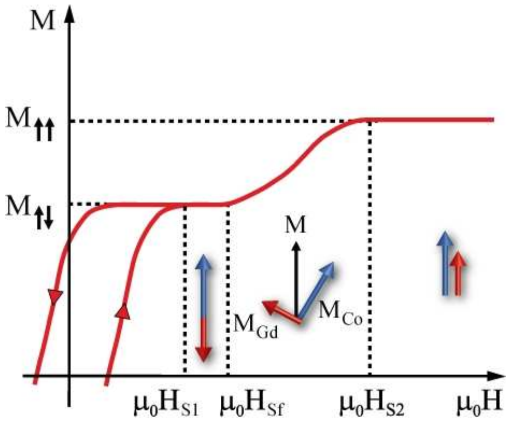

Figure 3.5: Illustration of the magnetization process in a ferrimagnetic material.

The antiparallel alignment of Gd and Co magnetic moments can be broken when a sufficiently high magnetic field is applied. This field is called spin-flop field[3] $\mu_0 H_{\mathrm{sf}}$. Above this field the two magnetic sublattices are no longer collinear and they rotate away from the applied magnetic field. The reorientation process, driven by the energy minimization and due to the dominance of the strong Co-Co ($3d$–$3d$) interaction, i.e. its rigid rotation in the external field, can be relatively complicated [99]. In the case of neglected magnetocrystalline anisotropy the spin-flop field reads [100]

$$\mu_0 H_{\mathrm{sf}} = \lambda \mu_0 |M_{\mathrm{Co}} - M_{\mathrm{Gd}}| \tag{3.4}$$

where $\lambda = \lambda_{GdCo} = \lambda_{CoGd}$ is the intrasublattice molecular field coefficient.

When the external field is high enough, a parallel state can be achieved. Such a magnetic field is then called the ferromagnetic saturation field $\mu_0 H_{\mathrm{s2}}$. Its amplitude can be calculated in the case of no magnetocrystalline anisotropy by using relation [100]

$$\mu_0 H_{\mathrm{s2}} = \lambda \mu_0 |M_{\mathrm{Co}} + M_{\mathrm{Gd}}|.$$

---

[3] The spin flop should not be mistaken with the spin flip term which is connected to the scattering mechanisms.

The critical fields $\mu_0 H_{\mathrm{sf}}$ and $\mu_0 H_{\mathrm{s2}}$ in the absence of the anisotropy were calculated by Nam [101] for $\mathrm{Gd_{0.2}Co_{0.8}}$. The obtained results in Fig. 3.6(a) show that ferromagnetic saturation field $\mu_0 H_{\mathrm{s2}}$ is several hundreds of Tesla, which is not experimentally attainable. Due to the fact that the spin-flop field $\mu_0 H_{\mathrm{sf}}$ is given by the magnetization difference, it is significantly lower and it even vanishes at the compensation temperature. The spin-flop was experimentally observed in $\mathrm{GdCo_5}$ single crystal by Kuz'min *et al.* [102]. In this case the measurement was performed on the non-compensated sample and using pulsed magnetic fields it was found that $\mu_0 H_{\mathrm{sf}} \simeq 46\,\mathrm{T}$. The temperature dependence of the spin flop field was studied by Nam [101] and the minimum value of the spin flop field was evidenced at the vicinity of the compensation temperature. However, the minimum measured spin flop field was $\mu_0 H_{\mathrm{sf}} \simeq 0.7\,\mathrm{T}$ and not zero as predicted by equation (3.4) due to the anisotropy.

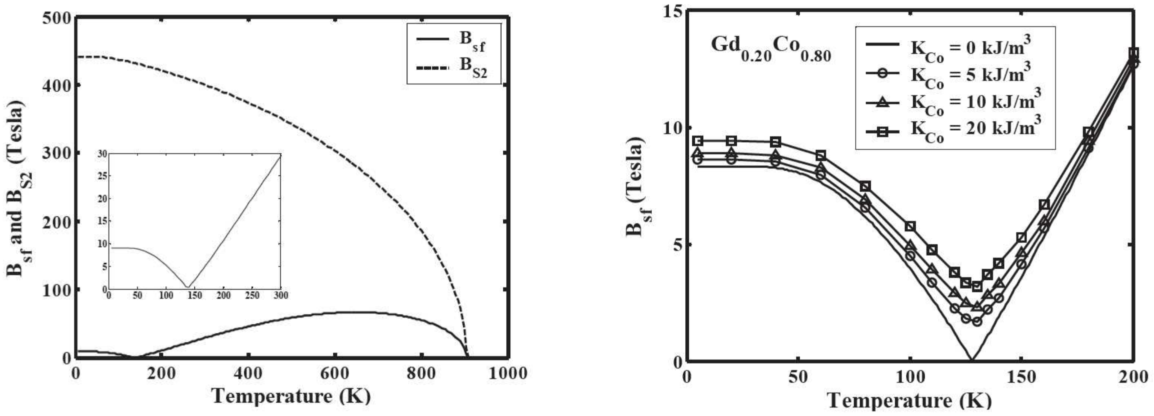

(a) (b)

Figure 3.6: (a) Calculated temperature dependence of the spin flop field ($\mu_0 H_{\mathrm{sf}}$) and the ferromagnetic saturation field ($\mu_0 H_{\mathrm{s2}}$) of $\mathrm{Gd_{0.2}Co_{0.8}}$ alloy in the case of no anisotropy. (b) Calculated impact of the anisotropy on the spin flop field. [101]

Nam included the magnetocrystalline anisotropy into the simulations and demonstrated its impact on the spin flop field in the compensation temperature vicinity. This result is shown in Fig. 3.6(b). In fact, the magnetocrystalline anisotropy starts to play an important role in the vicinity of the compensation temperature where the Zeeman energy vanishes. The anisotropy energy becomes comparable to the Zeeman energy and its impact on the spin flop phenomenon is pronounced. This explains the nonzero value of the spin flip field at the compensation temperature.

## 3.4 Characteristic temperatures

In comparison to a classical ferromagnet, three characteristic temperatures can be found in the amorphous ferrimagnetic alloy:

- **Crystallization temperature $T_{\mathrm{x}}$**
  All the amorphous alloys are in a metastable state and they tend to transform into a stable crystalline phase. The transition to the crystalline state is an exothermic reaction, so calorimetry is widely used to study temperature induced transitions in amorphous alloys. The magnitude of $T_{\mathrm{x}}$ strongly depends on the composition $x$. This dependence was summarized from various publications by Hansen [93] and is shown in Fig. 3.7.

  Amorphous alloys with a very low content of gadolinium ($x > 0.85$) exhibit crystallization temperature below room temperature so they no more show the desired properties of amorphous alloys at room temperature. $T_\mathrm{x}$ increases with decreasing concentration of the rare-earth element up to 600 K at $x \simeq 0.5$.

- **Curie temperature $T_\mathrm{C}$**
  constitutes the transition between the ferromagnetic and paramagnetic behaviour. The composition dependence of the Curie temperature is shown in Fig. 3.7(a). The initial slight decrease of $T_\mathrm{C}$ for Gd rich alloys is found similarly to diluted RE alloys, where the Co sublattice behaves as a nonmagnetic dilution. Similar behaviour was observed for example in amorphous Gd-Cu alloys [103]. When the Co portion is increased, the strong Co-Co exchange interaction rises $T_\mathrm{C}$. The Curie temperature interferes with the crystallization temperature which restricts the investigations of the properties in the amorphous state. The crossover between these two temperatures occurs at $x \simeq 0.7$ and $T \simeq 600\,\mathrm{K}$. For the Co composition $x \sim 0.8$ used in this thesis, direct measurement of $T_\mathrm{C}$ would indeed lead to the film crystallization and change of the magnetic properties.

  Above all, this imposes problems for experimental determination of the intrasublattice $\lambda_\mathrm{CoCo}$ coefficient. Due to the minimal impact of Gd-Gd and Gd-Co interaction on the Curie temperature, the evidence of the Curie temperature is a direct measurement of the Co-Co exchange constant $J_\mathrm{Co}$ (see equation (1.8)). This allows to calculate the intrasublattice $\lambda_\mathrm{CoCo}$ coefficient [104]

$$\lambda_\mathrm{CoCo} = \frac{Z_\mathrm{Co} J_\mathrm{Co}}{2\mu_\mathrm{B}^2 N_\mathrm{Co}}, \tag{3.5}$$

  where $Z_\mathrm{Co}$ is the number of nearest Co neighbours of a Co ion and $N_\mathrm{Co}$ is the number of Co atoms per volume unit. Due to the easy crystallization for $x > 0.7$ Co concentrations, the magnitude of $\lambda_\mathrm{CoCo}$ has to be only extrapolated or obtained from the Curie temperature of the crystallized structure. This fact is one of the main reasons for a wide range of incongruities in the published molecular coefficients.

- **Compensation temperature $T_\mathrm{comp}$**

  The total magnetization is given by equation (3.1). The temperature dependence of each sublattice is described by the Brillouin function (3.2). At the compensation temperature $T_\mathrm{comp}$ reads $\vec{M}_\mathrm{Co} = -\vec{M}_\mathrm{Gd}$ and the total magnetization vanishes. The compensation temperature very strongly depends on the alloy composition $x$. Experimentally measured values of the compensation temperature collected by Hansen are shown in Fig. 3.7(b). The most problematic part of these data is the accuracy of the composition measurement. For example, Taylor and Gangulee [94] have measured the composition by electron microprobe analysis with ±5 % accuracy. Such an accuracy is not precise enough to allow deducing the composition dependence of the compensation temperature. The mean slope of $T_\mathrm{comp}$ in Fig. 3.7(b) corresponds to $\simeq 70\,\mathrm{K/at\%}$.

  N. T. Nam [101] used in his calculations parameters based on the combination of early published transport and magnetometry measurements. He found that the composition dependence of the compensation temperature is about $\simeq 40\,\mathrm{K/at\%}$.

## 3.5 Mean-field model for Gd$_{1-x}$Co$_x$ alloy

The first modern theory of ferromagnetism was proposed by Pierre Weiss in 1906 and it remains useful up to this day. The magnetization of Co and Gd sublattice can be described by equation (3.2).

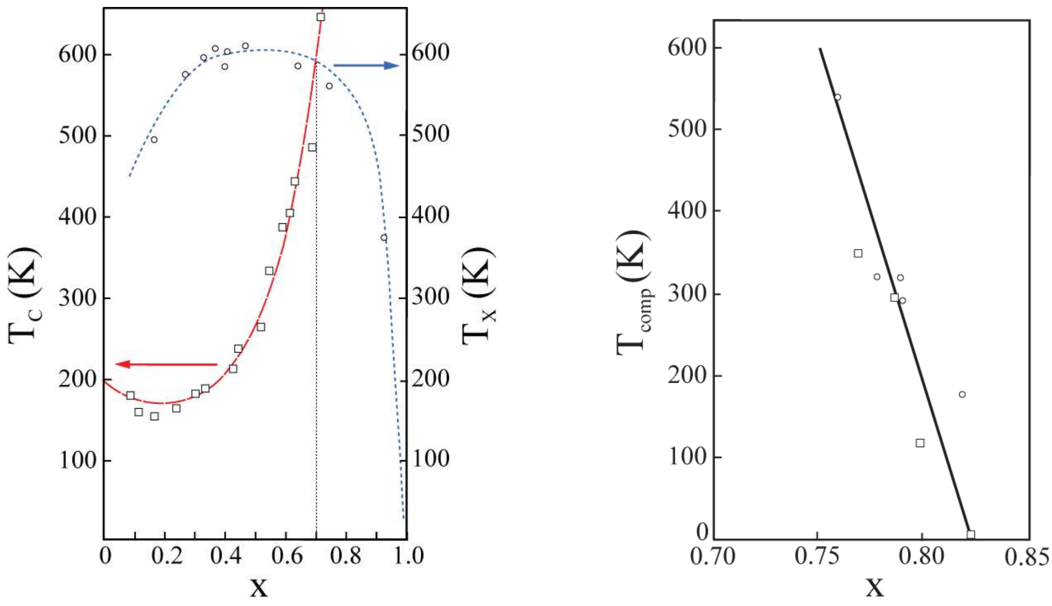

(a) (b)

Figure 3.7: (a) Composition dependence of the Curie temperature ($T_C$) and the crystallization temperature of several amorphous $\mathrm{Gd}_{1-x}\mathrm{Co}_x$ alloys. The experimental data are collected by Hansen in [93]. The corresponding curves serve as a guide for eyes. (b) Composition temperature as a function of composition. The experimentally measured data were collected by Hansen [93]. The mean slope corresponds to $\simeq 70\,\mathrm{K/at\%}$.

$$M_{\mathrm{Co}} = xN\mu_{\mathrm{Co}}B_{JCo}\left[\frac{\mu_0\vec{\mu}_{\mathrm{Co}}\left(\vec{H}_{\mathrm{app}} + \lambda_{\mathrm{CoCo}}\vec{M}_{\mathrm{Co}} - \lambda\vec{M}_{\mathrm{Gd}}\right)}{k_{\mathrm{B}}T}\right], \tag{3.6}$$

$$M_{\mathrm{Gd}} = (1-x)N\mu_{\mathrm{Gd}}B_{JGd}\left[\frac{\mu_0\vec{\mu}_{\mathrm{Gd}}\left(\vec{H}_{\mathrm{app}} + \lambda_{\mathrm{GdGd}}\vec{M}_{\mathrm{Gd}} - \lambda\vec{M}_{\mathrm{Co}}\right)}{k_{\mathrm{B}}T}\right], \tag{3.7}$$

where $x$ is the Co content. Typically, the molecular field coefficients are of the order $\lambda_{\mathrm{CoCo}} \sim 10^3$, $\lambda \sim 10^2$ and $\lambda_{\mathrm{GdGd}} \sim 10^1$. Since the Gd-Gd exchange interaction is very weak and has a minimum influence on the magnetization dependence, it is usually neglected. Hence the equation (3.7) can be simplified.

The parameters for mean-field calculations are chosen according to the fact that we work with the alloy composition $x \sim 0.8$, where the compensation temperature is close to ambient temperature. Here we list the parameters which are based on the data already published [104], [101]:

- Gd:

$$\begin{aligned} g_{\mathrm{Gd}} &= 2 \\ J_{\mathrm{Gd}} &= 3.5 \\ \mu_{\mathrm{Gd}} &= 7\mu_{\mathrm{B}} \end{aligned}$$

- Co:

$$\begin{aligned} g_{\mathrm{Co}} &= 2.22 \\ J_{\mathrm{Co}} &= 0.775 - 0.848\left(\frac{1-x}{x}\right)^{1.5} \\ \mu_{\mathrm{Co}} &= 2.22 J_{\mathrm{Co}} \mu_{\mathrm{B}} \end{aligned}$$

  The cobalt angular momentum is reduced due to the charge transfer with increasing Gd content since one of the $d$ half-bands in Co is filled. This empiric relation was obtained by fitting data which were measured experimentally by Taylor and Gangulee [94]. Similar behaviour was also described in the case of rare-earth-iron amorphous alloys [105].

- The mass density of GdCo$_4$ is: $\rho = 8500\,\mathrm{kg/m^3}$ [106], so the atom density $N = 6.51 \times 10^{28}\,\mathrm{at/m^3}$.

- From Fig. 3.7(a) follows that the Curie temperature in the case of $x \sim 0.8$ reads $T_C \simeq 750\,\mathrm{K}$. From equation (3.5) can be then obtained the Co-Co intrasublattice molecular field coefficient $\lambda_{\mathrm{CoCo}}$=840.

- $\lambda$=180.

The magnetization behaviour as a function of temperature, obtained by using the mean-field model in the case of $x = 0.78$ are shown in Fig. 3.8. The compensation temperature takes place at $T_{\mathrm{comp}} = 300\,\mathrm{K}$ which agrees with the data shown in Fig. 3.7(b). When $T < T_{\mathrm{comp}}$, the system is Gd-rich, so the Gd magnetic moments dictate the total magnetization orientation with respect to the applied magnetic field. If $H > H_{\mathrm{c}}$, below the compensation temperature the gadolinium sublattice magnetization is parallel to the applied field, whereas above the compensation temperature it becomes antiparallel to the field.

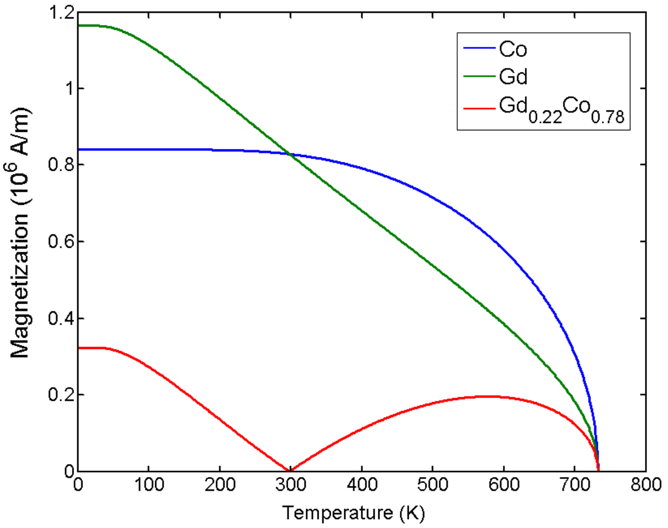

Figure 3.8: Calculated temperature dependence of the magnetization in the case of $x = 0.78$. The obtained compensation temperature $T_{\mathrm{comp}} = 300\,\mathrm{K}$.

The compensation temperature dependence as a function of the composition is presented in Fig. 3.9. The calculated $T_{\mathrm{comp}}$ distribution can be expressed, in a reasonable approximation, by a linear dependence which reads

$$\boxed{\frac{\Delta T_{\mathrm{comp}}}{\Delta x} = 44 \pm 1\,\frac{K}{\mathrm{at.\%}}}. \tag{3.8}$$

This relation shows that the compensation temperature depends very strongly on the composition. This yields experimental difficulties when a particular compensation temperature is desired. Strong compensation temperature dependence implies the need of a very high accuracy of the alloy composition.

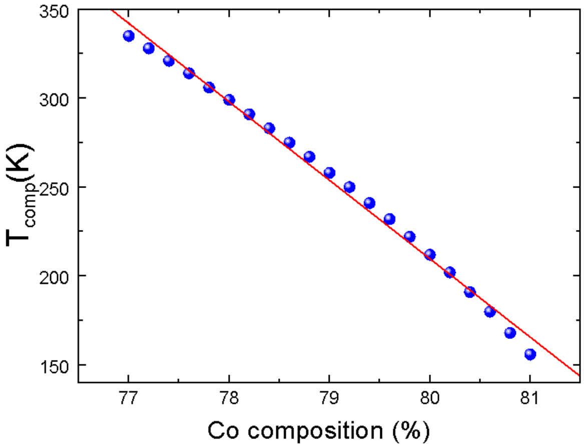

Figure 3.9: Calculated composition dependence of the compensation temperature $T_{\rm comp}$ as a function of Co content $x$. In the composition range $x \in (0.77, 0.81)$ the dependence was linearized by $\Delta T_{\rm comp} = 44 \pm 1\, K/\text{at.}\%$ (red line).

## 3.6 Film deposition

The $\text{Gd}_{1-x}\text{Co}_x$ films for our studies were prepared using the facing-target magnetron sputtering technique. A magnetic field is applied perpendicularly to the targets by placing large magnets behind the targets. This field traps the electrons near the target surface, and causes them to move in spiral motion until they collide with an Ar atom. This external magnetic field increases the scattering rate and enables to keep the high plasma ionization with a lower power. The magnetron sputtering technique (uniquely) gives rise to a strong perpendicular anisotropy in the amorphous ferrimagnet, as was mentioned in Section 3.3.1. In our case, the perpendicular anisotropy is obtained only for films thickness $\geq$ 40 nm. Using the facing-target configuration helps to overcome the problem with the difficulty to transmit the magnetic field through the thick magnetic target.

The sputtering system used at Institut Néel is presented in Fig. 3.10. The system consists of two parallel targets 50 mm apart. The targets have diameter of 30 mm and they are 4 mm thick. A couple of $\text{SmCo}_5$ permanent magnets arranged on the substrate holder create a magnetic field parallel to the sample surface. Typically, the vacuum chamber is pumped down to $\sim 10^{-8}$ mbar and then the Ar gas is injected into the chamber, with the gas pressure $P = 3 \times 10^{-3}$ mbar. The plasma is created by a dc magnetic field and by a current $I = 35$ mA. All the targets are cleaned by the plasma for 5 minutes before the layer deposition.

Two targets of $\text{Gd}_{14}\text{Co}_{86}$ and $\text{Gd}_{17}\text{Co}_{83}$ are used in our setup. The combination of these two different targets is used in order to obtain the compensation temperature close to room temperature, $T_{\rm comp} \geq$ RT. One can notice that the target composition differs from the obtained composition $x \sim 0.78$. The origin of the shifted composition of the deposited layers is attributed to preferential resputtering of Co on the film, to different atom masses or to different sputtering angles. In general, the deposition rate is angle dependent and can be described by a cosine law: $I = I_0 \cos\alpha$, where $\alpha$ is the angle normal to the sample surface and $I_0$ is the incoming flux density for the $\alpha = 0$ case. The

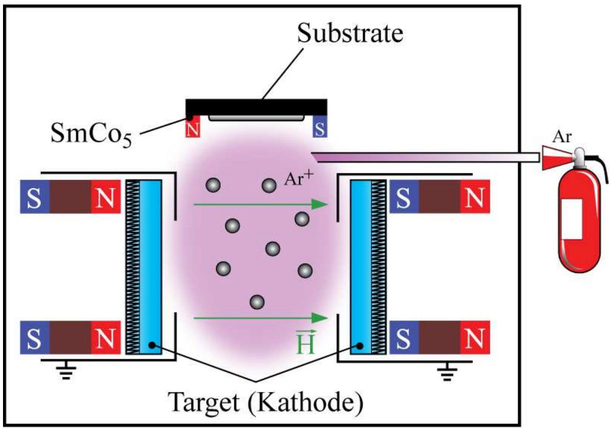

Figure 3.10: Scheme of facing-target magnetron sputtering deposition used at Institut Néel.

deposition ratios were measured by x-ray reflectometry technique for the used targets and are listed below.

| Target | Deposition rate (Å/s) |
|---|---|
| $Gd_{14}Co_{86}$+$Gd_{17}Co_{83}$ | 0.67 |
| Ti | 0.72 |

Due to all the listed facts, the precise composition of the $Gd_{1-x}Co_x$ thin film depends on the substrate position during the sputtering. A relatively homogeneous film can be obtained when the substrate is placed at the center of the substrate holder. When the substrate is placed away from the high symmetry position, an in-plane composition gradient is induced.

40 nm thick $Gd_{1-x}Co_x$ with $x \simeq 0.78$ were deposited onto Si(001) substrates using 3 nm thick Ti layers as buffer and capping layers to protect the films from a parasitic oxidation. From the oxidation point of view, it is rather gadolinium which is very susceptible to the oxidation, so film could become Co-rich when aging.

## 3.7 Patterning of the wires

The lithography techniques, on which the nanopatterning process are based, are usually classified according to the radiation source: optical (UV, deep-UV), electron-beam (e-beam), ion beam or X-ray lithography. The lithography resolution limit is determined by the radiation wavelength for optical lithography and by the electron beam size for e-beam lithography.

The **optical lithography** technique consists in the insolation of a photoresist by a UV lamp through a partially optically transparent mask. The resist is spread on a substrate by the spin-coating technique. The resist thickness is typically hundreds of nanometers to several microns, depending on the spinning speed and the resist composition. A soft-bake of the resist is necessary to remove the resist solvent. The wave length limit does not allow creating nanostructures smaller than the diffraction limit, which is defined as $0.61\lambda/\mathrm{NA}$, where $\lambda$ is the radiation wavelength and NA is the numerical aperture of the objective. Typically, the smallest feature size which can be created by the UV technique is $\sim 0.5 - 1\,\mu$m. This technique is not suitable for the fabrication of stripes for current-induced domain wall experiments, since very narrow stripes of the order of a few 100 nm with a minimal lateral roughness are required. However, due to its less demanding preparation time, it is often used for the fabrication of the micron-sized objects, such as electrodes or alignment marks.

The **e-beam lithography** technique uses an electron beam to expose an electron-sensitive resist. The most common electron-sensitive resist is the polymethylmethacrilate (PMMA). The exposure is usually done using the e-beam in a scanning electron microscope (SEM), which is driven at Institut Néel by a commercial Elphi interface. This technique allows fabricating features having lateral roughness down to tens of nanometers.

Once the insolation and resist development has been performed, we can employ various techniques to pattern the sample, including lift-off technique and ion-beam etching.

### 3.7.1 Lift-off technique

The bases of the lift-off technique are illustrated in Fig. 3.11. The desired material is deposited directly on the developed resist which was patterned either by UV-lithography or by e-beam lithography. The resist is consequently dissolved by a solvent (aceton or a resist remover). Only the part of the material, which was deposited directly on the substrate, remains. The rest is washed away along with the resist.

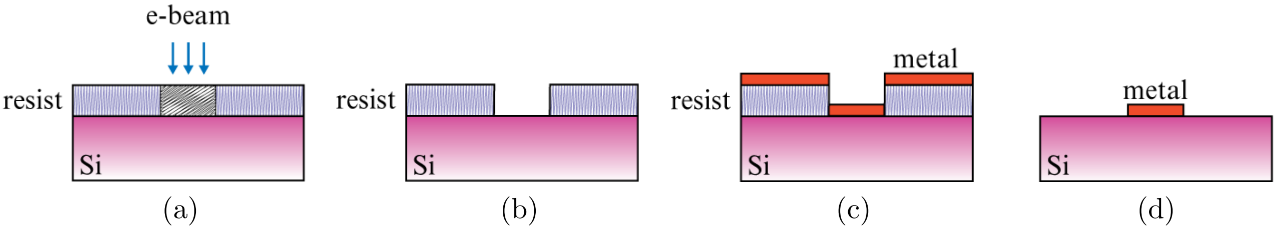

(a) (b) (c) (d)

Figure 3.11: Illustration of standard lift-off technique. (a) Photo- or electron-sensitive resist is spread on the sample and insulated through a partially transparent mask or by an electron beam. (b) The exposed areas are removed by a developer, in case of positive resist. In the case of negative resist, the non-insolated part of the resist is removed by a developer (not shown). (c) Material is deposited on the developed resist. (d) The resist is dissolved by a solvent and only the material which is deposited directly on the substrate remains.

In order to warrant the resist dissolvability, the thickness of the deposited material should not exceed approximately half of the resist thickness, which is of the order $\sim 100\,\mathrm{nm}$ for PMMA 2% resist. We have found, that probably due to the relatively thick Gd-Co films ($\sim 40\,\mathrm{nm}$), this method is not suitable for the fabrication of the Gd-Co nanostripes.

### 3.7.2 Ion-beam etching technique

The principles of ion-beam etching technique are schematized in Fig. 3.12. The magnetic layer is deposited on the Si substrate. In the next step, the mask, which can be either a negative resist or a metallic layer (Ti in our case), having the shape of the desired nanostructure is created by following the standard lift-off process. The sample is consequently etched using an ion beam. The Ti mask thickness is chosen so that its etching time is longer than that of the magnetic material. When the substrate is reached in the bare parts, a small thickness of Ti is left on the top of the nanostructure. In general, a reference sample consisting of Pt\Ti put beside the main sample, is used to monitor the Ti etching time. The Ti mask is about 2-5 nm thicker than that of the Ti reference sample. When the reference sample is completely etched, as detected by SIMS signal, the 2-5 nm of Ti are left on top of the nanostructures. Fig. 3.13 shows the process of etching with the corresponding SIMS signal. The residual titanium mask entirely oxidizes and becomes optically transparent.

It should be noted here, that very often a positive resist is used as mask, and this makes the whole lithography process less time demanding. However we have found that the resist is somewhat burned during the ion beam etching and becomes very difficult to dissolve. One could do it by an additional oxygen plasma etching, but due to the fact that our structures are very susceptible to oxidation this method is not suitable for the wire patterning. This is the reason why we have used a titanium mask.

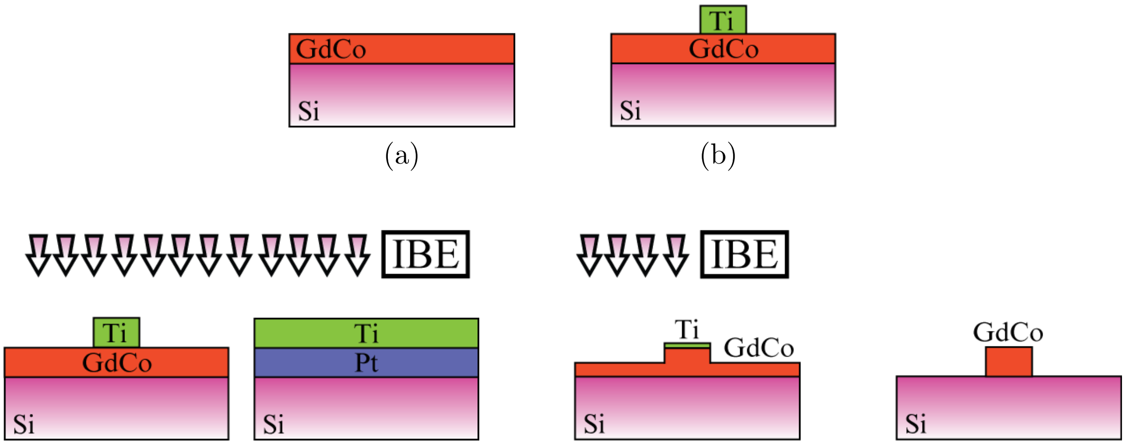

(a) (b)

(c) (d) (e)

Figure 3.12: Illustration of ion-beam etching technique. (b) Using the lift-off technique a Ti mask having a design of the desired final structure is created on the deposited layer. (c) The sample is etched by the ion-beam etching together with a reference sample. The reference sample allows measuring the etched thickness by a secondary ion mass spectrometry (SIMS) signal. (d) The desired structure is protected by the Ti mask whereas the bare part is exposed to the ion bombardment. (e) The final structure.

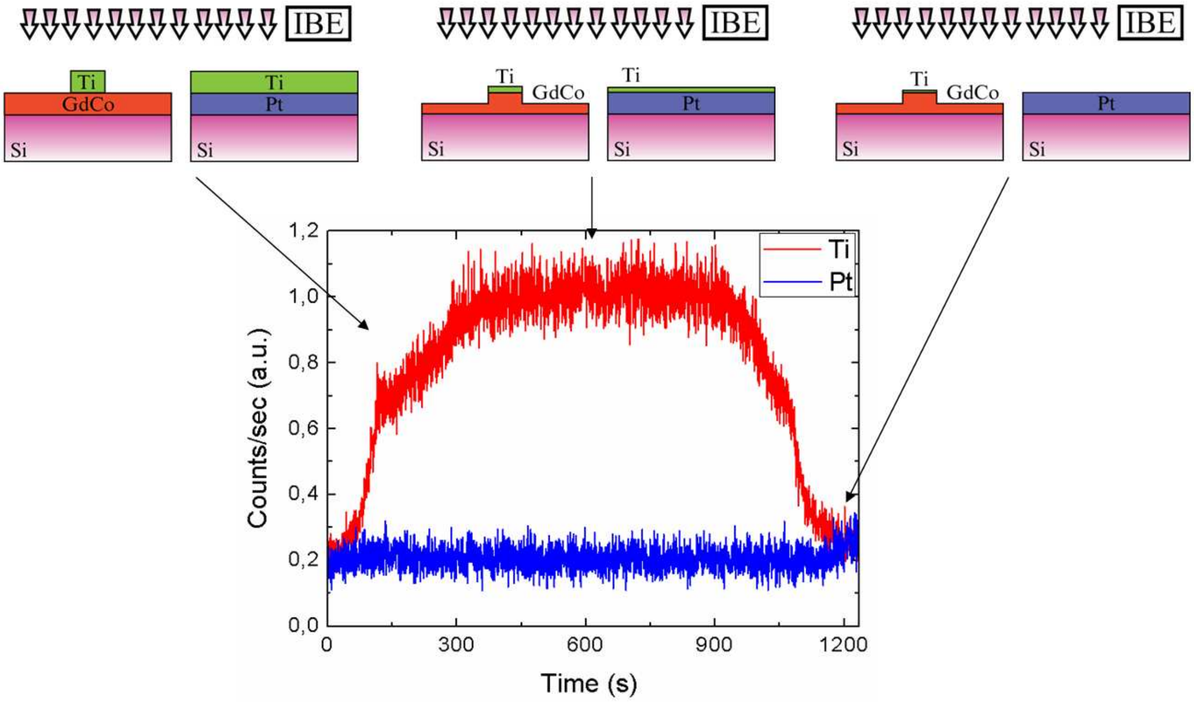

Figure 3.13: Illustration of ion-beam etching technique of 40 nm thick Gd$_{1-x}$Co$_x$ layer. The titanium mask is 55 nm thick and the reference sample consists of Pt(10 nm)\Ti(50 nm). The Ti and Pt SIMS signal are plotted as a function of etching time. The total etching time is $\sim$ 20 min.

## 3.8 Magnetic properties of Gd$_{1-x}$Co$_x$ film

The magnetization of Gd$_{1-x}$Co$_x$ films have been measured by a Superconducting Quantum Interference Device (SQUID) at Institut Néel. The SQUID utilizes a superconducting coil cooled with liquid helium, to create magnetic fields up to 7 T. The helium is also used to cool the sample chamber, providing temperature control between 1.8 K and 400 K. A sample can be mounted on the sample rod in such a way that the magnetic field can be applied either parallel or perpendicularly to the sample surface. The instrument sensitivity improves as the inverse square root of the averaging time which for 0.3 second averaging corresponds to $4 \times 10^{-8}$ emu resolution.

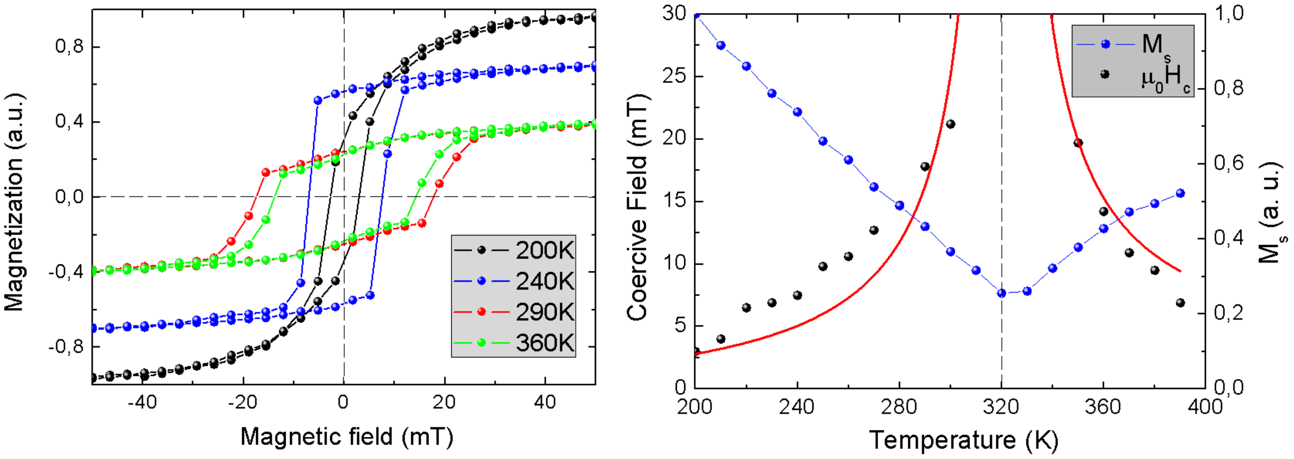

(a)

(b)

Figure 3.14: (a) Normalized hysteresis loops at different temperatures. (b) Temperature dependence of coercive field ($H_c$) and normalized magnetization. The red curve corresponds to $\mu_0 H_c \sim (T - T_{comp})^{-1}$ fit. The extrapolated compensation temperature $T_{comp} = 320$ K.

The hysteresis loops of the unpatterned sample Si\Si0$_2$\Ti(3 nm)\GdCo(40 nm)\Ti(3 nm) at different temperatures measured by SQUID are displayed in Fig. 3.14(a). The magnetization was normalized by the magnetization at 200 K, so it reads M(T)/M(200 K). Fig. 3.14(b) shows the extracted temperature dependence of coercive field and magnetization. The magnitude of the magnetization decreases in the vicinity of the compensation temperature. Although during the deposition the sample was installed at the center of the sample holder in order to get a homogeneous composition, the in-plane composition gradient is not entirely eliminated. Therefore, since a gradient of compensation temperature is induced in the sample, the magnetization does not drop to zero at a precise temperature but only establishes a minimum. Due to the fact that the Zeeman energy depends on the total magnetization via $\vec{M}_{tot} \cdot \mu_0 \vec{H}$ product, the coercive field diverges at the compensation temperature. The red curve in Fig. 3.14(b) corresponds to $\mu_0 H_c \sim (T - T_{comp})^{-1}$ fit. The extrapolated averaged compensation temperature is $T_{comp} \simeq 320$ K.

## 3.9 Compensation interface

In micromagnetic models, the spontaneous magnetization amplitude ($M_s$) is assumed to be constant and uniform. Experimentally $M_s$ cannot be usually tuned alone to verify its role in models. Nowadays, for example, describing the spin transfer torque term in the Landau-Lifschitz-Gilbert equation is the source of intense discussion. Even old questions such as the microscopic origin of coercivity are still lacking of a quantitative model. In order to change the magnetization amplitude, one can modify the material, but this in general influences most magnetic quantities but also the atomic structure and crystallographic texture. A different way is to heat up the sample close to the Curie temperature but this also modifies the magnetic anisotropy and of course the thermal excitations.

Compensated ferrimagnetic materials offer a different way to change $M_s$ without modifying much the other magnetic quantities. Ferrimagnetic films close to compensation with an in-plane composition gradient, and so a magnetization gradient, can be considered as a model system where $M_s$ can be varied continuously without varying the temperature. The very first material with controlled lateral magnetization gradient was described in 1973 [107]. The experimental system was a Ga substituted YIG ($Y_3Fe_{3.7}Ga_{1.3}O_{12}$ ) crystal, cut to 100 micron-thick platelets. A step-like gradient was induced by laser annealing. As regards spintronics, garnets are electrically insulating and rare-earth-transition metal alloys are a more interesting choice.

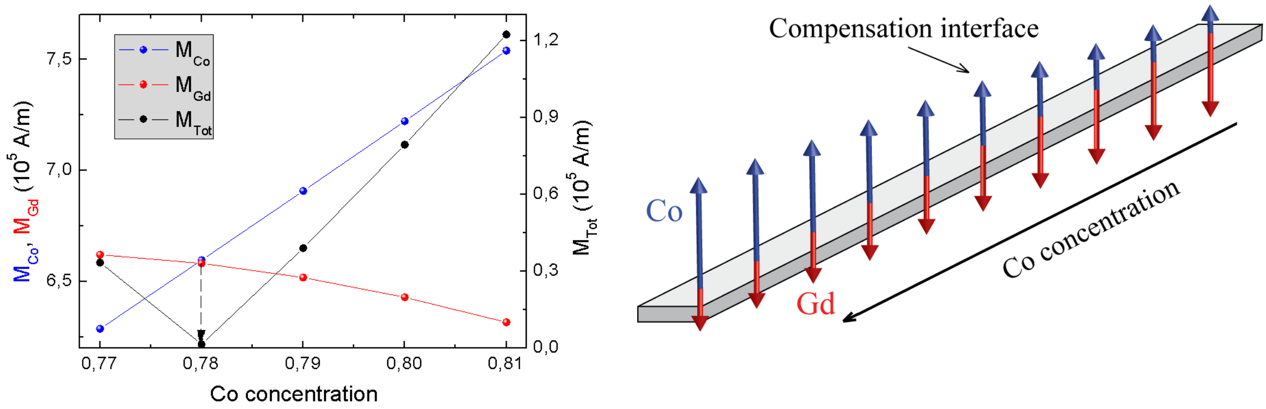

(a) (b)

Figure 3.15: (a) Calculated individual sublattice magnetizations and the total magnetization as a function of Co concentration at fixed temperature $T = 300\,\mathrm{K}$. The compensation composition at $T = 300\,\mathrm{K}$ occurs at $x_{\mathrm{comp}} \sim 0.78$. (b) Scheme of the compensation interface origin in a wire with a concentration gradient.

Our first aim is to locate the plane of the $Gd_{1-x}Co_x$ film having the composition $x_{\mathrm{comp}}$ for which the total magnetization vanishes at room temperature. The plane perpendicular to the substrate where

$$\vec{M}_{\mathrm{Gd}} = -\vec{M}_{\mathrm{Co}} \tag{3.9}$$

at $T =$ const. is called the **compensation interface**. The composition where equation (3.9) is satisfied, is called the compensation composition $x_{\mathrm{comp}}$. Calculated individual sublattice magnetizations as a function of Co concentration at fixed temperature $T = 300\,\mathrm{K}$ are displayed in Fig. 3.15(a). As expected, the Co sublattice magnetization increases with the Co concentration. For $x_{\mathrm{comp}} \sim 0.78$ the two sublattice magnetizations cancel each other and the total magnetization equals to zero.

The compensation interface is a very interesting and unusual micromagnetic object. Let us look at the evolution of the Co and Gd magnetization along the stripes. As sketched in Fig. 3.15(a), the magnetization increases linearly with $x$ on either side of $x_{\mathrm{comp}}$. $M_s$ is in the direction of the Gd moments below $x_{\mathrm{comp}}$ while it changes sign and becomes parallel to the Co moments when $x > x_{\mathrm{comp}}$. Macroscopically, the compensation interface is a domain wall (with vanishing magnetization and no exchange energy cost) as it separates two regions with opposite magnetization. We can expect that such an interface could be visible and would give rise to opposite contrasts if a magnetic imaging technique sensitive to the total magnetization was used. Microscopically however, the magnetization of both Co and Gd sublattices changes continuously across $x_{\mathrm{comp}}$ and does not rotate, so no discontinuity of the magnetic contrast is expected using a technique sensitive to one of the two magnetic sublattices.

## 3.10 Kerr effect in $\mathrm{Gd}_{1-x}\mathrm{Co}_x$ alloy

The magneto-optical effects in magnetic metal systems depend on intraband and interband optical transitions. The intraband transitions contribute to wavelengths above the infrared range while the interband transitions are dominant in the visible and the short-wavelength range of the magneto-optical spectra. The magnitude of the Kerr effect is primarily controlled by the spin-orbit coupling and the net spin polarization.

In the case of $\mathrm{Gd}_{1-x}\mathrm{Co}_x$ alloy, the Kerr rotation is a superposition of the Co and Gd sublattice rotations [108]:

$$\theta_{\mathrm{K}}(\vec{M}) = \theta_{\mathrm{K}}^{\mathrm{Gd}} - \theta_{\mathrm{K}}^{\mathrm{Co}}$$

At room temperature, a broad peak in the magneto-optical signal occurs between 1000 nm and 1500 nm [108]. The peak height is significantly reduced with the Co content, which demonstrates that the main contribution in the visible and infrared range has to be assigned to the Co sublattice. The magneto-optical effect of amorphous Gd-transition metal films in the visible and near infrared region essentially derives from the magneto-optical polarizability of the transition metal atom, which was also shown by Sato *et al.* [109]. The Kerr microscopy in the visible wavelength range in $\mathrm{Gd}_{1-x}\mathrm{Co}_x$ alloys is therefore a mirror of the Co magnetization.

This property allows us to use it as a detector of the compensation interface position.

## 3.11 Detection of the compensation interface and compensation domain wall

A composition gradient in the deposited magnetic layer was induced by placing the sample away from a high symmetry position and using not symmetrical targets. Our films include a composition $x \sim 0.78$ for which $T_{\mathrm{comp}}$ is close to room temperature. After the film deposition, UV lithography and lift-off techniques were used to pattern the film into $100\,\mu$m-wide stripes parallel to the gradient direction. The sublattice magnetizations, as well as the total magnetization, vary along the wire as shown in Fig. 3.15(b).

The magneto-optical Kerr microscopy image measured at room temperature for the as-deposited film is shown in Fig. 3.16(a). Apart from some inhomogeneities due to an uneven illumination, the magnetic contrast in Fig. 3.16(a) is constant in the probed region. This proves that the sample is not demagnetized, as it is found very often in ferromagnetic films with perpendicular magnetization. This comes from the fact that the demagnetizing field vanishes close to the $x_{\mathrm{comp}}$. As expected, no abrupt change in contrast is found along the stripe as the composition changes, since the direction of Co magnetization is the same all along the wire, as shows schematically inset of Fig. 3.16(a).

In order to locate the position of the compensation interface at room temperature with Kerr microscopy, we have applied a large magnetic field in the easy axis direction, perpendicular to the film plane. In the region of the sample where $M_{\mathrm{s}}$ is initially antiparallel to $H_{\mathrm{app}}$, the magnetization reverses and aligns with the field. The direction of the Co magnetization is then opposite on either side of the compensation composition and a contrast appears in the Kerr microscopy images, as shown in Fig. 3.16(b). Note that due to the divergence of the coercive field at $x_{\mathrm{comp}}$ an infinite field would have to be applied to visualize the exact location of the compensation interface (the interface visualized by applying $\mu_0 H_{\mathrm{app}} \sim 500\,\mathrm{mT}$ is $\sim 70\,\mu$m away from this interface). In these conditions, a chargeless Bloch domain wall is present in the Co and Gd sublattices at the compensation composition location.

The microscopic origin of such a Bloch wall is depicted in Fig. 3.17. In the as-deposited state the macroscopic magnetization changes linearly as a function of the composition and it changes its sign at $x_{\mathrm{comp}}$. The $x_{\mathrm{comp}}$ position then corresponds to the compensation interface where $M_{\mathrm{s}} = 0$. When an external magnetic field $H_{\mathrm{app}} \to \infty$ is applied, the magnetization reverses into the direction parallel to the applied field even in the case where $M_{\mathrm{s}} \to 0$. Then a 'classical' domain wall with

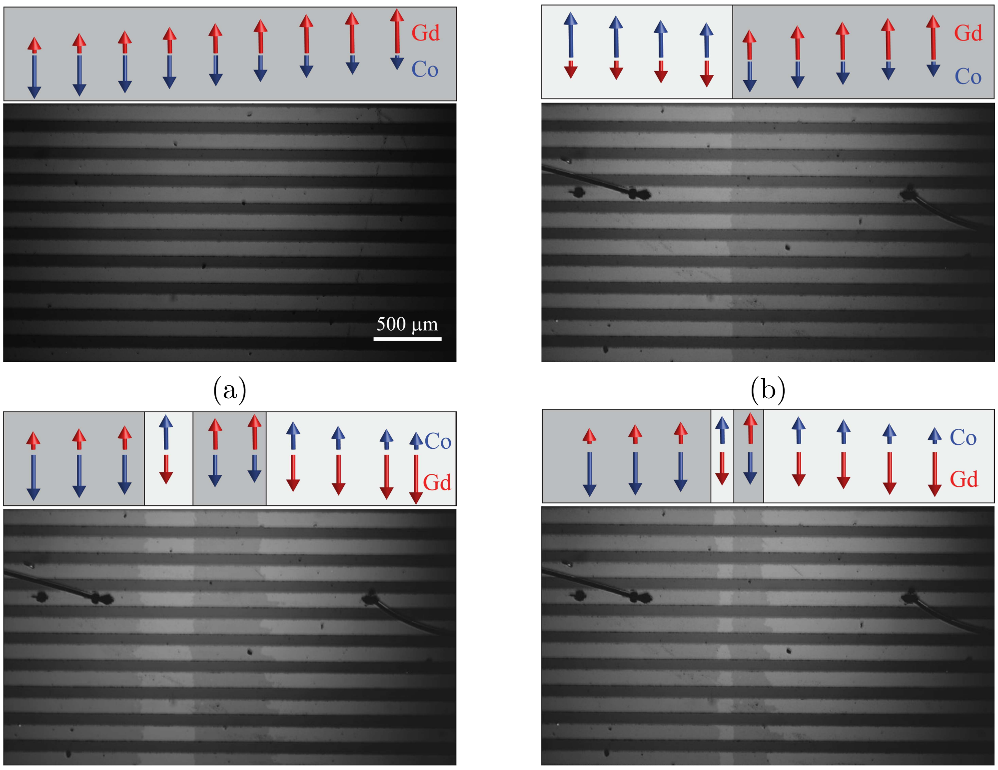

(a) (b)

(c) (d)

Figure 3.16: Kerr microscopy images of the GdCo wires and sketch of the corresponding Gd and Co magnetic moments. (a) Image of the as-deposited state. (b) Image taken after application of a 500 mT positive magnetic field. The compensation interface becomes visible. (c) Starting from (b) state, a field of -60 mT is applied in the opposite direction to reverse the magnetization. (d) Final state after application of -80 mT. The field of view is 3.3 × 1.9 mm$^2$.

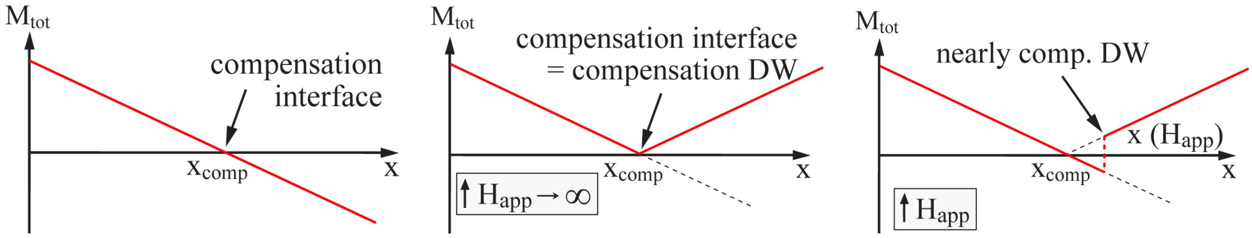

(a) (b) (c)

Figure 3.17: (a) Total magnetization dependence in the as-deposited state in the vicinity of compensation interface. (b) When an infinite external magnetic field is applied, $M_s$ becomes parallel to $H_{\text{app}}$ along the wire and a compensated domain wall appears at $x_{\text{comp}}$. (c) When an ordinary external magnetic field is applied, $M_s$ becomes parallel to $H_{\text{app}}$ only in the part of the strip where the Zeeman energy exceeds the potential barrier. Then a nearly compensated domain wall is created at a position $x(H_{\text{app}})$.

sublattices rotation takes place exactly at $x_{\text{comp}}$. This domain wall is in a region with $M_s \sim 0$ with no magnetic poles, so this domain wall should be a perfect 180° Bloch domain wall without any Néel caps, as was demonstrated in Fig. 1.10. However, due to the necessity of the infinite external magnetic field, this state is experimentally unachievable (by applying the magnetic field). The Zeeman energy of the system depends on the magnetic field amplitude. Then the magnetization is reversed only in region where the Zeeman energy exceeds a potential barrier (the origin of the potential barrier will be discussed later) and the position of the created domain wall $x(H_{\mathrm{app}})$ depends on the applied magnetic field amplitude. The higher the external magnetic field, the more compensated the domain wall.

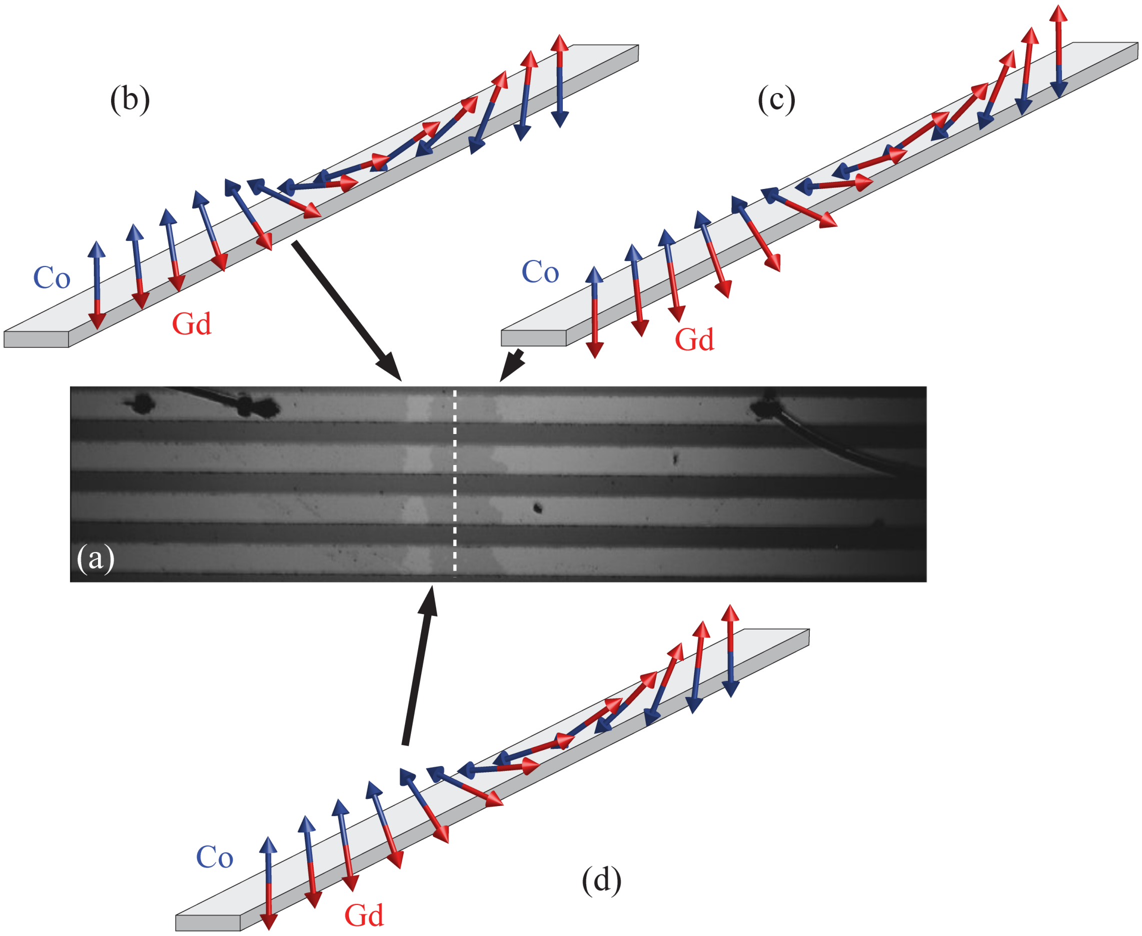

Figure 3.18: (a) Kerr microscopy image of the GdCo wires with multidomain structure. (b) Co-rich 180° Bloch domain wall. (c) Gd-rich 180° Bloch domain wall. (d) Compensated 180° Bloch domain wall. The dashed line labels the position of $x_{\mathrm{comp}}$.

The Kerr image in Fig. 3.18 shows a magnetic domain structure which can be typically found in a $\mathrm{Gd}_{1-x}\mathrm{Co}_x$ wire with a compositional gradient in the vicinity of $x_{\mathrm{comp}}$. Three domain walls are present. The central one is the (nearly) compensated domain wall, created with a strong external magnetic field. The two domain walls which are located at larger distance on either side of $x_{\mathrm{comp}}$ (dashed line) are not compensated and were created by applying a magnetic field opposite to the first one. These domain walls are not compensated and the microscopic difference between them is that the given domain wall is Co-rich (left) or Gd-rich (right) respectively. The magnetization within the three types of domain walls is schematized in Fig. 3.18(b)-(d).

## 3.12 Determination of composition gradient

In order to obtain quantitative information on the composition gradient along the wires, hysteresis loops were measured by extraordinary Hall effect as a function of temperature on a Hall cross patterned 1.9 mm away from the compensation interface at room temperature (inset of Fig. 3.19(b)).

Measurements were carried out in an area of $100 \times 100\,\mu\mathrm{m}^2$, between 50 K and 300 K in fields up to 6 T, using dc currents. The Hall resistance $R_\mathrm{H}$ was determined using $V = R_\mathrm{H} I/t$, where $t$ is the film thickness. The Hall resistivity of $\mathrm{Gd}_{1-x}\mathrm{Co}_x$ can be written as [101]:

$$\rho_H = \mu_0 R_\mathrm{Gd} M_\mathrm{Gd} + \mu_0 R_\mathrm{Co} M_\mathrm{Co},$$

where $R_\mathrm{Co}$ and $R_\mathrm{Gd}$ are respectively the Co and Gd extraordinary Hall effect coefficients. Nam in his PhD thesis found that $R_\mathrm{Co} \sim 3 \times 10^{-8}\,\Omega\mathrm{m}^2/\mathrm{A}$ and $R_\mathrm{Gd} \sim -3 \times 10^{-9}\,\Omega\mathrm{m}^2/\mathrm{A}$. Above $T_\mathrm{comp}$ the extraordinary Hall effect is positive, because both of Gd and Co moments have positive contributions. On the contrary, the extraordinary Hall effect is negative below $T_\mathrm{comp}$. This shows that $T_\mathrm{comp}$ can be detected by a change of the sign of the extraordinary Hall effect.

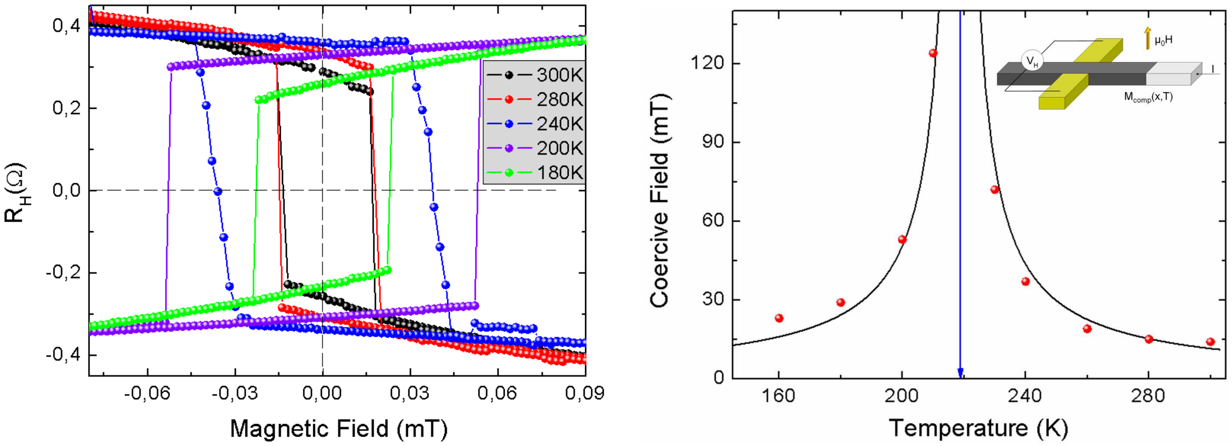

(a) (b)

Figure 3.19: (a) Extraordinary Hall effect loops measured at different temperatures. (b) Extracted coercive field as a function of temperature. The black curve corresponds to $\mu_0 H_\mathrm{c} \sim (T - T_\mathrm{comp})^{-1}$ fit, diverging at 218 K.

The extraordinary Hall effect loops as a function of applied magnetic field are presented in Fig. 3.19(a). One can notice that the extraordinary Hall effect loops are negative below 200 K and change into positive above 240 K. The compensation temperature in the region of the Hall cross then lies between these two temperatures. The coercive field as a function of temperature extracted from the measurements is shown in Fig. 3.19(b). The coercive field diverges at 218 K where the local magnetization vanishes. From the knowledge of the local compensation temperature ($T_\mathrm{comp}$=218 K) and its distance from the compensation interface at room temperature ($\Delta z = 1.9\,\mathrm{mm}$), one can deduce the compensation temperature gradient:

$$\boxed{\frac{\Delta T_\mathrm{comp}}{\Delta z} = 45\,\frac{\mathrm{K}}{\mathrm{mm}}.} \tag{3.10}$$

If we put together the data expressed by equation (3.8) and the data obtained by the mean-field theory expressed by equation (3.10), we find that the composition gradient along the wire is

$$\boxed{\frac{\Delta x}{\Delta z} = 1\,\frac{\%}{\mathrm{mm}}.} \tag{3.11}$$

The composition can also be measured directly by using an electron microscope in the Energy Dispersive Spectrometer (EDS) mode. Fig. 3.20(a) shows the electron microscope image illustrating

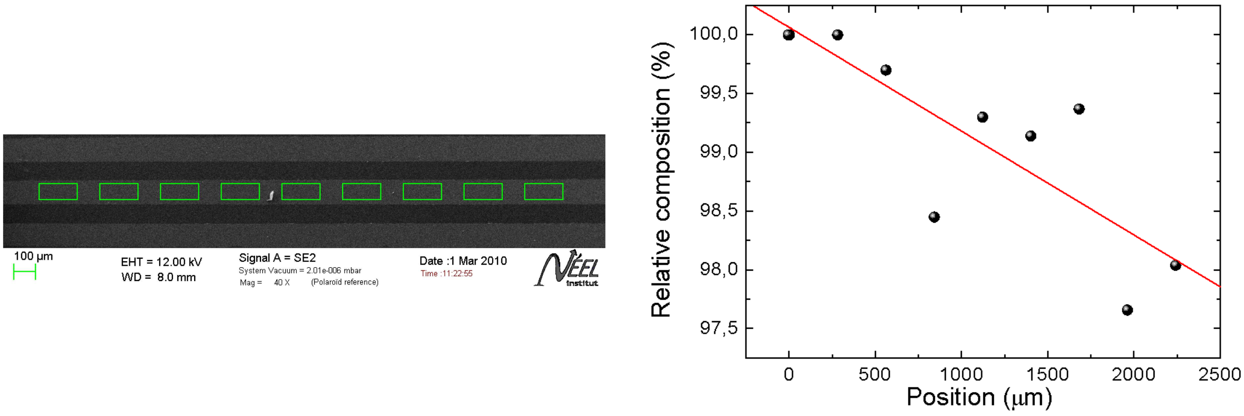

(a)

(b)

Figure 3.20: (a) Scanning electron microscope image of the wires. The green rectangles indicate the scanning area for EDS analysis. (b) The relative composition change as a function of the position. The red line corresponds to the linear fit giving the composition gradient of $0.88 \pm 0.25\,\frac{\%}{\mathrm{mm}}$.

the rectangular windows, 180 $\mu$m long along the gradient direction, used for the EDS scanning. The obtained data are presented in Fig. 3.20(b). The EDS scan along the wire gives a composition gradient:

$$\boxed{\frac{\Delta x}{\Delta z} = 0.88 \pm 0.25\,\frac{\%}{\mathrm{mm}}.} \tag{3.12}$$

It should be noted that EDS gives the global atomic composition of the film which can be different from the composition of the magnetic phase. This can occur, for example, in case of partial Gd oxidation or in case of Co clustering. The agreement between magnetic gradient and and composition gradient shows the local homogeneity and the absence of oxidation.

## 3.13 Coercive field in Gd$_{1-x}$Co$_x$ wire with composition gradient

We have shown in the previous section that the coercive field diverges when the magnetization goes to zero at the compensation temperature $T_{\mathrm{comp}}$. One can also expect a similar behaviour at a constant temperature, when the magnetization goes to zero at the compensation composition $x_{\mathrm{comp}}$. This has been proved using Kerr microscopy measurements at room temperature.

Starting from the magnetic configuration depicted in Fig. 3.16(b), where a domain wall has been created in the Co sublattice very close to the compensation composition using a 500 mT strong field, an opposite field of varying strength is applied to reverse the magnetization. An example of Kerr image, obtained with a field of -60 mT, is shown in Fig. 3.16(c).

Magnetic fields ranging from zero up to -80 mT were applied and the sequence of corresponding images was registered with steps of 0.5 mT. The images were analyzed using the method depicted in Fig. 3.21. Since the direction perpendicular to the wires is magnetically invariant, we have chosen to average the images of the parallel stripes , using the saturated images to normalize the illumination across the image. Each image is then reduced to a line along $x$. Such lines are gathered in the same 3D plot so that the position of the two domain walls appears as a function of applied field. The outcoming results are summarized in Fig. 3.22.

The magnetization reversal is governed by nucleation of reversed domains and their propagation along the wires. The magnetization reversal is initiated at the far edges of the stripes, outside the field of view presented in Fig. 3.16. Note that in all the stripes the nucleation field is systematically

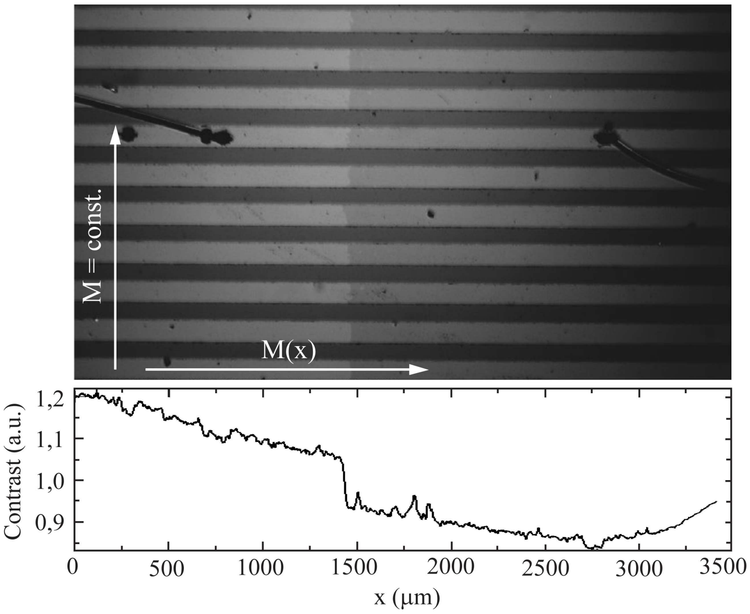

Figure 3.21: Kerr microscopy image of the GdCo wires with the averaged contrast along the magnetically invariant axis.

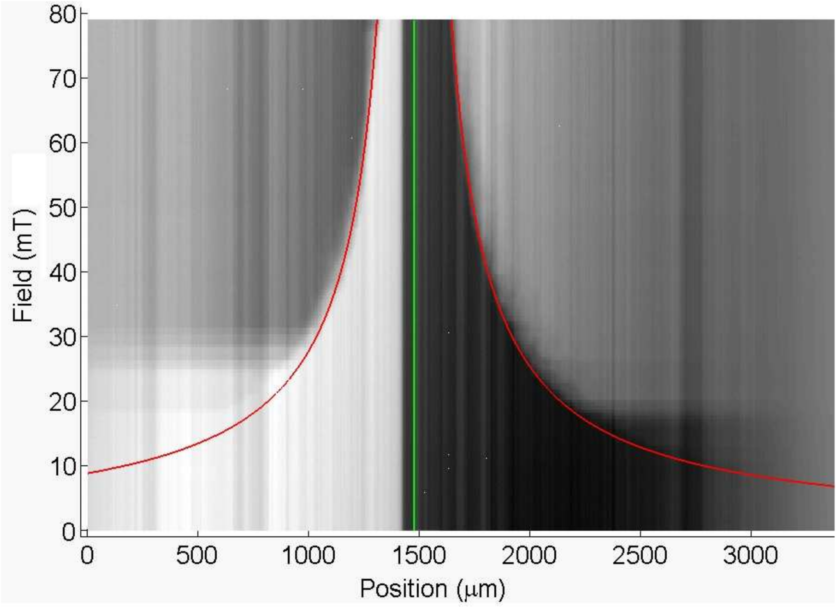

Figure 3.22: Three dimensional map of magnetic reversal process at room temperature. The vertical green line depicts the position of the compensation interface. and the red curves correspond to $E_\mathrm{p}/M_\mathrm{s}$ fit with $E_\mathrm{p} = 680\,\mathrm{J/m^3}$.

smaller on the Co-rich part of the wires ($\mu_0 H_\mathrm{N} \sim 20\,\mathrm{mT}$) than on the Gd-rich part ($\mu_0 H_\mathrm{N} \sim 27\,\mathrm{mT}$). This asymmetry can be explained by the fact that the magnetization is lower at the sample edge on the Gd-rich side as the edge is closer to the compensation interface.

In these films with composition (i.e. magnetization) gradient, for a fixed applied field, two domain walls propagate along the wires and stop when the Zeeman energy associated to the field is no longer sufficient to overcome the local propagation barrier. The value of the applied field is therefore a measure of the local coercive field at the position (i.e. for the composition) where the domain walls stop.

The magnetization is unreversed over a zone around $x_{\text{comp}}$ that gets narrower as the applied field increases. This is the consequence of the expected divergence of the local coercive field as the composition approaches the compensation composition. The domain wall can be understood as an elastic membrane which is pinned at its boundaries [110]. The magnetic field represents a pressure exerted on the membrane which is consequently distorted. The energy involved in this distortion is equal to the domain wall surface energy, which is estimated to be $\gamma$=1 mJ/m$^2$ ($A = 10\,\text{pJ/m}$, $K = 10^3\,\text{J/m}^3$). In the most general model [16], the coercive field is related to $M_{\text{s}}$ by the expression

$$\mu_0 H_{\text{c}} = \frac{E_{\text{p}}}{M_{\text{s}}}, \tag{3.13}$$

where $E_{\text{p}}$ is the propagation energy barrier and $M_s$ the local magnetization. The propagation energy barrier can comprise a variety of mechanisms like local modification of the intrinsic parameters ($A$, $K$, etc.), geometric effects changing the wall area or discontinuities of magnetization.

By using equation (3.13) we can fit the measured data in Fig. 3.22 (red curves). The pinning energy density is found to be $E_{\text{p}} = 680\,\text{J/m}^3$. If we consider that the domain wall is highly deformable, i.e. the surface energy is small compared to the energy involved in pinning on sites, we can find the relation between the propagation barrier and the distance between two pinning centers:

$$l = \frac{\gamma}{E_{\text{p}}} \sim 2\,\mu\text{m}.$$

This value is in qualitative agreement with Kerr microscopy measurements, which show in the creep propagation regime a fractal domain shape having the smallest fractal dimension of this order of magnitude.

Similarly to the $H_{\text{c}}(T)$ curve obtained with extraordinary Hall effect presented in Fig. 3.19, the $H_{\text{c}}(x)$ curve can be indeed fitted using the same expression for the coercive field. This demonstrates that the magnetization reversal mechanism close to $x_{\text{comp}}$ is controlled in our system by $M_{\text{s}}$ (Zeeman energy) and not by $T$ (thermal excitations), unlike usual ferromagnets where coercivity increases as magnetization increases at low temperature.

## 3.14 Temperature dependence of the compensation interface

Our knowledge of the GdCo system with composition gradient leads us to expect that the position of the compensation interface can be changed by changing its temperature. In order to prove this experimentally, we have connected the central stripe (visible in Fig. 3.22) to a current source delivering a dc current ranging from 0 up to 34 mA. This current heats the central wire due to Joule effect, and through thermal diffusion into the Si substrate, the stripes close to the central stripe are also heated.

Since the temperature itself is not able to exert a torque on the magnetization[4], experimentally, a dc magnetic field has to be applied during the experiment in order to keep the sample in the saturated equilibrium state. The difference between the initial magnetic configuration at room temperature and the magnetic configuration obtained in the presence of the dc current of 34 mA flowing in the central wire and of a field of ~ 500 mT is shown in Fig. 3.23.

The compensation interface was displaced by 0.87 mm, which according to our results corresponds to a temperature change of 38 K. Due to the important heat dissipation into the Si substrate, the wires close to the central wire considerably heat up. The position of the compensation temperature then maps the temperature distribution across the sample. From Fig. 3.23 follows that the temperature

---

[4] The spin Seebeck effect [111] producing pure spin current in temperature gradient system is negligible in this case.

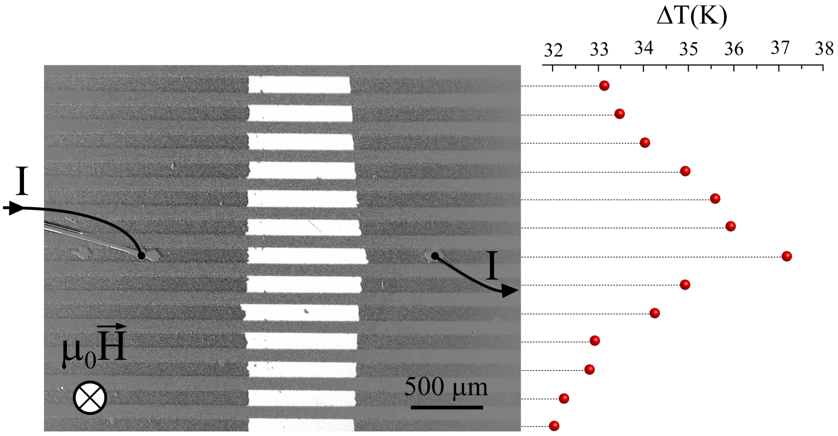

Figure 3.23: Differential Kerr microscopy image showing the displacement of the compensation interface position due to the Joule heating created by a dc current of 34 mA flowing in the central wire. Using our previous results expressed by equation (3.10), the temperature increase in the central wire with respect to room temperature can be estimated as $\Delta T = 39\,\mathrm{K}$.

decreases with increasing distance from the central wire. As a consequence of the presented compensation composition behaviour, with increasing temperature the compensation interface moves towards the Co-rich region.

Note that the position of the compensation interface can be used as a very sensitive thermometer: a 500 nm displacement corresponding to the spatial resolution of Kerr microscopy corresponds to a change in temperature of 20 mK. In our case however, the limiting factor defining domain wall position is the pinning centers distribution, which gives rise to domain wall roughening with average period of $2\,\mu$m corresponding to $\sim 100\,\mathrm{mK}$.

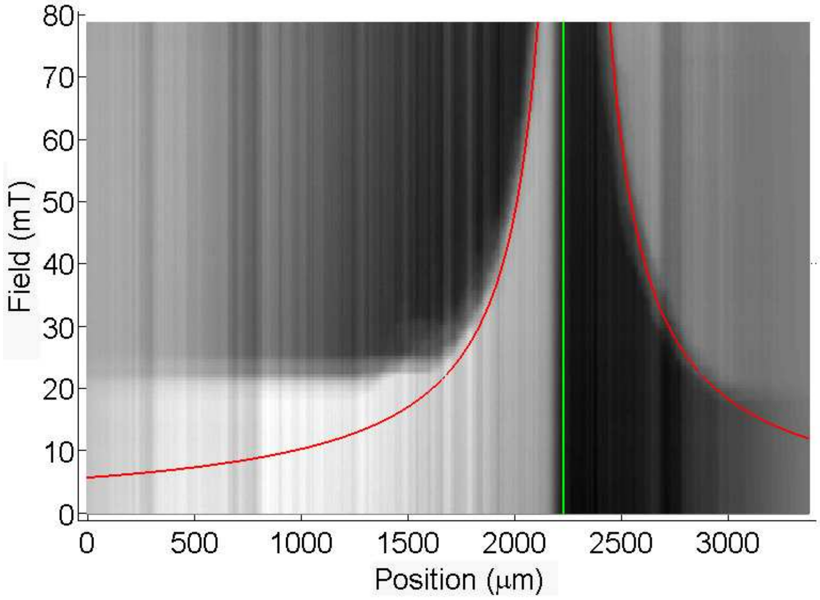

Figure 3.24: Three dimensional map of magnetic reversal process. The vertical green line depicts the position of the compensation interface. and the red curves correspond to $E_p/M_s$ fit with $E_p = 680\,\mathrm{J/m^3}$.

Finally, the magnetization reversal process was studied at high temperature. The wires were heated up by the electric current and the procedure depicted and described in Fig. 3.16 was used. The 3-dimensional map of magnetization reversal at $T = \mathrm{RT} + 35\,\mathrm{K}$ is presented in Fig. 3.24. We can see that the same behaviour $\mu_0 H_\mathrm{c} = E_\mathrm{p}/M_\mathrm{s}$ with $E_\mathrm{p} = 680\,\mathrm{J/m^3}$ is observed. In this case, the nucleation field on either sides of compensation interface is notably reduced with comparison to the case measured at room temperature. This demonstrates the effect of thermal excitations playing an important role in magnetic domain nucleation process.

## 3.15 Angular momentum compensation interface

In Section 3.11 we have described the compensation interface, which we have defined as the plane where the total magnetization cancels out. The transport properties are rather intimately connected with angular momentum momentum as discussed in Section 1.1. It is therefore interesting to find the relationship between the magnetization and angular momentum. Here we remind the connection between spin angular momentum $\vec{S}$, orbital angular momentum $\vec{L}$, total angular momentum $\vec{J}$ and magnetization $\vec{M}_s$, which can be depicted by a vector model shown in Fig. 3.25.

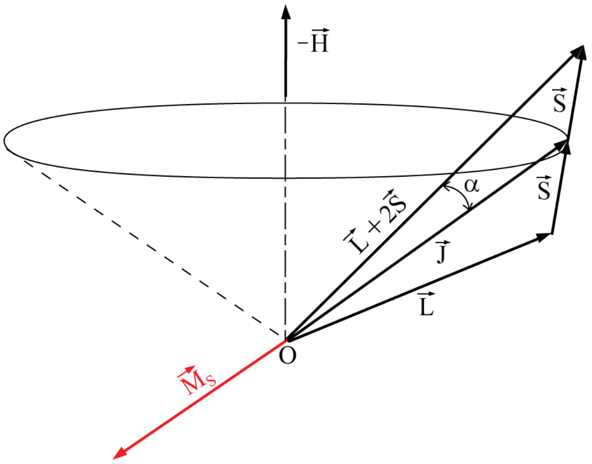

Figure 3.25: Vectorial model of angular momentum composition.

The total angular momentum is a superposition of $\vec{L}$ and $\vec{S}$:

$$\vec{J} = \vec{S} + \vec{L}$$

whereas the total magnetic moment can be expressed by

$$\vec{M} = \mu_\mathrm{B}\left(\vec{L} + 2\vec{S}\right). \tag{3.14}$$

When the vectors $\vec{L}$ and $\vec{S}$ are not collinear, the vector $\vec{L} + 2\vec{S}$ takes a different direction from $\vec{J}$. However, $\vec{L}$ and $\vec{S}$ precess around $\vec{J}$, so also the vector $\vec{L} + 2\vec{S}$ precesses around $\vec{J}$. Therefore the averaged magnetic moment becomes parallel to $\vec{J}$ and its magnitude is given by the projection on $\vec{J}$, so it reads

$$M_\mathrm{s} = -g\mu_\mathrm{B} J. \tag{3.15}$$

Comparing (3.14) and (3.15) and including the geometrical relations depicted in Fig. 3.25, it follows that

$$gJ = |\vec{L} + 2\vec{S}| \cos\alpha.$$

Due to the spin-orbit coupling these two quantities are closely related and $\alpha \to 0$, so the already discussed equation (1.23) for $g$-factor calculation is often used.

The situation is more complicated in the case of Gd$_{1-x}$Co$_x$ ferrimagnetic alloy which is composed of two antiparallel angular momentum sublattices: $\vec{J}_{\mathrm{Co}}$ and $\vec{J}_{\mathrm{Gd}}$. Due to the fact, that Gd has negligible orbital angular momentum $L_{\mathrm{Gd}} \to 0$ and the angular momentum is composed of a little contribution of $L_{\mathrm{Co}}$, the two $g$-factors are not equal [112]:

$$\begin{aligned} g_{\mathrm{Gd}} &\simeq 2 \\ g_{\mathrm{Co}} &= g_{\mathrm{Gd}} + \Delta g \end{aligned}$$

where $\Delta g \in (0.05, 0.2)$ [113].

The compensation of angular momentum occurs when

$$\vec{J}_{\mathrm{Gd}} = -\vec{J}_{\mathrm{Co}}$$

which is satisfied when

$$\frac{M_{\mathrm{Gd}}}{g_{\mathrm{Gd}}} = \frac{M_{\mathrm{Co}}}{g_{\mathrm{Co}}} \Rightarrow \frac{M_{\mathrm{Co}}}{M_{\mathrm{Gd}}} = 1 + \frac{\Delta g}{g_{\mathrm{Gd}}}.$$

Hence, the compensation of the angular momentum does not occur at the same position (temperature) as the compensation of angular momentum.

With the previously measured data we can estimate the position of the angular compensation interface on the film. According to the mean field calculation, the angular compensation composition occurs when $x \simeq 0.79$ at room temperature. In the case of $\Delta g = 0.1$, this value corresponds to a 1 mm shift away from the magnetization compensation surface, in the direction of the Co-rich region.

The coexistence of the two compensated planes at the same temperature at two different positions offers the very unusual possibility to use this model system for studying effects which depend either on the magnetization or on the angular momentum. This will be shown in next chapter.

# Chapter 4

# Magnetization dynamics in $\mathrm{Gd}_{1-x}\mathrm{Co}_x$

Magnetic domain walls can be manipulated and used to encode information for data storage. High-speed operation, and hence fast wall propagation, is an essential requirement for applications. The dynamics of domain walls under the effect of magnetic field or spin-polarized current was studied in many model systems [19], [29], [45], [51], [52], [53], [56], [57]. However, the direct impact of magnetization on domain wall dynamics cannot be checked in real systems, where its magnitude is fixed at a given temperature. The system with an induced magnetization gradient described in Chapter 3 features the interesting possibility to reveal the role of magnetization without changing other material parameters. We will show that the magnetization in this system is intimately connected to other dynamic parameters such as the damping parameter $\alpha$ or the gyromagnetic ratio $\gamma$.

This chapter deals with the experimental study of magnetization dynamics in the $\mathrm{Gd}_{1-x}\mathrm{Co}_x$ system with induced magnetization gradient. A key dynamic parameter for magnetic domain-wall motion is the domain-wall mobility $\mu$ which is the rate of change of domain wall velocity with external field or electric current density. First, we will demonstrate the impact of the magnetization on the field induced domain wall dynamics. Then we will discuss angular momentum transfer in such a system.

## 4.1 Field-induced domain wall motion

### 4.1.1 LLG equation for strongly coupled ferrimagnet

We have shown that the field-induced magnetization dynamics can be described by the LLG equation (1.18). However, this equation has to be extended in the case of a ferrimagnetic material [114]. The LLG equation for the ferrimagnetic $\mathrm{Gd}_{1-x}\mathrm{Co}_x$ system, neglecting anisotropy and demagnetizing fields reads

$$\begin{aligned} \frac{\partial \vec{M}_{\mathrm{Co}}}{\partial t} &= -\gamma_{\mathrm{Co}} \vec{M}_{\mathrm{Co}} \times \mu_0 \left( \vec{H}_{\mathrm{app}} + \lambda_{\mathrm{CoCo}} \vec{M}_{\mathrm{Co}} + \lambda \vec{M}_{\mathrm{Gd}} \right) + \frac{\alpha_{\mathrm{Co}}}{M_{\mathrm{Co}}} \left( \vec{M}_{\mathrm{Co}} \times \frac{\partial \vec{M}_{\mathrm{Co}}}{\partial t} \right), \\ \frac{\partial \vec{M}_{\mathrm{Gd}}}{\partial t} &= -\gamma_{\mathrm{Gd}} \vec{M}_{\mathrm{Gd}} \times \mu_0 \left( \vec{H}_{\mathrm{app}} + \lambda \vec{M}_{\mathrm{Co}} \right) + \frac{\alpha_{\mathrm{Gd}}}{M_{\mathrm{Gd}}} \left( \vec{M}_{\mathrm{Gd}} \times \frac{\partial \vec{M}_{\mathrm{Gd}}}{\partial t} \right), \end{aligned}$$

where $\alpha_{\mathrm{Co}}$ and $\alpha_{\mathrm{Gd}}$ are the damping parameters of the Co and Gd sublattices respectively.

When the intersublattice molecular field defined by the intersublattice coefficient $\lambda$ is strong enough to keep $\vec{M}_{\mathrm{Co}}$ and $\vec{M}_{\mathrm{Gd}}$ antiparallel at all times, one obtains:

$$\frac{\partial \vec{M}_s}{\partial t} = -\gamma_{\mathrm{eff}} \vec{M}_s \times \mu_0 \vec{H}_{\mathrm{eff}} + \frac{\alpha_{\mathrm{eff}}}{M_s} \vec{M}_s \times \frac{\partial \vec{M}_s}{\partial t} \tag{4.1}$$

where $\vec{M}_s = \vec{M}_{\mathrm{Co}} + \vec{M}_{\mathrm{Gd}}$, the effective gyromagnetic ratio is

$$\gamma_{\mathrm{eff}} = \frac{M_s}{\frac{M_{\mathrm{Co}}}{\gamma_{\mathrm{Co}}} - \frac{M_{\mathrm{Gd}}}{\gamma_{\mathrm{Gd}}}} = \frac{M_s}{\frac{M_{\mathrm{Co}}\hbar}{\mu_{\mathrm{B}} g_{\mathrm{Co}}} - \frac{M_{\mathrm{Gd}}\hbar}{\mu_{\mathrm{B}} g_{\mathrm{Gd}}}}, \tag{4.2}$$

the effective damping parameter

$$\alpha_{\mathrm{eff}} = \frac{\frac{\alpha_{\mathrm{Co}} M_{\mathrm{Co}}}{\gamma_{\mathrm{Co}}} + \frac{\alpha_{\mathrm{Gd}} M_{\mathrm{Gd}}}{\gamma_{\mathrm{Gd}}}}{\frac{M_{\mathrm{Co}}}{\gamma_{\mathrm{Co}}} - \frac{M_{\mathrm{Gd}}}{\gamma_{\mathrm{Gd}}}} \tag{4.3}$$

and the effective field

$$\vec{H}_{\mathrm{eff}} = \frac{M_{\mathrm{Co}}(\vec{H}_{\mathrm{app}} + \lambda_{\mathrm{CoCo}} \vec{M}_{\mathrm{Co}}) - M_{\mathrm{Gd}} \vec{H}_{\mathrm{app}}}{M_s}.$$

With the results obtained by the mean-field model, we can also calculate the evolution of the effective gyromagnetic ratio. The effective gyromagnetic ratio as a function of composition in the case of $\Delta g = 0.1$ is shown in Fig. 4.1. The effective gyromagnetic ratio diverges at $x \simeq 0.79$, where the angular momentum compensates. We should emphasize the fact that this calculation is based on the textbook parameters which were discussed in Chapter 3.

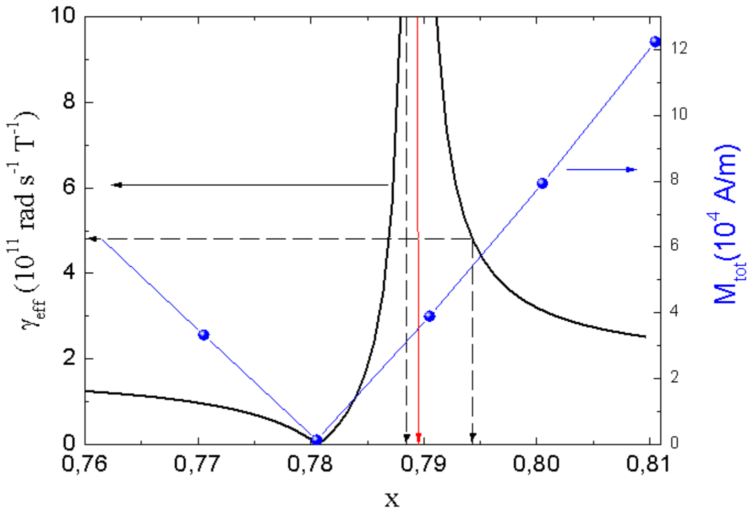

Figure 4.1: Calculated effective gyromagnetic ratio $\gamma_{\mathrm{eff}}$ and magnetization as a function of Gd$_{1-x}$Co$_x$ alloy composition $x$ at 300 K for $\Delta g = 0.1$. The red arrow indicates the position of angular momentum compensation. The dashed lines indicate the compositions at which the field-induced domain wall displacement was measured.

The magnetic resonance frequency of a ferrimagnetic system within the two-sublattice model was described by Wangsness [115], who also discussed the effective parameters $\gamma_{\mathrm{eff}}$ and $\alpha_{\mathrm{eff}}$ within this framework [116]. Experimentally, the divergence of the $\gamma_{\mathrm{eff}}$ parameter was observed in several systems - NiOFe$_{2-x}$Al$_x$0$_3$ [117], magnetic garnets [118] or in Gd-Fe garnet [119].

The role of $\gamma_{\mathrm{eff}}$ was also observed by Jiang *et al.* [120] who studied dependence of current-induced magnetization switching of ferrimagnetic GdCo free layers in spin valves.

### 4.1.2 Experimental setup

The field-induced domain wall dynamics of Gd$_{1-x}$Co$_x$ has been studied in the 100 $\mu$m wide stripes described in Chapter 3.

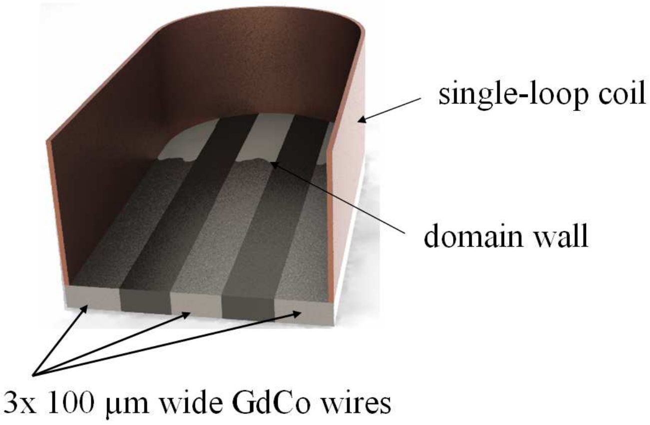

Figure 4.2: Scheme of the single-loop copper coil which is attached to the sample containing $Gd_{1-x}Co_x$ stripes. The stripes are parallel to the coil edges. The coil opening is large enough to observe the domain wall displacement by polar Kerr microscopy.

Measurements were carried out for two initial positions along the stripes, corresponding to magnetizations $M_1 = 5.1 \times 10^4$ A/m and $M_2 = 3.6 \times 10^4$ A/m (see Fig. 4.1). As we have shown in the previous chapter, a domain wall can be placed at a well defined position by tuning the external magnetic field $H_{\text{ext}}$. In fact the domain wall stops at the position where the Zeeman energy associated to the external field equals the local coercive field. The fact that the initial magnetization of the domains surrounding the domain wall can be chosen by tuning the external magnetic field is a unique property of this kind of material with composition gradient.

The sample was mounted at the bottom of a single-loop U-shaped copper coil as shown schematically in Fig. 4.2. The distance between the two parallel copper plates (500 $\mu$m) in the U-shaped coils is optimized so that the magnetic field is sufficient to move the domain walls along the stripe. At the same time, the geometry is compatible with the observation of the domain wall motion by polar magneto-optical Kerr microscopy. The $Gd_{1-x}Co_x$ stripes are parallel to the coil edges, so the magnetic field is constant along the propagation direction of the domain walls.

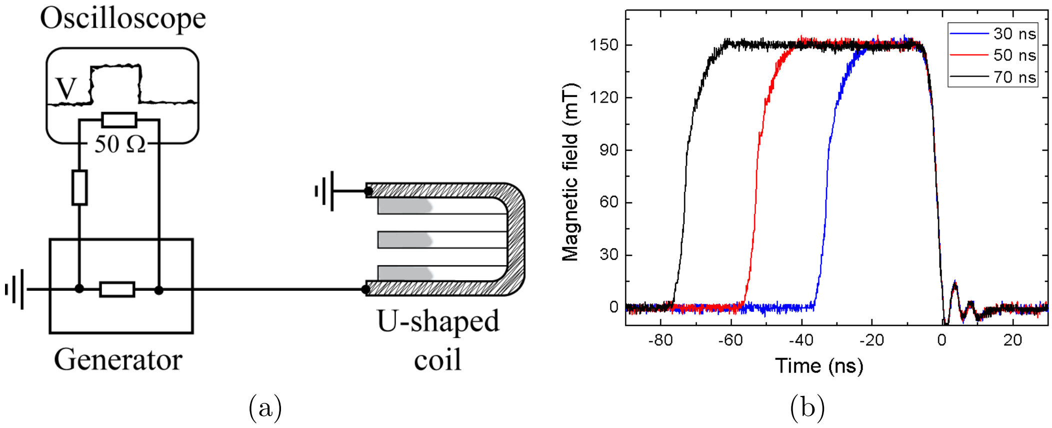

Figure 4.3: (a) Schema of the electrical circuit of the U-shaped coil. (b) Example of three current pulses injected into the coil, with measured width 30 ns, 50 ns and 70 ns.

The schema of the electrical circuit used in this experiment is shown in Fig. 4.3(a). A current pulse passing through the coil gives rise to a magnetic field. The map of the calculated perpendicular component of the magnetic field for a DC current of $I = 100\,\mathrm{A}$ is presented in Fig. 4.4(a). The arrows indicate the direction and magnitude of the vectorial magnetic field. The position of the sample is indicated by the dashed rectangle. The profile of the perpendicular component of the magnetic field in the magnetic film plane is presented in Fig. 4.4(b). The shape of the current pulse (and therefore of the magnetic field pulse) is monitored by an ultrafast oscilloscope, which allows us to determine the pulse width and amplitude. The calculated conversion between the injected current and the magnetic field at the center of the coil is

$$\boxed{100\,\mathrm{A} \equiv 81\,\mathrm{mT}} \tag{4.4}$$

The coil is able to provide magnetic fields in the range of 0-180 mT with a rise time of $\sim$ 18 ns and the calculated homogeneity of the field between the copper plates is $\sim$ 10%. The pulse length is taken as the full width at half maximum. Examples of three current pulses with 30 ns, 50 ns and 70 ns width are presented in Fig. 4.3(b).

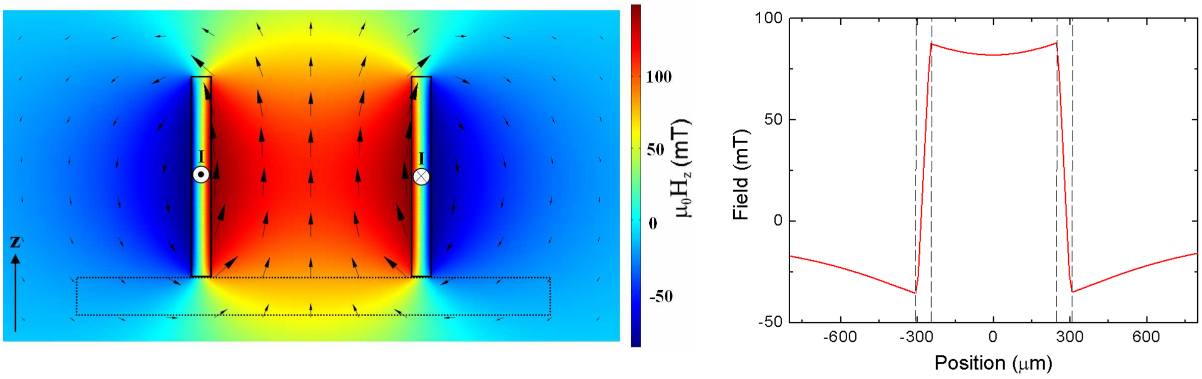

(a) (b)

Figure 4.4: (a) Calculated map of the perpendicular component of the magnetic field for a DC current of $I = 100\,\mathrm{A}$. The arrows indicate the direction and magnitude of the vectorial magnetic field. The distance between the two parallel copper plates is 500 $\mu$m. The position of the sample is indicated by the dashed rectangle. (b) Calculated profile of the perpendicular field component at the magnetic film surface. The dotted lines indicate the copper plates.

Domain wall displacements were recorded for different field pulses of the same amplitude and different durations. The velocity was then determined from the slope of a linear fit of the displacement data plotted against the pulse durations. This leads to the elimination of the effects of the transient parts of the pulses. Each pulse is repeated several times with 100 Hz repetition frequency in order to displace the domain wall by a distance compatible with the resolution of the Kerr microscope. Examples of three differential Kerr microscope images displaying the domain wall displacements induced by 2 pulses 30 ns, 50 ns and 70 ns long with a magnetic field of $\mu_0 H_{\mathrm{ext}} = 150\,\mathrm{mT}$ are shown in Fig. 4.5(b).

During the application of the field pulse, the domain wall travels a certain distance, along which the composition (i.e. magnetization) evolves. The maximum distance of the displaced domain wall was $\sim$ 100 $\mu$m, which corresponds to a composition change of 0.1 %. The distance covered by the domain wall is small enough for the magnetization to be assumed constant.

### 4.1.3 Results and discussion

Domain wall velocities were measured for fields up to 170 mT. For larger field amplitudes the nucleation of new domains occurs and starts disturbing the measured domain wall displacements. The domain wall displacements are no longer resolvable and the corresponding field amplitude constitutes the upper limit of the maximum usable magnetic field.

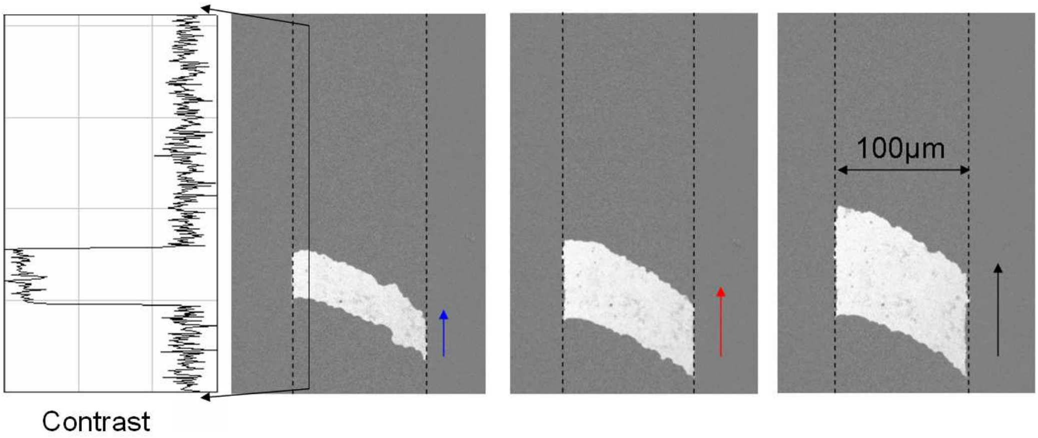

Figure 4.5: Differential Kerr microscope images corresponding to domain wall displacement induced by the pulses (x2) of corresponding lengths. $\mu_0 H_{\mathrm{ext}} = 150 \pm 1\,\mathrm{mT}$.

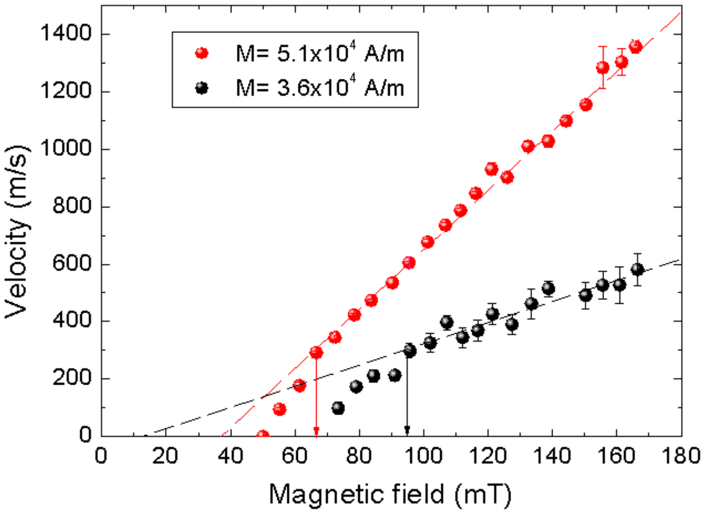

Figure 4.6: Domain wall velocity as a function of applied magnetic field measured for two different values of the magnetization. The dashed lines correspond to the fits of the linear regime. The arrows indicate the position of the depinning field.

### Domain wall mobility

- **High magnetization** ($M_1 = 5.1 \times 10^4\,\mathrm{A/m}$)
  The experimentally obtained results measured for this magnetization value are shown in red in Fig. 4.6. For low fields the domain wall dynamics is characterized by the so-called creep regime, where defects pin the domain walls. For fields above $\sim 65\,\mathrm{mT}$ the domain wall velocity depends on the applied field $H_{\mathrm{ext}}$ in a linear fashion, and can described by equation (2.2):

  $$v = \mu(\mu_0 H_{\mathrm{ext}} - \mu_0 H_0),$$

  where $\mu_0 H_0 = 38 \times 10^{-3}\,\mathrm{T}$ and the domain wall mobility $\mu = 1.10 \pm 0.05 \times 10^4\,\mathrm{m/s/T}$. The domain wall velocities achieve the extremely high value of 1400 m/s for an applied field of 170 mT.

  Note that the extrapolation of this linear regime to zero velocity does not pass through the origin.

This behaviour has been found for several earlier works [66], [67] and has been attributed to the fact that the insufficient applied field did not allow the system to exit the creep regime. On the other hand, a similar behaviour was also observed recently by Beach *et al.* [123] in Permalloy nanowires. In this case, while the extrapolation of the steady regime passed through the origin, the extrapolation of the precessional regime above Walker breakdown did not pass through the origin and be described by $v = \mu(\mu_0 H_{\text{ext}} - \mu_0 H_0)$. The microscopic origin of this threshold field $\mu_0 H_0$ is not understood. In our case, the flow linear regime is also very clearly reached.

- **Low magnetization** ($M_2 = 3.6 \times 10^4$ A/m)
  The experimentally obtained results measured for this magnetization value are shown in Fig. 4.6 by black dots. The domain wall velocity enters into a linear regime at 100 mT. The larger depinning field found for these measurements is consistent with the lower magnetization value. The solid line corresponds to the linear fit of the data described by the previously used equation (2.2):

  $$v = \mu(\mu_0 H_{\text{ext}} - \mu_0 H_0),$$

  where $\mu_0 H_0 = 12 \times 10^{-3}$ T and the domain wall mobility $\mu = 3.7 \pm 0.1 \times 10^3$ m/s/T. Note that the threshold field $\mu_0 H_0$ is lower than that obtained for the higher magnetization value.

The high mobility value of $\mu = 1.10 \times 10^4$ m/s/T obtained for the $M_1$ value can be compared with similar systems with perpendicular anisotropy. For example, Metaxas *et al.* [30] have found that the domain wall mobility is $\mu = 4 \times 10^2$ m/s/T in Pt\Co\Pt trilayers. Miron *et al.* [76] have found that in the case of asymmetric stacks of Pt\Co\AlO$_x$ the domain wall mobility $\mu = 1.5 \times 10^3$ m/s/T. A very high domain wall mobility $\mu = 1.2 \times 10^6$ m/s/T was observed in ultrathin Ag\Fe\Ag(001) films [67]. However, due to the nucleation of reversed domains at higher fields, the maximum velocity that could be observed in this experiment was about 250 m/s.

The measured domain wall mobility is larger for the composition corresponding to the higher magnetization. The expression of the mobility in the steady regime reads

$$\mu_{\text{st}} = \frac{\gamma_{\text{eff}} \Delta}{\alpha_{\text{st}}}. \tag{4.5}$$

Note that the gyromagnetic ratio $\gamma_{\text{eff}}$ diverges for the angular moment compensation composition, and is larger for the lower magnetization value [see Fig. 4.1]. Since experimentally the mobility is found to be larger for the larger magnetization value, the gyromagnetic ratio is not apparently the main parameter determining its value. Using expressions (4.3) and (4.2) it appears that the ratio $\gamma_{\text{eff}}/\alpha_{\text{eff}}$ varies linearly with the magnetization. This means that the increase of $\gamma_{\text{eff}}$ close to angular momentum compensation must be compensated by an increase of $\alpha_{\text{eff}}$. In conclusion, this gives rise to the following simpler expression of the domain wall mobility:

$$\mu_{\text{st}} \sim M_s \Delta. \tag{4.6}$$

If we suppose that the domain wall width remains unchanged by the change of composition, the domain wall mobility is then simply proportional to the total magnetization, as indicate our domain wall velocity measurements. The consequence is that the domain wall mobility vanishes at the magnetization compensation and it increases on either side of the compensation. This fact can be understood qualitatively, since the Zeeman energy delivered to the system via the magnetic field is proportional to the magnetization. The consequences of expressions (4.5) and (4.6) on the effective damping parameter will now be discussed.

### Damping parameter $\alpha$

- **High magnetization** ($M_1 = 5.1 \times 10^4$ A/m)

Our measurements clearly show the onset of a flow regime, but since the Walker breakdown is not seen, they do not allow us to claim whether the domain wall dynamics is in the steady or the precessional regime. In the steady regime the damping parameter $\alpha_{\mathrm{st}}$ for ferrimagnets reads

$$\alpha_{\mathrm{st}} = \frac{\gamma_{\mathrm{eff}}\Delta}{\mu_{\mathrm{st}}} \tag{4.7}$$

where $\gamma_{\mathrm{eff}}$ is the effective gyromagnetic ratio given by equation (4.2).

One can estimate the domain wall width by taking into account the Co exchange stiffness constant $A \simeq 10\,\mathrm{pJ/m}$ and the approximative anisotropy constant $K \simeq 10^3\,\mathrm{J/m^3}$. The estimated domain wall width is $\Delta \simeq 100\,\mathrm{nm}$. Inserting this value into equation (4.7) and using the value of $\gamma_{\mathrm{eff}}$ given by equation (4.2) with $\Delta g = 0.1$, the damping parameter is $\alpha \simeq 4.4$.

If we consider that the domain wall dynamics is in the precessional regime, the damping parameter $\alpha_{\mathrm{pr}}$ for ferrimagnets reads:

$$\alpha_{\mathrm{pr}} = \frac{\gamma_{\mathrm{eff}}\Delta \pm \sqrt{\gamma_{\mathrm{eff}}^2\Delta^2 - 4\mu}}{2\mu} = \frac{\gamma_{\mathrm{eff}}\Delta \pm \gamma_{\mathrm{eff}}\Delta\sqrt{1 - \frac{4\mu}{\gamma_{\mathrm{eff}}^2\Delta^2}}}{2\mu}. \tag{4.8}$$

The obtained values of damping are $\alpha_{\mathrm{pr}}^{+} \simeq 4.2$ and $\alpha_{\mathrm{pr}}^{-} \simeq 0.24$.

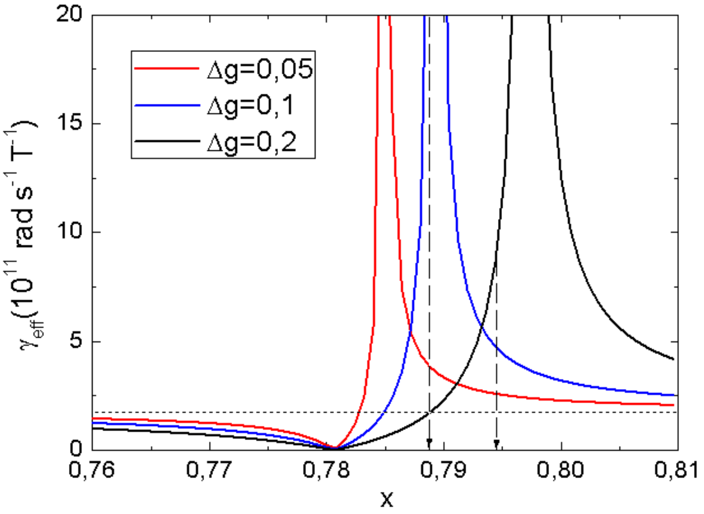

Figure 4.7: Calculated effective gyromagnetic ratio $\gamma_{\mathrm{eff}}$ as a function of $\mathrm{Gd}_{1-x}\mathrm{Co}_x$ alloy composition $x$ at 300 K for different $\Delta g$ parameters. The dashed lines indicate the compositions at which the field-induced domain wall displacement was measured.

- **Low magnetization** ($M_2 = 3.6 \times 10^4\,\mathrm{A/m}$)
  In the case of this magnetization the two calculated damping parameters read:

$$\alpha_{\mathrm{st}} \simeq 110 \tag{4.9}$$

$$\alpha_{\mathrm{pr}}^{+} \simeq 110 \tag{4.10}$$

$$\alpha_{\mathrm{pr}}^{-} \simeq 0.01 \tag{4.11}$$

These values of $\alpha_{\mathrm{st}}$ and $\alpha_{\mathrm{pr}}^{+}$ are unusually large. In pure cobalt thin layers, for example, the damping $\alpha \simeq 0.3$ [30] but in this case the gyromagnetic ratio is also an order of magnitude smaller. These measurements show that the magnetization dynamics close to compensation is a very complex problem, characterized by a deviation from linearity of all the relevant parameters. The large damping parameters obtained from the domain wall velocity measurements are connected to the large $\gamma_{\text{eff}}$ values which is closely connected with the choice of $\Delta g$ parameter. The sensitivity of the effective gyromagnetic ratio $\gamma_{\text{eff}}$ on the $\Delta g$ parameter is illustrated in Fig. 4.7 and the resulting dynamic parameters are summarized in Table 4.1.3.

| $\Delta g$ | $M$ | $\mu$ | $\Delta$ | $\gamma_{\text{eff}}$ | $\alpha_{\text{st}}$ | $\alpha_{\text{pr}}^{+}$ | $\alpha_{\text{pr}}^{-}$ |
|---|---|---|---|---|---|---|---|
| | $10^4$ A/m | $10^3$ m/s/T | nm | $10^{11}$ rad/s/T | | | |
| 0.05 | 5.1 | 11 | 100 | 2.6 | 2.4 | 1.8 | 0.55 |
| 0.1 | 5.1 | 11 | 100 | 4.8 | 4.4 | 4.2 | 0.24 |
| 0.2 | 5.1 | 11 | 100 | 8.2 | 7.4 | 7.3 | 0.14 |
| 0.05 | 3.6 | 3.7 | 100 | 3.8 | 10.2 | 10.1 | 0.01 |
| 0.1 | 3.6 | 3.7 | 100 | 41 | 110 | 110 | 0.01 |
| 0.2 | 3.6 | 3.7 | 100 | 1.8 | 4.8 | 4.6 | 0.22 |

Table 4.1: Calculated dynamic parameters for different $\Delta g = g_{\text{Co}} - g_{\text{Gd}}$.

A significant enhancement of $\alpha_{\text{eff}}$ in the vicinity of the angular compensation composition was observed by Stanciu *et al.* [121] in GdFeCo. Their data are in qualitative agreement with our findings.

## 4.2 Current-induced domain wall motion

The main goal of this part of my work was to demonstrate current-induced domain wall motion in a ferrimagnetic material close to the compensation composition at room temperature. The suitability of compensated ferrimagnets was studied theoretically by Komine *et al.* [78]. The analytical and micromagnetic study predicted critical current densities of the order of $10^{10}$ A/m$^2$ in the vicinity of the compensation composition, to be compared with the typical value of $10^{12}$ A/m$^2$ for Permalloy. The low critical current density is a very appealing issue, since the lowering of the power consumption is an essential requirement for applications.

This effect also reveals an interesting physics. We have just seen that the field-induced mobility of a domain wall is expected to vanish at the magnetization compensation composition (or temperature). On the contrary, theoretical models predict that domain walls should move more easily with the spin polarized current close to the compensation. This behaviour is opposite to that found in ferromagnets, where field or current induced mobilities have been found to scale in a linear way [75].

### 4.2.1 Angular momentum transfer at angular momentum compensation

In the steady regime the domain wall velocity is described by equation (1.41):

$$v_{\text{steady}} = \frac{\beta}{\alpha} \frac{P g \mu_{\text{B}}}{2eM_{\text{s}}} j. \tag{4.12}$$

This equation can be intuitively understood as the ratio of the magnetization of the conduction electrons and the local magnetization

$$v_{\text{steady}} \simeq \frac{M_{\text{cond}}}{M_{\text{loc}}}.$$

In other words, the spin-transfer torque efficiency is given by the magnetization carried by the conduction electrons which is transferred to the local magnetization when passing through a domain wall.

Equation (4.12) is valid for all the ferromagnetic materials. However, it is no longer valid in the case of $\text{Gd}_{1-x}\text{Co}_x$ where the temperature and composition dependence of angular momentum and magnetization differ. Since the current-induced motion is rather connected to a transfer of angular momentum than to a transfer of magnetization, the former process should be re-discussed. If in equation (4.12) the magnetization is replaced by the equivalent angular momentum, it becomes

$$v_{\mathrm{steady}} = \frac{\beta}{\alpha}\frac{P\hbar}{2eJ}j. \tag{4.13}$$

From this equation it follows that a reduction of the angular momentum $J$ close to the compensation should lead to an increase of the domain wall velocity. Therefore the compensated ferrimagnetic $\mathrm{Gd}_{1-x}\mathrm{Co}_x$ alloy might be a good candidate for current-induced domain wall displacement. This is schematically shown in Fig. 4.8 in the case of a magnetically compensated domain wall. A conduction electron carrying an angular momentum $1/2\,\hbar$ is entering the compensated domain wall. Due to the character of the band structure, the conduction electrons belong to the Co sublattice and through the $s-d$ exchange align with the Co sublattice magnetization direction. After passing through the domain wall (adiabatically or non-adiabatically) the electron has an angular momentum $-1/2\,\hbar$, which means that during the travel through the domain wall it has transferred an angular momentum $\hbar$. Since the domain wall is compensated, even a small transferred angular momentum should evoke relatively big changes in its position.

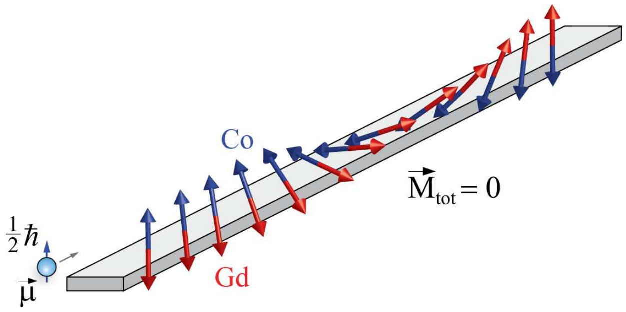

Figure 4.8: Illustration of a compensated Bloch domain wall in a $\mathrm{Gd}_{1-x}\mathrm{Co}_x$ nanowire. An electron carries an angular momentum $1/2\,\hbar$, transfers $\hbar$ when passing through the domain wall, and comes out with an angular momentum $-1/2\,\hbar$.

As was previously discussed, the transfer of angular momentum for each of the conduction electrons populations is not sufficient. When the populations of 'up' and 'down' conduction electrons are equally occupied, the transfer torques corresponding to each population cancel each other and the total transferred momentum is zero. The unbalance in 'up' and 'down' spin populations is expressed by the spin polarization $P$ which determines the polarization of conduction electrons. The spin polarization of the $\mathrm{Gd}_{1-x}\mathrm{Co}_x$ alloy near the compensation point was studied by Kaiser *et al.* [122] by utilizing superconducting tunneling spectroscopy and tunneling magnetoresistance measurements. The dependence of the spin polarization $P$ on Co fraction $x$ was described by the following relation [122]:

$$P = \mathrm{sgn}(x - x_{\mathrm{comp}})\left[P_{\mathrm{Co}}\frac{x}{x+\frac{1-x}{r}} - P_{\mathrm{Gd}}\frac{1-x}{1-x+xr}\right]$$

where $P_{\mathrm{Co}}$ and $P_{\mathrm{Gd}}$ are the spin polarizations of pure Co and Gd, respectively and $r$ is the ratio of the tunneling probabilities of the Co and the Gd sites. This equation shows that $\mathrm{Gd}_{1-x}\mathrm{Co}_x$ alloys can exhibit both positive and negative spin polarizations depending on their composition and temperature. The sign of the spin polarization changes step-likely at the compensation composition.

The spin polarization in the current-in-plane configuration differs from the one measured in the superconducting tunneling configuration. The existence of nonzero spin polarization at the compensation composition in the current-in-plane configuration was confirmed by Nam [101]. He used a

NiFe\Cu\Gd$_{1-x}$Co$_x$ junction for giant magnetoresistance (GMR) measurements. The observed sign reversal of GMR at $T_{\text{comp}}$ is attributed to the change of spin polarization in the ferrimagnetic layer.

### 4.2.2 Experimental procedures

In order to achieve the high current densities ($\sim 10^{12}$ A/m$^2$) typically needed to observe the current-induced domain wall motion, the sample has to be patterned into narrow wires. In general, a composition gradient is always present in our samples and it is important to be able to choose precisely the magnetically compensated region to be patterned. To do so, the magnetic properties of the Gd$_{1-x}$Co$_x$ films are studied by magneto-optic Kerr effect before patterning (see previous Chapter) and the position of the compensation composition carefully identified. The sample is consequently nanostructured using the etching technique described in Section 3.7. The structure consists of ten 50 $\mu$m long and 500 nm wide nanostripes. This allows obtaining statistics on several domain walls in a single measurement. The composition is approximately the same for all the nanowires and the change of composition along the length of the nanowires is negligible.

A gold wire was deposited crossing the magnetic wires to serve as a domain wall injector. When an electric current pulse is injected in the gold line, a magnetic Oersted field is created in the Gd$_{1-x}$Co$_x$ nanowires and will locally reverse its magnetization. A relatively high current density ($\sim 10^{13}$ A/m$^2$) is required for reaching an Oersted field sufficiently high for the local magnetization reversal. The value of the local coercive field depends on the alloy composition, but typically a few tens of mT are required for the reversal. In order to estimate the profile and the amplitude of the field, numerical calculations based on finite elements methods were performed. For this purpose the commercial program COMSOL was used.

The calculated distribution of the perpendicular component of the magnetic field is presented in Fig. 4.9(a). The wire is represented by the black rectangle which is delimiting the area with the homogeneous current density $j = 1\times 10^{13}$ A/m$^2$. The arrows indicate the direction and the magnitude of the vectorial magnetic field. Fig. 4.9(b) shows the profile of the field at the bottom surface of the wire.

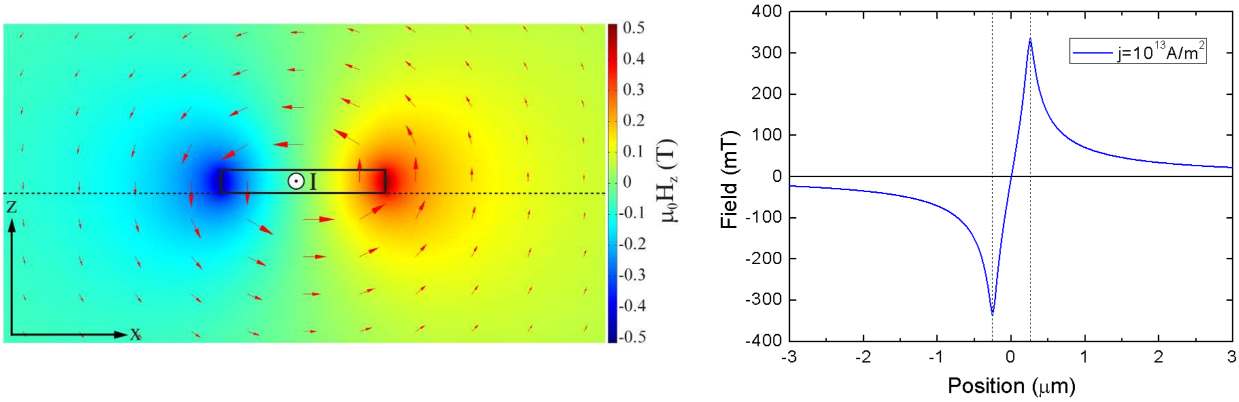

(a) (b)

Figure 4.9: (a) Computed distribution of the perpendicular component of the magnetic field around the gold wire. The wire contours are represented by a black rectangle with $500 \times 70$nm$^2$ dimensions. The uniform current density in the wire is $j = 1 \times 10^{13}$ A/m$^2$. The arrows indicate direction and magnitude of the vectorial magnetic field. (b) Distribution of the perpendicular component of the magnetic field as a function of position at the bottom surface of the wire.

The Joule heating associated with the high value of the current density can induce a significant wire damage. In order to minimize the Joule heating, the pulse duration has to be kept as short as possible. By keeping the current sense and changing the initial magnetization orientation we can inject domain walls on the opposite side of the wire. The typical effect of the Oersted field is shown in the differential Kerr microscope images in Fig. 4.10. Using this method, two domain walls are reproducibly created in the same positions of each wire and this is a good starting point for a study of spin-transfer torque induced domain wall motion.

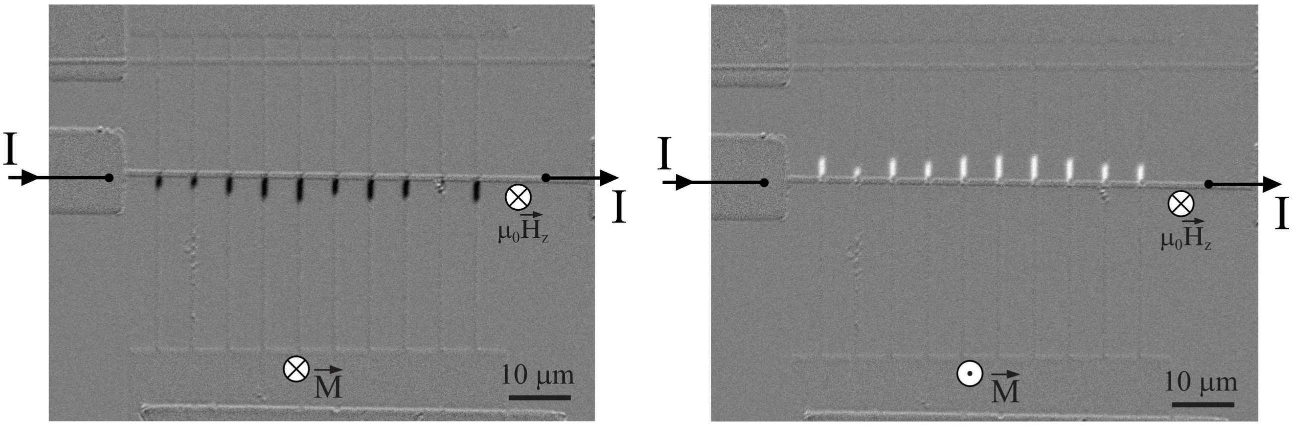

(a) (b)

Figure 4.10: Differential Kerr microscope images, displaying the effect of the Oersted field which is created by an electric current pulse passing through the Au wire. In both cases the current amplitude was kept constant and positive ($I \simeq 0.5\,\mathrm{A}$), but the initial magnetization state was reversed.

In the following, I will however discuss the case of a different sample, in which the domain walls are created using a different method, without the help of the Au line. Starting from a saturated state, magnetic field pulses are applied in order to reverse the sample magnetization. The magnetization will first reverse in the large $\mathrm{Gd}_{1-x}\mathrm{Co}_x$ pads and will then enter the lines at each end. Two domain walls will therefore be created for each wire, but their position within the wires can be different. Note that this method is much less reproducible and controllable than that shown before.

Once the domain walls are created in the wire, the next step is to move them by injecting the current pulses. Since theoretical work predicted that close to compensation the threshold current densities should be low, current pulses of the order of $10^{10}\,\mathrm{A/m^2}$ and different durations were first applied. No movement of domain walls was obtained. The current density was then increased to the values found for other systems. The typical differential Kerr microscopy image obtained after the application of a 2 ns-long current pulse with an amplitude of $3\times10^{12}\,\mathrm{A/m^2}$ is displayed in Fig. 4.11.

The figure shows that all the domain walls move towards the center on the line. So the domain walls at the bottom of the wires move in the direction of the electron flow, while the ones at the top move against the electron flow. Finally, some domains nucleate at the center of the wires. This behaviour is not consistent with spin torque effect. Since all the domain walls appear to move towards the center of the wires, where the temperature is larger, the observed displacements can rather be explained by the heating of the wires by Joule effect. Due to the reduced anisotropy with increasing temperature, the domain wall energy is expected to decrease in the middle of the wires.

In this respect, the main problem associated with the $\mathrm{Gd}_{1-x}\mathrm{Co}_x$ alloy is its electrical resistivity. The resistivity of $\mathrm{Gd}_{1-x}\mathrm{Co}_x$ amorphous alloy is $\rho_{\mathrm{GdCo}} = 200\,\mu\Omega\mathrm{cm}$ which is very high in comparison, for example, to the permalloy resistivity ($\rho_{\mathrm{Py}} = 10\,\mu\Omega\mathrm{cm}$). For current densities of the order of $10^{12}\,\mathrm{A/m^2}$, one can expect a significant Joule effect during the pulse duration. Since, as we will see in the next section, the temperature increases on the nanosecond scale during the application of current pulses, the material is no longer compensated. This may explain why the spin-torque effect has not been evidenced.

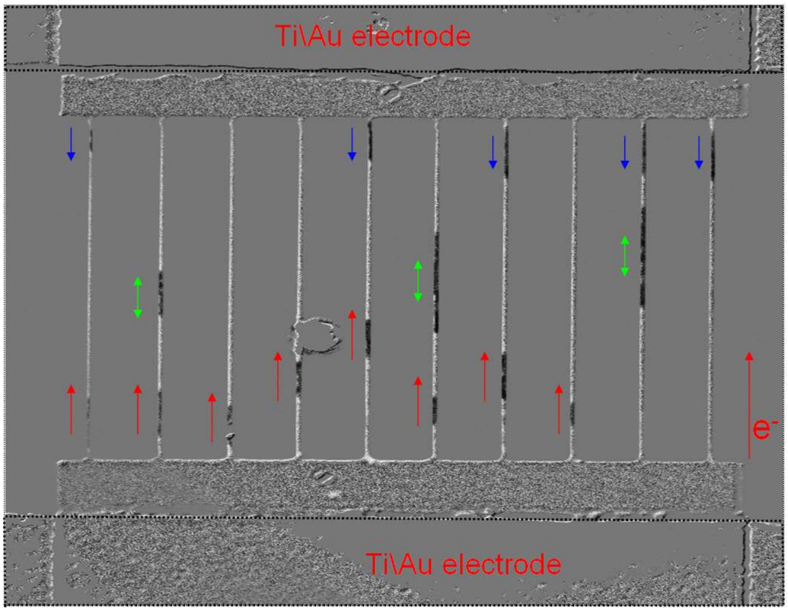

Figure 4.11: Differential Kerr microscope image obtained after application of 2 ns long current pulse with an amplitude of $3\times10^{12}$ A/m$^2$. The red arrows indicate domain wall displacements in the electron flow direction, blue arrows indicate domain wall displacements in the opposite direction to the electron flow and green arrows indicate nucleated domains.

In the next section we will show simulations of the temperature dynamics in such wires.

## 4.3 Calculations of temperature dynamics

We have shown that temperature plays an important role in the magnetization dynamics of our ferrimagnetic sample. Since measuring its evolution on sub-nanosecond scale is a very complicated task, the commercial program COMSOL was used to simulate its time evolution.

### 4.3.1 Calculations

A two-dimensional model schematized in Fig. 4.12 was used in our calculations. Our sample consists of the $Gd_{1-x}Co_x$ line of 500 nm×40 nm cross-section (through which passes a current of a given current density), a sapphire or a silicon substrate covered by a $SiO_2$ layer of various thicknesses and of air, which surrounds the sample. The initial temperature in all cases is chosen to be room temperature (300 K). The $Gd_{1-x}Co_x$ wire with a current density of $J = 5\times10^{12}$ A/m$^2$ can be regarded as a heat source of $W = 5.3\times10^{16}$W/m$^3$. In these calculations it is also necessary to define boundary conditions. The temperature is set to room temperature at the boundaries which are $\sim 5\,\mu$m far from the heat source.

In the following figures the results for four different sample substrates are displayed. Fig. 4.13(a) shows calculations for a pure silicon wafer, which is a hypothetical case since in reality in atmosphere the top layer is always oxidized. In order to reveal the influence of silicon oxide on the thermal properties, a second calculation, shown in Fig. 4.13(b), was performed for a silicon wafer with a native layer of $SiO_2$ (3 nm). The calculation displayed in Fig. 4.13(c) was performed for a silicon wafer with a 100 nm $SiO_2$ layer, which was also used in some of our experiments. The calculation presented in

| | Thermal conductivity $k$ (W/K m) | density $\rho$ (kg/m$^3$) | heat capacity $c_p$ (J/kg K) |
|---|---|---|---|
| Si | 163 | 2330 | 703 |
| $SiO_2$ | 1.4 | 2200 | 730 |
| Sapphire | 40 | 3980 | 778 |
| Air | 0.026 | 1.21 | 1005 |
| GdCo | 76 | 7870 | 440 |

Table 4.2: Parameters used in calculations.

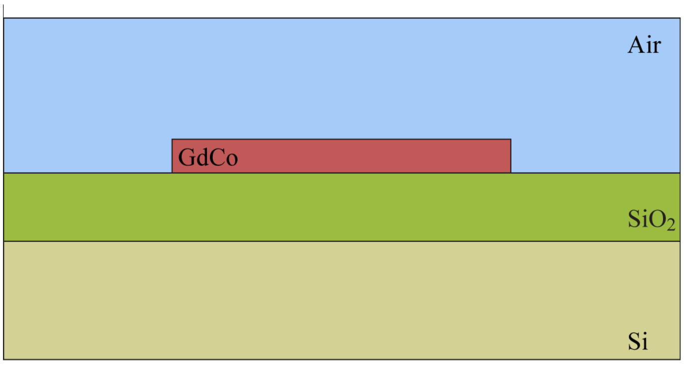

Figure 4.12: Schematic representation of the calculation model. A homogeneous current is passed through the GdCo wire which can be regarded as a heat source.

Fig. 4.13(d) include a sapphire wafer, which is a good electrical insulator and a relatively good thermal conductor at room temperature. The figure shows that the $Gd_{1-x}Co_x$ temperature increases rapidly with a 10 ns pulse in the case of $SiO_2$, while its temperature is significantly reduced when a pure Si or a sapphire substrate is used.

The calculated data for the different substrates are summarized in Fig. 4.14. Clearly, the $SiO_2$ layer constitutes a heat mirror which leads to fast wire heating.

### 4.3.2 Analytical model

An analytical model of the heat transfer is presented in this section in order to compare to the calculated numerical model. This will help to understand the role of the particular parameters presented in Table (4.3.1).

Let's consider a thin sheet of thickness d$x$ and cross-section $S$. Let's suppose temperature $t_1$ on the first surface, temperature $t_2$ on the second surface and a linear change of temperature between them. The quantity of heat $Q$ passed through the sheet after a time $\tau$ is then

$$Q = kS\frac{\mathrm{d}t}{\mathrm{d}x}\tau, \tag{4.14}$$

where the constant $k$ is the thermal conductivity.

One can define the heat flux density $q$ as:

$$q = \frac{Q}{S\tau}.$$

Then equation (4.14) can be rewritten as

$$q = -k\frac{\mathrm{d}t}{\mathrm{d}x}. \tag{4.15}$$

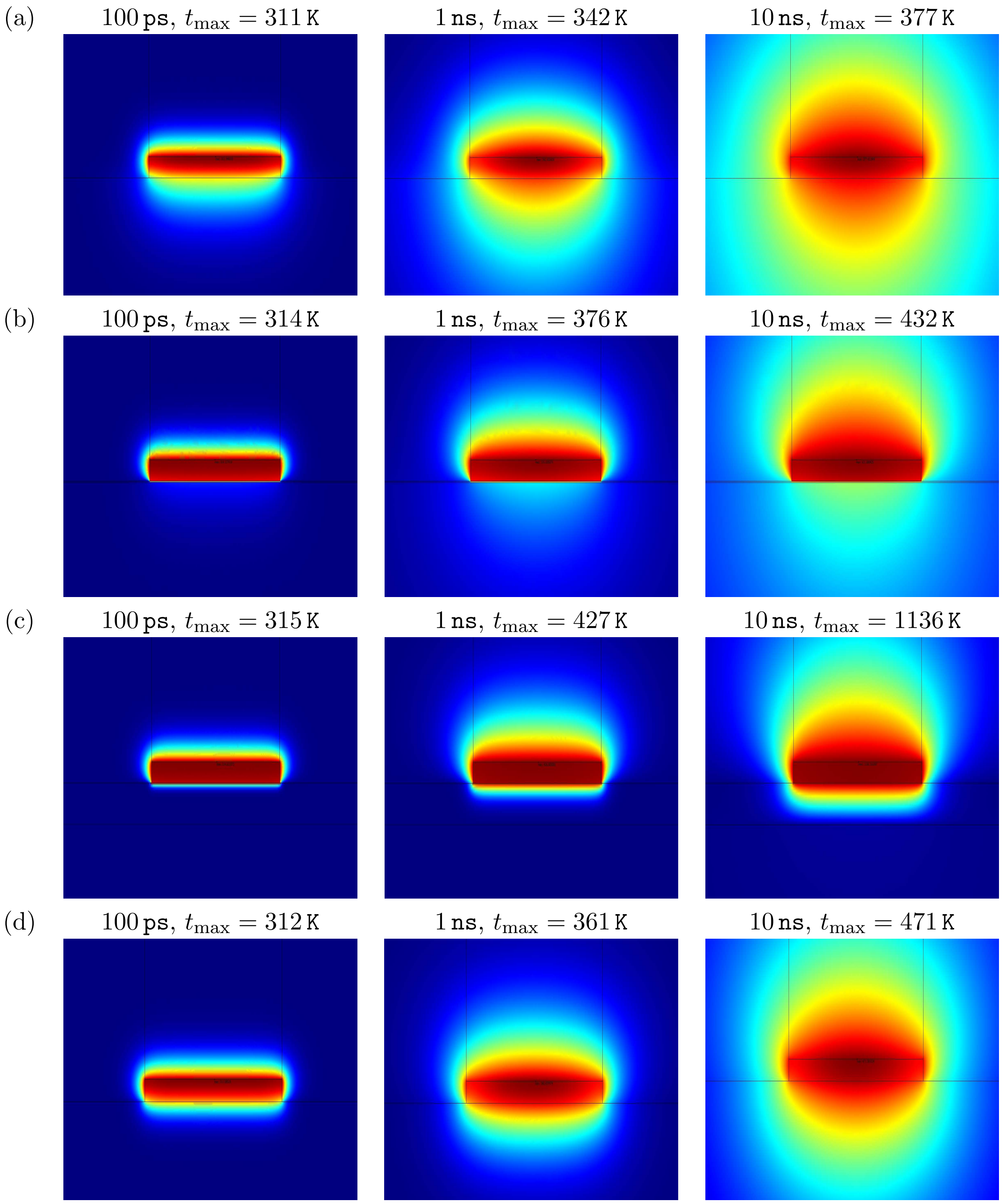

Figure 4.13: Calculated time-dependent temperature evolution for different substrates: (a) Pure Si substrate, (b) Si substrate with SiO$_2$(3 nm) layer, (c) Si substrate with SiO$_2$(100 nm) layer and (d) sapphire substrate. The current density in the Gd$_{1-x}$Co$_x$ line $J = 5 \times 10^{12}$ A/m$^2$ corresponds to a source of heat $5.3 \times 10^{16}$W/m$^3$.

Let's consider a volume with an ingoing heat $Q_1 = q_1 S \Delta\tau$ and an outgoing heat $Q_2 = q_2 S \Delta\tau$, where $q_1$ and $q_2$ is a heat flux density at the first surface and at the second surface, respectively. The temperature of the sheet is increased by the difference of these heats:

$$Q_1 - Q_2 = (q_1 - q_2) S \Delta\tau = -\Delta q S \Delta\tau. \tag{4.16}$$

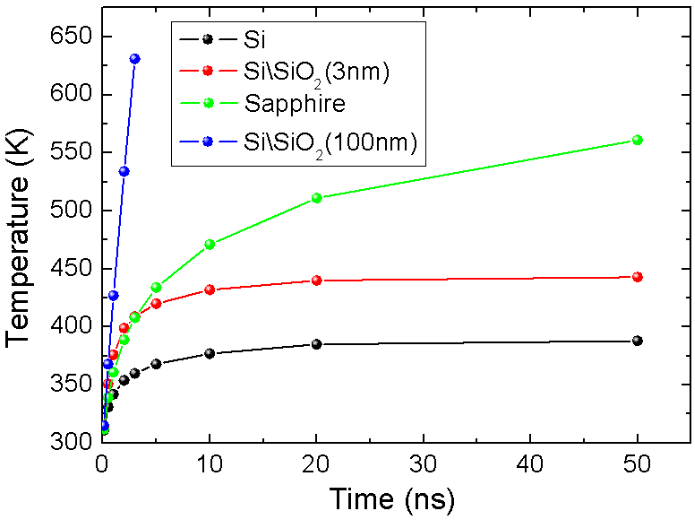

Figure 4.14: Calculated time dependent temperature for different sample substrates. The GdCo wire is a heat source of $53 \times 10^{16}\,\mathrm{W/m^3}$ power density.

If the heat capacity of the sheet is $c$ and its mass is $m = S\Delta x\rho$, then

$$Q_1 - Q_2 = c\Delta m\Delta t. \tag{4.17}$$

In the limit case, when $\Delta x \to 0$ and $\Delta\tau \to 0$, it follows from equations (4.16) and (4.17) that

$$\frac{\mathrm{d}q}{\mathrm{d}x} = -k\rho\frac{\mathrm{d}t}{\mathrm{d}\tau}. \tag{4.18}$$

By differentiation of (4.15) with respect to $x$ coordinate and by substitution of (4.18), one can obtain

$$\frac{\partial t}{\partial\tau} = \frac{k}{c\rho}\frac{\partial^2 t}{\partial x^2}.$$

The material constant

$$\lambda = \frac{k}{c\rho} \tag{4.19}$$

indicates the ability to equilibrate the temperature in a given material and it is called temperature conductivity coefficient.

In this respect, it is convenient to compare the values for the case of a silicon wafer and air. One can see from Table (4.3.1), that the value of the thermal conductivity for silicon is about three orders of magnitude higher than the value for air, while the density of silicon is about three orders of magnitude higher than the density of air. The relevant values of the temperature conductivity coefficients (4.19) are

$$\begin{aligned}\lambda_{\mathrm{Si}} = \frac{k_{\mathrm{Si}}}{c_{\mathrm{Si}}\rho_{\mathrm{Si}}} &= 9.96\cdot 10^{-5}\frac{\mathrm{m}^2}{\mathrm{s}},\\ \lambda_{\mathrm{air}} = \frac{k_{\mathrm{air}}}{c_{\mathrm{air}}\rho_{\mathrm{air}}} &= 2.56\cdot 10^{-5}\frac{\mathrm{m}^2}{\mathrm{s}}.\end{aligned}$$

Although the values of thermal conductivity are very different, the values of temperature conductivity are relatively similar. This explains why the temperature distribution in figure 4.13 is similar in the silicon layer and in air. Nevertheless, the temperature distribution does not indicate the heat flux. The GdCo stripe is still mainly cooled by the silicon substrate.

### 4.3.3 Perspectives

In conclusion, our measurements seem to contradict the theoretical expectations concerning low critical current densities around compensation. Our work has shown that the temperature raises considerably during the application of the current pulse, so the material is no longer compensated. This could be one of the explanations of the discrepancy with the theoretical work of Komine *et al.* [78].

The perspective is then logically reducing the dynamical effects of the Joule heating. One of the possibilities is the reduction of the magnetic wire thickness. Institut Néel has recently bought a new commercial sputtering machine and the very first tests showed that the GdCo layers exhibit a perpendicular anisotropy for films as thin as $\sim 5\,\text{nm}$. The impact of the thickness on the temperature evolution is demonstrated in Fig. 4.15.

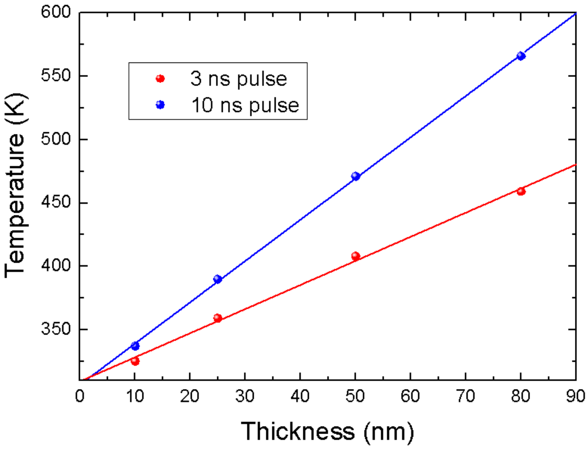

Figure 4.15: Calculated dependence of temperature as a function of the GdCo wire thickness for two different pulse lengths. The current density in both cases is $j = 5 \times 10^{12}\text{A/m}^2$.

One can see that the temperature of the wire depends linearly on the wire thickness. It follows then that the reduction of the wire thickness by a factor of 10 should lead to a significant decrease of the wire temperature.

Recently, current-induced motion of magnetic domain walls has been observed in TbFeCo wires induced by low-current density $5 \times 10^{10}\,\text{A/m}^2$ with the domain wall velocities up to $60\,\text{m/s}$ [124]. However, more precise information about the degree of the alloy compensation are in the publication missing, so it is difficult to identify the outstanding difference between the TbFeCo and GdCo alloys. As a consequence, the ferrimagnets still stay in the interest of spintronics.

## 4.4 Light-induced magnetization dynamics

We have shown that magnetism is intimately connected to the angular momentum. The speed of its transfer is one of the crucial points of fast magnetization reversal. In the previous sections we have discussed transfer of angular momentum between two electrons (localized and delocalized), however this are not the only angular momentum reservoirs between which angular momentum can be exchanged. The theory of elementary particles permits to attribute well-defined angular momentum expressions at any radiation field [125]. Viewing the photon in a 'classical' way, the spin of a photon can be $\pm 1$ in connection with rotating of a right-handed screw $(+1)$ or a left-handed screw $(-1)$. These specific quantum-mechanical photon spin-states are called helicity states. Mechanisms of an effective angular momentum transfer via electron-spin or phonon electrons spin coupling with a response faster than 100 fs are the subject of current research and active debates.

The ultrafast magnetization reversal on the 40 fs scale was demonstrated in an amorphous ferrimagnetic alloy of GdFeCo with strong perpendicular magnetic anisotropy. The state of the magnetization can be completely switched by circularly polarized light into an 'up' or 'down' state determined only by the helicity of the optical excitation. Moreover, this ferrimagnetic alloy represents a system where the laser-induced magnetization precession can be continuously tuned by changing temperature. Stanciu *et al.* [126] have observed high-speed and strongly damped spin dynamics in the vicinity of the compensation temperature of the angular momentum. Such a behaviour is ideal for ultrafast precessional switching in magnetic and magneto-optical recording. However, the mechanism for such a reversal is still a matter of debate. The role of angular momentum transfer, the role of heating and the role of reaching $T_c$ are not clarified. Recently, Radu *et al.* [127] explored the mechanism of the reversal in GdFeCo system and they discovered that the system undergoes a transient ferromagnetic-like state where the ferrimagnetic alignment is broken.

The $\mathrm{Gd}_{1-x}\mathrm{Co}_x$ sample with an induced composition gradient offers another way to imitate the temperature dependent behaviour by keeping constant $(T_c - T)$ distance. The composition gradient therefore brings a new degree of freedom in spin dynamics investigation. The samples, which were prepared and characterized at Institut Néel, were studied by T. Rasing's group at the Radboud University in Nijmegen.

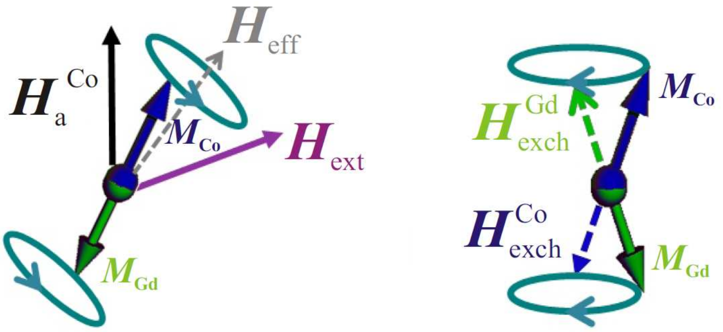

(a) (b)

Figure 4.16: Schematics illustrating (a) the precession of the magnetizations around the effective field $H_{\mathrm{eff}}$ and (b) the exchange fields $H_{ex}^{\mathrm{Co}}$ and $H_{ex}^{\mathrm{Gd}}$ which give rise to the FMR and exchange modes, respectively.

In this experimental setup, the laser-induced spin dynamics was investigated by an all-optical pump and probe technique using an amplified Ti:sapphire laser system with 100 fs laser pulses. The stronger pump pulse was focused onto a spot with a diameter around 400 $\mu$m. The weaker probe pulse, delayed by a certain time delay, was focused onto a smaller spot with a diameter around 50 $\mu$m. The experiment was performed at room temperature and the desired magnetic configuration is changed by laser spots scanning over the sample surface. Due to the sudden heating induced by the pump pulse, which is equal to a change of the effective magnetic field, the magnetization starts to precess around a new equilibrium position. The probe then measures one of the magnetization components and reveals its oscillations. In the ferrimagnetic material two types of resonant frequencies can be found:

- **Ferromagnetic mode**

$$\omega_{\mathrm{FMR}} = \gamma_{\mathrm{eff}} H_{\mathrm{eff}} \tag{4.20}$$

  where $\gamma_{\mathrm{eff}}$ is the effective gyromagnetic ratio given by equation (4.2).

  The ferromagnetic mode corresponds to the precession of the Co and Gd moments, which are rigidly antiferromagnetically coupled, around the effective field $H_{\mathrm{eff}}$ [Fig. 4.16(a)] and was described by equation (4.1). One can directly notice that this mode softens at the magnetization compensation composition and diverges at the angular momentum compensation composition.

- **Exchange mode**

$$\omega_{\text{ex}} = \lambda\gamma_{\text{Co}}\gamma_{\text{Gd}}\left[\frac{M_{Co}}{\gamma_{\text{Co}}} - \frac{M_{Gd}}{\gamma_{\text{Gd}}}\right] \tag{4.21}$$

  where $\lambda$ is the inter-sublattice exchange coupling coefficient representing the strength of the ferrimagnetic interaction.

  The unequal action of the laser pulse on the Gd and Co sublattices and two different precession rates induce a canting angle between the sublattices. Fig. 4.16(b) shows different magnetization precession paths around the exchange fields $\vec{H}_{\text{ex}}^{\text{Co}}$ and $\vec{H}_{\text{Gd}}^{\text{Gd}}$.

The observed spin dynamics for $x = 0.80$ is plotted in Fig. 4.17. One can notice, that within the first 50 ps oscillations with a short period dominates, followed by a longer period. This is confirmed by the fast Fourier transformation spectrum of these data, shown as inset in Fig. 4.17. The slow oscillations are denoted by the frequency $f_1$ and the fast oscillations as $f_2$.

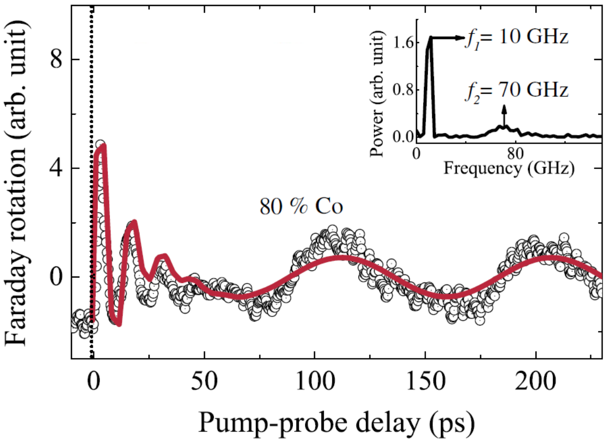

Figure 4.17: Optically induced magnetization dynamics for x=0.80. The vertical dotted line indicates zero delay between pump and probe pulses. Fast Fourier transformation of the plotted spectrum is shown as inset.

This dynamic response was measured as a function of applied magnetic field and also as a function of composition $x$. The results are summarized in Fig. 4.18. The frequencies as a function of the external magnetic field are plotted in Fig. 4.18(a). The frequency $f_1$ increases linearly with the applied field, whereas $f_2$ is not influenced by the magnetic field. This is in agreement with the behavior expected for ferromagnetic and exchange modes, respectively.

At a certain Co concentration ($x = 0.815$) $f_1$ reaches a maximum whereas $f_2$ is at its minimum value. This behaviour implies angular momentum compensation around $x \sim 0.815$ allowing to identify $f_1$ and $f_2$. The frequency $f_1$ corresponds to the ferromagnetic mode and $f_2$ to the exchange resonance mode.

Using optical pulses, the high-frequency exchange and low-frequency ferromagnetic spin resonance modes have been excited and detected in a Gd$_{1-x}$Co$_x$ ferrimagnetic thin film on both sides of its angular momentum compensation composition. The evidence of the two modes revealed the presence of the angular momentum compensation interface at $x \sim 0.815$. This is in the qualitative agreement with our estimations discussed in Section 3.15.

The increase of the ferromagnetic mode frequency around the angular compensation composition, which is shown in Fig. 4.18(b), qualitatively agrees with the increase of the gyromagnetic ratio expressed by (4.2). The increase of $\omega_{\text{FMR}}$ is related to the increase of $\gamma_{\text{eff}}$ which leads to an increase of the damping parameter $\alpha$. This qualitatively confirms the measured large damping parameter

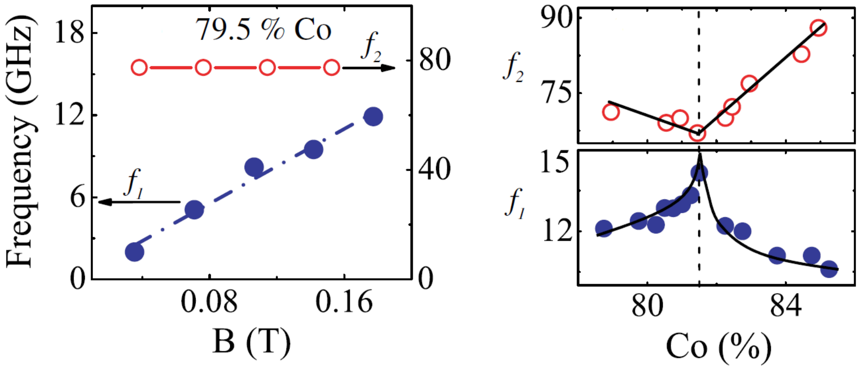

(a) (b)

Figure 4.18: (a) Oscillation frequencies for $x = 0.795$ as a function of the external magnetic field applied at ∼ 55° from the sample normal. (b) Oscillation frequencies as a function of cobalt concentration (symbols). Solid lines are guides to the eye.

discussed in the previous section. This strongly damped spin dynamics in the vicinity of the compensation of the angular momentum is very interesting for ultrafast precessional switching in magnetic and magneto-optical recording.

# Chapter 5

# Current-induced domain wall motion in Pt\Co\AlO$_x$ - state of the art

Pt\Co\AlO$_x$ trilayers were first proposed for spin-dependent tunneling in magnetic tunnel junctions [128]. Magnetic tunnel junctions are typically composed of two ferromagnetic layers separated by an oxide barrier (AlO$_x$, MgO, TaO$_x$, etc.). In such a configuration the electric current flows perpendicularly to the film plane and the tunneling transport is governed by the spin-dependent interfacial densities of states and the electronic states in the barrier. However, in experiments studying the current-induced domain wall displacement, the current flows in the film plane. Similar Pt\Co\AlO$_x$ trilayers have then been tested in the current-in-plane configuration and revealed to be extremely interesting for spin transfer torque studies.

Pt\Co\AlO$_x$ structures have been optimized by B. Rodmacq's group in Spintec so that a controlled perpendicular anisotropy can be designed in the ultrathin layer. More recently, current-induced domain wall motion in Pt\Co\AlO$_x$ trilayer has been investigated by the Spintec group in collaboration with the Institut Néel (Micro- et NanoMagnétisme) group and large domain wall velocities have been found [75]. The current-induced domain wall displacement in the symmetric Pt\Co\Pt trilayer was shown to be inefficient [129] as shown also recently by Kim *et al.* [74]. The maximum velocities obtained in the Pt\Co\Pt stack are several orders of magnitude lower than in Pt\Co\AlO$_x$. The crucial difference between these two systems is the broken symmetry in the case of Pt\Co\AlO$_x$ stack. Miron *et al.* [130] imputed the enhanced domain wall velocities in the asymmetric stack to the internal Rashba effect which enhances the spin-transfer torque.

In this chapter I will first describe the role of the Co\AlO$_x$ interface and the properties of the complete asymmetric stack. Thereafter the fabrication steps leading to these properties will be shown. I will also show for comparison some of the properties of the symmetric Pt\Co\Pt trilayer. In the second part of this chapter I will describe the effect of the effective transverse field acting on the magnetization, on a domain wall and on its dynamical behaviour. The results obtained in the Pt\Co\AlO$_x$ system will be reviewed.

## 5.1 Role of oxygen at the Co\AlO$_x$ interface

The work carried out by the SPINTEC group has shown that the Al oxidation is an essential parameter determining the presence of perpendicular anisotropy in Pt\Co\AlO$_x$ trilayer [131]. Here we will describe two possible scenarios at the Co\AlO$_x$ interface during the aluminium oxidation process and the role of the oxygen in the establishment of the magnetic anisotropy. This kind of interface was studied by Oleinik *et al.* [6] in magnetic tunnel junctions. The theoretical description of this interface is a very interesting issue but it is a very complicated problem from an experimental point of view, especially due to the amorphous character of the alumina layer.

The key factor leading to the perpendicular anisotropy is the aluminium oxidation time. The interface can be either underoxidized, i.e. aluminium terminated interface, or oxidized, i.e. oxygen terminated interface.

Fig. 5.1(a) depicts the interface structure in the case of aluminium terminated interface. The interfacial aluminium layer has a significant positive charge due to the charge transfer to the adjacent oxygen layer. This positive charge is screened by cobalt layers resulting in a reduction of the magnetic moment.

The oxygen terminated interface is influenced by the covalent bonding between the $2p$ oxygen orbitals and the $3d_{z^2}$ orbitals of cobalt. A charge transfer occurring between Co and O enhances the asymmetry of the valence band of Co, increasing the interfacial spin polarization. In the adjacent oxygen layer a small magnetic moment is created. This charge transfer reduces the energy of Co $d$ orbitals pointing towards O, creating a splitting between in-plane and out-of-plane orbitals. The hybridization leads to the strong perpendicular anisotropy despite the relatively weak spin-orbit coupling.

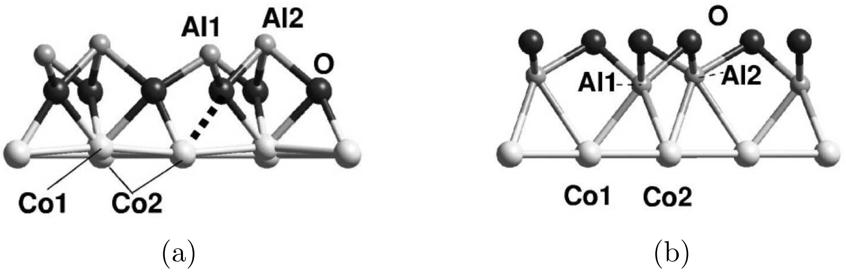

(a) (b)

Figure 5.1: Bonding geometry of aluminium terminated interface (a) and of oxygen terminated interface (b). [6]

## 5.2 Magnetic properties of Pt\Co\AlO$_x$

The films used for current-induced domain wall displacement studies were prepared at Spintec by S. Auffret. Pt\Co\AlO$_x$ films were initially studied in the context of magnetic tunnel junction systems and their fabrication was described in detail in [131]. We will just point out the main fabrication steps and the importance of the choice of the given procedures.

Multilayers of **Pt(3 nm)\Co(0.6 nm)\AlO$_x$(2 nm)** were deposited onto thermally oxidized silicon substrates with a 500 nm thick silicon oxide layer by conventional dc magnetron sputtering with a base pressure of $3.10^{-8}$ mbar. The Al layer is exposed to an oxygen rf plasma with a partial pressure of $3 \times 10^{-3}$ mbar. In comparison to the natural oxidation (0.6 nm), the plasma oxidation allows to deposit and oxidize thicker Al layers so no additional capping layer is needed.

### Plasma oxidation

The deposited film was oxidized in plasma for different oxidation times $t$. In terms of magnetic properties, one can distinguish four main oxidation regimes [131](p.115-116):

- When the oxidation time is too short, the oxidized part does not reach the bottom of the Al layer. The oxidation does not influence the crucial interface between Al and Co so the magnetization lies in the film plane.
- In the intermediate state, the oxidation starts to reach the Co\Al interface and to influence the magnetic anisotropy. These intermediate times lead to the formation of a perpendicular state having a remanence lower than 100%.

- When the oxidation time is optimal, the Co\Al interface is fully oxidized so the Co-Al bonds are replaced by Co-O bonds. Such an ideal case gives rise (together with the Pt\Co interface) to the highest perpendicular anisotropy which is strong enough to keep a monodomain state with 100% magnetization remanence.

- When the oxidation time is higher, the oxygen starts penetrating into the Co layer. The antiferromagnetic CoO layer starts forming and the rest of Co stays perpendicular with a low magnetization remanence.

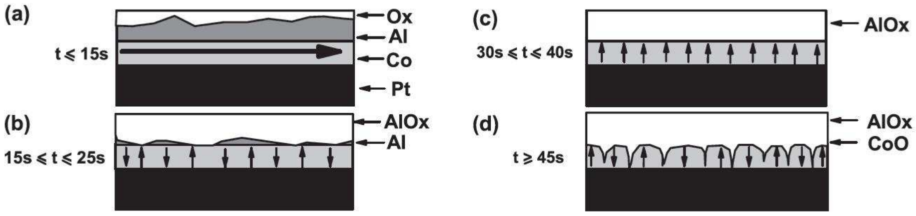

Figure 5.2: Schematics of oxygen influence on the Co layer in Pt\Co\AlO$_x$ trilayers. (a) For a very short oxidation time the magnetization stays in the film plane. (b) For a short oxidation times the oxide starts reaching the Co\Al interface and influencing the magnetic anisotropy. (c) For an ideal oxidation time the Co\Al is fully oxidized and the highes anisotropy state is achieved. (d) For long oxidation times the oxygen starts penetrating to the Co layer. [131]

**Sample annealing**

The effect of thermal annealing on AlO$_x$-based magnetic tunnel junctions was studied shortly after the first experimental evidence of large tunneling magnetoresistance [132]. The influence of thermal annealing in Pt(3 nm)\Co(0.6 nm)\AlO$_x$(2 nm) trilayers was studied by Rodmacq *et al.* [128]. The samples were annealed in a high vacuum furnace for 30 min. Magnetic properties were consequently measured for various oxidation times at room temperature. The authors conclude that three different regimes exist:

- For short oxidation times, when the Al layer is not entirely oxidized, the annealing leads to diffusion of the oxygen atoms toward the Co\AlO$_x$ interface and to its homogenization. This behaviour then results in the creation of perpendicular anisotropy.

- For intermediate oxidation times, the annealing does not change much the Co magnetic state, which stays out-of-plane. Annealing at $\sim$ 350°C leads to the high quality of the Co\AlO$_x$ interface and to the barrier homogenization giving rise to a maximum perpendicular anisotropy (Fig. 5.3). The effective anisotropy constant in this case is $K_{\mathrm{eff}} = 0.8\,\mathrm{MJ/m^3}$.

- The overoxidized films ($t > 45\,\mathrm{s}$) stay more or less uninfluenced until 450°C. At this temperature the oxygen atoms starts being reabsorbed towards the Co\Al interface and deoxidizing the Co layer. Rodmacq *et al.* showed that above 400°C, this process accompanied by the appearance of a magnetization together with the formation of an optimally oxidized Co\AlO$_x$ interface, also gives rise to the perpendicular magnetic anisotropy [128].

In general, Pt\Co\AlO$_x$ trilayers exhibit larger perpendicular anisotropy and thermal stability than Pt\Co\Pt trilayers. The oxidation times and annealing temperatures add an extra degree of freedom to achieve the desired magnetic properties.

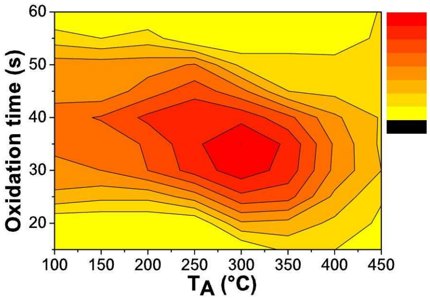

Figure 5.3: Map of the anisotropy field in Pt\Co\AlO$_x$ trilayers for various oxidation times and annealing temperatures. The scale is in 100 mT. [128]

## 5.3 Spin transfer torque in Pt\Co\AlO$_x$

### 5.3.1 Current-induced domain wall motion

The Spintec and Institut Néel groups initially studied domain wall motion in Pt\Co\AlO$_x$ nanowires induced by nanosecond current pulses [75] and elucidated recently the underlying mechanism in this trilayer [76]. A structure containing an array of twenty parallel 500 nm wide and 10 $\mu$m long wires was used. Such a structure allows measuring the domain wall displacement simultaneously in the twenty wires, making the statistics more robust. The domain wall displacements were visualized by wide-field polar Kerr microscopy.

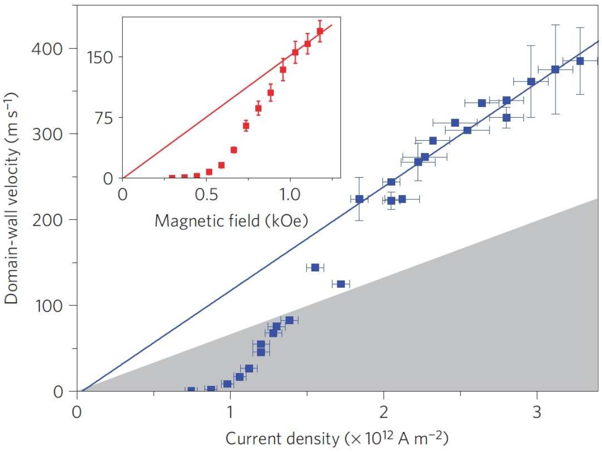

Figure 5.4: Domain wall velocity as a function of current density. The solid line is a fit of the domain wall velocity in the flow regime which appears for current densities higher than $1.8 \times 10^{12}$ A/m$^2$. The shaded area shows the possible domain wall velocities compatible with the precessional regime. The inset shows the domain wall velocity as a function of applied magnetic field. The domain wall mobility saturates for magnetic fields higher than 0.1 T demonstrating a similar behaviour to the current-induced velocity. [76]

The obtained domain wall velocities are shown in Fig. 5.4. For low current densities the domain walls are strongly pinned by defects, velocity is low and the domain wall motion is in the creep regime. As the current density increases, the domain wall mobility becomes constant, which indicates that the flow regime is reached. Velocities as high as 400 m/s are obtained for current densities $j \simeq 3 \times 10^{12}$ A/m$^2$ [76]. The shaded area maps the possible domain wall velocities calculated for the precessional regime where $v \simeq u$ [see equation (1.42)]. The measured domain wall mobility exceeds by a factor of $\sim 2$ the domain wall mobility in the precessional regime, even when assuming the full current polarization (P=1). This rules out the scenario of domain wall dynamics in the precessional regime. The high domain wall mobility can only be explained by including the $\beta/\alpha$ 'correction factor' used in the steady domain wall motion where $v = (\beta/\alpha)u$ [see equation (1.41)]. Then in the range of current densities used in the experiment, the domain wall moves steadily under the effect of the non-adiabatic torque.

The high domain wall velocity in this system was a breakthrough result since in the previously studied systems with perpendicular magnetic anisotropy, the current-induced domain wall velocities were much slower. Recently, Kim *et al.* [74] reported on current-induced domain wall displacement in the symmetric Pt\Co\Pt trilayer. The maximum domain wall velocities obtained in this trilayer are about $10^{-4}$ m/s for applied current densities of $j \simeq 1.10^{11}$ A/m$^2$.

### 5.3.2 Spin torque meter

The different behaviour of the symmetric Pt\Co\Pt and the asymmetric Pt\Co\AlO$_x$ trilayer has been studied by Miron *et al.* [58]. In order to clearly identify the difference between the two structures, the growth conditions of the Pt\Co layers were kept the same and only the upper layer was replaced. The impact of the electric current on a pinned elastic domain wall was measured by the anomalous Hall effect in a double-cross configuration which is presented in Fig. 5.5 [58]. A domain wall is injected into the wire and stays pinned between two points while it is free to deform under the action of field and current. Two simultaneous torques originating from AC magnetic field and from AC electric current are exerted on the domain wall. In a certain range of exerted torques, the elastic domain wall breathes under the action of these two torques. The accuracy of the Hall effect electrical signal is equivalent to a $\sim 10^{-2}$ nm spatial resolution. The quantitative information about the exerted torque can be calculated from the balance between the known magnetic field torque and the unknown spin-transfer torque.

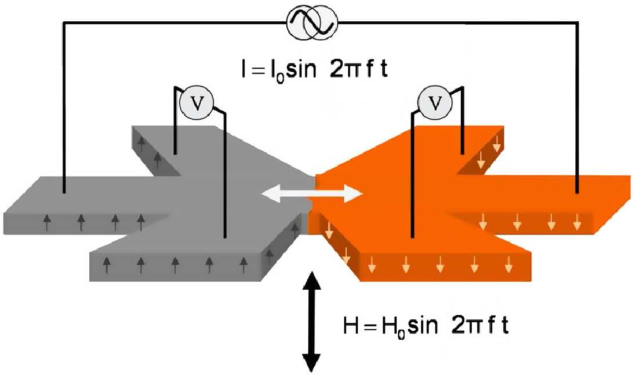

Figure 5.5: Schematics of the double-cross experimental configuration. [58]

In the case of electric current, the domain wall deformation is caused by the combination of adiabatic and non-adiabatic torques. While the non-adiabatic contribution is always proportional to the current, the adiabatic torque pushes the domain wall only when the critical current density limit is exceeded [51]. When the current density is higher than the critical current density, it is impossible to distinguish between the two contributions. However, in these measurements Miron *et al.* have not observed a step-like behaviour indicating the evidence of critical current. It could then be deduced that the domain wall deformation is caused by the non-adiabatic torque.

From the previous discussion, the spin-transfer-torque efficiency depends on several factors:

- The **magnetization** was measured before sample patterning and was found to be similar for both types of trilayers.

- The **current polarization** difference scenario causing two orders of magnitude difference is unrealistic due to the similar anomalous Hall effect amplitudes.

- The spin transfer torque depends also on the ratio of the $s-d$ exchange interaction and the spin scattering time ($\beta = \tau_{ex}/\tau_{sf}$). As will be discussed later, in the case of asymmetric Pt\Co\AlO$_x$ trilayer, electrons freely propagating in the Co layer experience a magnetic Rashba field.

  We have seen that in systems with broken symmetry the D'yakonov Perel' mechanism of spin relaxation can play an important role. The loss of the coherent spins rotation due to the precession around the Rashba field leads to an increase of the spin flip rate. According to equation (1.34)

  $$\tau_{\mathrm{sf}} = \frac{1}{\Omega_{\mathrm{av}}^2 \tau_{\mathrm{s}}},$$

  where $\tau_{\mathrm{s}}$ is the scattering time and $\Omega_{\mathrm{av}}$ is the averaged magnitude of Larmor frequency. The presence of the Rashba field gives rise to a lower spin relaxation time $\tau_{\mathrm{sf}}$ in the asymmetric stack and therefore to a larger $\beta$ parameter.

  Since the first two scenarios can be excluded, Miron *et al.* then attributed the different spin transfer torque efficiency in Pt\Co\Pt and Pt\Co\AlO$_x$ to the different $\beta$ term.

The non-adiabatic part of the spin-torque expressed by the constant $\beta$ was found to be $\beta_{\mathrm{AlOx}} = 1$ in the case of Pt\Co\AlO$_x$ whereas $\beta_{\mathrm{Pt}} \simeq 0.01$ for Pt\Co\Pt.

### 5.3.3 Domain wall motion vs. electron flow

The observed direction of the domain wall displacement under the effect of spin transfer torque in the Pt\Co\AlO$_x$ is opposed to the electron flow. This is not the only reported case in the literature, as it was already observed in (Ga,Mn)As [71]. According to the theory described in Section 1.8.2, three different scenarios leading to the opposite domain wall motion can be distinguished:

- $\beta > \mathbf{0}$, $\mathbf{P} < \mathbf{0}$
  The negative spin polarization corresponds to the current which is carried by minority electrons. Then all the dynamical properties would be identical as for positive spin polarization, except of the domain wall motion direction.

- $\beta < \mathbf{0}$, $\mathbf{P} > \mathbf{0}$
  The negative value of beta corresponds to the negative non-adiabatic spin torque contribution. Therefore, according to equations (1.41) and (1.42), the domain wall would move in the opposite direction only below the Walker breakdown.

- $\beta < \mathbf{0}$, $\mathbf{P} < \mathbf{0}$
  When both $\beta < 0$ and $P < 0$ parameters are negative, the domain wall would move in the opposite direction only above the Walker breakdown.

Since the Walker breakdown has not been directly evidenced in such a system, it is difficult to identify the microscopic origin of the direction of the domain wall propagation. However, as the analysis of measured data presented in Fig. 5.4 rules out the scenario of precessional motion, we can exclude the third scenario. However, the scenarios $\beta < 0$, $P > 0$ and $\beta > 0$, $P < 0$ still stay undistinguishable.

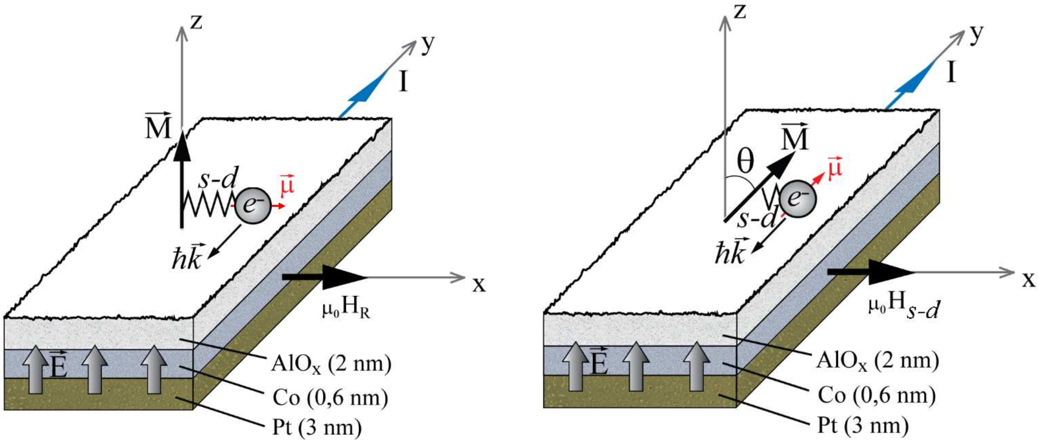

(a) (b)

Figure 5.6: (a) When an electric current passes through the wire with the internal electric field $\vec{E}$, the magnetic moment $\vec{\mu}$ of a conduction electron experiences a magnetic field $\vec{H}_{\mathrm{R}} \sim \vec{E} \times \vec{k}$. (b) The magnetic moment influences the position of the local magnetization via the $s-d$ interaction canting the magnetization into the plane of the wire which is defined by the angle $\theta$.

## 5.4 Domain wall propagation under the effect of Rashba field

In the case of Pt\Co\AlO$_x$ system the symmetry breaking gives rise to an electric field perpendicular to the film plane. When a conduction electron with a momentum $\hbar\vec{k}$ passes through the wire, it experiences the Rashba field acting on the electron spin $\vec{s}$, as it is schematized in Fig. 5.6(a). The magnetic field has a strength given by the product $\vec{H}_{\mathrm{R}} \sim \vec{E} \times \vec{k}$ and lies in the transverse direction to the nanostripe. The magnetic moment of the conduction electron $\vec{\mu} = -g\mu_{\mathrm{B}}\vec{s}$ then tends to align with the transverse field. In a ferromagnet, the action of $H_{\mathrm{R}}$ combines with the $s-d$ exchange interaction that couples the conduction electron spin to the local magnetization. Therefore localized ($3d$) and delocalized ($s$) magnetic moments tends to align in parallel [Fig. 5.6(b)]. The resulting magnetization cants with respect to out-of-plane direction by an angle $\theta$ which depends on the current density passing through the wire. The equilibrium position is given by the sum of all competing energies. It follows, that the Rashba field exerts on the magnetization an exchange-mediated effective field $H_{sd}$ via the spin-orbit interaction. In the following text, we will refer to the exchange-mediated effective field $H_{sd}$ as the effective transverse magnetic field.

The effect of the $H_{sd}$ field in uniformly magnetized Pt\Co\AlO$_x$ wires is depicted in Fig. 5.7(a)-(d). When no current passes through the wire, no $H_{sd}$ field is present and the magnetization stays out-of-plane [Fig. 5.7(a)]. The presence of a charge current $\vec{j} = (0, j, 0)$ induces a net effective field $\mu_0\vec{H}_{sd} = (\mu_0 H_{sd}, 0, 0)$ giving rise to a torque which acts on the magnetization. The amplitude of the effective transverse magnetic field $H_{sd}$ depends on the current density, so it increases when the current density is increased, as shown in Fig. 5.7(b) and (c). Hence the canting angle $\theta$ depends on the current density. The magnetization turns into the plane when the effective transverse magnetic field magnitude equals the anisotropy field of the wire [Fig. 5.7(d)].

The presence of the Rashba field influences the static and dynamic properties of a domain wall. In a material containing 180° Bloch walls, one can distinguish two possible senses of screw rotation of the magnetization. The two domain wall chiralities are illustrated in Fig. 5.8. Both types of chiralities have the same energy and therefore the abundance of the two domain wall types is statistically equal in the system.

In the translation regime below the Walker breakdown the maximal value of the in-plane angle is

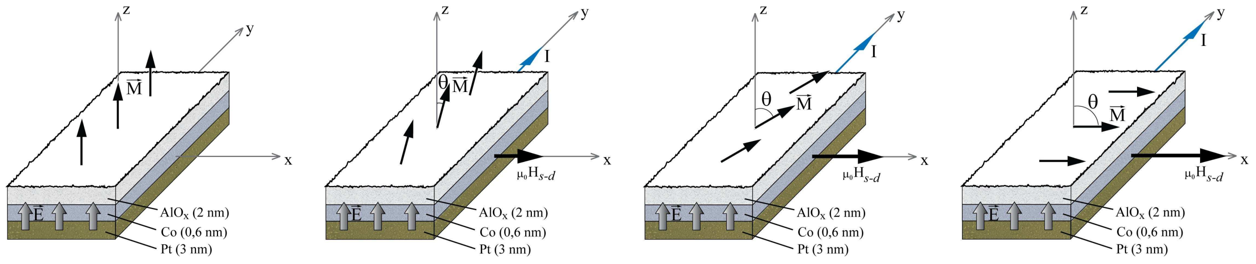

(a) (b) (c) (d)

Figure 5.7: Influence of the current density on the magnetization configuration in a uniformly magnetized wire. The magnetization canting angle $\theta \in < -\pi/2, \pi/2 >$ depends on the current density $\vec{j}$.

$\varphi = 45°$. This deformation is reversible, so when the current is switched off the $\varphi$ angle turns back to its initial position $\varphi = 0°$. When the current density exceeds the Walker breakdown the domain wall motion gets in the precessional motion regime. The angle $\varphi$ goes periodically from 0° to 360°. The structure of the domain wall changes accordingly: for $\varphi = 0°$ and $\varphi = 180°$ the wall is purely of Bloch type, with opposite chirality, while for $\varphi = 90°$ and $\varphi = 270°$ the wall becomes of purely Néel type. When the domain wall undergoes these transitions the velocity also periodically changes from a minimal value when the structure is purely of Bloch or Néel type.

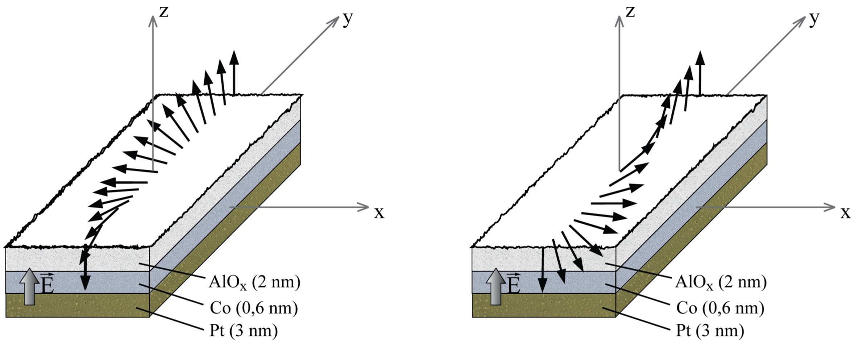

(a) (b)

Figure 5.8: Two possible Bloch domain wall chiralities: (a) Right-handed screw rotation. (b) Left-handed screw rotation.

Since the $H_{sd}$ field points in-plane, transverse to the wire axis, the domain wall will prefer the chirality where the magnetization is parallel to the $H_{sd}$ field. It follows that the $H_{sd}$ field lifts the chiral degeneracy. Then the corresponding energy for the two antiparallel cases is different: $E(\varphi = 90°) \neq E(\varphi = 270°)$ so the $H_{sd}$ field raises an additional potential barrier to the domain wall transformations and shifts the Walker breakdown limit to higher values. In other words, the effective transverse field $H_{sd}$ restrains the Bloch domain wall transformations and allows larger velocities to be obtained. This is a very interesting property of the domain wall dynamics where obtaining higher velocities is a very important issue.

Such a behaviour demonstrated by Miron *et al.* [76] is shown in Fig. 5.9. In order to prove the lifted chiral degeneracy, the initial domain wall chirality [either Fig. 5.8(a) or (b)] was initialized by an external in-plane magnetic field applied transverse to the wire. Then the domain wall was displaced by a fixed current density $j = 1.4 \times 10^{12}\,\mathrm{A/m^2}$ for different pulse lengths. This sequence was repeated 10 times in order to obtain a visible domain wall displacement. The displacement of the wall having initial chirality adjusted parallel to $H_{sd}$ field is shown in red. The displacement of the wall having opposite initial chirality to the effective transverse field $H_{sd}$ is shown in blue. Such a domain wall has to undergo one transition before it reaches the stable position parallel to $H_{sd}$. This transformation slows down the domain wall motion during the first transition and then it moves on without any transformations with the identical velocity. When the domain wall chirality is not defined by the external field, it is automatically 'selected' by the $H_{sd}$ field after the first pulse. Therefore, the displacements obtained in this case are identical to those obtained when the chirality was prepared parallel to the external field.

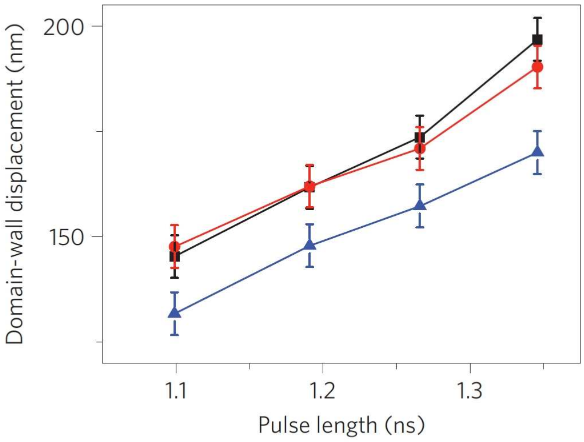

Figure 5.9: Domain wall displacement as a function of pulse length with a fixed current density $j = 1.4 \times 10^{12}\,\mathrm{A/m^2}$. The external transverse field of 1.3 kOe is applied in parallel to the $H_{sd}$ field (red), the applied field opposes the $H_{sd}$ field (blue), no external field is applied (black). [76]

We have shown the domain wall chirality selective-like character of the Rashba field. However, this is not the only influence of this field on the domain wall as it has also a direct impact on the shape of the Bloch wall. As soon as a current is passing through the wire, the wall is no longer a 180° Bloch domain wall. The domain wall shapes under the effect of different external transverse field ($\mu_0 H_{\mathrm{app}} < 0$) are schematically illustrated in Fig. 5.10(b),(c) and (d). As the current increases, the domain wall distortion gets more and more pronounced.

The corresponding spheres of magnetization for the given examples are shown in Fig. 5.10(d)-(f). The quantum $\hbar$ of angular momentum involved in this rotation must be conserved, and is consequently transferred to the magnetization within the wall. The electron is incoming with initial angular momentum $j_z = 1/2\hbar\cos\theta_{\mathrm{L}}$ which after passing through the domain wall changes to $j_z = 1/2\hbar\cos\theta_{\mathrm{R}}$. The total transferred angular momentum is then equal to $\Delta j = \hbar\sin\theta_{\mathrm{L}}$. However, the lowered amount of transferred angular momentum required for magnetization reversal is compensated by the lowered amount of incoming angular momentum. Therefore, by using hand-wavy arguments, this fact should not influence the domain wall mobility.

## 5.5 Extended Landau-Lifshitz-Gilbert equation

In order to include the effect of the Rashba field into the micromagnetic simulations, the Landau-Lifshitz-Gilbert equation (1.38) can be extended with the new term modifying solely the effective field term [58], so the equation reads

$$\frac{\partial\vec{M}}{\partial t} = -\gamma\vec{M}\times\mu_0\left(\vec{H}_{\mathrm{eff}}+\vec{H}_{\mathrm{R}}\right)+\frac{\alpha}{M_s}\left(\vec{M}\times\frac{\partial\vec{M}}{\partial t}\right)-\left(\vec{u}\cdot\vec{\nabla}\right)\vec{M}+\frac{\beta}{M_{\mathrm{s}}}\vec{M}\times\left[\left(\vec{u}\cdot\vec{\nabla}\right)\vec{M}\right], \qquad (5.1)$$

where $\mu_0\vec{H}_{\mathrm{R}}$ is the Rashba field.

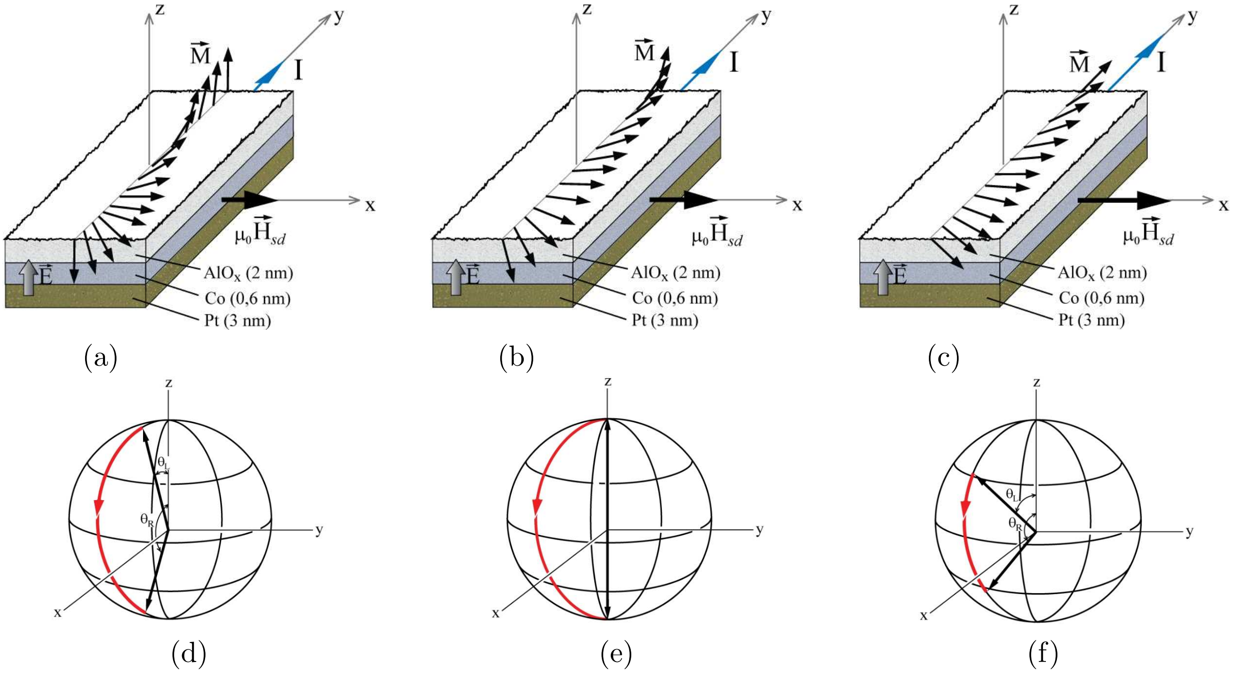

Figure 5.10: (a)-(c) Schematic domain wall shape under the influence of $H_{sd}$ field of different amplitudes. (d)-(f) Corresponding path of magnetization in the domain wall. $\theta_\mathrm{L}$ and $\theta_\mathrm{R}$ represent tilt of the left and right domain respectively.

# Chapter 6

# Domain wall dynamics in Pt\Co\AlO$_x$ under a transverse magnetic field

In the previous Chapter we have shown the principles of current-induced domain wall motion in the Pt\Co\AlO$_x$ system. Due to the Rashba field arising from the lacking symmetry, an effective magnetic $H_{sd}$ field acts as a transverse magnetic field and is expected to have a strong influence on the current-induced domain wall dynamics. This behaviour logically arises a question: 'How is the magnetization dynamics influenced by an additional external magnetic field, applied parallel or antiparallel to the effective transverse field $H_{sd}$?'. In this chapter we will demonstrate the impact of such an additional external magnetic field. One can expect that such a field can enhance or compensate the effect of the intrinsic magnetic field, depending on the mutual magnetic field orientation (parallel or antiparallel) and its amplitude.

In this chapter I will describe the sample preparation for current-induced domain wall experiments, the experimental techniques, the difficulties of the experiment realization and the obtained results.

## 6.1 Experimental setup

The films were prepared at Spintec by the procedure described in Section 5.2. The films were deposited on a silicon substrate with a 500 nm thick thermally oxidized SiO$_2$ layer, preventing the electric current leakage to the substrate. The Pt(3 nm)\Co(0.6 nm)\AlO$_x$(2 nm) multilayer was prepared by sputtering technique at a base pressure of $3.10^{-8}$ mbar. The AlO$_x$ layer was prepared by plasma oxidation. This oxide layer provides sufficient protection from the parasitic cobalt oxidation so no additional capping layer is needed. The absence of the capping layer makes the cobalt layer more easily observable by the Kerr microscopy. The sample was not annealed, except of resist annealing process (120°C) during the lithography procedure. The magnetic properties of the film measured by extraordinary Hall effect are shown in Fig. 6.1. The measured coercive field is $\mu_0 H_\mathrm{c} = 2.1\,\mathrm{mT}$ and the anisotropy field is $\mu_0 H_\mathrm{K} = 710\,\mathrm{mT}$.

The sample was consequently patterned by the combination of electron beam lithography and wet and ion beam etching by the procedure illustrated in Fig. 6.2. A titanium mask (15 nm) consisting of twenty identical wires was created by e-beam lithography (NANOFAB facility). The chosen width of the wires is 500 nm, which is slightly above the optical resolution limit of the Kerr microscope (~300 nm-500 nm). The wire repetition period is 2.5 $\mu$m so all twenty wires fit in the microscope field of view. For the current injection we use a voltage source which can operate up to 16 V. The maximum possible applicable current is then limited by the sample resistance. In principle, the shorter the wires, the lower the resistance, so the wire length is minimized. However, in order to observe the domain wall displacement, the wires have to be reasonably long. The chosen length of the wires is 10 $\mu$m. The wires are terminated by triangles [Fig. 6.2(b)].

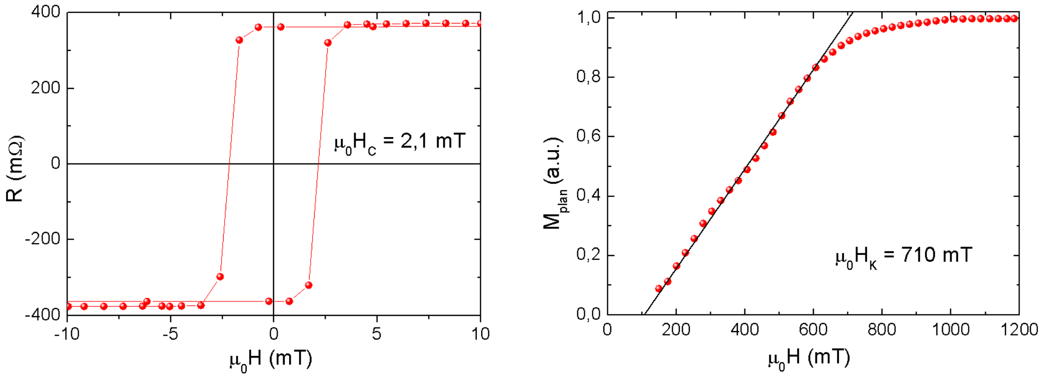

(a) (b)

Figure 6.1: (a) Extraordinary Hall effect measurement of the $M_z$ component as a function of out-of-plane field. The measured coercive field is $\mu_0 H_\text{c}$=2.1 mT. (b) In plane component of the magnetization as a function of in-plane field. The measured anisotropy field is $\mu_0 H_\text{k}$=710 mT.

In the next step, the sample was etched in a diluted solution of $H_3PO_4$ which with the ultrasound vibrations leads to the aluminium oxide removal. The magnetic properties of the cobalt layer hidden under the titanium mask are retained due to the fact that the acid does not underetch the mask. On the other hand, the bare ultrathin cobalt layer oxidizes and loses its ferromagnetic behaviour [Fig. 6.2(c)].

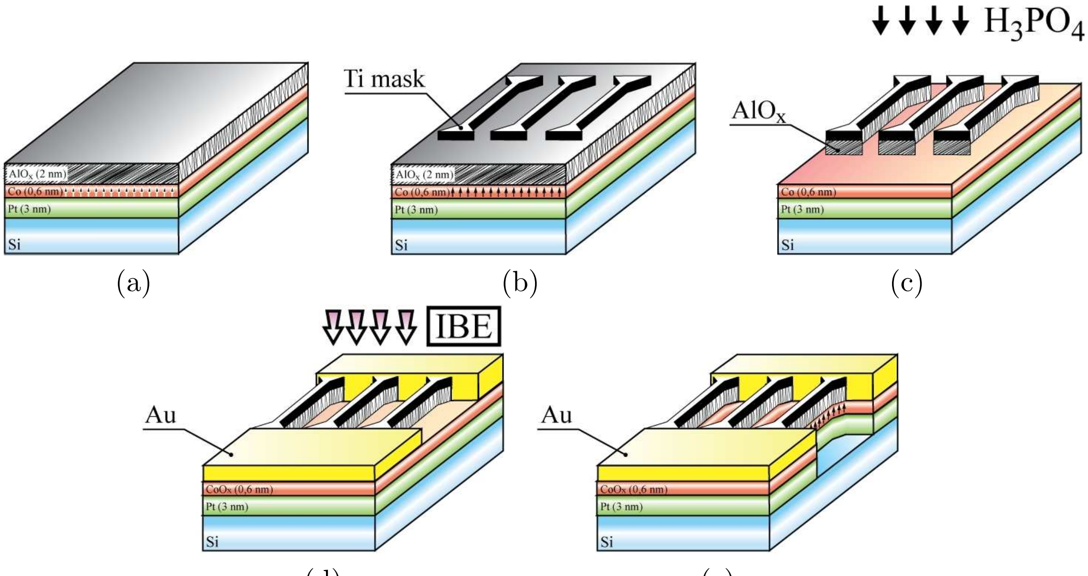

(a) (b) (c)

(d) (e)

Figure 6.2: Illustration of the film patterning.

The Ti(3 nm)\Au(20 nm)\Ti(10 nm) electrodes are created in the second step of e-beam lithography in such a way that they are partially covering the terminal triangles [Fig. 6.2(d)]. The sample is then etched by ion beam milling together with a Ti reference sample ($\sim 2-5$ nm thinner than the Ti mask) which allows us to make sure that the magnetic trilayer in the wires remains untouched. The residual thin layer of titanium oxidizes and becomes optically more transparent and electrically insulating [Fig. 6.2(e)]. The SEM image of the final structure is shown in Fig. 6.4.

Here we justify the 2$\mu$m interwire separating distance. Fig. 6.3(a) shows the calculated map of the $y$-component of the induced Oersted field in the case of three wires separated by $2\mu$m gap. The arrows indicate the direction and magnitude of the vectorial magnetic field. The current density in each of the wires is $1 \times 10^{12}$ A/m$^2$. Fig. 6.3(b) compares the profiles of the vertical field component in the plane of the wire in the case of the three wires [compatible with Fig. 6.3(a)] and in the case of one single wire with the same current density. The Oersted field distribution within the wire (dotted lines) is very similar for both cases, so we can conclude that the distance between the wires excludes the mutual Oersted field influence. Moreover, interaction between magnetic domain walls is typically observed on a $10^2$ nm scale [133], so the $2\,\mu$m interwire separation used here also excludes the mutual domain wall stray field interaction.

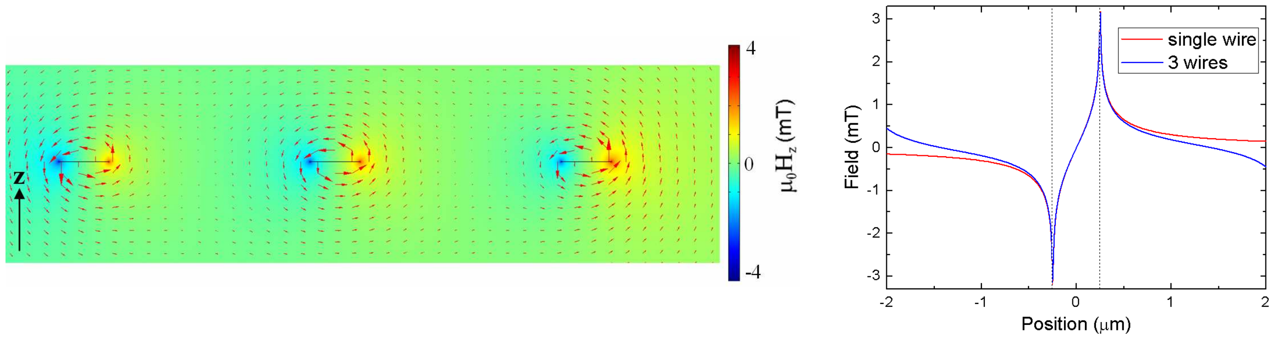

(a) (b)

Figure 6.3: (a) Calculated distribution of the perpendicular component of the magnetic field. The arrows indicate the direction and magnitude of the vectorial magnetic field. The current density in the three wires is $1 \times 10^{12}$ A/m$^2$. (b) Comparison of the distribution of the perpendicular magnetic field component in the wire plane for the three wires (blue) and for one single wire (red). The considered wire dimensions are $500 \times 3\,\mathrm{nm}^2$.

Our voltage source is an ultrafast pulse generator which provides dipolar pulses in the time span of 0.5 ns -10 ns and with voltage amplitudes up to 16 V. The current passes first through the sample (~220 Ω) which is microbonded to a 50 Ω impedance-adapted sample holder, and then to the oscilloscope which is used to monitor the voltage (current) amplitude and the pulse shape. The 50 Ω impedance matching in the circuit is important for minimizing the reflections back to the voltage source. The pulse source can be externally triggered, which allows us to apply a series of pulses with different repetition times. This is especially important for low current density regimes where the domain wall velocity is very low. In this case, even after the longest possible pulse (10 ns) the displacement is too short to be detected with the microscope resolution so a number of pulses has to be applied.

Two different coils are used in our experimental setup. The first electromagnet is installed below the sample, providing a magnetic field perpendicular to the sample surface which is capable of saturating the sample magnetization. This coil has no magnetic core in order to avoid influencing the magnetic field produced by the second coil. The second coil is used to apply a dc magnetic field up to ~220 mT in the plane of the sample, transverse to the wire.

An extremely important point is the in-plane character of the transverse field. We will show hereafter the measurement of the out-of plane field component.

## 6.2 Domain wall injection process

A very helpful property for the current-induced domain wall motion studies is the reproducible domain wall injection into the wires. There are several possibilities to create a domain wall in the wire but only

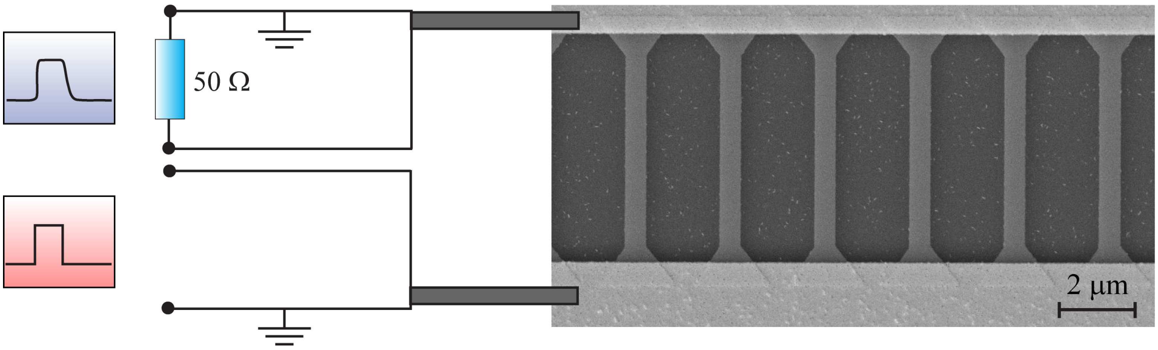

Figure 6.4: SEM picture of the sample with magnetic 500 nm wide wires which are connected to the same two Au pads. The sample is micro-bonded to a 50 Ω impedance adapted sample holder. The current will then simultaneously push the domain walls in all twenty wires providing robust statistics of the domain wall displacement.

few of them are reproducible. The recipe for reproducible domain wall injection helps to effectively re-initiate the experiment and to collect robust statistics of the motion. Here we will describe the technique used in our experiments.

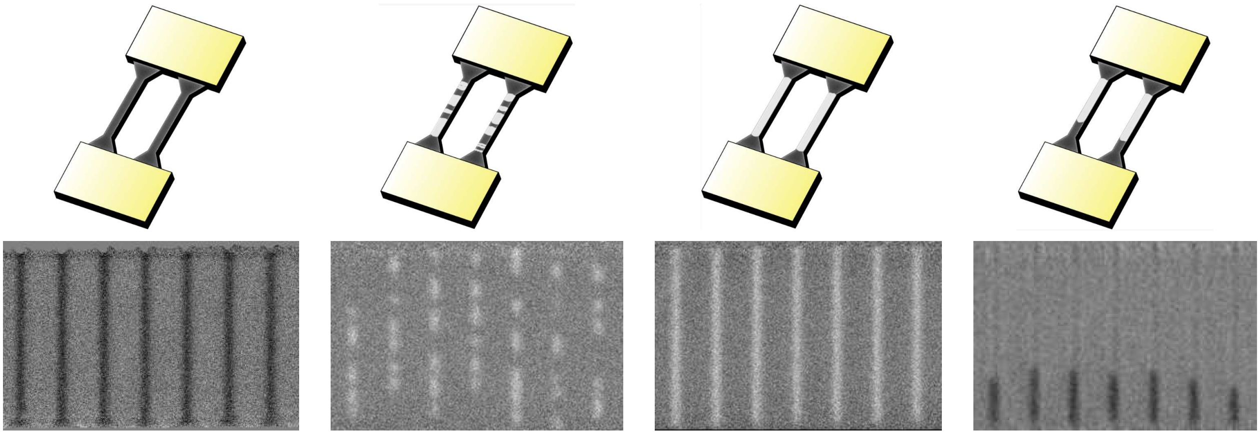
(a) (b) (c) (d)

Figure 6.5: Domain wall injection process: (a) The sample is fully saturated by an external magnetic field. (b) Domains are nucleated by a high density current pulse which is able to sufficiently heat up the narrow part of the wires. (c) The narrow part of the wires is saturated by an external magnetic field with the opposite polarity. The domain wall cannot expand into the triangular part due to the additional domain wall energy cost. (d) The domain walls are injected into the wires by a short current pulse.

At the beginning the magnetic structure is saturated by a strong positive (or negative) magnetic field [Fig. 6.5(a)]. In the second step, a high current density pulse is passed through the wires. If the pulse is sufficiently strong and long, the pulse leads to the nucleation of reversed domains in the wires. On the other hand, if the pulse length and amplitude are well adjusted, the power is not sufficient to heat the triangular regions, due to the larger cross-section. Hence, the triangular region at the ends of the wires stays uniformly magnetized and the regions with reversed magnetization are created only in the narrow wires [Fig. 6.5(b)]. Consequently we apply a small negative (or positive) magnetic field. This field leads to the expansion of the nucleated domains. Due to the additional cost of the domain wall energy in the wide triangular regions, the domain walls can propagate only until the beginning of the triangular part. The domain wall cannot expand further if the field is not high enough [see equation (1.14)]. The domain walls stay pinned at these 'corners' when the field is turned off [Fig. 6.5(c)]. If we use such a domain wall position as the initial state, the domain wall velocity distribution can be influenced by the pinning at the corners. That is why as a last step we apply a small current pulse in order to inject the domain walls into the wires and start the experiment [Fig. 6.5(d)].

## 6.3 Measure of the effective transverse magnetic field

We will show here that the strength of the effective transverse magnetic field can be obtained indirectly from a measure of the nucleation probability of reversed magnetic domains.

In our measurement the current density amplitude is fixed ($J = 1.2 \times 10^{12}$ A/m$^2$) and therefore also the amplitude of the effective transverse field. As already said, this field causes the magnetization to cant in the direction transverse to the nanostripes, as shown in Fig. 6.6(a). When an external magnetic field $\mu_0 H_{\mathrm{app}}$ is applied parallel to the effective transverse magnetic field, this helps the magnetization to turn towards the effective transverse magnetic field direction $\rightarrow \theta = \pi/2$ [Fig. 6.6(b)]. On the other hand, a field applied opposite to the effective transverse field helps the magnetization to turn back towards the out-of-plane direction. In the extreme case when the external magnetic field and the effective transverse magnetic field have the same amplitude and are antiparallel, i.e. $\mu_0 H_{\mathrm{app}} = -\mu_0 H_{sd}$, then the two torques exerted on the magnetization cancel out and the magnetization stays perpendicular to the plane [$\theta = 0$ - Fig. 6.6(c)]. In principle, the effective strength of the $H_{sd}$ field can thus be determined measuring this compensation field.

In order to detect this compensation field a method based on the reversed domain nucleation probability was used. Let us first consider a simple system with no symmetry breaking. The magnetization reversal can be described by the Stoner-Wohlfarth theory which is based on the Brown's equations mentioned in Chapter 1. This simplest situation can be described by the black curve in Fig. 6.6(d). The black dot represents the initial state of the system $\theta = 0$ corresponding to the magnetization pointing 'up'.

In order to reverse the magnetization to the second, energetically equivalent, state $\varphi = \pi$ by the nucleation of reversed domains, an energy barrier centered at $\theta = \pi/2$ has to be overcome. There are several ways to do this (applying an antiparallel magnetic field, a spin-polarized current, etc.) but our objective here is to study thermally-assisted reversal. According to the Arrhenius law, the probability to overcome the energy barrier decreases with increasing temperature, and the barrier is canceled when $\Delta E \simeq k_{\mathrm{B}} T$. In our case the temperature is increased by Joule effect by applying a current pulse. This was already illustrated in the case of $\mathrm{Gd}_{1-x}\mathrm{Co}_x$ nanowires and the calculated time evolution of the temperature was shown in Fig. 4.13.

The energy landscape changes in an asymmetric structure, in which during the application of a current pulse an effective transverse field acts on the magnetization [Fig. 6.6(d)]. In the absence of an external magnetic field, the magnetization tilts by an angle $\theta$ which depends on the $H_{sd}$ field amplitude (green line). The energy barrier is therefore reduced with respect to the symmetric case and the probability to nucleate reversed domains therefore increases. The energy barrier farther decreases when the external field is applied parallel to $H_{sd}$ while it increases when the external field is antiparallel to $H_{sd}$. When the external magnetic field compensates $H_{sd}$ field the magnetization stays perpendicular to the plane and the energy barrier has the maximum value (black line), equivalent to that of the symmetric structure. In the other extreme case, when the total magnetic field ($\mu_0 H_{\mathrm{app}} + \mu_0 H_{\mathrm{sd}}$) acting on the magnetization reaches the anisotropy field value, the barrier is canceled and the probability to nucleate reversed domains is maximum [red curve in Fig. 6.6(d)]. This position becomes metastable when the current pulse is over and the wire becomes demagnetized (zero remanence). To summarize, the probability to nucleate reversed domains depends on the strength and direction of the

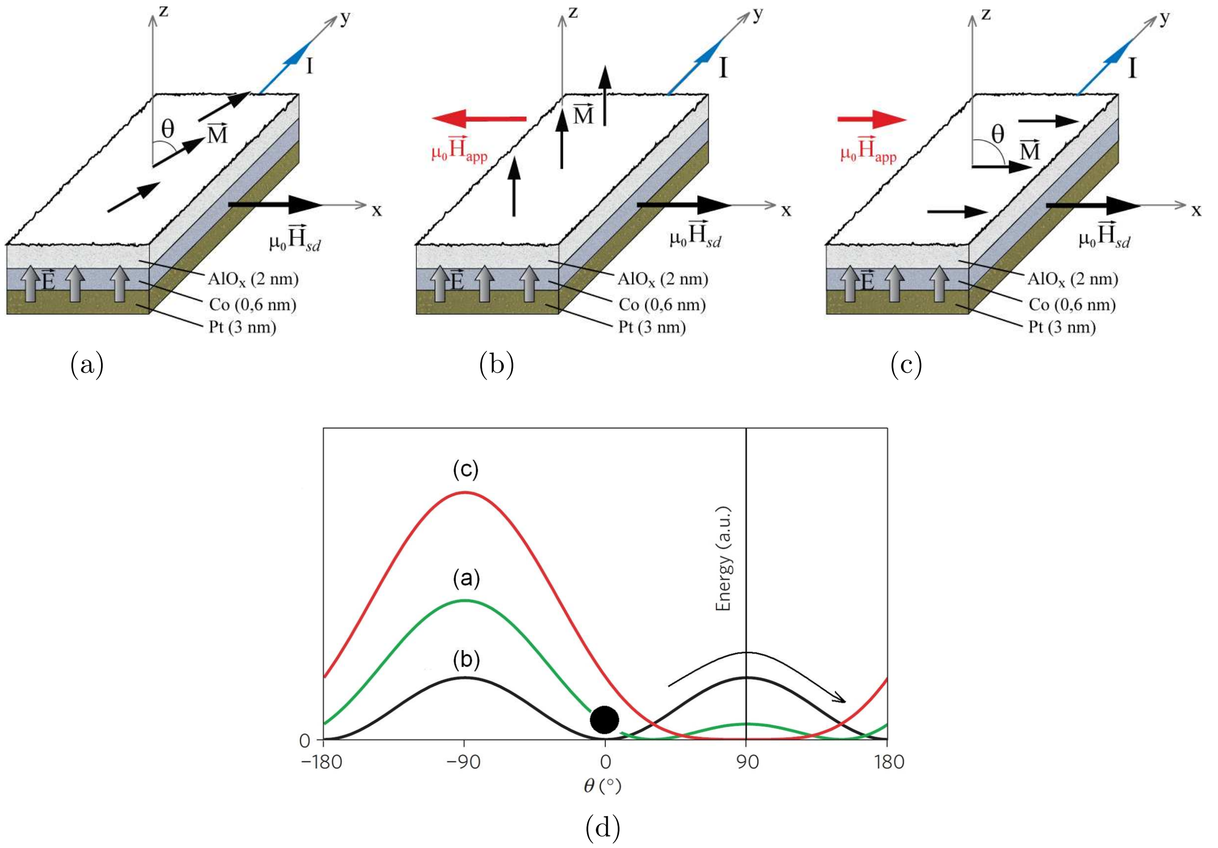

Figure 6.6: (a) Rashba field induced magnetization canting in the absence of external magnetic field. (b) The magnetization canting can be cancelled out by applying an external field antiparallel to the $H_{sd}$ field direction when $\mu_0 H_{\text{app}} = -\mu_0 H_{\text{sd}}$. (c) The external field which is applied parallel to $H_{sd}$ field can cause the tilt of the magnetization into the wire plane when $\mu_0 H_{\text{app}} + \mu_0 H_{\text{sd}} \geq \mu_0 H_{\text{k}}$ where $H_{\text{k}}$ is the anisotropy field. (d) Energy landscape for the case (a) shown by green curve, (b) shown in black and (c) shown by red curve. [130]

total (effective plus external) transverse magnetic field.

Let us see how we proceed experimentally to nucleate the reversed domains. The magnetization of the sample is first saturated (up or down) and starting from short pulses of amplitude $j = 1.2 \times 10^{12}\,\text{A/m}^2$ the pulse duration (i.e. the temperature of the system) is gradually increased until nucleation is observed. Due to the stochastic character of the nucleation barriers, reversed domains do not appear at the same time (i.e. for the same pulse length) in the different wires.

We define as the nucleation threshold, which will be characterized here by a defined applied pulse length, the state for which nucleated domains are observed in 50% of the twenty parallel wires. Such process is repeated for several values of the external transverse magnetic field (ranging between from -220 mT up to +220 mT) oriented parallel and antiparallel to the effective transverse field. The data are shown in Fig. 6.7. From the previous discussion follows that the shorter the current pulse needed to reach nucleation, the smaller the nucleation energy barrier, and therefore the larger the nucleation probability.

In order to exclude the influence a remaining out-of-plane magnetic field component, the nucleation probability was measured for all possible symmetries, as indicated in the inset of Fig. 6.7. Note in fact that the nucleation probability is sensitive to any out-of-plane field component, so any small deviation from the field direction calibration would induce significant deviations between the nucleation probabilities for the two $M_+$ or $M_-$ initial magnetization states. The small discrepancies between the

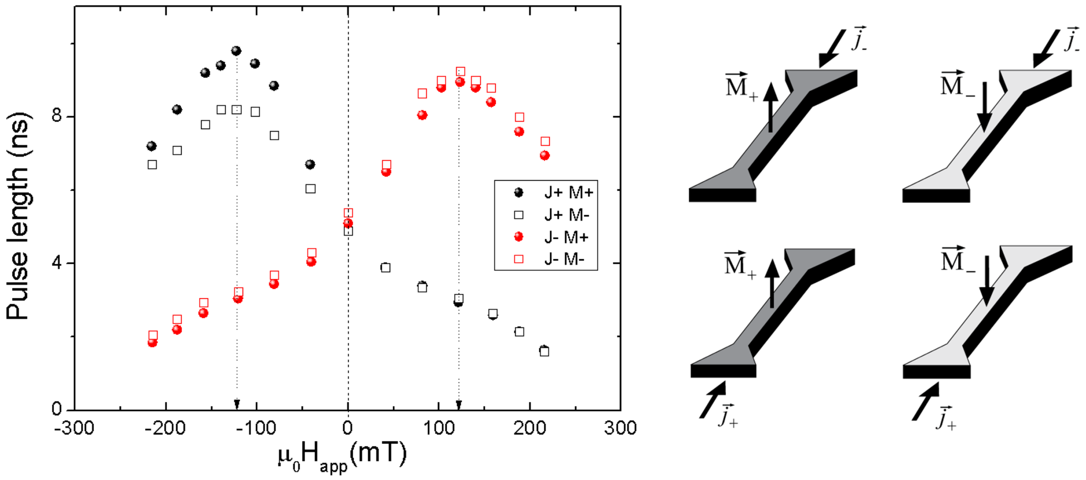

Figure 6.7: Graph of the pulse lengths for which nucleation of reversed domains takes place in 50% of the wires, as a function of the external transverse magnetic field. The fixed value of the current density is $j = 1.2 \times 10^{12}$ A/m$^2$. The red squares (black squares) give the nucleation threshold for the positive (negative) current pulse, while the filled and empty squares correspond to the two opposite initial magnetization states.

four measured configurations indicate that the out-of-plane component of the field is negligible.

The longest current pulse, corresponding to the minimum of the nucleation probability, was found in all cases for $\mu_0 H_{\mathrm{app}} = 122\,\mathrm{mT}$. This is the condition for which the external transverse field has the same amplitude as the effective transverse magnetic field and is opposed to this field. Since the magnitude of the current density is known ( $j = 1.2 \times 10^{12}$ A/m$^2$) our measurement therefore allows us to access to the strength of the effective transverse field $H_{sd}$:

$$\boxed{\mu_0 H_{sd}/j = 100\,\mathrm{mT}/(10^{12}\mathrm{A/m^2})} \tag{6.1}$$

Fig. 6.8(a) shows the results of the same experiment carried out for several current density values within the range $1 \times 10^{12}$ A/m$^{12}$-$1.67 \times 10^{12}$ A/m$^{12}$. As expected, for the same positive or negative external field the nucleation probability increases as the current density increases. This is due to the fact that the effective transverse field is proportional to J. Note that for the lowest current density values we were not able to heat up the wire sufficiently to induce domain nucleation ($j \leq 1.2\,\mathrm{A/m}^{12}$) due to the fact that the maximum available pulse length is 10 ns. The value of the external field corresponding to the minimum nucleation probability increases as the density increases, as shown in Fig. 6.8(b). The fit of such data gives the variation of the effective transverse field strength as a function of current density:

$$\boxed{\mu_0 H_{sd}/j = 90 \pm 5\,\mathrm{mT}/(10^{12}\mathrm{A/m^2})} \tag{6.2}$$

The results based either on a single current-density measurement or multiple current-density measurements, lead to similar results.

The behaviour of the nucleation probability vs. applied field allow of course to deduce not only the strength but also the direction of the in-plane effective transverse field $H_{sd}$. The direction of $H_{sd}$ field is predicted to be given by the equation:

$$\vec{H}_{\mathrm{sd}} \sim \alpha_{\mathrm{R}} \left( \vec{e}_z \times \vec{k} \right)$$

where $\alpha_{\mathrm{R}}$ is a parameter depending on the spin-orbit coupling. This parameter can take a positive or negative value, depending on the spin-orbit interaction and the spin polarization of the current.

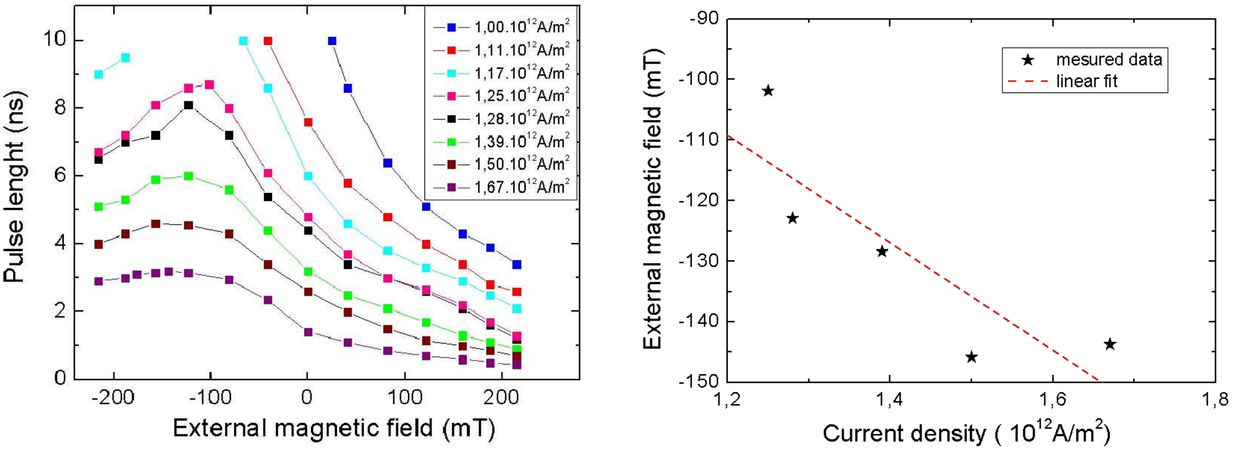

(a) (b)

Figure 6.8: (a) Graph of the pulse lengths for which nucleation of reversed domains takes place in 50% of the wires, as a function of external transverse magnetic field for various current densities. (b) Extracted $H_{sd}$ field value as a function of the current density (stars). The linear fit (red dashed line) corresponds to $\mu_0 H_{sd}/j = 90 \pm 5\,\mathrm{mT}/(10^{12}\mathrm{A/m}^2)$.

Without the knowledge of the exact character of the spin-orbit interaction and of the spin polarization of the material, this equation cannot predict the direction of the electric field inside the trilayer.

Note that effect of the Rashba field on current-induced domain wall motion was also recently studied by Suzuki *et al.* [77] for Ta\CoFeB\MgO nanowires. The authors find that the Rashba field has the opposite direction with respect to the one presented here. The difference found between the two systems may be caused by opposite electric field directions or by opposite $s-d$ exchange coupling. Finding out which term plays the major role is beyond the scope of this work.

## 6.4 Current-induced domain wall motion

The effect of spin polarized current on the domain wall motion in Pt\Co\AlO$_x$ has been already described in several publications by Miron *et al.* [58], [75], [130], [76]. A key element of the domain wall dynamics, as already anticipated in Chapter 5, is the presence of the effective transverse magnetic field associated with the current passing through the wire. The strength of the total transverse magnetic field acting on the magnetization can be tuned by applying an external magnetic field of varying amplitude. In this section we will experimentally demonstrate the impact of the transverse field on the domain wall velocity.

The domain walls are injected into the wires by the procedure described in Section 6.2. The domain wall velocity is always measured in a given range of current densities for three different pulse lengths. The upper limit of the pulse length is given by the appearance of the nucleation due to Joule heating or by the limit of the voltage source. The bottom limit is given by the rise time because for pulses shorter than $\sim 0.4$ ns the current density does not reach the 'plateau' value. Each pulse is repeated several times with 1 MHz frequency in order to displace the domain wall by a resolvable distance. This allows us to overcome limitations of spatial resolution for the small displacements. Fig. 6.9(a) shows the three shortest pulses used in the experiment for $J = 1.64 \times 10^{12}$ A/m$^2$. The pulse length is defined as the full width at half maximum. Fig. 6.9(b)-(d) shows corresponding examples of the domain wall displacement induced by the application of 30 pulses of 0.8 ns, 0.94 ns and 1.01 ns length.

In order to extract domain wall velocities, the images are processed in LabView environment. Every image is considered as a matrix and every wire is represented by approximately (200x10) pixels

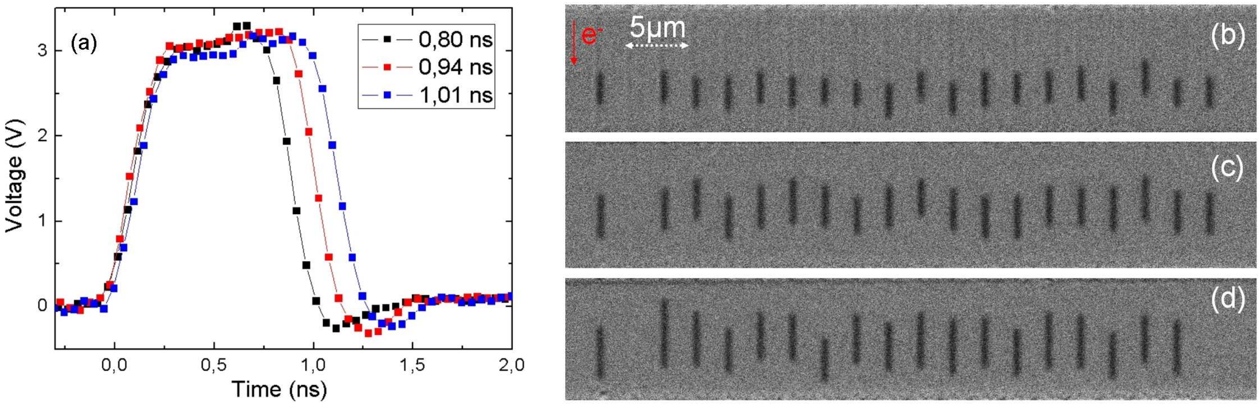

Figure 6.9: (a) Example of three current pulses of nominal length 0.30 ns, 0.35 ns, 0.40 ns. The measured half-width corresponds to 0.80 ns, 0.94 ns, 1.01 ns. (b)-(d) Differential Kerr microscope image corresponding to domain wall displacement induced by 30 pulses of lengths: (a) 0.8 ns, (b) 0.94 ns, (c) 1.01 ns with $J = 1.64 \pm 0.04 \times 10^{12}\,\mathrm{A/m^2}$.

as is schematically shown in Fig. 6.10. The wire contrast can be reduced to one dimensional graph as it is depicted in the inset of Fig. 6.10. The displacement can be measured simultaneously in the twenty wires, so that one Kerr image can provide up to twenty measurements.

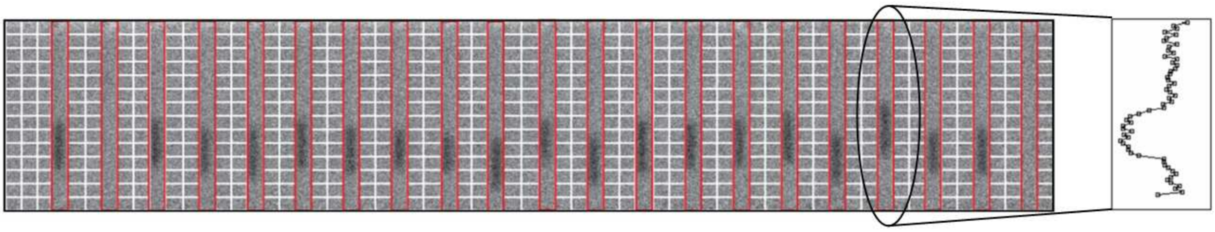

Figure 6.10: Illustration of the mathematical image processing. The domain wall displacement in each wire is obtained from the horizontal averaging of 10 pixels of the measured contrast.

Each pulse sequence was repeated three times, so each point is obtained from statistics up to 60 (3x20) displacements. Domain wall displacement as a function of pulse length, corresponding to the pulses illustrated in Fig. 6.9(b), is shown in Fig. 6.11. The velocity corresponds to the slope of the fitted linear dependence. This recipe was repeated for different current densities and for different values of the external transverse field.

However, this method has also some drawbacks. The results shown in Section 6.3 clearly show that by increasing the length of the current pulse within the range 2-10 ns, we can considerably change the temperature of the wire. Every domain wall displacement, used to define the domain wall velocity presented in Fig. 6.11, is measured for different pulse lengths and therefore inherently for different temperatures. The domain wall reaches more easily the flow regime with longer pulses, due to the thermal excitations $\sim k_{\mathrm{B}}T$.

In order to demonstrate this behaviour we have measured the domain wall velocity for two different sets of displacements. The maximum pulse length which can be used for domain wall displacement is limited by the nucleation of reversed domains. This is indicated by blue stars in Fig. 6.12(a). The domain wall displacement is always measured for three different pulse lengths below this nucleation limit. The red crosses in Fig. 6.12(a) indicate the used pulse lengths. The choice of the set of pulse

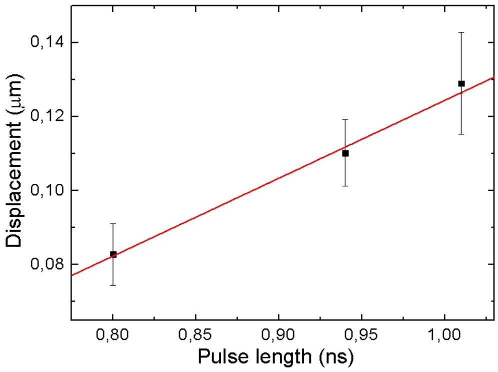

Figure 6.11: Domain wall displacement as a function of pulse length of $J = 1.64 \pm 0.04 \times 10^{12}\,\mathrm{A/m^2}$, obtained from the statistics of 60 measurements.

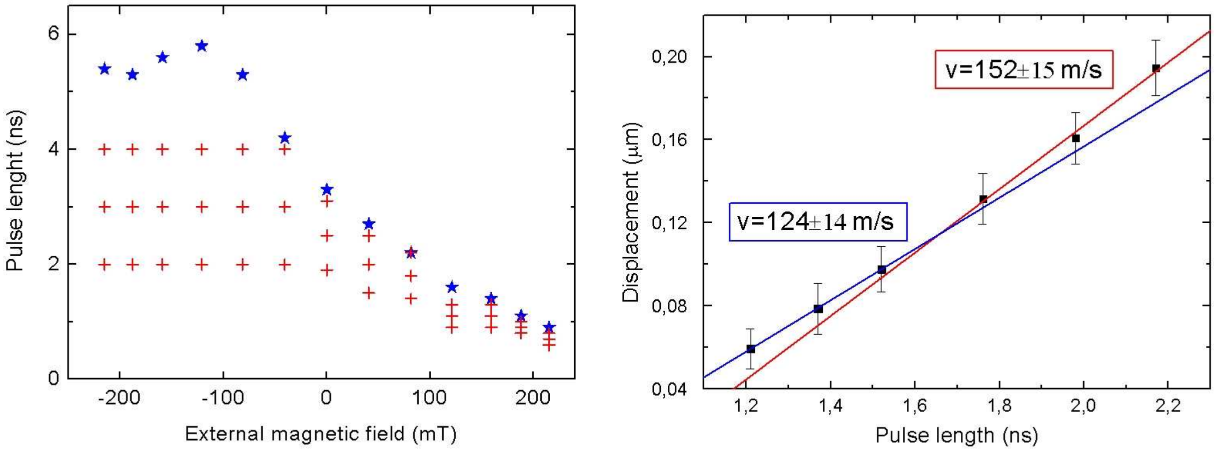

(a) b

Figure 6.12: (a) Pulse lengths $\Delta t_\mathrm{N}$ needed to reach the nucleation limit for $J = 1.39 \times 10^{12}\,\mathrm{A/m^2}$ at zero external transverse magnetic field (blue stars). The red crosses depict the pulse lengths used for domain wall velocity determination. (b) Measured domain wall velocities for two different sets of pulse lengths (1.21 ns, 1.37 ns, 1.52 ns and 1.76 ns, 1.98 ns, 2.17 ns). The domain wall velocity for the short pulses (blue) $v = 124 \pm 14\,\mathrm{m/s}$ and for the long pulses (red) $v = 152 \pm 15\,\mathrm{m/s}$.

lengths influences the measured velocity. This is demonstrated in Fig. 6.12(b) which shows the two different sets of displacements for two sets of pulse lengths. The determined velocity is about ten percent lower for the shorter pulses. This is caused by the difference in the wire temperature. The longer pulse heats the wire more so the domain wall is able to overcome more easily the pinning potential.

The fact that we are forced to use shorter pulses in the case of fields which are applied parallel to the Rashba field, influences the determined domain wall velocity, which is slightly underestimated in comparison to the case with antiparallel transverse field.

The obtained domain wall velocities as a function of current density for several amplitudes of external transverse magnetic field are shown in Fig. 6.13. The vertical error bars are calculated as the error of the linear regression. The velocity dependence in the absence of the external field is shown in violet colour.

The domain wall dynamics strongly depends on the amplitude of the external transverse field.

Without the applied transverse field, the domain wall velocities are similar to those obtained by Miron *et al.* [76] which were shown in Fig. 5.4. It is clear that, even for the highest current densities, the domain wall mobility does not enter the flow regime. It follows from [76], that the current density $J = 2 \times 10^{12}\ \mathrm{A/m^2}$ corresponds to the frontier between creep and flow regime. The dotted violet line represents domain wall mobility obtained by Miron *et al.* [76].

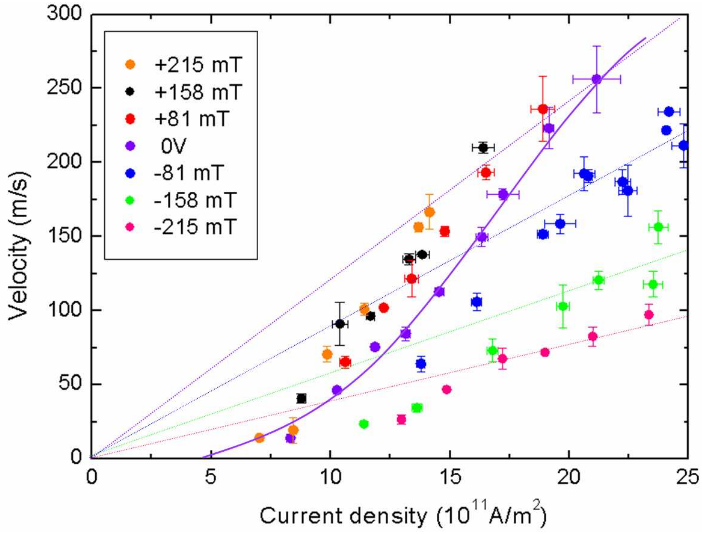

Figure 6.13: Domain wall velocity as a function of current density for corresponding external transverse field. Positive and negative fields, correspond to fields which are parallel and antiparallel to $H_{sd}$ field respectively. The violet line is a guide to the eye of the zero external field dependence, which constitutes the border between parallel and antiparallel field. The dotted line corresponds to the domain wall mobility obtained by Miron *et al.* [76].

When the external magnetic field is applied parallel to the $H_{sd}$ field, i.e. $\vec{H}_{\mathrm{app}} \parallel \vec{H}_{\mathrm{sd}}$, the domain velocities appear to increase with respect to the $H_{\mathrm{app}} = 0$. Note however, that the domain wall dynamics studied in the range of current densities used in this experiment, does not allow to reach the flow regime. Hence the observed domain wall dynamics is still in the creep regime. In these conditions it is difficult to extract a quantitative information from these results.

For negative values of the applied transverse field, where $\vec{H}_{\mathrm{app}}$ is antiparallel to $\vec{H}_{\mathrm{sd}}$, the domain wall velocities appear to significantly decrease with respect to the $H_{\mathrm{app}} = 0$. The depinning currents also appear to decrease in this case, so the domain wall mobility saturates and the domain wall dynamics enters the flow regime.

The domain wall mobility $\mu$ as a function of external magnetic field is shown in Fig. 6.14. The black line corresponds to the linear fit. The mobility dependence then writes:

$$\boxed{\frac{\mu}{\mu_0 H_{\mathrm{app}}} = 38 \pm 2 \frac{\frac{\mathrm{m}}{\mathrm{s}}}{10^{12}\frac{\mathrm{A}}{\mathrm{m}^2}\mathrm{T}}} \tag{6.3}$$

which is found for $H_{\mathrm{app}} \leq 0$. The domain wall mobility for the parallel magnetic field cannot be determined since the flow regime is not reached.

## 6.5 Discussion

Recently, Miron [134]*et al.* have studied the effect of a longitudinal field on the magnetization reversal in Pt\Co\AlO$_x$ trilayers. The magnetization reversal was investigated in a $500 \times 500\,\mathrm{nm}^2$ dot shown

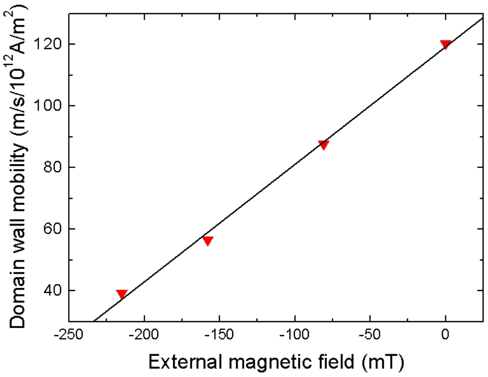

Figure 6.14: Domain wall mobility as a function of external field applied antiparallel to the Rashba field . The black line corresponds to the linear fit characterized by equation (6.3).

in Fig. 6.15(a). The bottom Pt layer was etched into a cross-shaped structure for current injection and Hall voltage measurements allowed to identify the perpendicular magnetization $M_z$ of the dot.

The outstanding result of their study is presented in Fig. 6.15(b). First, the magnetization reversal was observed during a single sweep of the magnetic field applied parallel to the current injection line, with a small tilt to the $z$ direction ($\theta = 92°$, $\phi = 0°$). The magnetization is thus reversed due to the residual component of the magnetic field in the $z$ direction. The magnetization reverses at $\mu_0 H_c = 300\,\text{mT}$. This experiment was repeated but the field sweep was stopped for each value of magnetic field and a positive current pulse (black squares) and negative current pulse (red circles) were injected. $M_z$ was measured after each pulse application. Surprisingly, the injected current pulse of $I_p = 2.6\,\text{mA}$ leads to magnetization reversal down to $\mu_0 H_c \sim 5\,\text{mT}$. This magnetization switching cannot be explained by considering only the in-plane Rashba field, the Oersted field or the Joule effect since all the mentioned effects would lead to a demagnetized state.

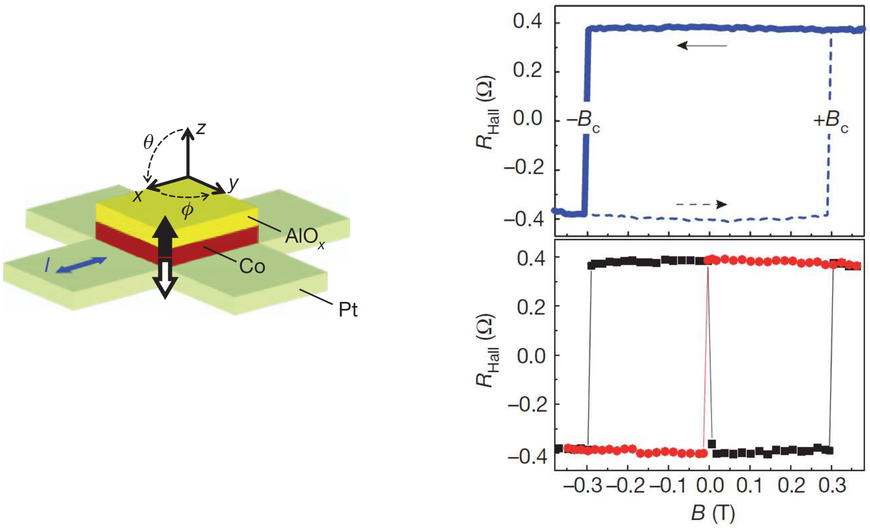

(a) (b)

Figure 6.15: (a) Hall cross geometry with black and white arrows indicating the 'up' and 'down' equilibrium magnetization states. (b) $M_z$ component measured by extraordinary Hall effect in the absence of current with longitudinal magnetic field $\theta = 92°$ (upper graph) and in the case of applied electric pulses of $I_p = 2.6\,\text{mA}$. [134]

After a systematical investigation of the reversal process, the authors attributed the observed reversal to the existence of an additional magnetic field in the $z$ direction:

$$\vec{B}_{sz} \sim \vec{B}_R \times \vec{B} \sim \left(\hat{z} \times \vec{j}\right) \times \vec{B}, \tag{6.4}$$

where $\vec{B}_R$ is the Rashba field. This magnetic field thus reverses sign either by reversing the magnetic field $\vec{B}$ or the electric current $\vec{j}$. As already said above, in a ferromagnet the external field $\vec{B}$ has no direct impact on the conduction electrons. This action is mediated via the internal exchange field produced by the local magnetization $\vec{M}$. Therefore $B_{Sz}$ should be considered as the perpendicular component of an effective magnetic field, where the orientation of $\vec{M}$ is initially determined by $\vec{B}$:

$$\vec{B}_{sz} \sim \vec{B}_R \times \vec{M}. \tag{6.5}$$

Although there is no theory predicting the magnetization reversal in such a geometry, the authors offer two possible phenomena responsible for the spin accumulation in the $z$ direction:

1) A similar effect was observed in InGaAs heterostructures [135], where a magnetic field applied parallel to the electric current induces a spin polarization component perpendicular to the plane of the current. This phenomenon has been explained by the action of the Rashba field and spin-dependent electron mobility induced by impurity scattering and non-parabolic electron band dispersion [136].

2) Thin Pt layers are known for giving rise to a high spin Hall effect [137]. The spin Hall effect is a conversion of a longitudinal charge density $j$ into a transverse spin current density $j_s$ and its strength is often expressed by the spin Hall effect angle $\theta_{\mathrm{SH}} = j_s/j$. Values reported for the spin Hall angles in Pt differ by one order of magnitude, ranging between $\theta_{\mathrm{SH}} \in (0.004, 0.076)$. This effect, observable in nonmagnetic metals and semiconductors, originates from the spin-orbit scattering. The absorption of this current, polarized along the $y$ direction, is equivalent to a torque acting on the Co magnetization. The torque exerted by spin Hall effect on the Co layer reads [134]:

   $$\tau_{\mathrm{SH}} = \zeta \theta_{\mathrm{SH}} \frac{j \mu_{\mathrm{B}}}{et}, \tag{6.6}$$

   where $t$ is the thickness of Co layer, and $\zeta$ is a correcting factor taking into account the finite spin diffusion length in Pt $\lambda_{\mathrm{sf}}$:

   $$\zeta = 1 - \mathrm{sech} \frac{t_{\mathrm{Pt}}}{\lambda_{\mathrm{sf}}}. \tag{6.7}$$

   However, the scenario corresponding to the largest exerted torque, taking into account $\lambda_{\mathrm{sf}} = 3\,\mathrm{nm}$, $\theta_{\mathrm{SH}} = 0.076$, predicts a torque equivalent to a magnetic field $\mu_0 H_{\mathrm{SH}} = 16\,\mathrm{mT}$ considering the current density $j = 10^{12}\mathrm{A/m^2}$. This value is approximately 5 times smaller than the one experimentally observed.

Miron et *al.* [134] conclude that due to the fact that the spin Hall effect in the Pt layer is too weak to account for the efficiency of the switching field, a rather complex mechanism is at work where the Rashba effect plays a role.

This effect may also help to explain the change of mobility expressed by equation (6.3). The major difference between the scenario described in this section and our experimental setup, is the absence of applied longitudinal magnetic field. However, in our case this field is substituted by the simultaneous action of adiabatic and non-adiabatic torques. This is illustrated in Fig. 6.16 on the magnetization in the middle of the distorted Bloch domain wall. The indicated non-adiabatic torque $\vec{\tau}_{\mathrm{NA}}$ acts on the magnetization and cants it into the $y$ direction. As soon as an $y$ component of the magnetization appears, a corresponding magnetic field described by equation (6.5) starts to push the magnetization into the $z$ direction assisting the magnetization reversal.

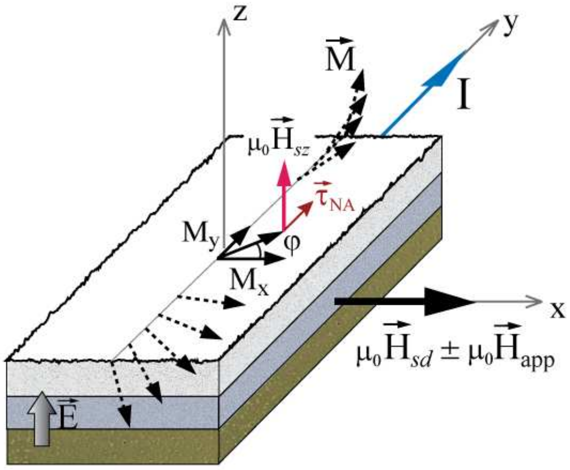

Figure 6.16: Illustration of the distorted Bloch domain wall with indicated directions of the effective switching field $\mu_0 H_{Sz}$.

In equation (6.5) the action of the external transverse magnetic field is implicitly expressed in the magnetization term since the magnetization orientation is given by the sum of all the exerted torques. The $M_y$ component is then directly influenced by $\vec{H}_{\text{app}}$ and so the mobility of the domain wall. In order to understand this behaviour qualitatively, micromagnetic simulations are in progress.

## 6.6 Perspectives

We have demonstrated the effect of the transverse magnetic field on the current-induced domain wall dynamics, which is only a small piece of work to the entire mosaic, necessary to understand the magnetization dynamics process in this system. One could also expect that the broken symmetry leading to the existence of the Rashba electric field could be reached by using similar oxides of metals such as MgO or $\mathrm{TiO_2}$. Effect of an in-plane vectorial field as well as the use of different oxide layers is already a subject of a thesis carried-out between Spintec laboratory and Institut Néel.

Nevertheless, already the mechanism of magnetization reversal in uniformly magnetized $\mathrm{Pt\backslash Co\backslash AlO}_x$ dot is not completely understood. Profound description of the torque exerted on the magnetization in this case would help to identify one of the component of the torque acting in the domain wall. We have already started to work on time-resolved measurements in such a uniformly magnetized system. As a probing tool we use XMCD-PEEM technique, which has a long tradition at Institut Néel. Up to now, the experiment was carried out at the SOLEIL synchrotron in the eight-bunch mode, exploiting 1 of 8 bunches, i.e. at a frequency of 846 kHz. This experiment should yield the time scale of the magnetization reversal as well the mechanism (nucleation, propagation, coherent rotation).

# Conclusion

The goal of the work presented in this manuscript was to study domain wall dynamics in two materials, potential candidates for applications of fast current-induced domain wall motion. Both materials exhibit strong perpendicular anisotropy which leads to out-of-plane magnetization. While in Pt\Co\AlO$_x$ samples the domain walls are very narrow, domain walls as large as in Permalloy stripes are present in the GdCo sample close to the compensation composition. The presence of narrow domain walls may lead to an effective spin-transfer torque and therefore to fast domain wall motion. So far, probably due to the strong intrinsic pinning, only in a few experiments on materials with perpendicular anisotropy have current-induced domain wall displacements been observed.

In the first part of the thesis I described the interesting Gd$_{1-x}$Co$_x$ ferrimagnetic system, which belongs to the family of amorphous rare-earth - transition-metal alloys. In these materials the magnetic properties can be changed either by changing the temperature or the composition. The Gd$_{1-x}$Co$_x$ magnetic layers were prepared by magnetron sputtering in such a way that a linear composition gradient was obtained along the sample. The growth process gives rise to a perpendicular anisotropy strong enough to induce an out-of-plane magnetization configuration. The variation of the composition at a constant temperature implies a change of magnetization along the sample. The continuous variation of the magnetization is a very interesting property from several points of view. Such a change of magnetization without substantially varying the other magnetic properties (anisotropy, sublattice magnetization, thermal excitations, ...) opens an unusual way to check the role of magnetization in magnetization dynamics process.

The composition of the deposited Gd$_{1-x}$Co$_x$ alloys was chosen in such a way that a magnetically compensated interface of composition $x_{\text{xomp}}$ could be found on the studied sample at room temperature. Within this interface the Gd and Co sublattice magnetizations cancel out and the total magnetization vanishes. Macroscopically, the compensation interface is a domain wall as it separates two film regions with opposite magnetization. In order to quantitatively describe the properties of the Gd$_{1-x}$Co$_x$ films with induced composition gradient, simulations based on mean-field model and extraordinary Hall effect were employed. We have found that the induced gradient is 1 at.% per millimeter which corresponds to change of compensation temperature of 45 K per millimeter.

The magnetization configuration close to the compensation composition and its dynamics were probed by polar Kerr microscopy. Since the Kerr rotation in the Gd$_{1-x}$Co$_x$ alloys depends mostly on the Co sublattice orientation, the Kerr microscopy mirrors the Co sublattice behaviour. Due to this property we could identify the position of the compensation interface on the Gd$_{1-x}$Co$_x$ films. We have shown that such an interface can serve as a proof for demonstrating the equivalence between the composition gradient and the compensation temperature gradient. To do so, the sample was inhomogeneously heated by an electric current. The compensation interface then moved according to the film temperature and its position can be used as a local thermometer. The shape of the interface contours the isotherm and maps therefore the temperature distribution across the film.

We have also demonstrated the dependence of the coercive field on the magnetization. The $H_c$ behaviour at constant temperature was shown by Kerr microscopy and we have found that the coercive field scales as $1/M_s$ as the compensation interface is approached. Similar dependence of $H_c$ as a function of temperature was shown by extraordinary Hall effect measurements at low temperature.

The $\mathrm{Gd}_{1-x}\mathrm{Co}_x$ films with well-defined gradient then became the subject of the study of the domain wall dynamics, induced either by magnetic field or spin-polarized current. First, field-induced domain wall motion was observed for two different positions on the stripes close to the compensation compositions, so the influence of the magnetization on the domain wall dynamics could be observed. The domain wall mobility was found to be higher at the position having higher magnetization. One can expect such a behaviour since the applied magnetic field is able to exert a higher pressure on the domain wall when the magnetization is higher. The observed domain wall velocities reached values as high as 1400 m/s for a field of 170 mT.

An outstanding property of our $\mathrm{Gd}_{1-x}\mathrm{Co}_x$ films is the coexistence of magnetization compensation composition and angular momentum compensation composition. These two compositions differ due to the different $g$-factors. The theory predicts [114] that a divergence of the effective gyromagnetic ratio, and therefore of the damping parameter $\alpha$, occurs at the angular momentum compensation. The measured domain wall mobilities vs. field indeed indicate an increase of $\alpha$ close to the angular compensation composition. Other experimental confirmations of these theoretical predictions are important for magnetic recording, since the combination of a high frequency and large damping of the spin precession would provide ultrafast magnetization reversal via precessional motion.

Within a collaboration with the group of T. Rasing from Radboud university in Nijmegen, optically excited magnetization dynamics was studied on the $\mathrm{Gd}_{1-x}\mathrm{Co}_x$ films with induced composition gradient. It was shown that the excitations of the ferrimagnet by a sub-picosecond laser pulse are able to excite both ferromagnetic and exchange spin resonance modes, which were identified by the Fourier transform of the obtained response. At a certain Co concentration the exchange mode frequency reaches a maximum whereas the frequency of the ferromagnetic mode is at its minimum value. This behaviour qualitatively agrees with what is theoretically expected at angular momentum compensation. This experiment thus demonstrates the coexistence of the two different compensation surfaces in our samples.

Since the main goal of this work was to study the interaction between spin polarized current and domain walls, we focused on the perspectives of the $\mathrm{Gd}_{1-x}\mathrm{Co}_x$ alloys. Komine *et al.* [78] theoretically predicted that compensated ferrimagnets are potentially good candidates for an efficient spin transfer torque which should lead to low critical current densities and to fast domain wall motion. Due to the tunable magnetization, our system allows observing the influence of the 'degree of compensation' on the spin transfer torque efficiency. At the angular momentum compensation, the polarization of the conduction electrons stays unchanged while the localized angular momentum vanishes. Therefore the transfer of angular momentum in the domain wall into the vanishing localized angular momentum should provoke large domain wall displacements.

In order to verify this, $\mathrm{Gd}_{1-x}\mathrm{Co}_x$ films were patterned in the compensated region into narrow wires allowing to obtain the high current densities typically needed for observation of the current-induced domain wall displacement. However, all of our tests revealed unsuccessful. No domain wall displacements were observed for the current densities predicted by theory and current densities could not be increased beyond $\sim 10^{12}\,\mathrm{A/m^2}$ because of domain wall nucleation due to Joule heating. The elevated temperatures are caused by the high resistivity associated with the amorphous character of the alloy. Nevertheless, these results clearly show that the typical current densities needed in other materials do not lead to current-induced domain wall motion. One of the possible reasons for this behaviour is the temperature evolution during the current pulse. Since the temperature increases on the nanosecond scale during the application of current pulses, the material is no longer compensated and this may explain the deviation from the theoretical prediction of our experimental results.

In the second part of this work we have focused on $\mathrm{Pt\backslash Co\backslash AlO}_x$ trilayers. The magnetic Co layer is sandwiched between layers in such a way that a strong perpendicular anisotropy is induced. Moreover, this asymmetric configuration gives rise to an electric field in the Co layer. When an electric current passes in such a layer, the electrons experience the Rashba field which via the $s-d$ interaction acts on the localized magnetic moment. This field has a transverse-like character. In order to prove the transverse character of the effective field, we have studied the effect of an applied transverse field on current-induced magnetization dynamics. By using a method based on the measurement of the nucleation rate vs. applied field, we have determined the absolute value of the effective transverse field which is $100\,\mathrm{mT}/10^{12}\,\mathrm{A/m}^2$. The domain wall velocity was also measured as a function of applied transverse field. It was found, that the (current-induced) domain wall mobility depends linearly on the transverse magnetic field. The domain wall mobility decreases with the magnetic field applied antiparallel to the $s-d$ field.

The effect of an applied longitudinal magnetic field on the magnetization reversal of a uniformly magnetized $\mathrm{Pt\backslash Co\backslash AlO}_x$ dot was recently demonstrated by Miron et *al.* [134]. In our case, the absence of the longitudinal field is substituted by the simultaneous action of adiabatic and non-adiabatic torques creating a torque on the magnetization in the longitudinal direction. It can then be demonstrated that the total torque acting on the domain wall has a component in the perpendicular direction, which is proportional to the current density and explains qualitatively the behaviour of the domain wall mobility.

# Conclusion

Le but des travaux présentés dans ce manuscrit a été d'étudier la dynamique de parois de domaine dans deux matériaux, potentiellement candidats pour des applications de déplacement rapide de parois de domaine induit par un courant électrique. Les deux matériaux présentent une forte anisotropie perpendiculaire qui mène à une aimantation hors-plan. Alors que dans les échantillons de $\mathrm{Pt}\backslash\mathrm{Co}\backslash\mathrm{AlO}_x$, les parois de domaines sont très étroites, des parois de domaine aussi larges que dans des bandes Permalloy sont présents dans l'échantillon $\mathrm{Gd}_{1-x}\mathrm{Co}_x$ près de la composition de compensation. La présence de parois de domaines ètroites peut conduire à un transfert de spin efficace et donc à un rapide mouvement des parois de domaines. Jusqu'à présent, et probablement en raison du fort piégeage intrinsèque, seulement quelques expériences réalisées sur des matériaux à anisotropie perpendiculaire ont permis d'observer des déplacements de parois induits par un courant électrique.

Dans la première partie de la thèse, j'ai décrit le systeme ferrimagnétique $\mathrm{Gd}_{1-x}\mathrm{Co}_x$, qui appartient à la famille des alliages amorphes entre métal de terres rares et métal de transition. Dans ces matériaux, les propriétés magnétiques peuvent être modifiées en changeant la température ou leur composition chimique. Les couches magnétiques $\mathrm{Gd}_{1-x}\mathrm{Co}_x$ ont été préparées par pulvérisation magnétron de telle sorte qu'un gradient de composition linéaire est obtenu le long de l'échantillon. Le processus de croissance donne lieu a une anisotropie perpendiculaire suffisamment forte pour induire une configuration d'aimantation hors-plan. La variation de la composition à température constante implique un changement de l'aimantation le long de l'échantillon. La variation continue de l'aimantation est une propriété très intéressante selon plusieurs points de vue. Un tel changement d'aimantation sans modifications substantielles d'autres propriétés magnétiques (anisotropie, aimantation des sous-réseaux, excitations thermiques ...) ouvre une voie inhabituelle pour vérifier le rôle de l'aimantation lors d'un processus d'aimantation dynamique.

La composition des couches de $\mathrm{Gd}_{1-x}\mathrm{Co}_x$ déposées a été choisie de sorte qu'une interface magnétiquement compensée, de composition $x_{\mathrm{comp}}$, peut être trouvée sur l'échantillon étudié à température ambiante. Dans cette interface, les sous-réseaux d'aimantation de gadolinium et de cobalt s'annulent et l'aimantation totale disparaît. Macroscopiquement, l'interface de compensation est une paroi de domaine car elle sépare deux régions de film d'aimantation opposée. Afin de décrire quantitativement les propriétés des couches de $\mathrm{Gd}_{1-x}\mathrm{Co}_x$ avec un gradient de composition induit, des simulations basées sur le modèle de champ moyen et sur l'effet Hall extraordinaire ont été utilisées. Nous avons trouvé que le gradient induit est de 1 % atomique par millimetre, correspondant à un changement de température de compensation de 45 K par millimètre.

La configuration d'aimantation proche de la composition de compensation et sa dynamique ont été étudiées par microscopie Kerr polaire. Etant donné que la rotation Kerr dans l'alliage de $\mathrm{Gd}_{1-x}\mathrm{Co}_x$ dépend essentiellement de l'orientation des sous-réseau de cobalt, la microscopie Kerr reflète le comportement des sous-réseau du cobalt. Grâce à cette propriété nous avons pu identifier la position de l'interface de compensation sur les couches de $\mathrm{Gd}_{1-x}\mathrm{Co}_x$. Nous avons montré qu'une telle interface peut servir de modèle pour démontrer l'équivalence entre le gradient de composition et le gradient de température de compensation. Pour ce faire, l'échantillon a été chauffé de manière inhomogène par un courant électrique. L'interface de compensation s'est ensuite déplacée en fonction de la température de la couche dont la position peut alors etre utilisée comme un thermomètre local. La forme de l'interface délimite l'isotherme et dresse la carte de distribution de la température à travers la couche.

Nous avons également démontré la dépendance du champ coercitif sur l'aimantation. Le comportement $H_c$ à température constante a été démontré par microscopie Kerr et nous avons constaté que le champ coercitif s'établit a $1/M_s$ lorsque l'on approche de l'interface de compensation. Des relations de dépendances similaires de $H_c$ en fonction de la température ont été démontrées par des mesures d'effet Hall extraordinaire à basse température.

Les couches de $\mathrm{Gd}_{1-x}\mathrm{Co}_x$ présentant un gradient bien défini ont ensuite fait l'objet de l'étude de la dynamique des parois de domaines - induite soit par un champ magnétique, soit par un courant polarisé en spin. Tout d'abord, des déplacements de parois de domaine induits par champ magnétique ont été observés pour deux positions différentes sur les bandes proches de la compensation. Ainsi, l'influence de l'aimantation sur la dynamique de paroi de domaine ont pu être observée. Nous avons découvert que la mobilité des parois de domaines était supérieure pour une position à magnétisation supérieure. Un tel comportement pouvait être attendu du fait que le champ magnétique appliqué est capable d'exercer une pression plus forte sur les parois de domaine lorsque l'aimantation est plus élevée. Les vitesses de parois de domaine observées ont atteint des valeurs de l'ordre de 1400 m / s pour un champ magnétique de 170 mT.

Une propriété remarquable de ces couches de $\mathrm{Gd}_{1-x}\mathrm{Co}_x$ est la coexistence de la composition de compensation d'aimantation et de la composition de compensation du moment angulaire. Ces deux compositions different en raison des différents facteurs $g$. La théorie prédit [114] qu'une divergence de rapport gyromagnétique effectif, et donc du paramètre d'amortissement $\alpha$, a lieu lors de la compensation du moment angulaire. En effet, les déplacements de parois de domaine mesurés indiquent une augmentation de $\alpha$ à l'approche de la compensation du moment angulaire. D'autres confirmations expérimentales de ces prédictions théoriques seraient importantes pour l'enregistrement magnétique. En effet, l'amortissement fort, associé à une haute fréquence de la précession du spin, permettrait un renversement d'aimantation ultra-rapide par mouvement précessionel.

Au sein d'une collaboration avec le groupe de T. Rasing de l'Université Radboud de Nimègue, la dynamique d'aimantation optiquement excitée a été étudiée sur les couches de $\mathrm{Gd}_{1-x}\mathrm{Co}_x$ avec un gradient de composition induit. Il a été démontré que les excitations du matériau ferrimagnétique par impulsion sub-picoseconde d'un laser sont capables d'exciter a la fois le mode ferromagnétique et le mode d'échange de résonance de spin. Ces modes ont été identifiés par la transformée de Fourier de la réponse obtenue. Pour une concentration de cobalt donnée, la fréquence du mode d'échange atteint un maximum alors que la fréquence du mode ferromagnétique est à sa valeur minimale. Ce comportement est en accord de manière qualitative avec ce qui est théoriquement attendu à la compensation du moment angulaire. Cette expérience démontre donc la coexistence des deux surfaces de compensation différentes dans nos échantillons.

Etant donné que le but principal de ces travaux était d'étudier l'interaction entre le courant polarisé en spin et les parois de domaine, nous nous sommes concentrés sur les perspectives offertes par l'alliage de $\mathrm{Gd}_{1-x}\mathrm{Co}_x$. Komine *et al.* [78] Komine avait prédit que les matériaux ferrimagnétiques compensées sont de bons candidats potentiels pour un transfert de spin efficace entraînant des densités de faible courant critique, et de rapides mouvements de parois de domaine. Grâce au réglage de son aimantation, notre système permet d'observer l'influence du "degré de compensation" sur l'efficacité du transfert de spin. Lors de la compensation du moment angulaire, la polarisation des électrons de conduction reste inchangée alors que le moment angulaire localisé disparaît. Par conséquent le transfert du moment angulaire dans la paroi de domaine vers le faible moment angulaire localisé devrait provoquer d'importants déplacements de parois de domaine.

Afin de vérifier ceci, des couches de $\mathrm{Gd}_{1-x}\mathrm{Co}_x$ ont été façonnées au niveau de leur région compensée en d'étroits nanofils permettant d'obtenir de hautes densités de courant, généralement nécessaires pour l'observation de déplacements de parois de domaine induit par un courant électrique. Cependant, l'ensemble de nos tests s'est révélé infructueux. Aucun déplacement de parois de domaine a été observé pour les densités de courant prédites par la théorie. Ces densités de courant ne pouvaient pas être augmentées au-delà de $\sim 10^{12}$ A/m$^2$ en raison de la nucléation de domaines - résultant du chauffage par effet Joule. Les températures élevées sont causées par la haute résistivité associée au caractère amorphe de l'alliage. Néanmoins, ces résultats montrent clairement que les densités de courant typiquement nécessaires dans d'autres matériaux ne conduisent pas ici à un mouvement de parois de domaine. Une des raisons possibles à ce comportement est l'évolution de la température lors de l'impulsion du courant électrique. Comme la température augmente à l'échelle nanoseconde pendant l'application d'impulsions de courant, le matériau n'est plus compensé, ce qui peut expliquer l'écart entre la prédiction théorique et nos résultats expérimentaux.

Dans la seconde partie de ce travail nous nous sommes concentrés sur les tricouches Pt\Co\AlO$_x$. La couche magnétique est en sandwich entre des couches de telle manière qu'une forte anisotropie perpendiculaire est induite. Par ailleurs, cette configuration asymétrique donne lieu à un champ électrique dans la couche de cobalt. . Quand un courant électrique passe dans une telle couche, le champ Rashba agit sur les électrons de conduction qui via l'interaction *sd* agit sur le moment magnétique localisé. Ce champ a un caractère transverse. Afin de prouver le caractère transverse du champ effectif, nous avons étudié l'effet d'un champ appliqué transversalement aux nanostructures sur la dynamique de l'aimantation induite par courant. En utilisant une méthode basée sur la mesure de la taux de nucléation vs champ appliqué, nous avons déterminé la valeur absolue du champ transverse efficace, qui est de $100\,\mathrm{mT}/10^{12}$ A/m$^2$. La vitesse de paroi de domaine a aussi été mesurée en fonction du champ transverse appliqué. Il a été trouvé, que la mobilité de parois (induite par courant) dépend linéairement du champ magnétique transversal. La mobilité diminue avec le champ magnétique appliqué antiparallèlement au champ *sd*.

L'effet d'un champ magnétique longitudinal sur le retournement de l'aimantation d'un plot de Pt\Co\AlO$_x$ uniformément aimanté a été récemment démontré par Miron et *al.* [134]. Dans notre cas, l'absence du champ longitudinal est remplacée par l'action simultanée des couples de transfert de spin adiabatique et non adiabatique qui créent un couple sur l'aimantation dans la direction longitudinale. Il peut alors être démontré que le couple total agissant sur la paroi de domaine a une composante dans la direction perpendiculaire, qui est proportionnelle à la densité de courant et explique qualitativement le comportement de la mobilité des parois.

# Bibliography

[1] S. Blundell, Magnetism in Condensed Matter (Oxford university press, 2008).

[2] A. Sugiyama, Theory of Formation Energy of the External and the Internal Surface for Free Electron Metals, J. Phys. Soc. Jpn. **15**, 965 (1960).

[3] G. Bihlmayer, Yu. M. Koroteev, P. M. Echenique, E. V. Chulkov, S. Blügel, The Rashba-effect at metallic surfaces, Surf. Science **600**, 3888 (2006).

[4] N.W. Ashcroft, N.D. Mermin, Solid State Physics (Holt, Rinehart & Winston, New York, 1976).

[5] E. I. Rashba, Sov. Phys. Solid State **2**, 1109 (1960).

[6] I. I. Oleinik, E. Y. Tsymbal, D. G. Pettifor, Structural and electronic properties of Co/$Al_2O_3$/Co magnetic tunnel junction from first principles, Phys. Rev. B **62**, 3952 (2000).

[7] O. Krupin, G. Bihlmayer, K. M. Döbrich, J. E. Prieto, K. Starke, S. Gorovikov, S. Blügel, S. Kevan, G. Kaindl, Rashba effect at the surfaces of rare-earth metals and their monoxides, New J. Phys. **11**, 013035 (2009).

[8] G. van der Laan, M. A. Hoyland, M. Surman, C. F. J. Flipse, B. T. Thole, Surface orbital magnetic moment of ferromagnetic nickel studied by magnetic circular dichroism in Ni3*p* core level photoemission, Phys. Rev. Lett. **69**, 3827 (1992).

[9] W. Weber, A. Bischof, R. Allenspach, Ch. Würsch, C. H. Back, D. Pescia, Oscillatory Magnetic Anisotropy and Quantum Well States in Cu/Co/Cu(100) Films, Phys. Rev. Lett. **76**, 3424 (1996).

[10] D. Weller, J. Stöhr, R. Nakajima, A. Carl, M. G. Samant, C. Chappert, R. Mégy, P. Beauvillain, P. Veillet, G. A. Held, Microscopic Origin of Magnetic Anisotropy in Au/Co/Au Probed with X-Ray Magnetic Circular Dichroism, Phys. Rev. Lett. **75**, 3752(1995).

[11] O. Krupin, G. Bihlmayer, K. Starke, S. Gorovikov, J. E. Prieto, K. M. Döbrich, S. Blügel, G. Kaindl, Rashba effect at magnetic metal surfaces, Phys. Rev. B **71**, 201403 (2005).

[12] D. C. Ralph, M. D. Stiles, Spin transfer torques, J. Magn. Magn. Mater. **320**, 1190–1216 (2008).

[13] J. M. D. Coey, Magnetism and Magnetic Materials (Cambridge University Press, 2010).

[14] W. F. Brown, Jr., Micromagnetics (Interscience, New York, 1963).

[15] A. Hubert, and R. Schäfer, Magnetic Domains (Springer, 2000).

[16] É. Trémolet de Lacheisser, D. Gignoux, and M. Schlenker, Magnetism, Vol. 1 (Kluwer, 2003).

[17] J. I. Martin, J. Nogues, K. Liu, J. L. Vicent, and I. K. Schuller, Ordered magnetic nanostructures: fabrication and properties. J. Magn. Magn. Mater. **256**, 449 (2003).

[18] M. Kläui, Head-to-head domain walls in magnetic nanostructures. J. Phys.: Condens. Matter **20**, 313001 (2008).

[19] Y. Nakatani, A. Thiaville, and J. Miltat, Head-to-head domain walls in soft nano-strips: a refined phase diagram, J. Magn. Magn. Mater. **290-291**, 750 (2005).

[20] J. C. Slonczewski, Theory of domain-wall motion in magnetic films and platelets, J. Appl. Phys. **44**, 1759 (1973).

[21] S. Emori, G. S. D. Beach, Enhanced current-induced domain wall motion by tuning perpendicular magnetic anisotropy, Appl. Phys. Let. **98**, 132508 (2011).

[22] L. D. Landau, E. M. Lifshitz, Phys. Z. Sowjetunion **8**, 153 (1935).

[23] T. L. Gilbert, A phenomenological theory of damping in ferromagnetic materials, IEEE Trans. Magn. **40**, 3443 (2004).

[24] J. Mallinson, On the damped gyromagnetic precession, IEEE Trans. Magn. **23**, 2003 (1987).

[25] M. Bauer, R. Lopusnik, J. Fassbender, B. Hillebrands, Suppression of magnetic-field pulse-induced magnetization precession by pulse tailoring, Appl. Phys. Lett. **76**, 2758 (2000).

[26] C. H. Back, R. Allenspach, W. Weber, S. S. P. Parkin, D. Weller, E. L. Garwin, H. C. Siegman, Minimum Field Strenght in Precessional Magnetization Reversal, Science **285**, 864-867 (1999).

[27] H. W. Schumacher, C. Chappert, P. Crozat, R. C. Sousa, P. P. Freitas, J. Miltat, J. Fassbender, B. Hillebrands, Phase Coherent Precessional Magnetization Reversal in Microscopic Spin Valve Elements, Phys. Rev. Let. **90**, 017201 (2003).

[28] I. Tudosa, C. Stamm, A. B. Kashuba, F. King, H. C. Siegmann, J. Stohr, G. Ju, B. Lu, D. Weller, The ultimate speed of magnetic switching in granular recording media, Nature **428**, 831 (2004).

[29] A. Mougin, M. Cormier, J. P. Adam, P. J. Metaxas, J. Ferré, Domain wall mobility, stability and Walker breakdown in magnetic nanowires, Eur. Phys. Let. **78**, 57007 (2007).

[30] P. J. Metaxas, J. P. Jamet, A. Mougin, M. Cormier, J. Ferré, V. Baltz, B. Rodmacq, B. Dieny, R. L. Stamps, Creep and Flow Regimes of Magnetic Domain-Wall Motion in Ultrathin Pt/Co/Pt Films with Perpendicular Anisotropy, Phys. Rev. Let. **99**, 217208 (2007).

[31] S. Brazovskii, T. Nattermann, Pinning and sliding of driven elastic systems: from domain walls to charge density waves, Adv. Phys 53, 177 (2004).

[32] S. Lemerle, J. Ferré, C. Chappert, V. Mathet, T. Giamarchi, and P. Le Doussal, Domain Wall Creep in an Ising Ultrathin Magnetic Film, Phys. Rev. Let. **80**, 849 (1998).

[33] J. Lu, X. R. Wang, Motion of transverse domain walls in thin magnetic nanostripes under transverse magnetic fields, J. Appl. Phys. **107**, 083915 (2010).

[34] M. T. Bryan, T. Schrefl, D. Atkinson, D. A. Allwood, Magnetic domain wall propagation in nanowires under transverse magnetic fields, J. Appl. Phys. **103**, 073906 (2008).

[35] J. Yang, G. S. D. Beach, C. Knutson, J. L. Erskine, Magnetic domain-wall velocity enhancement induced by a transverse magnetic field, arXiv:1103.6056v1 (2011).

[36] V. Uhlíř, S. Pizzini, N. Rougemaille, V. Cros, E. Jiménez, L. Ranno, O. Fruchart, M. Urbánek, G. Gaudin, J. Camarero, C. Tieg, F. Sirotti, E. Wagner, J. Vogel, Direct observation of Oersted-field-induced magnetization dynamics in magnetic nanostripes, Phys. Rev. B **83**, 020406 (2011).

[37] C. H. Marrows, Spin-polarised currents and magnetic domain wall, Adv. Phys. **54**, 585-713 (2005).

[38] R. A. de Groot, F. M. Muelle, P. G. van Engen, K. H. J. Buschow, New Class of Materials: Half-Metallic Ferromagnets, Phys. Rev. Lett. **50**, 2024 (1983).

[39] R. Danneau, P. Warin, J. P. Attané, I. Petej, C. Beigné, C. Fermon, O. Klein, A. Marty, F. Ott, Y. Samson, M. Viret, Individual Domain Wall Resistance in Submicron Ferromagnetic Structures, Phys. Rev. Let. **88**, 157201 (2002).

[40] J. M. Luttinger, Theory of the Hall effect in ferromagnetic substances, Phys. Rev. **112**, 739 (1958).

[41] L. Berger, Side-jump mechanism for the Hall effect of ferromagnets, Phys. Rev. B 2, 4559 (1970).

[42] S. A. Crooker, M. Furis, X. Lou, C. Adelmann, D. L. Smith, C. J. Palmstrřm, P. A. Crowell, Imaging Spin Transport in Lateral Ferromagnet/Semiconductor Structures, Science **309**, 2191 (2005).

[43] J. Fabian, S. Das Sarma, Spin relaxation of conduction electrons, J. Vac. Sci. Technol. B **17**, 1708 (1999).

[44] B. Raquet, M. Viret, E. Sondergard, O. Cespedes, R. Mamy, Electron-magnon scattering and magnetic resistivity in 3d ferromagnets, Phys. Rev. Lett. B **66**, 024433 (2002).

[45] L. Berger, Prediction of a domain-drag effect in uniaxial, non-compensated, ferromagnetic metals, J. Phys. Chem. Solids **35**, 947(1974).

[46] J. C. Slonczewski, Current-driven excitation of magnetic multilayers, J. Magn. Magn. Mater. **159**, L1(1996).

[47] D. M. Edwards, J. Mathon, R. B. Muniz, M. S. Phan, Phys. Rev. Lett. **67**, 493 (1991).

[48] D. Houssameddine, U. Ebels, B. Delae, B. Rodmacq, I. Firastrau, F. Ponthenier, M. Brunet, C. Thirion, J.-P. Michel, L. Prejbeanu-Buda, M.-C. Cyrille, O. Redon, B. Dieny, Spin-torque oscillator using a perpendicular polarizer and a planar free layer, Nature mat. **6**, 447 (2007).

[49] G. Bertotti, C. Serpico, I. D. Mayergoyz, A. Magni, M. d'Aquino, R. Bonin, Magnetization Switching and Microwave Oscillations in Nanomagnets Driven by Spin-Polarized Currents, Phys. Rev. Lett. **94**, 127206 (2005).

[50] Y. B. Bazaliy, B. A. Jones, Shou-Cheng Zhang, Modification of the Landau-Lifshitz equation in the presence of a spin-polarized current in colossal- and giant-magnetoresistive materials, Phys. Rev. B **57**, R3213 (1997).

[51] A. Thiaville, Y. Nakatani, J. Miltat, N. Vernier, Domain wall motion by spin-polarized current: a micromagnetic study, J. Appl. Phys **95**, 7049 (2004).

[52] S. Zhang, P. M. Levy, A. Fert, Mechanisms of Spin-Polarized Current-Driven Magnetization Switching, Phys. Rev. Let. 88, 236601 (2002).

[53] G. Tatara, H. Kohno, Theory of Current-Driven DomainWall Motion: Spin Transfer versus Momentum Transfer, Phys. Rev. Lett. **92**, 086601 (2004).

[54] N. Vernier, D. A. Allwood, D. Atkinson, M. D. Cooke, R. P. Cowburn, Domain wall propagation in magnetic nanowires by spin-polarized current injection, Europhys. Lett. **65**, 526 (2004).

[55] A. Thiaville, Y. Nakatani, J. Miltat, Y. Suzuki, Micromagnetic understanding of current-driven domain wall motion in patterned nanowires, Europhys. Lett. **69**, 990 (2005).

[56] A. Vanhaverbeke, M. Viret, Simple model of current-induced spin torque in domain walls, Phys. Rev. B **75**, 024411 (2007).

[57] S. Zhang, Z. Li, Roles of Nonequilibrium Conduction Electrons on the Magnetization Dynamics of Ferromagnets, Phys. Rev. Lett. **93**, 127204 (2004).

[58] I. M. Miron, P.-J. Zermatten, G. Gaudin, S. Auffret, B. Rodmacq, A. Schuhl, Domain Wall Spin Torquemeter, Phys. Rev. Lett. **102**, 137202 (2009).

[59] L.Néel, Anisotropie magnétique superficielle et surstructures d'orientation, J. Phys. Rad. **15**, 225–239 (1954).

[60] N. Nakajima, T. Koide, T. Shidara, H. Miyauchi, H. Fukutani, A. Fujimori, K. Iio, T. Katayama, M. Nývlt, Y. Suzuki, Perpendicular Magnetic Anisotropy Caused by Interfacial Hybridization via Enhanced Orbital Moment in CoPt Multilayers: Magnetic Circular X-Ray Dichroism Study, Phys. Rev. Lett. **81**, 5229 (1998).

[61] H. Takahashi, S. Tsunashima, S. Iwata, S. Uchiyama, Measurement of magnetostriction constants in polycrystalline alloy and multilayer films of PdCo and PtCo, J. Magn. Magn. Mater. **126**, 282-284 (1993).

[62] F.J.A. den Broeder, W. Hoving, P.J.H. Bloemen, Magnetic anisotropy of multilayers, J. Magn. Magn. Mater. **93**, 562-570(1991).

[63] M. T. Johnson, P. J. H. Bloemen, F. J. A. den Broeder, J. J. de Vries, Magnetic anisotropy in metallic multilayers, Rep. Prog. Phys. **59**, 1409–1458 (1996).

[64] A. Lyberatos, J. Ferré, Domain wall velocity in ultra-thin magnetic films with perpendicular anisotropy, J. Phys. D: Appl. Phys. **33**, 1060 (2000).

[65] A. Dourlat, V. Jeudy, A. Lemaître, C. Gourdon, Field-driven domain-wall dynamics in (Ga,Mn)As films with perpendicular anisotropy, Phys. Rev. B **78**, 161303 (2008).

[66] A. Kirilyuk, J. Ferré, J. Pommiera, D. Renard, Domain wall dynamics in ultrathin Au/Co/Au films, J. Magn. Magn. Mat. **121**, 536 (1993).

[67] R. P. Cowburn, J. Ferré, S. J. Gray, J. A. C. Bland, Domain wall mobility in ultrathin epitaxial Ag/Fe/Ag.001. films, Appl. Phys. Lett. **74**, 1018 (1999).

[68] S. Jung, W. Kim, T. Lee, K. Lee, H. Lee, Current-induced domain wall motion in a nanowire with perpendicular magnetic anisotropy, Appl. Phys. Lett. **92**, 202508 (2008).

[69] S. Fukami, T. Suzuki, N. Ohshima, K. Nagahara, N. Ishiwata, Micromagnetic analysis of current driven domain wall motion in nanostrips with perpendicular anisotropy, J. Appl. Phys. **103**, 07E718 (2008).

[70] C. Burrowes, D. Ravelosona, C. Chappert, S. Mangin, E. E. Fullerton, J. A. Katine, B. D. Terris, Role of pinning in current driven domain wall motion in wires with perpendicular anisotropy, Appl. Phys. Lett. **93**, 172513 (2008).

[71] M. Yamanouchi, D. Chiba, F. Matsukura, T. Dietl, H. Ohno, Velocity of Domain-Wall Motion Induced by Electrical Current in the Ferromagnetic Semiconductor (Ga,Mn)As, Phys. Rev. Lett. **96**, 096601 (2006).

[72] H. Tanigawa, K. Kondou, T. Koyama, K. Nakano, S. Kasai, N. Ohshima, S. Fukami, N. Ishiwata, T. Ono, Current-Driven Domain Wall Motion in CoCrPt Wires with Perpendicular Magnetic Anisotropy, Appl. Phys. Express **1**, 011301 (2008).

[73] T. Koyama, G. Yamada, H. Tanigawa, S. Kasai, N. Ohshima, S. Fukami, N. Ishiwata, Y. Nakatani, T. Ono, Control of Domain Wall Position by Electrical Current in Structured Co/Ni Wire with Perpendicular Magnetic Anisotropy, Appl. Phys. Express **1**, 101303 (2008).

[74] K. Kim, J. Lee, S. Yun, G. Gim, K. Lee, S. Choe, K. Shin, Electric Control of Multiple Domain Walls in Pt/Co/Pt Nanotracks with Perpendicular Magnetic Anisotropy, Appl. Phys. Exp. **3** 083001 (2010).

[75] T. A. Moore, I. M. Miron, G. Gaudin, G. Serret, S. Auffret, B. Rodmacq, A. Schuhl, S. Pizzini, J. Vogel, M. Bonfim, High domain wall velocities induced by current in ultrathin Pt/Co/AlO$_x$ wires with perpendicular magnetic anisotropy, Appl. Phys. Lett. **93**, 262504 (2008).

[76] I. M. Miron, T. A. Moore, H. Szambolics, L. D. Buda-Prejbeanu, S. Auffret, B. Rodmacq, S. Pizzini, J. Vogel, M. Bonfim, A. Schuhl, G. Gaudin, Fast current-induced domain-wall motion controlled by the Rashba effect, Nature Mat. **10**, 419 (2011).

[77] T. Suzuki, S. Fukami, N. Ishiwata, M. Yamanouchi, S. Ikeda, N. Kasai, H. Ohno, Current-induced effective field in perpendicularly magnetized Ta/CoFeB/MgO wire, Appl. Phys. Lett. **98**, 142505 (2011).

[78] T. Komine, K. Takahashi, A. Ooba, R. Sugita, Reduction of intrinsic critical current density for current-induced domain wall motion by using a ferrimagnetic nanowire with perpendicular magnetic anisotropy, J. Appl. Phys. **109**, 07D503(2011).

[79] D. Ravelosona, A. Cebollada, F. Briones, C. Diaz-Paniagua†, M. A. Hidalgo, F. Batallan, Domain-wall scattering in epitaxial FePd ordered alloy films with perpendicular magnetic anisotropy, Phys. Rev. B **59**, 4322 (1999).

[80] U. Ruediger, J. Yu, S. Zhang, A. D. Kent, S. S. P. Parkin, Negative Domain Wall Contribution to the Resistivity of Microfabricated Fe Wires, Phys. Rev. Lett. **80**, 5639 (1998).

[81] M. Hayashi, L. Thomas, R. Moriya, Ch. Rettner, S. S. P. Parkin, Current-Controlled Magnetic Domain-Wall Nanowire Shift Register, Science **320**, 209 (2008).

[82] C. Burrowes, A. P. Mihai, D. Ravelosona, J.-V. Kim, C. Chappert, L. Vila, A. Marty, Y. Samson, F. Garcia-Sanchez, L. D. Buda-Prejbeanu, I. Tudosa, E. E. Fullerton, J.-P. Attané, Non-adiabatic spin-torques in narrow magnetic domain walls, Nature Phys. **6**, 17 (2010).

[83] J.-Y. Chauleau, R.l Weil, A. Thiaville, J. Miltat, Magnetic domain walls displacement: Automotion versus spin-transfer torque, Phys. Rev. B **82**, 214414 (2010).

[84] D. Atkinson, D. A. Allwood, G. Xiong, M. D. Cooke, C. C. Faulkner, R. P. Cowburn, Magnetic domain-wall dynamics in a submicrometre ferromagnetic structure, Nature Mat. **2**, 85 (2003).

[85] J.-P. Adam, N. Vernier, J. Ferré, A. Thiaville, V. Jeudy, A. Lemaître, L. Thevenard, G. Faini, Nonadiabatic spin-transfer torque in (Ga,Mn)As with perpendicular anisotropy, Phys. Rev. B **80**, 193204 (2009).

[86] J. J. M. Franse, R. J. Radwanski, Magnetic properties of binary rare-earth 3*d*-transition metal intermetallic compounds, in Handbook of Magnetic Materials, ed. K. H. J. Buschow, vol. 7 (North-Holland, Amsterdam, 1993).

[87] S. K. Malik, F. J. Arlinghaus, W. E. Wallace, Spin-polarized energy-band structure of $YCo_5$, $SmCo_5$, and $GdCo_5$, Phys. Rev. B **16**, 1242 (1977).

[88] G. A. N. Connell, Magneto-optics and amorphous metals: an optical storage revolutuion, J. Mag. Mag. Mat. **54**, 1561 (1986).

[89] J. Daval, B. Bechevet, Rare earth transition metal alloys for magneto-optical recording, J. Mag. Mag. Mat. **129**, 98 (1994).

[90] J. Orehotsky, K. Schröder, Magnetic Properties of Amorphous Fex Gdy Alloy Thin Films, J. Appl. Phys **43**, 2413 (1972).

[91] D. Mergel, H. Heitmann, P. Hansen, Pseudocrystalline model of the magnetic anisotropy in amorphous rare-earth–transition-metal thin films, Phys. Rev. B **47**, 882 (1993).

[92] T. Mizoguchi, G. S. Cargill III, Magnetic anisotropy from dipolar interactions in amorphous ferrimagnetic alloys, J. Appl. Phys. **50**, 3570 (1979).

[93] K. H. J. Buschow, Handbook of magnetic materials, Vol. **6** (North-Holland, Amsterdam, 1991).

[94] R. C. Taylor, A. Gangulee, Magnetization and magnetic anisotropy in evaporated GdCo amorphous films, J. Appl. Phys. **47**, 4666 (1976).

[95] L. J. Maksymowicz, L. Dargel, M. Lubecka, M. Pyka, Pair ordering and perpendicular anisotropy in RE-TM amorphous thin films, J. Mag. Mag. Mat. **35**, 281 (1983).

[96] K. Twarowski, H. K. Lachowicz, M. Gutowski, H. Szymczak, On the origin of the perpendicular anisotropy and magnetostriction in amorphous RF sputtered Gd-Co films, Phys. Stat. Sol.(a) **63**, 103 (1981).

[97] H. Takagi, S. Tsunashima, S. Uchiyama, T. Fuji, Stress induced anisotropy in amorphous Gd-Fe and Tb-Fe sputtered films, J. Appl. Phys. **50**, 1642 (1979).

[98] S. R. Herd, TEM observation on the source of perpendicular anisotropy in amorphous $GdCo(O_2)$, Phys. Stat. Sol.(a) **44**, 363 (1977).

[99] R. J. Radwanski, Anisotropic ferrimagnets in high magnetic fields, Physica B **142**, 57 (1987).

[100] A. E. Clark, E. Callen , Néel Ferrimagnets in Large Magnetic Fields, J. Appl. Phys. **39**, 5972 (1968).

[101] N. T. Nam, Fabrication and study of magnetic and transport properties of GdCo thin films, GdCo-based multilayers and Fe/Cr multilayers, PhD. Thesis, Université Joseph Fourier, Grenoble (2007).

[102] M. D. Kuz'min, Y. Skourski, D. Eckert, M. Richter, K.-H. Müller, K. P. Skokov, I. S. Tereshina, Spin reorientation in high magnetic fields and the Co-Gd exchange field in $GdCo_5$, Phys. Rev. B **70**, 172412 (2004).

[103] N. Heiman, N. Kazama, Magnetization of amorphous $RE_x$-$Cu_{1-x}$ alloys (RE=Gd, Tb, Dy, Ho), J. Appl. Phys. **49**, 1686 (1978).

[104] N. H. Duc, T. D. Hien, D. Givord, J. J. M. Franse, F. R. de Boer, Exchange interactions in rare earth-transition metal compounds, J. Mag. Mag. Mat. **124**, 305 (1993).

[105] N. Heima, K. Lee, R. I. Potter, S. Kirkpatrick, Modified mean-field model for rare-earth–iron amorphous alloys, J. Appl. Phys. **47**, 2634 (1976).

[106] W. B. Pearson, Structure Reports for 1961 : Metals, Inorganic and Organic Sections, Vol.**26** (Springer,1961).

[107] J. Krumme, P. Hansen, A new type of magnetic domain wall in nearly compensated Ga-substituted YIG, Appl. Phys. Lett. **22**, 312 (1973).

[108] P. Hansen, C. Clausen, G. Much, M. Rosenkranz, M. Witter, Magnetic and magneto-optilcal properties of rare-earth transition-metal alloys containing Gd, Tb, Fe, Co, J. Appl. Phys. **66**, 756 (1989).

[109] K. Sato, Y. Togami, Magneto-optical spectra of RF-sputtered amorphous Gd-Co and Gd-Fe films, J. Mag. Mag. Mat. **35**, 181 (1983).

[110] P. Gaunt, Domain wall pinning as a source of magnetic hardening in alloys, J. App. Phys. **43**, 637 (1972).

[111] K. Uchida, S. Takahashi, K. Harii, J. Ieda, W. Koshibae, K. Ando, S. Maekawa, E. Saitoh, Observation of the spin Seebeck effect, Nature **455**, 778 (2008).

[112] Pelzl, R. Meckenstock, D. Spoddig, F. Schreiber, J. Pflaum, Z. Frait, Spin–orbit-coupling effects on g-value and damping factor of the ferromagnetic resonance in Co and Fe films, J. Phys.: Condens. Matter **15**, S451 (2003).

[113] G. G. Scott, Review of Gyromagnetic Ratio Experiments, Rev. Mod. Phys. **34**, 102 (1962).

[114] M. Mansuripur, The Physical Principles of Magneto-Optical Recording (Cambridge University Press, 1995).

[115] R. K. Wangsness, Magnetic Resonance in Ferrimagnetics, Phys. Rev. **93**, 68 (1954).

[116] R. K. Wangsness, Effective Parameters in Ferrimagnetic Resonance, Phys. Rev. **111**, 813 (1958).

[117] R. K. Wangsness, Sublattice Effects in Magnetic Resonance, Phys. Rev. **91**, 1085 (1953).

[118] G. P. Rodrigue, H. Meyer, R. V. Jones, Resonance Measurements in Magnetic Garnets, J. Appl. Phys. **31**, S376 (1960).

[119] S. Geschwind, L. R. Walker, Exchange Resonances in Gadolinium Iron Garnet near the Magnetic Compensation Temperature, J. Appl. Phys. **30**, S163 (1959).

[120] X. Jiang, L. Gao, J. Z. Sun, S. S. P. Parkin, Temperature Dependence of Current-Induced Magnetization Switching in Spin Valves with a Ferrimagnetic CoGd Free Layer, Phys. Rev. Lett. **97**, 217202 (2006).

[121] C. D. Stanciu, A. V. Kimel, F. Hansteen, A. Tsukamoto, A. Itoh, A. Kirilyuk, Th. Rasing, Ultrafast spin dynamics across compensation points in ferrimagnetic GdFeCo: The role of angular momentum compensation, Phys. Rev. B. **73**, 220402 (2006).

[122] C. Kaiser, A. F. Panchula, S. S. P. Parkin, Finite Tunneling Spin Polarization at the Compensation Point of Rare-Earth-Metal-Transition-Metal Alloys, Phys. Rev. Lett. **95**, 047201 (2005).

[123] G. S. D. Beach, C. Nistor, C. Knutson, M. Tsoi, J. L. Erskine, Dynamics of field-driven domain-wall propagation in ferromagnetic nanowires, Nature Mat. **4**, 741 (2005).

[124] D. Ngo, K. Ikeda, H. Awano, Direct Observation of Domain Wall Motion Induced by Low-Current Density in TbFeCo Wires, Appl. Phys. Express **4**, 093002 (2011).

[125] J. A. Balseiro, Angular Momentum of Photons, Phys. Rev. **71**, 79 (1947).

[126] C. D. Stanciu, A. Tsukamoto, A. V. Kimel, F. Hansteen, A. Kirilyuk, A. Itoh, Th. Rasing, Subpicosecond Magnetization Reversal across Ferrimagnetic Compensation Points, Phys. Rev. Lett. **99**, 217204 (2007).

[127] I. Radu, K. Vahaplar, C. Stamm, T. Kachel, N. Pontius, H. A. Dürr, T. A. Ostler, J. Barker, R. F. L. Evans, R. W. Chantrell, A. Tsukamoto, A. Itoh, A. Kirilyuk, Th. Rasing, A. V. Kimel, Transient ferromagnetic-like state mediating ultrafast reversal of antiferromagnetically coupled spins, Nature **472**, 205 (2011).

[128] B. Rodmacq, A. Manchon, C. Ducruet, S. Auffret, B. Dieny, Inluence of thermal annealing on the perpendicular magnetic anisotropy of $Pt\backslash Co\backslash AlO_x$ trilayers, Phys. Rev. B **79**, 024423 (2009).

[129] M. Cormier, A. Mougin, J. Ferré, A. Thiaville, N. Charpentier, F. Piéchon, R. Weil, V. Baltz, B. Rodmacq, Effect of electrical current pulses on domain walls in Pt/Co/Pt nanotracks with out-of-plane anisotropy: Spin transfer torque versus Joule heating, Phys. Rev. B **81**, 024407 (2010).

[130] I. M. Miron, G. Gaudin, S. Auffret, B. Rodmacq, A. Schuhl, S. Pizzini, J. Vogel, P. Gambardella, Current-driven spin torque induced by the Rashba effect in a ferromagnetic metal layer, Nature Mat. **9**, 230–234 (2010).

[131] A. Manchon, Magnetoresistance et transfert de spin dans les jonctions tunnel magnetiques, Phd. thesis, Spintec, Grenoble (2007).

[132] R. C. Sousa, J. J. Sun, V. Soares, P. P. Freitas, A. Kling, M. F. da Silva, J. C. Soares, Large tunneling magnetoresistance enhancement by thermal anneal, Appl. Phys. Lett. **73**, 3288 (1998).

[133] L. O'Brien, D. Petit, H. T. Zeng, E. R. Lewis, J. Sampaio, A. V. Jausovec, D. E. Read, R. P. Cowburn, Near-Field Interaction between Domain Walls in Adjacent Permalloy Nanowires, Phys. Rev. Lett. **103**, 077206(2009).

[134] I. M. Miron, K. Garello, G. Gaudin, P.-J. Zermatten, M. V. Costache, S. Auffret, S. Bandiera, B. Rodmacq, A. Schuhl, P. Gambardella, Perpendicular switching of a single ferromagnetic layer induced by in-plane current injection, Nature **476**, 189 (2011).

[135] Y. K. Kato, R. C. Myers, A. C. Gossard, D. D. Awschalom, Current-induced spin polarization in strained semiconductors, Phys. Rev. Lett. **93**, 176601 (2004).

[136] H.-A. Engel, E. I. Rashba, B.I. Halperin, Out-of-Plane Spin Polarization from In-Plane Electric and Magnetic Fields. Phys. Rev. Lett. **98**, 036602 (2007).

[137] O. Mosendz, J. E. Pearson, F.Y. Fradin, G. E. W. Bauer, S. D. Bader, A. Hoffmann, Quantifying Spin Hall Angles from Spin Pumping: Experiments and Theory, Phys. Rev. Lett. **104**, 046601 (2010).

# Abstract

Within the last two decades, domain wall manipulation became one of the undetachable parts of spintronics. The interaction between spin-polarized conduction electrons and localized magnetic moments in terms of giant magnetoresistance in 1988 and in terms of spin-transfer torque in 1996, launched an avalanche of experimental work on current-induced magnetization dynamics. Despite the very intensive research in this field, many fundamental questions stay unanswered. For example, the origin of the phenomenological parameters alpha and beta, being at the heart of the description of the magnetization dynamics, is not fully understood. Usually, in the experimentally studied systems the micromagnetic parameters are fixed, so that it is impossible to verify their role in magnetization dynamics. For example, changing parameters like magnetization or angular momentum, domain wall width, etc., would shed more light on the understanding of the field- or current-induced domain wall dynamics process. In the first part of my work I will describe an alloy of $Gd_{1-x}Co_x$ with a composition, i.e. magnetization, gradient. The alloy composition is chosen in a way that a magnetically compensated interface is present in our thin films. Such a thin film serves as an ideal model system with a continuous change of magnetization at a constant temperature. This system is the subject of a study of field- current- and light-induced magnetization dynamics. In the second part of the work, $Pt/Co/AlO_x$ trilayer, a system already shown to be suitable for fast and reproducible domain wall manipulation is studied. I experimentally tested and proved the hypothesis connecting the spin-transfer torque efficiency with a transverse magnetic field having as origin the Rashba field at the Co interfaces.

# Résumé

Pendant les deux dernières décennies, la manipulation des parois de domaines est devenue l'une des parties inamovibles de la spintronique. L'interaction entre les électrons de conduction polarisés en spin et les moments magnétiques localisés en termes de magnétorésistance géante en 1988 et en termes de couple de transfert de spin en 1996, a lancé une avalanche de travaux expérimentaux sur la dynamique de l’aimantation induite par un courant polarisé. Malgré les recherches très intensives dans ce domaine, de nombreuses questions fondamentales restent sans réponse. Par exemple, l'origine des paramètres phénoménologiques alpha et bêta, étant au cœur de la description de la dynamique de l'aimantation, n'est pas entièrement comprise. Habituellement, dans les systèmes étudiés expérimentalement les paramètres micromagnétiques sont fixés, de sorte qu'il est impossible de vérifier leur rôle dans la dynamique de l'aimantation. Par exemple, un changement d’un paramètres tel que l’aimantation ou le moment angulaire, la largeur de paroi de domaine, etc, pourrait éclaircir la compréhension de la dynamique de parois induite par du champ ou de courant. Dans la première partie de mon travail que je vais décrire un alliage de Gd1-xCox avec un gradient de composition (et donc d’aimantation). La composition de l’alliage est choisi de façon que une interface magnétique compensée est présente dans nos couches minces. Une telle couche mince sert de système modèle idéal avec un changement continu d’ aimantation à une température constante. Ce système fait l'objet d'une étude sur la dynamique de l'aimantation induite par le courant electrique, le champ magnétique et la lumière. Dans la seconde partie de l'ouvrage des tricouches Pt/Co/AlOx, un système déjà montré être adapté à la manipulation des parois de domaines rapide et reproductible, est étudiée. J'ai testé expérimentalement et prouvé l'hypothèse reliant le rendement du couple de transfert de spin à le présence d’un champ magnétique transverse ayant pour origine l’effet Rashba aux interfaces du cobalt.